Applications of ERS satellite radar altimetry in the Lambert Glacier - Amery Ice Shelf system, East Antarctica

by

Helen Amanda Phillips

B. Sc. Hons (University of London)

Submitted in fulfilment of the requirements for the degree of Doctor of Philosophy

Antarctic CRC and Institute of Antarctic and Southern Ocean Studies,
University of Tasmania, Hobart, Australia

12th March 1999

Declaration

I received assistance from others for some of the work presented in this thesis. Development of the ERS altimeter processing software suite (Chapters 3 and 5; Appendix B) was a collaborative effort, with Glenn Hyland of the Antarctic CRC taking the lead role. Processing of the GPS survey data (Chapter 4) was carried out with the help of Peter Morgan of the University of Canberra and Rachael Manson of the University of Tasmania. Roland Warner of the Antarctic CRC was a collaborator with in the flowline and balance flux work (Chapter 7).

The radar altimeter data from the European Space Agency's ERS satellites used in this thesis were provided as part of their Announcement of Opportunity Research Program through Project Id. ERS-A02-AUS103 (Principal Investigator: N. Young). The altimeter data is Copyright ESA 1991, 1992, 1993, 1994, 1995, and 1996.

Apart from those cases already mentioned, this thesis contains no material which has been accepted for a degree or diploma by the University or any other institution, except by way of background information and duly acknowledged in the thesis. To the best of my knowledge and belief no material previously published or written by another person except where due acknowledgment is made in the text of the thesis.

Helen Amanda Phillips

Helen Amanda Phillips

Authority of access

This thesis may be made available for loan and limited copying in accordance with the Copyright Act 1968.

In addition to the above copyright conditions, any material that includes altimeter data or results of analyses, extracted or quoted from this thesis and presented elsewhere, needs to include an acknowledgement to ESA as the source, and the copyright statement.

Helen Amanda Phillips

....

Helen Amanda Phillips

Supporting publications

Some of the work presented in this thesis appears in published papers. Where substantial parts of these papers are reproduced in this thesis, it is in all cases my own original contribution to those papers that is transposed.

The papers directly related to this thesis are:

Chapter 5 (Section 5.2)

Phillips, H. A., I. Allison, R. Coleman, G. Hyland, P. Morgan, and Young, N. W. (1998). Comparison of ERS satellite radar altimeter heights with GPS-derived heights on the Amery Ice Shelf, East Antarctica. *Annals of Glaciology*, 27, in press.

Chapter 8 (Section 8.3)

Phillips, H. A. (1998). Surface meltstreams on the Amery Ice Shelf, East Antarctica. *Annals of Glaciology*, 27, in press.

We came to probe the Antarctic's mystery, to reduce this land in terms of science, but there is always the indefinable which holds aloof yet which rivets our souls.

Sir Douglas Mawson

Abstract

The Lambert Glacier–Amery Ice Shelf system is a major component of the East Antarctic ice sheet. Few accurate elevation data exist for the system, and many of its important glaciological parameters remain uncertain, including the mass budget and location of the grounding zone. This study uses European Remote Sensing satellite (ERS) radar altimeter waveform data to expand knowledge of the system's structure and surface properties.

Surface elevations are derived by retracking ERS-1/2 altimeter waveforms, making corrections for slope-induced error and tides, and are validated against in-situ Global Positioning System (GPS) observations. Elevation differences, at the intersections of the ERS-1 ground tracks with the GPS survey, have a mean of 0.0 ± 0.1 m and RMS of 1.7 m, and are spatially correlated with topographic variations. Two Digital Elevation Models (DEMs) are constructed from the calibrated altimeter heights: one on a 1-km grid for the Amery Ice Shelf only (AIS-DEM), which exhibits unprecedented resolution, and another on a 5-km grid for the entire basin (LAS-DEM). The altimeter DEMs allow new insight into the glaciology of the system.

The AIS-DEM is combined with measured ice thicknesses and a simple density model to derive a 'hydrostatic height anomaly' term (i.e., the excess height above that required for buoyancy). Where this term is close to zero indicates floating ice; this occurs over most of the ice shelf and up the trunk of the Lambert Glacier. Significantly positive values of the term occur around the margins of the floating ice, identifying the location of the grounding zone. A region in the north-west of the shelf, where the ice is known to be afloat, displays anomalous values of the hydrostatic height anomaly term. This is an area of marine ice accretion, where the ice thickness sounder only detected the upper boundary of the accreted layer. These results reveal that the Amery Ice Shelf extends much further south than previously reported, and that the marine ice is up to 200 m thick, oriented along the ice flow direction and restricted to the west of the shelf.

The LAS-DEM is used to define flowlines for the grounded ice within the drainage basin, where the average surface slope determines ice flow direction. These are combined with accumulation distributions to derive balance fluxes for the system. Comparison with flux measurements from a traverse program suggests that the interior of the system has a slightly positive mass budget. The DEMs also provide reference surfaces against which to monitor any future change.

Near-surface snow parameters are estimated from the ERS waveform data using a surface and volume scattering model in the retracking. These indicate that surface scattering dominates the altimeter return power over most of the ice shelf, whilst volume scattering predominates elsewhere. Standing water is detected on the ice shelf by the occurrence of specular returns. This melt-water flowed along surface troughs observed in the AIS-DEM. Backscatter observations along a 3-day repeat track of ERS-1 showed variations in meltstream onset, extent and duration between the 1991-92 and 1993-94 summers.

This study, using derived high-precision altimeter products, has quantified many parameters of the Lambert-Amery system that were previously unknown, and provided a reference against which to monitor any future change in the system. The new findings are consistent with observed *in situ* data and sub-ice shelf model results, and provide credence for the long-term use of altimetric data for ice sheet studies.

Acknowledgements

I must start by thanking the trustees of the 'Northcote Graduate Scholarship' from the Britain-Australia Society. I could never had carried out my studies at the University of Tasmania without this scholarship.

I have been lucky to have had three great supervisors for this degree. Richard Coleman persuaded me I wanted to come and live in Hobart, tempting me with pamphlets containing pictures of Antarctica. I am extremely grateful to Richard for his continued support and faith in me. Ian Allison has also been a great support throughout this project. It turned out well for me that Ian could be in Hobart for the last four weeks of my writing, as he really helped me get through it. Neal Young has also been very helpful, supportive and encouraging. A special note of thanks goes to Neal for making his cakes (almost) vegan so I can eat them!

Glenn Hyland has been a huge support on the software side of things, and also with many other aspects of the project. I am very grateful to Glenn for all the time he spent helping me. Thanks also go to Roland Warner who worked with me on the balance flux work. He was also very helpful and I enjoyed working with him. Peter Morgan has been a significant person in this work right from the start, helping me with the GPS side of things and by reviewing my GPS chapter. At the end of the email-line, on the other side of the world, Jeff Ridley was always there for me and provided me with many useful suggestions. He also reviewed some of the early versions of this work, and I thank him for his ideas and encouragement. Thanks also go to Dave Mantripp for his input at the start of this project, during his visit here.

The Amery survey was a focal point of my project, and I would like to thank everyone involved with that. Mike Craven, our team leader, was excellent to work with and I am sure a vital key to the survey's success. Mike also supplied me with a few figures for my thesis, and I thank him for always being so helpful. Rachael Manson was a great cabin-mate and team buddy in Antarctica, and has remained a good friend throughout my thesis. Thanks also to the other Amery team members: Andrew Ruddell, Peter Johnson, Scott Anglesey and Phil Scholtz. Also everyone who was at Davis during the summer of 1995-96, I will never forget it.

I would like to thank everyone in my room here in IASOS: Katrina, Irina, Andy, Brendan and Anne: thanks for helping me through these last few weeks and I'm sorry I was here for a little longer than I said. Thanks also go to Karen Viggers and Barbara Smith for proof reading early versions of chapters. I am also grateful to everyone in the IASOS/Antarctic CRC and the Antarctic Division Glaciology section, for all their support and for creating an inspiring and friendly work-place.

I want to thank all my family and friends all over the world:

- My wonderful parents, Patricia and David, and my brother Robert;
- My friends and family at home, especially Jacqui, Ros, Gemma and Kate; and my friends here in Australia, especially Cath, Sally, Mandy, Ilse, Paul, Roscoe, Denbeigh and Michelle;
- Sue, Eric and Nanny, my surrogate family in Hobart.

Thanks to all of you for your continued faith in me that I would hang in there and get it finished.

I must also thank the Tasmania University Underwater club and my Underwater Hockey team for helping to keep me sane during my leisure time.

My final acknowledgement goes to Glyn. Without him I would have struggled even harder through this last year. He has been just wonderful in every way ranging from taking me sailing and diving; helping me to relax; and even generating thesis figures for me. It hasn't been easy getting to the end of this tough time, but we have got there, finally. I look forward to the next phase of our lives together.

Table of contents

Chapter 3 **The ERS radar altimeters: operating principles and processing of data collected over ice**

Chapter 4

The Amery Ice Shelf GPS survey

Chapter 5

Validation of ERS heights and generation of Digital Elevation Models

Chapter 6

Application of the Amery Ice Shelf Digital Elevation Model

Chapter 8

Retrieval of surface properties from ERS-1 waveforms over the Lambert-Amery system

List of figures

List of tables

List of acronyms and abbreviations

AGC	*Automatic Gain Control*
AIS	*Amery Ice Shelf*
AIS-DEM	*Amery Ice Shelf DEM*
ANARE	*Australian National Antarctic Research Expeditions*
AUSLIG	*Australian Surveying and Land Information Group*
AVHRR	*Advanced Very High Resolution Radiometer*
AWS	*Automatic Weather Station*
BAS	*British Antarctic Survey*
BL	*Beaver Lake*
BLTM	*Beaver Lake Tide Model*
BoM	*Bureau of Meteorology*
W1 to E13	*Amery Ice Shelf GPS grid: western nodes*
C1 to C13	*Amery Ice Shelf GPS grid: central nodes*
E1 to E13	*Amery Ice Shelf grid: eastern nodes*
C/A code	*Coarse/Acquisition code*
CRC	*Cooperative Research Centre*
CSIRO	*Commonwealth Science and Industrial Research Organisation*
CTD	*Conductivity, Temperature and Depth*
DEM	*Digital Elevation Model*
DEOS	*Delft Institute for Earth Oriented Space Research*
DMSP	*Defense Meteorological Satellite Program*
ECMWF	*European Centre for Medium-Range Weather Forecasts*
EGM-96	*Earth Geodetic Model 1996*
ENVI	*Environment for Visualising Images (image processing package)*

EODC	*Earth Observation Data Centre*
ERS-1	*The first European Remote Sensing satellite*
ERS-2	*The second European Remote Sensing satellite*
ESA	*European Space Agency*
ESRIN	*European Space Research Institute*
ESTEC	*European Space and Technology Centre*
GAMIT	*GPS at MIT (software suite for GPS processing)*
GASP	*Global Atmospheric Assimilation and Prediction Scheme*
GCM	*Global climate model*
GLAS	*Geoscience Laser Altimeter System*
GPS	*Global Positioning System*
GSLIB	*Geostatistical Software LIBrary*
HRPT	*High Resolution Picture Transmission*
HSSW	*High Salinity Shelf Water*
IDL	*Interactive Data Language*
IGS	*International Geoid Service*
IGS	*International GPS Geodynamics Service*
ISW	*Ice Shelf Water*
IPCC	*Intergovernmental Panel on Climate Change*
JPL	*Jet Propulsion Laboratory*
LARGE	*Lambert-Amery Regional Glaciology Experiment*
LAS-DEM	*Lambert-Amery system DEM*
LG	*Lambert Glacier*
LGB	*Lambert Glacier Basin*
LGDB	*Lambert Glacier Drainage Basin*
LGB35	*Lambert Glacier traverse station number 35*

MIT	*Massachusetts Institute of Technology*
MSS	*Multi-Spectral Scanner*
MSSL	*Mullard Space Science Laboratory*
NASA	*National Aeronautics and Space Administration*
NOAA	*National Oceanic and Atmospheric Administration*
NSIDC	*National Snow and Ice Data Center*
NTF	*National Tidal Facility*
OCOG	*Offset Centre-of-Gravity*
P-code	*Precise Code (GPS)*
PLF	*Pulse Limited Footprint*
PRARE	*Precise Range And Range-rate Equipment*
PRN	*Pseudo Random Noise*
RES	*Radio Echo Sounding*
SAR	*Synthetic Aperture Radar*
SCAR	*Scientific Committee for Antarctic Research*
SIO	*Scripps Institute of Oceanography*
SKI	*Static KInematic (GPS processing software)*
SSM/I	*Special Sensor Microwave/Imager*
S/V	*Surface and volume scattering [model]*
TOPEX	*Ocean Topography Experiment*
TEC	*Total Electron Content*
TECU	*Total Electron Content Units*
TM	*Thematic Mapper*
UK-PAF	*UK Processing and Archiving facility*
UTM	*Universal Transverse Mercator*
WGS-84	*World Geodetic System 1984*

List of symbols

Symbol	*Parameter*
T	Travel time of radar pulse
R	Range from satellite to Earth's surface
c	Propagation speed of electromagnetic waves in free space
A	Satellite altitude
h	Surface elevation
φ	Latitude
λ	Longitude
θ_A	Antenna beam-width
t_0	Transmission time
τ	Pulse width
A_f	Area of pulse limited footprint
D_f	Diameter of pulse limited footprint
σ_s	Root-mean-square wave-height
P_R	Power received back at the altimeter
P_T	Transmitted pulse profile
P_S	Function incorporating antenna gain, range distribution and backscattering properties of surface scatters
P_{FS}	Flat surface impulse response of the scattering elements
q	Delay time distribution
Q	Range delay distribution
σ_0	Backscatter
P_T	Transmitted power
ΔR_{dry}	Dry tropospheric correction
ΔR_{wet}	Wet tropospheric correction
ΔR_{ion}	Ionospheric correction
P_0	Surface air pressure
W	Total integrated water content
T	Surface air temperature
E	Total Electron Content
f	Frequency of the altimeter signal
β_1-β_9	Parameters in NASA retracker
A	Amplitude of box in OCOG retracker
p_n	Power in the nth range bin
$T_{x\%}$	Threshold for OCOG retracker(x% of A)
P_t	Transmitted power
P_r	Reflected power
P_{vol}	Volume-scattered return power
θ	Angular distance of volume element from nadir
t''	Two-way incremental ranging time

c_s	Speed of propagation of electromagnetic radiation in surface layer
A''	Amplitude
β_τ	Pulse-width constant
k_e	Extinction coefficient of the surface layer
k_a	Absorption coefficient
k_s	Scattering coefficient
P_{surf}	Surface-scattered return power
γ	Antenna one-way beam-width coefficient
θ_{3db}	Antenna half power beam width antenna
K	Volume scattering coefficient
θ	Surface slope magnitude
ϕ	Surface slope direction
R_m	Measured (retracked) range
R_c	Corrected (relocated) range
R_s	Distance from satellite to centre of Earth
r_α	Radius of curvature of the Earth
a	Semi-major axis of the Earth
e	Eccentricity
γ	Angle subtended at centre of Earth
d	Distance from original point on Earth's surface to relocated point
h_t	Instantaneous surface elevation
h_0	Tide-free elevation component
Δh_{tide}	Temporal tidal elevation component
ρ	Pseudorange GPS observable
ϕ	Phase GPS observable
$\Delta t'$	Biased time delay
ϕ_{total}	Total phase
N	Ambiguity
ε	Error term
Φ	Range
x^i_i	Parameter x from satellite i at receiver j
H	Orthometric surface elevation
$\overline{H}$	Measured orthometric height
Z	Ice thickness
$\overline{Z}$	Measured ice thickness
Z_{mi}	Thickness of marine ice layer
ρ_w	Column-averaged density of sea-water
ρ_i	Column-averaged density of ice
$\underline{\hat{t}}$	Unit tangent
Δs	Distance step
S	Closed area
Ψ_{out}	Outflow

Ψ_{in}	Inflow
$a(x,y)$	Accumulation
$\underline{V}$	Column-averaged velocity vector
β	Velocity azimuth (relative to grid north)
V	Velocity magnitude
θ	Angle of velocity relative to polar stereographic Y-axis
u and v	X and Y components of velocity
$\underline{\Phi}$	Observed flux vector
$\overline{Z}$	Average ice thickness
L	Length of line sector
$\underline{\hat{n}}$	Unit normal
ψ	Observed orthogonal flux component
ϕ	Angle between flux vector and unit normal

Chapter 1 Introduction

1.1 Overview

This study is concerned with applications of ERS satellite radar altimeter data over the Antarctic Ice Sheet. In particular, high precision altimeter products are derived and used to measure and monitor some climatically important ice sheet and ice shelf variables. As part of global climate studies, there is a requirement to establish routine methods through which ice sheet and ice shelf parameters can be monitored. Quantities must be assigned to parameters such as: surface elevation; grounding zone location; amount of basal melting and freezing; amount of surface melting; and mass budget. These are all parameters which may respond to an altered climate, and therefore should be monitored continuously.

Geographically, this thesis concentrates on the Lambert Glacier-Amery Ice Shelf system, one of the major drainage basins of Antarctica. Ways in which the effects of climate change may manifest themselves within the glacial systems are discussed in the context of this system. Examples are given of the application of satellite radar altimetry to the monitoring of ice sheet change, and to understanding the processes of ice sheet-climate interaction. It is demonstrated that radar altimetry, in conjunction with other data, has the potential not only to measure ice sheet topography, but also to map the ice shelf grounding zones, provide information on the processes of melting and freezing underneath the shelves, and to detect changes in surface snow and ice properties. All of these applications contribute to detection of climate change in Antarctica.

1.2 Climate change and Antarctica

1.2.1 Recent climate change facts

In 1995, the Intergovernmental Panel on Climate Change (IPCC) reported that there is evidence to suggest that human activities are having a discernible influence on global climate (Houghton *et al.* 1996). They concluded that increasing greenhouse gas emissions since pre-industrial times have resulted in enhanced radiative forcing of climate, leading to some systematic global changes. IPCC reported that over the last century, average global temperatures have risen by 0.3 to 0.6°C, global sea level has risen by 100 to 250 mm, and Alpine glaciers have generally retreated. They stated that over the last 40 years, where records are more reliable, temperatures have risen by up to 0.2°C.

An announcement released on 8 June 1998 from The White House, in conjunction with scientists from the National Oceanic and Atmospheric Administration (NOAA), stated that 1997 was the warmest year on record (NOAA 1998). The announcement also reported that global mean temperatures for January-May 1998 were the highest on record (since 1895), combined land and ocean temperatures exceeding the former record by 0.25°C. Independent evidence, such as tree-ring and other proxy measurements, indicate that these are the warmest temperatures experienced on Earth for the last 600 years (NOAA 1998).

Temperature records from Antarctic stations also indicate a regional warming trend (Vaughan and Doake 1996a, Jacka and Budd 1998). Vaughan and Doake (1996) reported a regional warming at Faraday Station (on the Antarctic Peninsula) of 0.056°C a^{-1}, based on records since 1945. Jacka and Budd (1998) estimated a mean warming in Antarctica of 0.012°C a^{-1}, based on temperature measurements collected over the last 100 years at inhabited Antarctic stations.

1.2.2 The importance of climate change research

The increasing acceptance of an anthropogenic impact on the Earth's climate on the time scale of a human lifetime has led to worldwide concern among scientists, politicians, and the general public over the last decade. Such changes to our climate might dominate those that occur naturally, and could have devastating long-term effects on the entire planet, its ecosystems and the sustainable future of mankind. This awareness has provoked a new and urgent motivation for studies of the Earth system, and how it may evolve under an unnaturally-altered climate, which is among the most significant research priorities facing scientists today.

The demand for information on the Earth system comes at a time when available technology, such as satellite sensors and computing systems, are well advanced. This is no coincidence, since such advances have occurred in parallel with industrial advances, with which unnatural climate change is intrinsically linked. To ensure optimum management of the Earth's resources in the future, an essential companion to any further development, both in industry and technology, is to increase knowledge of the effects of such developments on the Earth system. Climate change research, at a rate that keeps pace with industrial, agricultural and social development, therefore has an essential role in our future.

1.2.3 Antarctica's role in the global climate system

The Earth is an open system, of continuously interacting components, that imports energy from the sun (solar radiation) and exports energy back into space (terrestrial radiation). The main components of this system (Figure 1.1) are the geosphere (solid surface of the Earth); the biosphere (the region of the Earth's crust where living matter is found); the oceans; the atmosphere; and the cryosphere (ice sheets, glaciers, snow, permafrost and sea-ice).

The Antarctic ice sheet and surrounding sea-ice form important components of the total Earth system, which interact uniquely with the atmosphere and ocean through complex exchanges of energy and mass. While the ice sheet and sea-ice components are relatively stable elements of the system, the effects of climate change have been predicted to be detected first in the polar regions. The Antarctic ice sheet has the potential to play a major role in any sea-level change induced by climate change (Meier 1993; Oppenheimer 1998). The volume of water stored in the grounded Antarctic ice sheet is equivalent to an estimated sea-level rise of 55 m (Drewry 1982), therefore changes in the total ice volume of less than 1% would be significant in global sea level change (Zwally 1978).

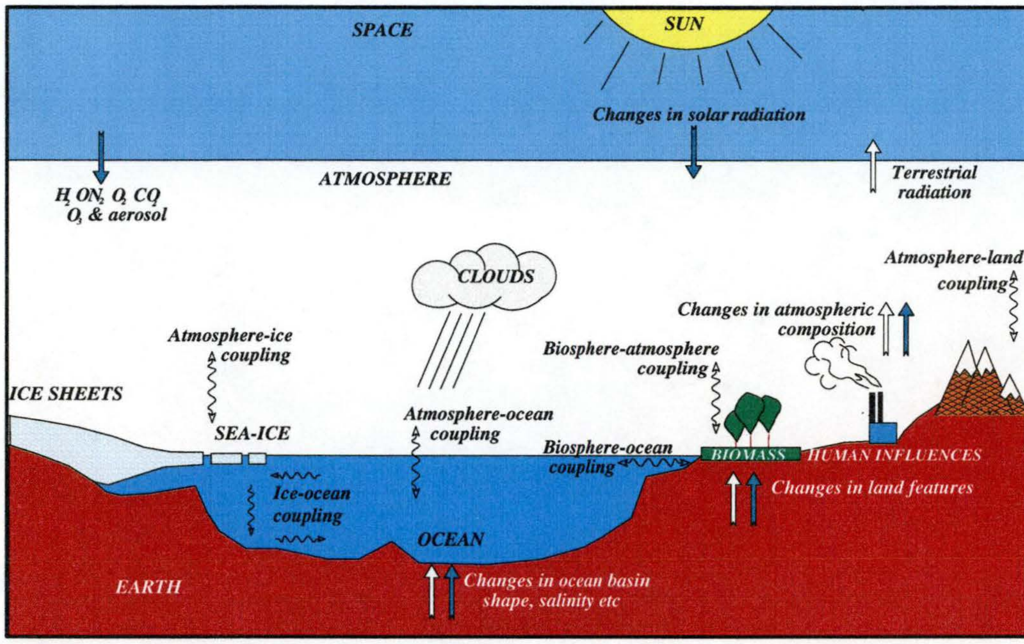

Figure 1.1 *Schematic diagram illustrating the major internal components of the Earth's climate system (in capitals) and their principal interactions. Spiral arrows represent the major coupling that takes place within the system. Green arrows indicate processes external to the Earth climate system and white arrows indicate internal processes in climatic change (adapted from Houghton 1994).*

The mass loss through melt and calving of icebergs from the Antarctic ice sheet is replaced by the accumulation of snow on its surface. There are three major terms in the total mass budget equation for the ice sheet: accumulation (including basal accretion), basal melting and iceberg calving, and the actual mass budget is the difference between the gain terms and the loss terms. For the mass of the ice sheet to remain constant, the difference between the total mass of ice added (by accumulation) and the total mass lost (as icebergs and by melting) must be zero. Any significant change in climate will alter the magnitude of each of these terms, and the mass of the Antarctic ice sheet may be changed. This in turn will influence sea level. It is still not known conclusively whether an increase in global temperature will lead to an increase or decrease in the total volume of ice held in the Antarctic ice sheet (Warrick *et al.* 1996). Furthermore, scientists are unsure about the time-scales over which any changes could take place. A warmer climate is expected to increase the accumulation rates and lead to a greater mass input and therefore a thickening in some regions of the ice sheet, whereas on the ice shelves increased ocean temperatures may lead to enhanced basal melting and increased calving rates. Present evidence is inconclusive as to whether there has already been any significant change in the total mass balance of the Antarctic ice sheet over the last 100 years (Warrick *et al.* 1996). The sheer size of the Antarctic ice sheet presents a major problem in total mass budget studies.

Mass budget estimates for the whole Antarctic ice sheet are difficult to calculate since there are large uncertainties attached to all three components of the mass budget equation. Present estimates of the total mass budget for the continent are subject to differences in sign as well as in magnitude. Jacobs *et al.* (1992) estimated basal melt rates from oceanographic data, yielding an overall (small) negative Antarctic mass balance of 469 Gt yr^{-1} (mass loss). This figure was derived from 2144 Gt yr^{-1} accumulation, (20% uncertainty), 2016 Gt yr^{-1} iceberg calving (33% uncertainty), 544 Gt yr^{-1} (50% uncertainty), and 53 Gt yr^{-1} run-off (50% uncertainty). King and Turner (1997) pointed out that this imbalance is of no great significance, due to the large uncertainties involved, and proposed that the Antarctic ice sheets are probably close to equilibrium at present. Jacobs *et al.* (1996) used revised (higher) estimates of basal melt for some parts of the coast. They concluded that ice shelf melt accounts for more than 25% of the total mass loss, and that there is currently a net mass loss from the Antarctic ice sheet to the ocean.

It is clear from the above discussion that there is a need to establish routine methods for assessing mass balance changes in Antarctica, and to obtain precise measurements of parameters that may change. One of the aims of this thesis is to quantify parameters that may be susceptible change in the Lambert Glacier – Amery Ice Shelf system, using satellite radar altimetry.

1.3 Antarctic glacier-ice shelf systems

1.3.1 Ice sheet drainage basins

The Antarctic Ice Sheet contains several large drainage basins and glacier-ice shelf systems (Figure 1.2). In these systems, the ice originating from the continental interior flows in fast moving ice streams and glaciers, and eventually into an ice shelf, where it meets the ocean.

Climate change will not occur uniformly over the whole of the Antarctic continent; it is more likely to be exhibited as regions of localised warming, and others of cooling.

For this reason, examination of individual drainage basins and glacier-ice shelf systems, rather than of the whole Antarctic ice sheet, is perhaps the most appropriate way to monitor change. This will lead to determination of individual basin responses to climate change. It also ensures that the area of study is on a more manageable scale. Examples of such systems include the drainage basins of the Ross and Filchner-Ronne ice shelves in West Antarctica and the Lambert Glacier-Amery Ice Shelf system in East Antarctica. The latter is the subject of this thesis.

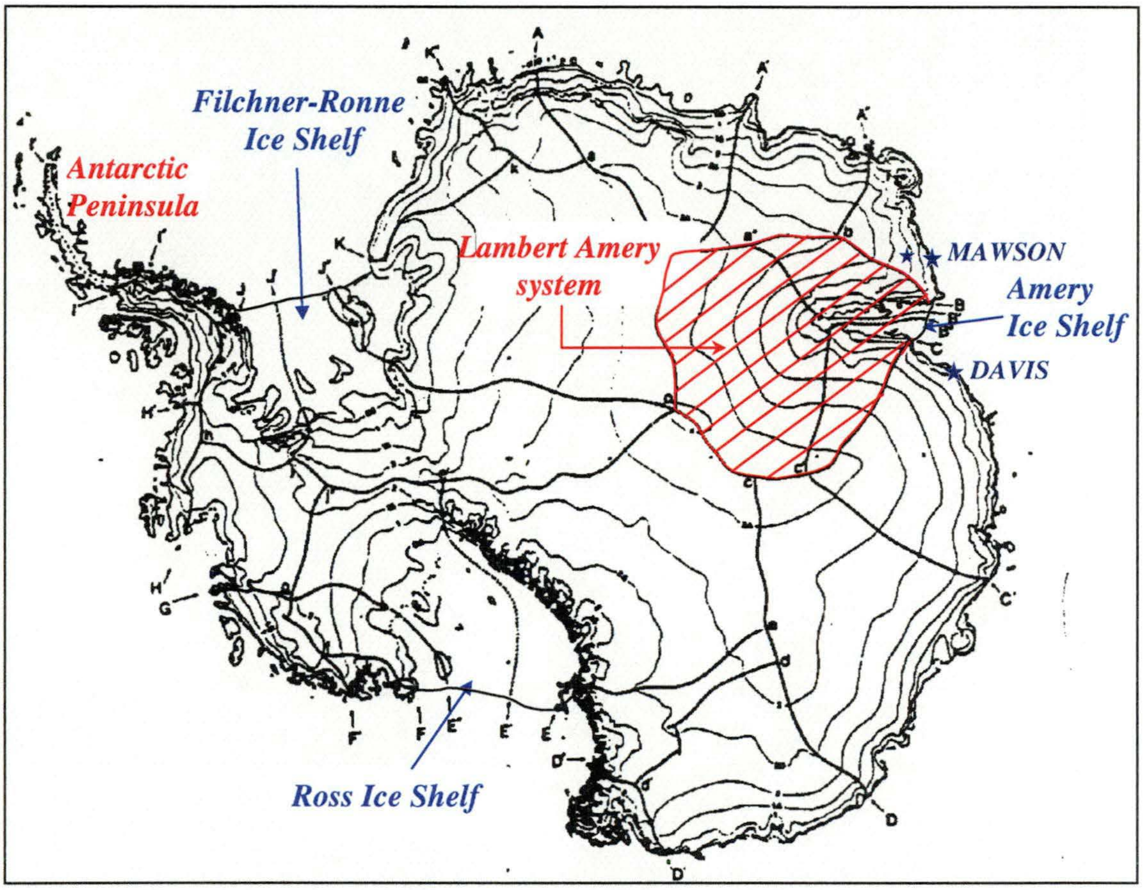

Figure 1.2 *The major ice shelf systems of Antarctica. The Lambert–Amery system is hatched in red. Map taken from Giovinetto and Bentley (1985).*

1.3.2 Lambert Glacier-Amery Ice Shelf system

The Lambert Glacier-Amery Ice Shelf system (hereafter referred to as the 'Lambert-Amery system') is located between latitudes 67°S and 75°S and longitudes 68°E and 75°E, and is the largest glacier-ice shelf system entirely within East Antarctica (Figure 1.2). The Lambert-Amery system is defined in this thesis as: *that portion of the Antarctic ice sheet containing ice that drains through the front of the Amery Ice Shelf.* The Lambert-Amery system covers approximately 13% of the grounded

Antarctic ice sheet (Allison 1979), whereas the Amery Ice Shelf front accounts for only about 1.7% of the total Antarctic coastline (Giovinetto and Bentley 1985). Thus the Lambert-Amery system is highly dynamic, and an important drainage basin in terms of the total mass budget of Antarctica.

1.3.3 Antarctic ice shelves

Floating ice shelves occupy 44% of the Antarctic coastline (Drewry 1983a), 10.8% of the area, and 2-3% of the volume of the entire Antarctic ice mass (Barkov 1985). Most of the mass loss from the Antarctic continent takes place from the ice shelves, via iceberg calving from their outer margins and basal melting beneath them. Ice shelves are thought to be particularly susceptible to climatic change, since a rise in oceanic temperatures would enhance basal melting (Williams *et al.* 1998). A decrease in total ice shelf volume would not contribute directly to sea level change, since floating ice shelves already displace their equivalent mass in sea water. However, since the ice shelves play a buttressing role in ice stream dynamics (Hughes 1992), a reduction in ice shelf volume could increase flow velocities in these streams, leading to a greater discharge of grounded ice.

Mercer (1978) suggested that the Antarctic Peninsula ice shelves (Figure 1.2) were particularly vulnerable to collapse should global temperatures rise, and urged that their status be regularly monitored. Over the last decade there have been numerous reports of recession and break-up of ice shelves on the Antarctic Peninsula (e.g. Doake and Vaughan 1991; Skvarca 1993; Rott *et al.* 1996; Vaughan and Doake 1996b). The mechanism driving the observed ice shelf collapse is not fully understood, although the cause has been linked to a regional warming trend (Vaughan and Doake 1996b; Rott *et al.* 1996; Doake *et al.* 1998). Oceanographic measurements across the front of the Pine Island Glacier have shown that warm Circumpolar Deep Water impacts directly on the base of the floating ice tongue via a deeply-cut channel (Jacobs *et al.* 1996). Jacobs *et al.* 1996 estimated basal melt rates as high as 11.6 m a^{-1}, and suggest that such high melt rates may also apply to other floating ice masses in the South Pacific sector of Antarctica where the continental shelf is relatively narrow.

As the Amery Ice Shelf is at a similar latitude to the major ice shelves of the Antarctic Peninsula, it may also be susceptible to change as a result of rising global temperatures. However, the Amery is a confined bay ice shelf and therefore is protected from the potentially destructive action of the ocean, making it very different to the unprotected, fringing ice shelves of the Antarctic Peninsula.

1.4 Some key variables in Antarctic ice sheet change

The variables included here are those which, as shown in this thesis, can be quantified from the application of satellite radar altimetry.

1.4.1 Surface elevation

A direct method available for determining the state of balance of the ice sheets is the continuous accurate monitoring of the ice surface elevation, as it provides a direct indicator of change. The most accurate method available uses repeat Global Positioning System (GPS) surveys. However, GPS surveys are time-consuming, and can generally only be carried out during summer. Therefore, only limited regions of Antarctica can be surveyed by GPS. GPS surveys could never provide the coverage necessary for building up a Digital Elevation Model (DEM) of a large region with sufficient resolution to answer some of the key climate change questions.

Satellites provide the only practical means of collecting such information. Satellite radar altimeters are currently the most suitable instruments available to measure the surface topography of the Antarctic ice sheet to the desired accuracy and spatial resolution. To address the major climate change questions, accurate satellite radar altimeter maps must be generated in a consistent reference frame for use in future baseline studies. Elevation maps from future altimetric missions (such as the Geoscience Laser Altimeter System (GLAS) on board ICESAT, scheduled for launch in 2001) can then be compared with these baseline maps to assess elevation change.

Periodic measurement of ice sheets by satellite radar altimeters was first suggested by Robin (1966). Altimeters permit the rapid collection of data over large, remote areas that are otherwise inaccessible. Radar remote sensing instruments are invaluable in Antarctica, since they are operated independently of lighting conditions, which facilitates continuous monitoring. In addition, microwave radiation penetrates clouds. There have been several altimeter missions, intended originally for ocean studies, that have provided useful topographic information over Antarctica, eg. the US Navy's Seasat (1978) and Geosat (1985-90) missions, which covered the continent as far as 72.12°S. The European Space Agency (ESA) placed ERS-1 (1991-1996) and ERS-2 (1995-present) in an orbit which extended coverage to 82°S. The ESA altimeters incorporated a specialised 'ice mode' for improved operation over ice.

Data from early satellite altimeter missions have been used to assess elevation changes on the ice sheets (eg. Zwally *et al.* 1989, Lingle *et al.* 1994, Lingle and Covey 1998). However, none of these studies have been able to demonstrate conclusively whether the Antarctic ice sheet is growing or shrinking. Satellite altimeter DEMs of Antarctica have been generated (for the portions of Antarctica within each satellite's coverage) from Seasat data (eg. Zwally *et al.* 1983), Geosat data (Mantripp *et al.* 1992), fast delivery ERS-1 data (Ridley *et al.* 1993; Bamber 1994) and recently from fully processed ERS-1 waveform data (Bamber and Bindschadler 1997).

1.4.2 Ice shelf grounding zones

Systematic monitoring of ice shelf grounding zone locations provides another useful indicator of change within a glacier-ice shelf system. The 'grounding zone' is the transition region between the floating shelf and the sliding ice stream that feeds it (Bentley 1987). The position of the grounding zone is sensitive to changes in ice thickness, sea level and ocean temperatures. Therefore, it could be an important climate indicator. Accurate delineation of the grounding zone of a glacier-ice shelf system is essential in order to assess whether any change in its location has occurred. Various methods have been suggested and applied to locating grounding lines. These include repeat kinematic GPS survey across the grounding zone (Vaughan 1994); tiltmeter measurements (Stephenson *et al.* 1979); and satellite interferometric techniques (Rignot 1998). Time series of static GPS measurements have also been used to reveal tidal motion (Phillips *et al.* 1998; see Chapter 4). Surface elevation measurements made by satellite altimeters can also be used, in combination with ice thickness measurements (Bamber and Bentley 1994), to locate the boundary between floating and grounded ice, which is the location where the buoyancy condition becomes invalid (Chapter 6).

1.4.3 Basal melting and refreezing under the ice shelves

Another important contribution to the mass budget of Antarctica is the amount of basal melting and refreezing that takes place underneath the ice shelves. Since the structure of thermohaline circulation under the Antarctic ice shelves results in a melting/freezing pattern that is linked with ocean temperature (Williams *et al.* 1998b), monitoring the amount of basal melting and refreezing might provide insight into the underlying oceanic conditions. The distribution of melting and refreezing is difficult to determine, since it requires knowledge of the ice shelf structure in its most inaccessible region.

The sub-ice shelf processes can be investigated using ice shelf-ocean models (e.g. Jenkins and Doake 1991; Hellmer and Jacobs 1992, Williams *et al.* 1998b). To validate the sub-ice shelf models, observations of the amount of marine ice accretion need to be made, which is difficult to quantify over large areas. Since ice frozen onto the base of ice shelves contains saline impurities which differentiates it from continental ice, boreholes drilled through the ice shelves can provide measurements of the marine ice layer thickness (Morgan 1972; Engelhardt and Determann 1987; Nicholls *et al.* 1991). However, since the ice is up to 800 m thick in some ice shelves, borehole drilling is time-consuming and logistically difficult to organise. Furthermore, each borehole provides only a single measurement.

Ice thickness maps over parts of Antarctica have been produced from radio-echo sounding (RES) measurements (e.g. Drewry 1983b; Shabtaie and Bentley 1982). However, in regions of the shelf where there is accreted marine ice, the radar may not penetrate to the bottom of the shelf, but obtains a clear reflection from the top of the marine ice layer (Vaughan *et al.* 1995). Under these circumstances, a RES-derived ice thickness map could be compared with one inverted from a satellite altimeter DEM by applying the buoyancy condition (e.g. Bamber and Bentley 1994), which could then be used to derive the marine ice layer thickness, under certain assumptions.

1.4.4 Near surface snow properties

Alterations to climate, and their effects on Antarctic glacier-ice shelf systems, will contribute to altering the surface and near-surface properties of the snow within those systems. Observations of surface properties of the system, both temporally and spatially, are potentially useful for monitoring change within a glaciological system.

Various remote sensing techniques have been employed for monitoring changes in surface properties including optical satellite imagery (Vornberger and Bindschadler 1992) and SAR (Rott and Matzler 1987; Fahnestock and Bindschadler 1993; Fahnestock *et al.* 1993). The satellite altimeter has been used to extract surface property information (Ridley and Partington 1988; Davis and Zwally 1993), with varying degrees of success. Much information is contained in the satellite altimeter return waveform, as its shape is determined by physical characteristics of the target (temperature, density, grain-size and shape, and surface geometry). These properties may be extracted from the waveform through the use of models that describe the instrument and surface microwave properties, and their continuous monitoring might provide insight into changes that are taking place within a glacial system.

1.4.5 Surface melting

Surface melting occurs mostly during summer on some low-lying regions of the Antarctic ice sheet. Melting takes place mainly in the blue ice areas of the glacier-ice shelf systems, where the surface albedo is low. To a lesser extent, melting also occurs in the snow-covered accumulation zone, if air temperatures are high enough. Melt-water is transported downslope in 'melt-water runoff streams' (Winther *et al.* 1996) (hereafter referred to as 'meltstreams'), and collects in surface hollows forming melt-water lakes (Mellor and McKinnon 1960). Meltstreams lead to a redistribution of mass within a glacier-ice shelf system and a loss of mass if they reach the ice front or penetrate the ice shelf at moulins. There are large annual variations in meltstream flow rates, spatial distribution, onset time and duration (Winther *et al.* 1996). These features could be an important factor in the surface mass balance of an ice shelf, and monitoring their distribution could provide a sensitive indicator of regional climatic variability.

Apart from *in situ* observations during summer field programs, surface meltstreams are difficult to monitor each year since they are short-lived and not always found at the same locations. Surface melting has been delimited and timed by various satellite sensors such as SSM/I (Ridley 1993, Zwally and Fiegles 1994) and the ERS scatterometer (Young and Hyland 1998). However, since the spatial resolution of these instruments is only of the order of 25 km, they are not capable of monitoring meltstreams on a kilometre scale. Meltstreams are discernible in satellite imagery from instruments such as Landsat and SAR, but due to the similarity in appearance of wet snow and refrozen water surfaces, it is difficult to monitor their onset time and duration from these images. Satellite radar altimeters have a footprint on the ground of several kilometres. When a strong radar reflector, such as a stretch of open water, is present in the altimeter footprint, a specular return combined with an increase in the measured backscatter will result. Satellite altimetry therefore has the potential, subject to the orbital repeat period and position of its ground tracks with respect to melt regions, to monitor the time of onset and spatial distribution of surface meltstreams (Chapter 8; Phillips 1998). However, reliable monitoring of the duration of meltstream activity remains a problem since a smooth refrozen ice surface will also give rise to a specular return and a high backscatter measurement.

1.5 Thesis aims and structure

The aim of this thesis is to extend the knowledge of the Lambert–Amery system, through the application of ERS satellite radar altimeter data, in synthesis with new and existing *in situ* data. This chapter has discussed the importance of this work, and outlined some of the parameters that can be measured by satellite radar altimeters.

Chapter 2 summarises the existing state of knowledge of the Lambert-Amery system, based on Australian field work carried out between 1962 and 1995, and some remote sensing studies. This information highlights parameters that were unknown when the current work was proposed.

Chapter 3 provides an overview of satellite radar altimetry theory, outlining the major problems encountered over ice-covered surfaces, and discusses methods that have been developed to overcome them. Where a choice of processing techniques are available, a critical analysis is given. These techniques are used to process the ERS-1 and ERS-2 data in this thesis.

The fourth chapter describes a static and kinematic GPS survey designed to validate the ERS altimeter heights on the Amery Ice Shelf. Some subsidiary results of the survey, relevant to the dynamics of the shelf, are also presented.

Chapter 5 presents the results of applying the techniques introduced in Chapter 3 to ERS-1 geodetic phase data over the Lambert-Amery system. A comparison is made between the ERS heights and the GPS heights over the Amery Ice Shelf survey region. After validation, two DEMs are constructed. The first is for the Amery Ice Shelf (AIS-DEM) at 1-km spatial resolution, and the second is for the entire Lambert Amery system (LAS-DEM) at 5-km spatial resolution.

Chapters 6 and 7 present some applications of the AIS-DEM and the LAS-DEM respectively. The AIS-DEM is used, in conjunction with RES data, to locate the boundary between floating and grounded ice and regions of basal ice accretion. The LAS-DEM is used to compute flowlines and balance fluxes for the Lambert-Amery system. The results of these two chapters provide valuable new information about the Lambert-Amery system.

The surface property component of the project is addressed in Chapter 8. This chapter describes the de-convolution of near surface properties from the ERS altimeter waveforms over the Lambert-Amery system using a waveform model. Spatial patterns in the resulting waveform parameters are presented and discussed. On the Amery Ice Shelf, a sudden change in surface properties resulting in a transition to specular return and high backscatter values is investigated, and attributed to the presence of meltwater on the shelf.

Chapter 9 brings together the conclusions of the thesis. The chapter summarises the contribution made by the ERS satellite radar altimeters to the knowledge of the Lambert-Amery system.

Chapter 2 Previous observations in the Lambert-Amery system

2.1 Introduction

The Lambert Glacier-Amery Ice Shelf system is the largest glacier-ice shelf system in East Antarctica. This thesis examines the extent to which the ERS satellite radar altimeters can contribute to the knowledge of the glaciological configuration of the Lambert-Amery system. The purpose of this chapter is to provide background information and a context for this work, by summarising the existing knowledge of the Lambert-Amery system, identifying gaps in this knowledge and areas that require further investigation.

The Lambert-Amery system lies between the Australian Antarctic stations of Mawson and Davis (see Figure 1.2), and has been the subject of many extensive Australian National Antarctic Research Expedition (ANARE) and Soviet glaciological field programs since 1956 (e.g. Budd 1965; Budd *et al.* 1982; Higham and Craven 1997). In the last 15 years, since satellite data have been available, scientists from other countries have also become interested in the Lambert-Amery region, and remote sensing studies have been undertaken using data obtained with various sensors (e.g Brooks *et al.* 1983; Partington *et al.* 1987; Lingle et *al.* 1994; Hambrey and Dowdeswell 1994).

This chapter presents an overview of all major research carried out in the region, including Australian field-work, previous satellite altimeter studies and other remote sensing studies.

2.2 Previous *in situ* observations in the Lambert-Amery system

The Amery Ice Shelf was first sighted by air on 11 February 1931 by Sir Douglas Mawson (Corry 1986). The first ANARE activities in the region took place in January 1955, when the ice shelf front was charted by ship (Law 1967). The first ANARE glaciologist to work on the Amery Ice Shelf was Malcolm Mellor who, from a base at Beaver Lake in 1957, conducted snow and ice studies, supported by fixed wing aircraft. This work was reported in the first paper to be published about the region, 'The Amery Ice Shelf and its Hinterland' by Mellor and McKinnon (1960). The following extract is from this paper, which introduces the general morphology of the area:

> "The land boundaries of the floating ice shelf are well-defined by steep slopes of surrounding continental ice, and by the occasional nunataks and mountains which break through the ice. On the western side continental ice conforms to the subglacial relief. A number of ice streams push out into the ice shelf, flowlines showing up clearly on their wind-swept surfaces, and pressure rolls are formed on the surface of the ice shelf."

From an airborne radar altimeter profile collected over the region, Mellor and McKinnon (1960) observed a discontinuity in the surface slope at 71.5°S, and suggested that this was due to the transition from grounded to floating ice. They observed hard snow-free continental ice surface in this zone, where the ice forms large hummocks, and attributed this to katabatic wind action. They added that layers of snow accumulation gradually bury the continental ice as it moves downstream. Mellor and McKinnon (1960) noted that, during the summer, extensive melting takes place forming 'rivers' and melt-water lakes, on the ice and in rock bowls.

Table 2.1 outlines the major ANARE fieldwork undertaken in the Lambert-Amery system, and the main measurements collected during each field program. The first field program was in 1962 (Law 1967). A party travelled from Mawson in tractors, and then used a dog team to traverse the ice shelf (Budd 1965). In 1971-2, the first air-supported glaciology surveys of the region took place, enabling some more remote parts of the system to be visited and airborne RES

TABLE 2.1 SUMMARY OF MAJOR ANARE FIELDWORK IN THE LAMBERT–AMERY SYSTEM BEFORE THE 1995/6 SEASON.

Dates	Location	Main measurements	Reference
		FIRST GENERATION	
October 1962-January 1963	*AIS (69 to 71°S)*	*Accumulation, strain*	*Budd (1965)*
October 1963-January 1964	*AIS (69 to71°S)*	*Accumulation, strain, borehole temperatures*	*Budd (1965)*
November 1964-January 1965	*AIS (69 to 71°S)*	*Accumulation, strain, relative surface elevation, borehole temperatures*	*Budd (1965)*
		SECOND GENERATION	
March 1968- March 1969	*AIS (69 to 71°S)*	*Accumulation, elevation (optical levelling), deep borehole drilling, micro-meteorology & climatology*	*Budd (1982)*
December 1969-January 1970	*AIS (69 to 71°S)*	*Accumulation, velocity, thickness*	*Budd (1982)*
		THIRD GENERATION	
January-February 1972	*LGB ~1500 m contour*	*Elevation (trigonometrical)*	*Allison (1979)*
	LGB, LG & AIS (71 to 75°S)	*Thickness (airborne RES)*	*Morgan and Budd (1975)*
January-February 1973	*LGB, LG & AIS (71 to 75°S)*	*Thickness (airborne RES)*	*Morgan and Budd (1975)*
January-February 1974	*LGB ~1500 m contour*	*Accumulation, elevation & velocity (trigonometrical)*	*Allison (1979)*
	LGB, LG & AIS	*Thickness (airborne RES)*	*Morgan and Budd (1975)*
		FOURTH GENERATION	
December 1988-January 1989	*AIS & tributaries (70 to 72°S)*	*Accumulation, elevation & velocity (GPS), thickness (RES)*	*Allison (1991)*
January 1990-February 1990	*AIS & tributaries (70 to 72°S)*	*Accumulation, elevation & velocity (GPS) , thickness (RES)*	*Allison (1991)*
December 1990-February 1991	*AIS & tributaries (70 to 72°S)*	*Accumulation, elevation & velocity (GPS)*	*Allison (1991)*
1989-95	*LGB ~2500 m contour*	*Accumulation, elevation & velocity (GPS), thickness (RES), ice cores, borehole temperatures*	*(Higham and Craven 1997)*

The regional acronyms AIS, LG and LGB stand for Amery Ice Shelf, Lambert Glacier and Lambert Glacier Drainage Basin respectively.

data to be collected (Morgan and Budd 1975, Allison 1979). In the late 1980s, the introduction of GPS technology saw the first of a series of GPS surveys take place in the region (Allison 1991).

2.2.1 ANARE Amery Ice Shelf field observations 1962-65

The first major ANARE studies of the Lambert-Amery system were ground-based surveys on the Amery Ice Shelf, which took place over three summer seasons between 1962 and 1965 (Budd 1965; Budd 1966; Budd *et al.* 1967). The primary aim of these early surveys was to collect snow accumulation and strain rate information. Figure 2.1 is the original sketch map (Budd 1966) of the measurement stations established and traverse route followed during these surveys. The traverse route consisted of one longitudinal line (T4-T5), aligned along what was believed to be the central flow-line, and two transverse lines: one in the north (Depot E-T1); and one further south (T3-T2) terminating at Beaver Lake.

During the first season, a 4 m pit was dug at Depot E to obtain a 7-year accumulation record (Budd 1965). A further nine 2 m deep pits were dug along a north-south line (see Figure 2.1) to investigate the change in accumulation rates with distance from the ice front (Budd 1965). A strain grid was set up at Depot E and re-measurement over a four-week period provided the first deformation measurements for the Amery Ice Shelf (Budd 1965). In addition, the ice front was mapped from a ship. A landing was made on the ice front and an astrofix obtained on the same feature used in a previous (Russian) expedition in 1957, to obtain the rate of forward motion of the ice shelf front (Budd *et al.* 1967).

During the second season (1963-64) stakes were placed every 3.2 km along the traverse routes (Figure 2.1) to determine accumulation rates after re-measurement during the following season (G1 to T4; E to T1 and T3 to T2) (Budd *et al.* 1967). Pits were dug to a depth of two metres at each station along the route, and at several intermediate points along the central line. At the same locations, 10 m ice cores were taken, and the temperatures in the boreholes were measured to determine the variation of mean annual temperature with distance from the ice front (Budd 1965). Strain grids were established at G1, G2 and G3, to measure longitudinal and transverse strain rates (Budd 1965). Sun azimuth determinations and position fixes were obtained, to measure orientation and surface ice flow velocity at E, G1, G2, and G3 (Budd 1965).

In the third season (1964-65), the 1963-64 route was followed, with a new site being established at T5 (Figure 2.1). The 1963-64 accumulation stakes were remeasured, and more 3 m deep pits were dug along the central flow line (Budd *et al.* 1967). Ice cores were taken to 6 m, and temperatures measured in the boreholes. The existing strain grids were resurveyed and further strain grids were established at T4 and T5 (Budd 1965). Azimuths and astronomical fixes were repeated at E, G1, G2 and G3, and resections to prominent rock features provided a check on absolute velocity at these sites (Budd 1965). The relative surface elevation profile over the traverse route was measured with three digital barometers, the slopes being checked by theodolite (Budd 1965), providing the first surface elevation information on the Amery Ice Shelf.

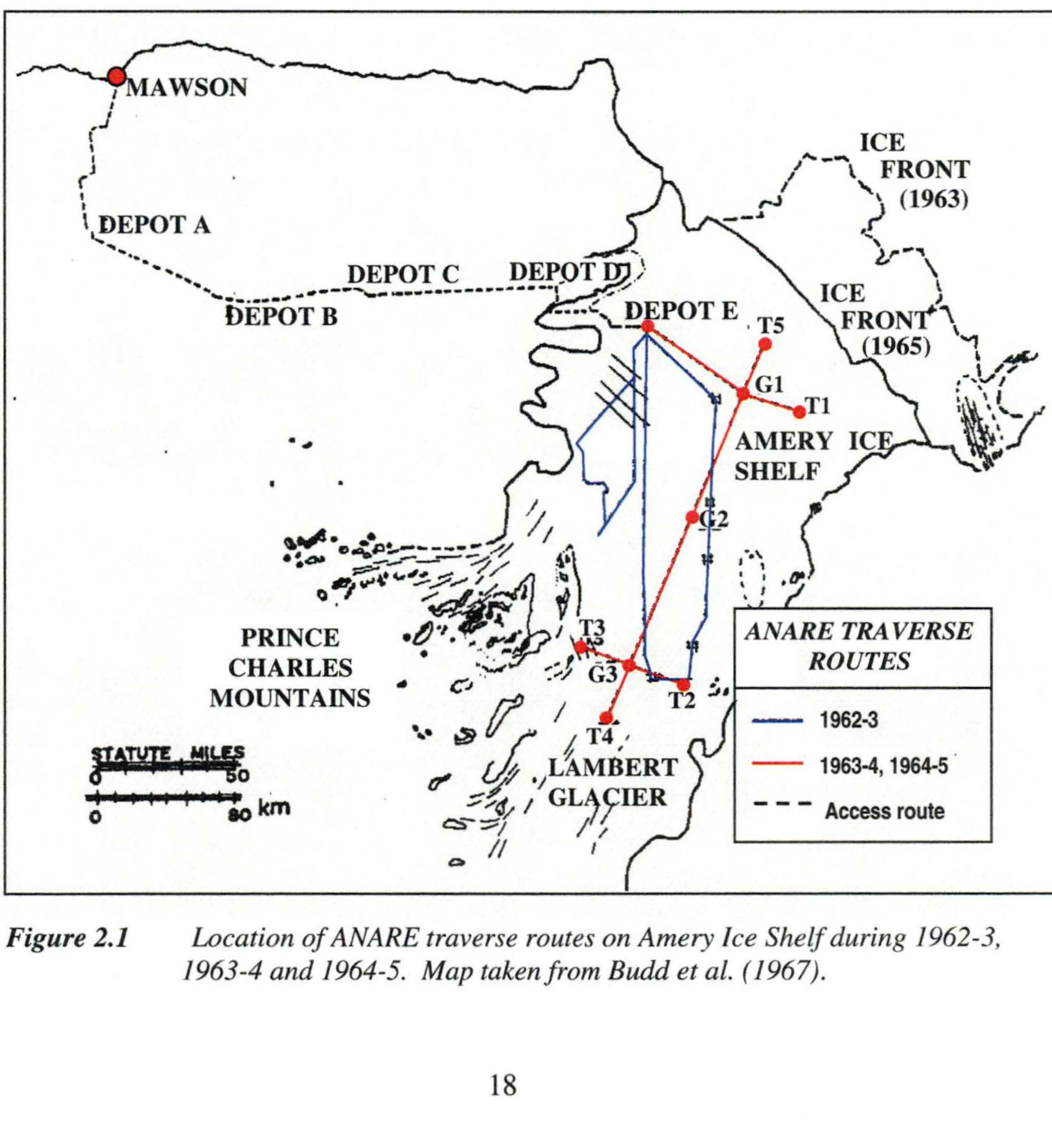

Figure 2.1 *Location of ANARE traverse routes on Amery Ice Shelf during 1962-3, 1963-4 and 1964-5. Map taken from Budd et al. (1967).*

Interpretation of field observations

Budd (1966) completed an analysis of velocity and strain data collected during the 1962-65 surveys, to assess the dynamics of the Amery Ice Shelf. He reported that the surface slopes measured on the ice shelf were very small, increasing gradually from 0.3×10^{-4} near the ice front to 1.2×10^{-4} at G3. The slope was larger (2.0×10^{-4}) where the Lambert Glacier was thought to meet the ice shelf (T4, Figure 2.1). Budd (1966) estimated the ice thicknesses from the surface elevation measurements at the ice front, G1, G2, G3 and T4, assuming hydrostatic equilibrium and using a mean ice density previously calculated for the Ross Ice Shelf. This calculation resulted in the first ice thickness profile of the Amery Ice Shelf. Budd (1966) interpreted the data to show that the ice thickness increases slowly in thickness from the ice front (200 m) to G3 (330 m) and to T4 where there was a marked increase in thickness (530 m).

Budd (1966) reported that, apart from some large tension crevasses parallel to the ice front near T5, and some transverse undulations at the southern end near T4, the central section of the ice shelf was smooth, flat and lacking in features. He found that the ice velocities (at the points E, G_1, G_2 and G_3) increased rapidly towards the ice shelf front (from 410 m a^{-1} to 1500 m a^{-1} at the ice front). Strain rates at these points increased in the same manner. He proposed that the increase in velocity towards the ice front led to longitudinal strain and the formation of crevasses.

Budd (1966) proposed, from energy and mass budget considerations, that the Amery Ice Shelf was in a process of continual (very slow) change, ie., it was advancing and thinning at its front. Over time, this spreading and thinning, combined with ocean interaction (tides, currents and swell) led to the episodic calving of icebergs from the ice front. He proposed that the period of this change of form was about 40 years. A massive iceberg (9600 km^2), approximately one-fifth of the total ice shelf area, calved off the front in 1963 (Budd 1965). From Budd's (1966) estimate, the next break-out is expected around 2003.

Budd (1966) reported that the accumulation rates increased to the north, from net ablation on the Lambert Glacier to 1 m of snow accumulation at the ice shelf front, and decreased from the centre of the shelf towards the katabatic zones on its periphery. Analyses of the core and pit information revealed that accumulation rates had been similar in previous years (Budd 1966). Budd *et al.* (1967) further examined the accumulation pattern of the ice shelf, and its variation since 1956, and constructed isopleths of mean accumulation over the shelf. From this distribution, they calculated the total mass gain of the ice shelf due to accumulation.

Budd *et al.* (1967) estimated transverse velocity profiles across the shelf through G1 and G3 from the velocity and strain measurements. Using these velocity profiles and the ice thickness estimates of Budd (1966), they derived mass fluxes through cross sections at G1, G3 and the ice front. The mass flux across G3 due to ice flow was estimated at $8.8 \times 10^{12} \pm 45\%$ kg a^{-1}, and that across G1 at $17.8 \times 10^{12} \pm 30\%$ kg a^{-1} (Budd *et al.* 1967). Budd *et al.* (1967) attributed the increase to a combination of two factors: the extra inward flow from the ice boundaries further north; and accumulation over the intervening surface. They estimated these two components at $1.6 \times 10^{12} \pm 40\%$ kg a^{-1}, and $6.2 \times 10^{12} \pm 15\%$ kg a^{-1} respectively. Given the large errors associated with each calculation, Budd *et al.* (1967) concluded that the ice shelf was close to balance. However, they noted that it could be slightly negative, with the supply of ice up to 20% lower than the loss at the front, resulting in a thinning of the shelf of up to 6 cm a^{-1}. Budd *et al.* (1967) calculated the total accumulation over the interior, from estimates of accumulation in the interior of the Lambert Glacier system. This appeared to be 3 times greater than that required to balance the discharge of the Amery Ice Shelf, which implied a positive mass budget for the interior of the system (Budd *et al.* 1967).

2.2.2 ANARE Amery Ice Shelf field observations 1968-70

The second generation of ANARE field programs in the Lambert-Amery system was composed of two campaigns on the ice shelf (Budd *et al.* 1982). During the first campaign, a base camp was established at G1 (see Figure 2.1) and occupied between March 1968 and January 1969. At this site, an ice core was drilled to 315 m depth into the shelf to obtain the vertical ice temperature distribution and to allow ice core sampling (Budd *et al.* 1982). During the spring and summer, a survey to measure the surface elevation profile of the ice shelf was carried out over the route shown in Figure 2.1, using a Tellurometer MRA-2 microwave electronic distance meter and an automatic optical level. Markers were placed for ice movement stations, to allow reoccupation in the following season. The survey was tied to fixed points on rock, at Sandefjord Bay, Jetty Peninsula, Manning Nunataks and Fisher Massif, by astronomical techniques (Budd *et al.* 1982).

The following summer (1969-70) the markers were relocated and re-levelled and the snow accumulation measured. Ice thickness measurements were made along most of the traverse route using a ground-based radio echo sounder (Budd *et al.* 1982).

Results of 1968-70 surveys

The results of the 1968-70 surveys were reported by Budd *et al.* (1982). These authors estimated that, after reduction of the levelling data, the height error over the entire network amounted to 0.5 m; the relative error over several kilometres being within 10 mm. From the new ice surface elevations Budd *et al.* (1982) found that the surface of the Amery Ice Shelf had a steeper slope than previously measured, at 1.8×10^{-4} on the large scale.

Budd *et al.* (1982) examined the relationship between the surface elevations and ice thickness along the centre line of the traverse route (measured in 1969-70 and 1971-74). The surface and basal profiles they obtained are shown in Figure 2.3. Small-scale (1-5 km) surface and basal undulations were revealed that appeared to be linked. The ratio between surface elevation and thickness increased to the north, from 0.113 (near T4) to 0.160 (near the ice front). Budd *et al.* (1982) attributed this to the increasing snow accumulation towards the ocean, which reduces the vertically averaged density of the ice column and increases its overall buoyancy. About 3 km south of T4, a maximum change in surface slope (14 m in 19 km) accompanied by only a small deviation in ice thickness was interpreted to indicate the grounding line, and a small amount of thickening was noticed north of this point. Budd *et al.* (1982) noted that this was a region of ablation, with a high density 'blue-ice' surface, which extended for approximately 19 km. At G1, the elevation and ice thickness were 64 m and 450 m respectively, implying an averaged density of 890 kg m^{-3}, which matched the borehole measurements (Budd *et al.* 1982). Small-scale fluctuations were observed, on the surface over wavelengths several times the ice thickness, which Budd *et al.* (1982) interpreted as partial groundings.

Budd *et al.* (1982) concluded that the velocity distribution over the ice shelf (Figure 2.2) was governed primarily by the substantial surface slope towards the ice front, and the high restraining shear stress along the sides. They noted that this resulted in a northerly increase in observed ice velocities along the central flow-line, reaching 1200 m a^{-1} at the ice front, and a lateral decrease in velocities moving away from the central line, tending to zero at the sides.

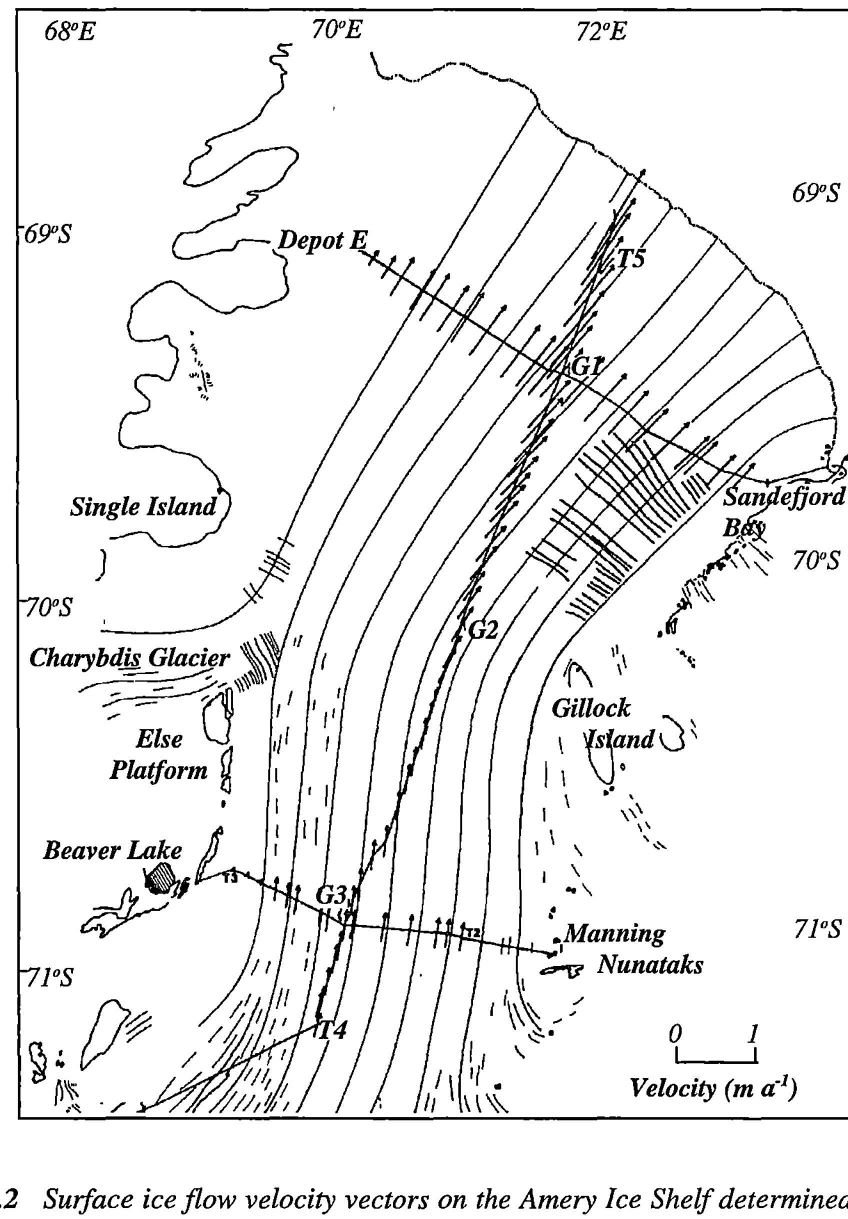

Figure 2.2 *Surface ice flow velocity vectors on the Amery Ice Shelf determined during the 1968-70 surveys, together with estimated flowlines from the vectors and satellite imagery. Taken from Budd et al. (1982).*

The ice core taken at G1 was chemically analysed to determine the ratio of $^{18}O/^{16}O$ isotopes (Morgan 1972). The results, presented by Morgan (1972), showed that the

Amery Ice Shelf consists of three distinct layers each containing ice from a different source. Morgan (1972) and Wakahama and Budd (1976) identified these layers as:

i) a firn layer (0-70 m) formed by the accumulation of snow on the ice shelf;

ii) a continental ice layer (70-270 m) consisting of continental ice flowing from the Lambert Glacier; and

iii) a marine ice layer (below 270 m) formed by the refreezing of the sea-water onto the base.

Morgan (1972) inferred that the thickness of the marine ice layer was 158 m (from the radar-measured ice thickness of 428 m at G1). Using the measured ice velocities and distances, and the total thickness of 428 m, he calculated a basal refreezing rate of 0.3 ma^{-1}. The freezing rate was later estimated from the borehole temperature profile as approximately 0.6 m a^{-1} (Budd *et al.* 1982).

To derive particle paths along the centre-line, Budd *et al.* (1982) calculated transverse and longitudinal strain-rates from the velocity data along the central flow-line, which they used to calculate vertical strain-rates. Combined with velocity and ice thickness data, this allowed determination of the relative vertical particle spacing, and therefore of particle paths (Figure 2.3). Budd *et al.* (1982) suggested that the paths taken by particles deposited on the surface were controlled by surface elevation and accumulation. They proposed that the difference between calculated basal particle paths and the measured base gave the freezing rate.

Budd *et al.* (1982) noted that the integrated amount of ice frozen onto the base was greater than the thickness of the actual layer because of thinning. Their computed basal growth rate suggested a significant build-up of ice under the ice shelf from T4 until around 70 km from the ice front. The profile, which was confirmed by observations in the G1 core, predicted an accumulated marine ice layer with a maximum of 200 m near G1 and minimum of 100 m near the ice front. Budd *et al.* (1982) proposed that the reduction in the amount of marine ice occurred due to an increasing rate of strain thinning, which reduced the total ice thickness as the ice moved northwards. They added that this thinning periodically led to iceberg calving, suggesting that this was the major limiting factor to the forward growth of the ice shelf, as opposed to melting.

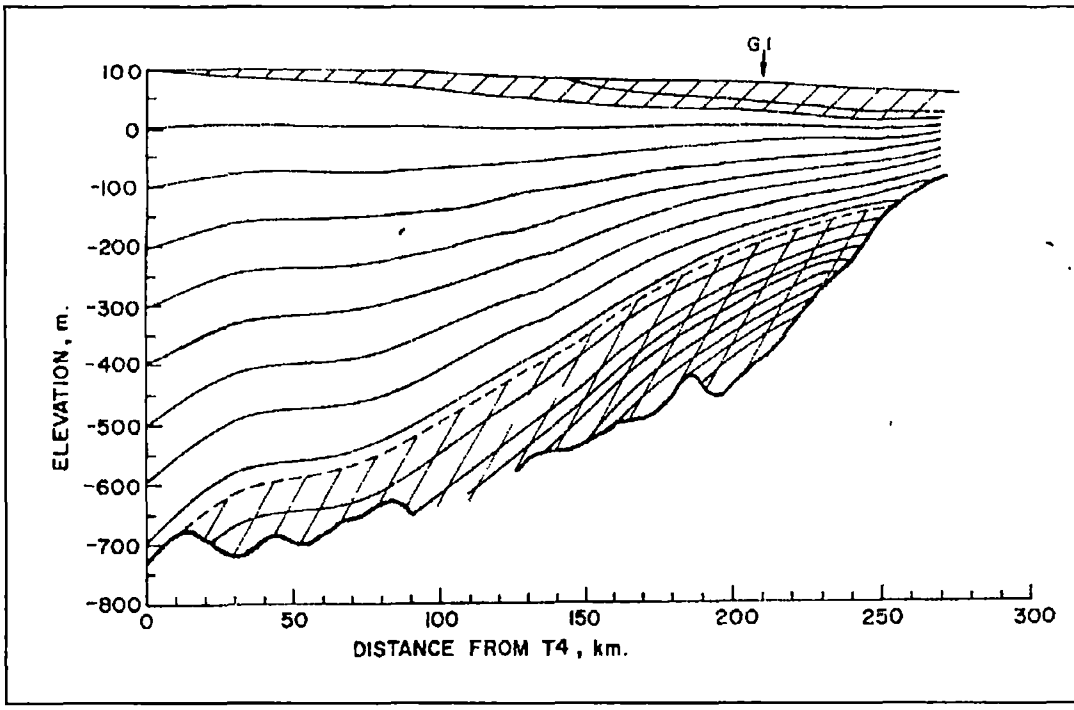

Figure 2.3 *Thickness distribution of surface firn layer, continental ice layer and marine ice layer along the central flowline of the Amery Ice Shelf. Particle paths derived from observed deformation data are also shown, together with the location of the G1 core. Taken from Budd et al. (1982).*

2.2.3 Amery Ice Shelf fieldwork 1971-74

The third generation of ANARE field operations in the Lambert-Amery system took place south of the Prince Charles Mountains, during three air-supported campaigns in the 1971-72, 1972-73 and 1973-74 summer seasons (Allison 1979, Morgan and Budd 1975). Eleven ice movement stations were established in 1971-72 in a perimeter around the ice streams of the Lambert Glacier system (see Figure 2.4), and their positions obtained by MRA-3 Tellurometer and theodolite measurement (Ian Allison, personal communication, 1998). Elevations were determined to second order accuracy by measuring reciprocal vertical angles to surrounding mountains (Allison 1979). The sites were re-occupied two years later, providing ice velocities. Aerial RES data were collected during all three seasons using Mount Cresswell as a base camp (Morgan and Budd 1975).

Results of 1971-74 fieldwork

Morgan and Budd (1975) presented the major results of the 1971-72 and 1973-74 RES measurements. They stated that during these flights, navigation was controlled mainly by line of sight to principal topographic features. Positioning errors were estimated at 5 km at the end of the longer lines. Values of ice thickness and surface elevation were obtained from the films at 3-km and 10-km intervals respectively, along a total length of 6900 km (Morgan and Budd 1975). From these data, Morgan and Budd (1975) constructed contour maps of surface elevation, ice thickness and bedrock elevation, which they overlaid onto Band-7 Landsat-1 images to aid their interpretation. Morgan and Budd (1975) reported that the Lambert Glacier lay in a vast, deep subglacial valley, and bedrock elevation in the region varied between 2000 m below sea-level and 3000 m above sea-level (at Mount Menzies). They noted that deep valleys and ridges with relief greater than 1000 m channelled ice into the main Lambert Glacier. Morgan and Budd (1975) reported a maximum ice thickness measurement of 2500 m, in the subglacial bedrock depression in the region of confluence of the three major ice streams, the Lambert, Mellor and Fisher Glaciers. The RES profiles here indicated a significant back-slope in the bedrock topography. This, when combined with evidence for high melt production in this region and a strong echo from the bedrock, suggested the presence of a basal melt lake in the depression. Deep subglacial streams, which penetrated well below the ice surface, were also revealed in the radar echoes. The surface topography channelled the ice from these streams into the Amery Ice Shelf (Morgan and Budd 1975).

Allison (1979) used the field data collected between 1968 and 1974 to estimate the mass budget of the Lambert Glacier Drainage Basin (LGDB). The LGDB is enclosed entirely within the Lambert-Amery system, and is that part of the system which drains through the major ice streams entering the rear of the Amery Ice Shelf (see Figure 2.4). It does not include any ice that originates from the part of the Lambert-Amery system to the west or east of the Amery Ice Shelf. Allison (1979) divided the

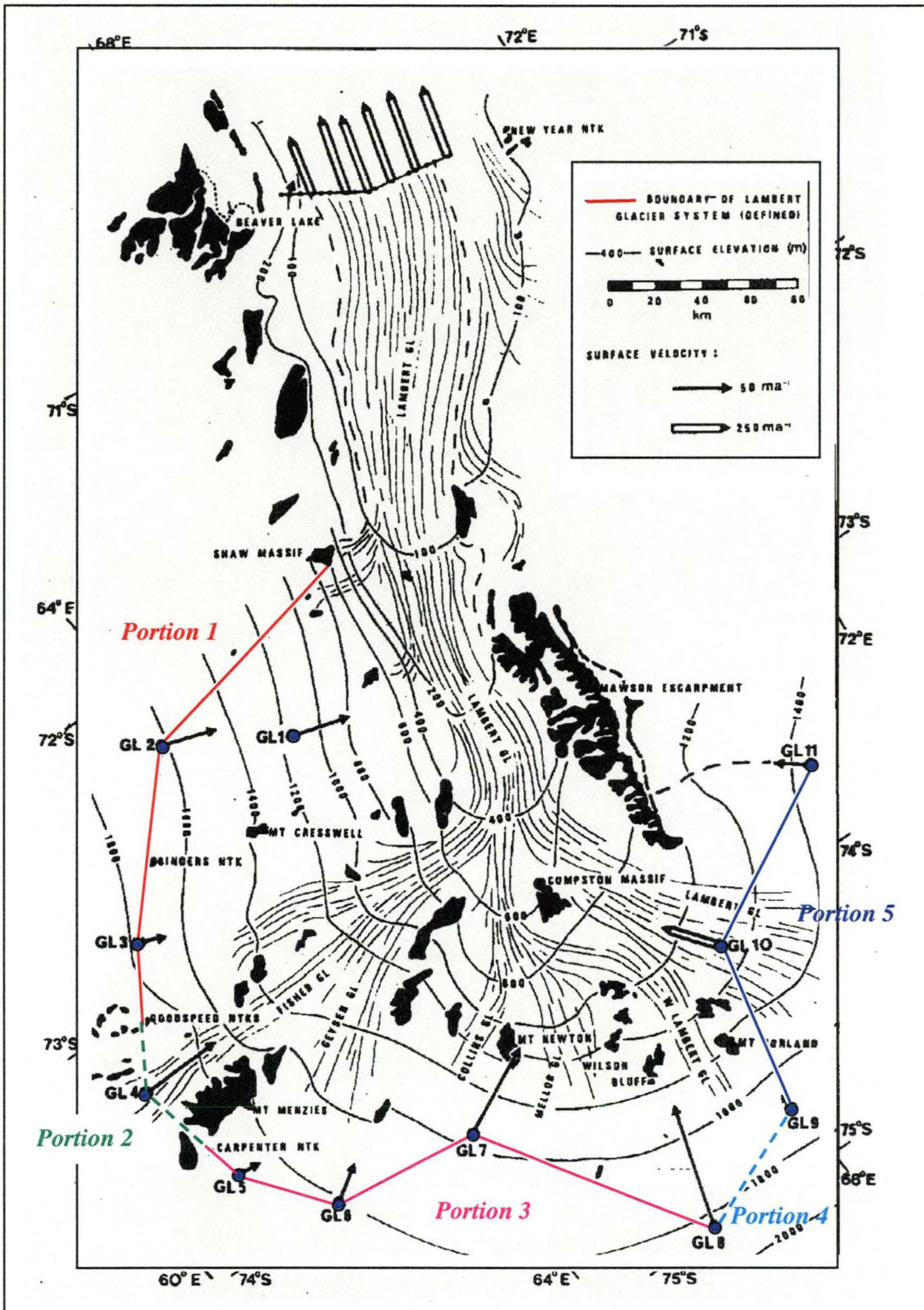

Figure 2.4 *Location of the Lambert Glacier system defined by Allison 1979 (1979) illustrating the location of the GL sites (GL1 to GL11) and the five portions used for flux calculations. Taken from Allison (1979).*

LGDB into two sub-regions, one upstream and one downstream, separated by a boundary defined by the eleven ice movement stations established during the 1971-

72 season. The upstream region was the inland accumulation area (interior basin) that drained into the downstream region (the Lambert Glacier system), which included the southern Amery Ice Shelf up to latitude 71°S.

Allison (1979) estimated the area of the interior basin (from contours on the American Geographical Society 1: 5 000 000 map of Antarctica (1970) supplemented with 1971-72 ANARE and JARE data) at 1.09×10^6 km$^2 \pm 20\%$. For the accumulation distribution, he used a Russian compilation, that included Australian and Russian accumulation measurements. This compilation was modified so that the 100 kg m^{-2}a^{-1} isopleth passed north of the Lambert Glacier, to agree with the low values measured at the ice movement stations. Allison (1979) obtained an estimate for the total flux into the interior basin of 60 Gt a^{-1}, equivalent to an average net accumulation over the basin of 55 kg m^{-2}a^{-1}.

Allison (1979) divided the 730 km GL line into 5 portions (Figure 2.4), and estimated the total flux across the line, from ice velocities measured at GL1 to GL11 combined with ice thicknesses. He reported that the greatest measured ice velocity was upstream of the Lambert Glacier (230 m a^{-1}), where the highest strain rates were also measured. Allison (1979) interpolated velocities at between-station points, using Landsat imagery to identify fast moving streams where interpolation errors would be larger. He used a surface velocity ratio (i.e. the ratio of the depth-averaged column velocity to the surface velocity) of 0.8. Angles between the GL line and the ice flow direction between-station points were estimated from the Landsat imagery combined with surface slope information from the elevation contours of Morgan and Budd (1975). Table 2.2 summarises Allison's (1979) results.

The total flux into the Lambert Glacier system was estimated to be approximately 30 Gt a^{-1} (Table 2.1). Of this total, 39% was transported in the main Lambert Glacier across 23% of the total length of the GL line (Portion 4). Allison (1979) estimated a total error of 30% in the calculated value of the total ice flux, by repeating calculations with slightly varied input data.

At the downstream boundary of the Lambert Glacier system, where it met the Amery Ice Shelf, Allison (1979) performed flux calculations using ice surface velocities derived during the 1968-70 ANARE surveys and RES measurements of ice thickness. He estimated the width of this section across the Amery (containing ice originating in the Lambert Glacier system) at 50 km using flowlines from Landsat imagery. As the ice is freely floating here, the surface velocity ratio was taken to be 1.0. Allison (1979) estimated the total mass flux through this section across the ice shelf as 11.1 Gt $a^{-1} \pm 15\%$.

TABLE 2.2 MASS FLUX ESTIMATES INTO LAMBERT GLACIER SYSTEM, FROM ALLISON (1979).

Portion	*Name*	*Length (km)*	*Flux (Gt a^{-1})*
1	*north-west*	*223*	*3.5*
2	*Fisher Glacier*	*49*	*1.5*
3	*southern sector*	*178*	*7.8*
4	*West Lambert Glacier*	*111*	*5.5*
5	*Lambert Glacier*	*169*	*11.5*
	TOTAL	***730***	***29.7***

Ice losses in the Lambert Glacier system occur via two processes: surface ablation and basal melting (Allison 1979). Allison (1979) estimated the total area of the ablation regions in the system from blue ice areas observed in Landsat imagery. He estimated mean ablation rates for these areas based on mean air temperatures. Allison (1979) estimated the total loss at 5 Gt a^{-1} (1.7 Gt a^{-1} to 6.7 Gt a^{-1}). By computing the basal shear stress for the grounded ice, using ice thickness and surface slopes derived from Morgan and Budd 1975, Allison (1979) estimated the amount of basal melting (upstream of T4) as 2 Gt $a^{-1} \pm 100\%$. These results combined to yield a total estimated ice loss of 7 Gt a^{-1} for the entire system, with lower and upper limits of about 2 and 13 Gt a^{-1} (Allison 1979).

Allison's (1979) estimated a mass influx for the interior region of the LGDB of 60 Gt a^{-1}. When combined with his estimate of outflux into the main channel of the Lambert Glacier (30 Gt a^{-1}) this yielded an overall mass budget for the interior of +30 Gt a^{-1}. Allison (1979) stated that, of this 30 Gt a^{-1} received by the Lambert Glacier system, 7 Gt a^{-1} was lost to ablation and basal melting and 11 Gt a^{-1} via outflow into the Amery Ice Shelf. From these results, he proposed that the system had a positive mass budget of 12 Gt a^{-1}. Allison (1979) calculated that his estimates were equivalent to a surface rise of 0.03 m a^{-1} (water equivalent) averaged over the interior basin and 0.04 m water equivalent averaged over the total drainage basin. By considering geomorphological evidence from the southern Prince Charles Mountains, which revealed that ice levels in the Lambert Glacier system have fallen in the past, Allison (1979) suggested that this imbalance could be due to the build-up of ice following a surge.

McIntyre (1985a) re-calculated the mass budget of the LGDB, using revised estimates of both the area of the LGB and the accumulation rates in the basin. He estimated the area of the basin from an improved surface elevation data set, which included altimetry from RES and constant density balloons. This resulted in an area that was 17% less than Allison's (1979) estimate. Furthermore, by interpreting the dark regions in Landsat imagery as patches of bare ice, McIntyre (1985a) proposed that the accumulation rate was much lower than Allison (1979) had estimated. He suggested that the entire LGDB was subject to strong katabatic wind action, leading to high surface ablation rates. This was supported by an analysis of passive microwave data carried out by Zwally and Gloersen (1977), who found anomalously low brightness temperature values in the Lambert Glacier Basin. McIntyre (1985a) estimated the total mass influx into the interior basin as only 32 Gt a^{-1}, close to the mass outflux to the Lambert Glacier system, suggesting a slight positive mass budget of 2 Gt a^{-1} $\pm$ 13 Gt a^{-1}.

Allison *et al.* (1985) responded to McIntyre's (1985a) revision by criticising his interpretation of the Landsat imagery. These authors suggested that some of the dark patches on the imagery, taken as bare ice, were in fact accumulation areas subject to winter surface glazing. They further suggested that strong katabatic winds would not cause high ablation rates because of the low temperatures encountered in the basin. Allison *et al.* (1985) pointed out that low passive microwave values could result from different crystal structures in the snow-pack as a result of wind glazing. Using McIntyre's (1985a) value for the area of the basin, Allison *et al.* (1985) obtained an updated estimated mass input of 50 Gt a^{-1}, and an output of 30 Gt a^{-1}. Allison *et al.* (1985) noted that this estimate left the system still substantially in positive balance.

In his final correspondence, McIntyre (1985b) pointed out that measurements at Mizuho station revealed that strong katabatic winds could lead to ablation, even at very low temperatures. He informed that the low brightness temperature measurements obtained by Zwally and Gloersen (1977) did not just occur in the wind-glazed areas, but were found over the whole basin. McIntyre (1985b) and Allison *et al.* 1985 agreed that more ground truth data, particularly for accumulation rates, were required. These studies of the LGDB demonstrate that conventional methods of calculating mass budget are extremely sensitive to estimates of the size of the catchment and the distribution of accumulation.

2.2.4 Lower Lambert Glacier ANARE surveys 1988-91

The fourth generation of ANARE surveys in the Lambert-Amery system took place during three consecutive summer seasons between 1988 and 1991 (Allison 1991). These studies were part of the Lambert-Amery Regional Glaciology Experiment (LARGE), and were the first ANARE surveys to use GPS. The campaigns served to provide a reference for past and future studies for the monitoring of any changes, and to make measurements with emphasis on (Allison 1991):

i) Large scale structure	Determination of the structure of the glacier streams Definition of the grounding zone Estimation of the ocean depth below the ice shelf
ii) Mass budget	Estimation of mass flux across sections perpendicular to glacier flowlines and into the Amery Ice Shelf from major tributary glaciers and across its margins
iii) Small scale structure	Investigation of surface processes on the glacier and ice shelf (accumulation, snow properties, melt rates, sastrugi orientation).

In the 1988-89 summer season, twenty-nine ice movement stations (GA1 to GA29) were established using single frequency GPS receivers (Allison 1991). Of these stations, 10 were located around the supposed grounding zone (near 71.5°S), 13 near the confluence of the Charybdis and Scylla glaciers and 6 upstream, on the Charybdis and Scylla glaciers themselves (Allison 1991). Airborne RES measurements were collected from a Twin Otter aircraft, over more than 4500 km, of the Lambert Glacier, and six transects across the Amery Ice Shelf (Allison 1991). More detailed RES was carried out in the supposed grounding zone from a helicopter. Shallow

(2 m) cores were taken from 12 locations in the confluence region between the Charybdis and Scylla glaciers and the Amery Ice Shelf (180-200 km from the ice front), and eight locations in the supposed grounding zone. Accumulation stakes were placed at these locations, which were remeasured in 1989-90 and 1990-91 (Allison 1991).

The following season (1989-90), fifteen of the ice stations were reoccupied with dual frequency GPS receivers (Allison 1991). Measurements of accumulation and gravity were also made at these sites, and ice cores were taken for stratigraphic analysis. RES measurements by helicopter were completed (Allison 1991).

During the 1990-91 season, the 1988-89 stations were again re-occupied, and eight new stations were added in the vicinity of the supposed grounding zone (Allison 1991). Two of the 1968 Amery Ice Shelf survey markers were also relocated. Gravity and barometric levelling traverses were completed across the ice shelf from Else platform to Corry Rocks, from Beaver Lake to Anniversary Nunataks and along the ice shelf spanning the supposed grounding zone (Allison 1991). Other measurements carried out throughout the season included: snow accumulation (relocated stakes from 1988-89), shallow core sampling, surface snow structure, extent of surface melt, and orientation of sastrugi and dunes (Allison 1991).

Results of 1988-90 surveys

Data from these early GPS surveys were noisy, due to a combination of high ionospheric noise, associated with a period of high solar activity, and the unsophisticated GPS receiver technology (Chapter 4). Initial analysis of the single frequency GPS data produced low quality results, although velocities over the 1988-89 to 1990-91 time interval were adequate (Ian Allison, personal communication, 1998). The measurements were summarised, and preliminary conclusions made, by Allison (1991). The additional velocity measurements contributed to the pattern of the overall ice shelf dynamics.

Allison (1991) reported that a large volume of ice flowed into the Amery Ice Shelf from the eastern margins, near Pickering Nunatak. This volume was substantially more than from near Fisher Massif on the western side. Along the 'centre-line' of the shelf, velocities decreased from 400 m a^{-1} at the most upstream points measured, to 330 m a^{-1} at the supposed grounding line, accompanied by a decrease in surface slope and change in ice thickness and ice stream width. Beyond this point, the ice accelerated as it spread and thinned, reaching a speed of 480 m a^{-1} between Single and Gillock Islands. In the Charybdis and Scylla Glaciers, ice flow velocities were low upstream, where the ice was up to 3-km deep. Velocities increased downstream to 250 m a^{-1} where these glaciers merged with the ice shelf, between Single Island and Else Platform (see Figure 2.2). At this point, the ice shelf flowed NNE at around 480 m a^{-1}, and large strain rates occurred here due to the shear between converging streams (Allison 1991).

Relocation of two 1968 survey markers allowed determination of the long term velocity of the ice, averaged over 22 years, which was compared with the velocity derived from re-measurement in 1970 (Allison 1991). The velocities agreed to within 0.5%, and Allison (1991) concluded that there had been no apparent change in velocity over this time. Allison (1991) also reported that the elevations measured in 1990-91 were within 2-3 m of those measured in 1968-69. He added that this was within the reasonable limits of longitudinal surface undulations, and the different survey methods used. It therefore provided no evidence of surface elevation change. Although there were no apparent changes in velocities or surface elevations, Allison (1991) did note that surface conditions varied significantly, even over the three years spanned by these surveys. Over these seasons, the large melt lakes along the length of the glacier (upstream of the proposed grounding zone) had advanced downstream by 15 km. Allison (1991) suggested that this reflected inter-seasonal variations in summer conditions, and did not signify any major change.

Allison (1991) reported that the accumulation pattern measured during 1988-91 was consistent with that derived from previous measurements. He stated that ablation rates in the zone upstream of T4 (Figure 2.2) ranged from -0.1 to -0.2 km $m^{-2}a^{-1}$. He added that the net accumulation increased from zero at G3 to 0.5 m a^{-1} in the confluence region between Single and Gillock Islands.

The gravity data were used to estimate the depth of the bedrock lying under the ice shelf, revealing a uniform depth of about 1000 m beneath the centreline (Allison

1991). This was confirmed by bathymetric observations in Prydz Bay and ice thicknesses measured by RES near T4. From the 1988-89 RES data the depth of the ocean layer beneath the ice shelf was estimated at 150-200 m below G3, and 350-400 m below the confluence of the Charybdis Glacier (GA7) (Allison 1991).

Goodwin and Allison (unpublished data) characterised the nature of the Amery Ice Shelf surface, based on their summer field observations, and determined its temporal surface mass balance. They reported that the main part of the Amery Ice Shelf had little micro-relief, with surface micro-relief restricted to the periphery of the ice shelf, where the katabatic wind intensity was high. Goodwin and Allison (unpublished) noted that surface characteristics followed a distinct pattern with corresponding topographic changes along the shelf. In the ablation area, the surface was covered by bare ice, wave ogives, and undulating ice ridges, which separated the ice streams. Melt lakes occupied the surface depressions between the ogives and ridges. Three large surface streams drained surface summer meltwater northwards, onto the part of the ice shelf that had continuous snow cover. Much of the melt refroze as super-imposed ice (Ian Allison, personal communication, 1998). Analysis of Landsat imagery from consecutive summers revealed that the volume of water carried in these streams varied greatly (Goodwin and Allison, unpublished). The downstream sections of the meltstreams lay in a marginal accumulation zone and were hidden by snow cover during the colder months, until the summer when surface melting occurred. On the eastern side of the ice shelf, surface hoar was observed, possibly originating from moisture evaporated from the melt-lakes and water bodies, carried down-glacier by katabatic winds (Goodwin and Allison, unpublished).

Goodwin and Allison (unpublished) reported that the ice front had advanced approximately 25 km between 1964 (after the calving event) and 1990.

2.2.5 Lambert Glacier Basin traverse 1989-95

The Lambert Glacier Basin (LGB) Traverse program took place over five seasons between 1989 and 1995 (Higham and Craven 1997). The traverse route from Mawson to Davis stations, approximately followed the 2500-m contour for 2200 km around the interior of the Lambert Glacier drainage basin. The traverse program was part of ANARE's Lambert Amery Regional Glaciology Experiment (LARGE), which aimed to investigated the dynamics and mass budget of the Lambert Glacier-Amery Ice Shelf system (Higham and Craven 1997).

Seventy-three ice movement stations (LGB00-LGB72) were established at approximately 30-km spacing along most of the LGB traverse route, and at 15-km spacing across the major streams (Higham and Craven 1997; Figure 2.5). At the LGB stations, static GPS observations and gravity measurements were made. Ice cores were also taken to measure: stratigraphy; 10-m firn temperature; stable isotope ratio; and density. Surface microrelief and climatology measurements were made at each station, and automatic weather stations (AWS) were established at six stations (LGB00, LGB10, LGB20, LGB35, LGB46 and LGB59). Between each pair of LGB stations, measurements of surface elevation and ice thickness were made, by barometric levelling and ice radar sounding respectively. Canes were placed at 2-km intervals for snow accumulation measurements (Higham and Craven 1997).

Results of LGB traverse (1989 to 1995)

The LGB traverse resulted in a vast quantity of glaciological measurements. Some of the results have been reported in Higham *et al.* (1995) and Higham and Craven (1997). Higham *et al.* (1995) presented the main results of the radar sounding. They reported that the major sub-glacial feature along the route was a 350-km wide region where the bedrock was below sea level. This depression was south of the Prince Charles Mountains, extending approximately from LGB33 to LGB53. Higham *et al.* (1995) identified the depression as a southern extension of the Lambert Glacier graben, and noted that the two major streams of the Lambert-Amery system, i.e., the Lambert and the Mellor Glaciers, lay within it. Along the remainder of the traverse, the bedrock was above sea level (Higham *et al.* 1995).

Other results from the LGB traverse are discussed and used in this thesis. Observations collected at the AWS stations are used in the atmospheric calculations for the ERS altimetry (Chapter 3). The GPS elevations at the LGB stations are used to compare with an ERS-derived surface (Chapter 5). In Chapter 7, the surface ice velocities and ice thicknesses are used in flux calculations. Surface observations and pit measurements are used in Chapter 8.

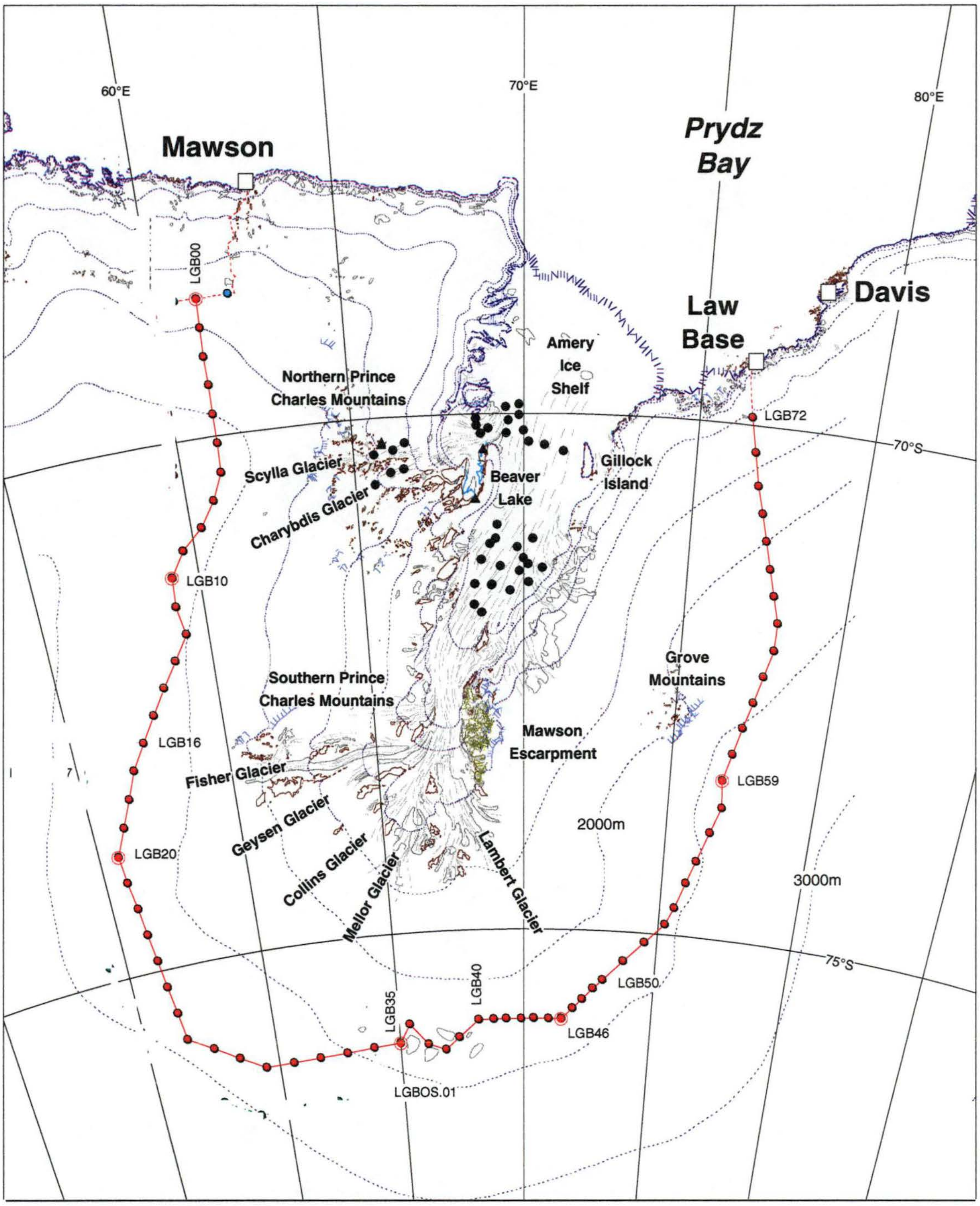

Figure 2.5 *Location map of the Lambert Glacier Traverse route (1989-1995). Red circles correspond to ice movement stations along the traverse route (LGB00 to LGB72). Automatic Weather Stations (AWS) are located at LGB00, LGB10, LGB20, LGB35, LGB46 and LGB59. Map provided by Mike Craven, Antarctic CRC/Australian, Antarctic Division.*

2.3 Remote sensing observations of Lambert-Amery system

The Lambert-Amery system has been the subject of several studies using satellite data, including satellite radar altimetry and satellite imagery (Table 2.3). This section summarises the major findings of these studies.

TABLE 2.3 SUMMARY OF THE MAIN REMOTE SENSING STUDIES CARRIED OUT IN THE LAMBERT – AMERY SYSTEM (PRE-1995).

Epoch	*Instrument*	*Reference*
1972-4 & 1978	*Landsat MSS & Seasat altimeter*	***Brooks et al. 1983***
1978	*Seasat altimeter, Landsat, AVHRR*	*Partington et al. 1987; Partington 1988*
1972-4 & 1978	*Landsat TM & Seasat altimeter*	*Zwally et al. 1987*
1972-4	*Landsat MSS*	*Swithinbank et al. 1988*
1978 & 1987-89	*Seasat altimeter & Geosat altimeter*	***Herzfeld et al. 1994; Lingle et al. 1994***
1973-74	*Landsat MSS*	*Hambrey and Dowdeswell 1994*
1986-89	*Geosat altimeter*	*Herzfeld et al. 1993*

The sensor acronyms MSS, AVHRR and TM stand for Multi Spectral Scanner; Advanced Very High Resolution Radiometer; and Thematic Mapper respectively.

2.3.1 Satellite radar altimeter observations

The Seasat altimeter, which operated from 10 July – 9 September 1978, was the first satellite-borne altimeter to provide coverage of the Amery Ice Shelf (Brooks *et al.* 1983). The Amery Ice Shelf was the largest ice shelf to fall within Seasat's coverage (Partington *et al.* 1987) and the pattern of ground tracks at the orbital limit resulted in a relatively dense data set for the region. Several research groups completed studies of the Lambert-Amery system using data from the Seasat altimeter (e.g. Brooks *et al.* 1983, Zwally *et al.* 1987,Partington *et al.* 1987).

Brooks *et al.* (1983) chose the Amery Ice Shelf as a test region, to assess the capability of the Seasat altimeter for retrieving surface height information over Antarctic ice shelves. Their study used data from 43 passes of Seasat over the ice shelf from July-October 1978, resulting in 6016 surface height measurements. The waveform data were retracked using the Offset Centre of Gravity method (see Chapter 3), to the 50% threshold point. A crossover adjustment was carried out, which was constrained so that elevations over the ocean matched those of the Schwiderski tide model and the GEM 10B geoid model (Brooks *et al.* 1983). Brooks *et al.* (1983) gridded the Seasat data onto a 0.125° grid (13.9 km in latitude, 4.3 - 5.0 km in longitude) using a weighted average technique. They plotted surface elevation contours at 5 m intervals over the entire ice shelf, adding 1 m contours where appropriate. This provided the first detailed surface elevation map of the Amery Ice Shelf, at an estimated precision of $\pm$ 0.47 m (Brooks *et al.* 1983). These authors superimposed their contour map onto a Landsat MSS mosaic, composed of Band-7 images collected between 1972 and 1974. They compared the elevations with the observed ice flow features in the mosaic, to provide additional insight into the ice shelf dynamics.

Brooks *et al.* (1983) detected two fracture zones in the Landsat mosaic: one on the east side of the Amery Ice Shelf, downstream of Gillock Island; and another on the western side, downstream of Jetty Peninsula. In the eastern zone, they noted that fractures (individually up to 40 km in length) were present in the ice shelf surface, from the northern point of Gillock Island to the ice front, a total distance of 130 km. They suggested that these fractures were a result of Gillock Island obstructing the ice flow. On the opposite side of the ice shelf, Brooks *et al.* (1983) reported linear fractures 10-15 km wide, extending from the northern end of Jetty Peninsula to the centre of the ice front. They suggested that these fractures were caused by the entry of the Charybdis Glacier into the ice shelf. Brooks *et al.* (1983) stated that the surface topography along the fracture zones had rapid elevation fluctuations of ~5 m amplitude in individual profiles of the altimetry, adding that this variation was averaged out in the contouring process. They also noted two topographic maxima, (located at 70°35' S, 70°15' E and 71°05' S, 69°35' E) and interpreted them as localised partial groundings of the ice shelf.

Brooks *et al.* (1983) compared their Seasat elevations with results from the ANARE 1968-70 Amery Ice Shelf traverse (Budd *et al.* 1982) along the centre-line profile. They reported that the two profiles were similar in shape in the portion from 20 to 220 km from the ice front. However, the altimeter-derived heights were lower than survey measurements, the differences increasing with distance from the ice front. On the western side of the shelf, the Seasat elevations were higher than the survey measurements, indicating that this region may have been subject to an elevation increase. These results led to Brooks *et al.* (1983) hypothesising that the Lambert Glacier was retreating, possibly in response to the 40 km calving at the ice shelf front between 1955 and 1965 (Budd 1966). They also proposed that the Charybdis Glacier was experiencing a surge. A steep change in slope was evident in the (Brooks *et al.* 1983) altimeter profile 320 km from the ice front (near T4).

Zwally *et al.* (1987) generated a second topographic map for the Amery Ice Shelf region using 83 orbits of Seasat data. These data were retracked using the β-parameter method (see Chapter 3). There were two main differences between this map and that of Brooks *et al.* 1983. The first was a feature 200-km in length, in the latitude 70 to 72°S with an undulating surface and a low mean surface slope was interpreted as a region of partial grounding with 'sticky spots' (i.e. a transition zone). The second was a new elevation maximum 40 km from the ice front at 69 15°S 71 30°E, which was apparent in 4 orbits.

Zwally *et al.* (1987) adopted the 'slant-range' method, first introduced by Thomas *et al.* (1983), to map the front of the Amery Ice Shelf using Seasat data. Thomas *et al.* 1983 showed that even though the altimeter lost lock when it encountered the abrupt step in elevation at the ice shelf front, the approximate location of this step could be inferred from the behaviour of the range measurements just before tracking was lost. Using seventeen passes of Seasat data that crossed the Amery Ice Shelf front Zwally *et al.* (1987) mapped 40% of the ice front, with an estimated horizontal accuracy of $\pm$ 1 km. By comparing the position of the altimeter-derived ice front with that observed in a 1974 Landsat image, they concluded that the central part of the ice shelf had moved forwards with no significant calving between 1974 and 1978 at a velocity of 1.5 $\pm$ 0.6 kma^{-1}. This was confirmed by the ANARE measured ice velocity of 1.2 $\pm$ 0.1 km a^{-1} reported by Budd et al. 1982 (Zwally *et al.* 1987).

Partington *et al.* (1987) completed a further study on the Amery Ice Shelf with Seasat waveform data, combined with Landsat and Advanced Very High Resolution Radiometer (AVHRR) imagery, together with ANARE survey data. By retracking the Seasat waveforms both to the first-return and the 50% power point, Partington *et al.* (1987) obtained estimates of the waveform leading edge width. Given that altimeter waveforms became distorted over rough topography (Chapter 3), this provided an estimate of the degree of distortion (Partington *et al.* 1987). The criterion Partington *et al.* (1987) used to define a crevassed region was an elevation difference of 1.5 m. Using 57 orbits of Seasat, they identified the same two crevassed zones reported by Brooks *et al.* (1983). They also located a shear zone on the edge of a stagnant region found during the 1968 ANARE survey on the western edge of the Amery, downstream from the Charybdis Glacier, and number of other possible crevassed regions.

Partington *et al.* (1987) noted that the waveform sequence across the supposed grounding zone (near T4) conformed to those simulated over a change in slope by Rapley *et al.* (1985). Partington *et al.* (1987) proposed that the return pulse was focussed by the surface shape associated with the change in slope, therefore only the first-return method was a reliable method for ranging across the supposed grounding line. Using this method and the 'slant range' method of (Thomas *et al.* 1983), Partington *et al.* (1987) located the position of the supposed grounding zone with an accuracy of $\pm$ 0.5 km at 2.8 km north-east of T4. The first-return elevation profile across the supposed grounding zone exhibited two features that arose from the altimeter receiving a return from off-nadir. Partington *et al.* (1987) suggested that this was because there were grounded regions to one side of the ground track, and that the supposed grounding line was not a line but a wavy zone of unknown length or width.

Studies have also been performed in the Lambert-Amery system using data from the Geosat altimeter (coverage to 72.18°S) alone, and in combination with Seasat data (Herzfeld *et al.* 1993, Lingle *et al.* 1994). Herzfeld *et al.* (1993) used Geosat Exact Repeat Mission (ERM) data from 1986-89 to compute a DEM of part of the Lambert Glacier-Amery Ice Shelf system, on a 3-km grid using kriging (Figure 2.6). Although major topographic features can be seen in this DEM, many small-scale features such as crevasses are not able to be resolved. This is a result of the wide track spacing of the Geosat ERM tracks (~25-30 km at 71°S).

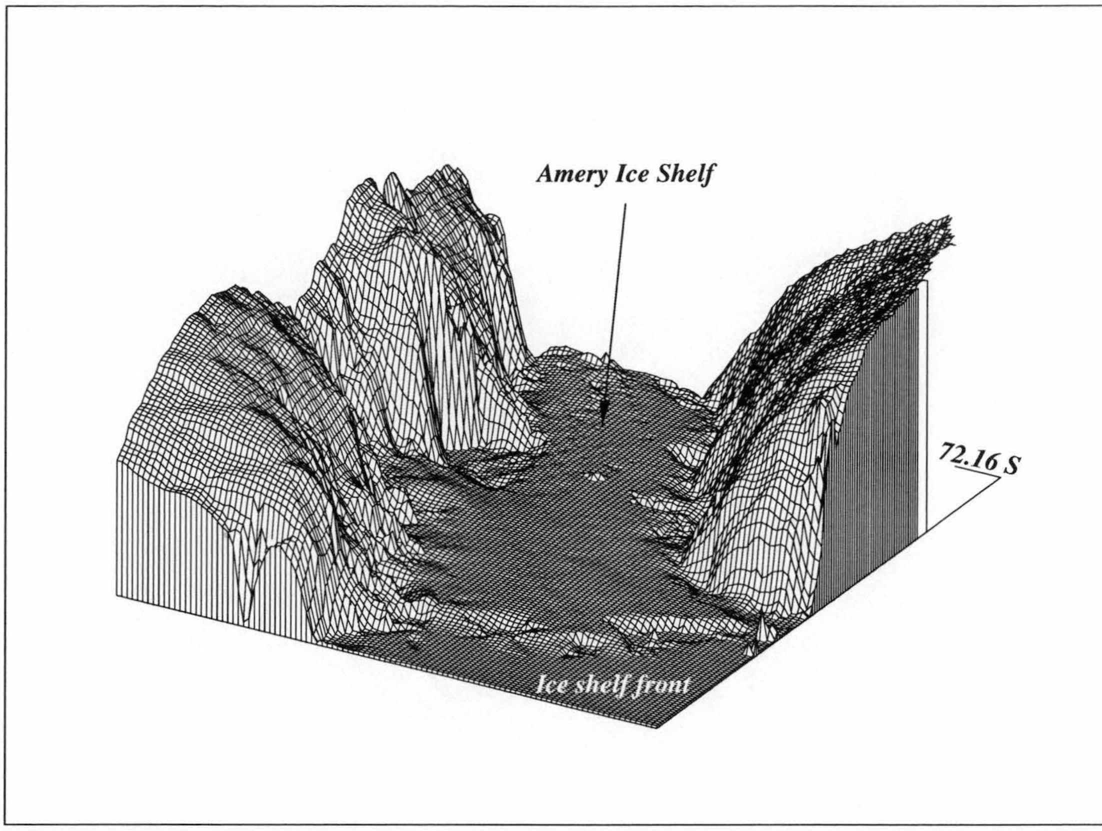

Figure 2.6 *DEM of a section of the Lambert– Amery system produced from Geosat data from 1987-1989 (Herzfeld et al. 1993; Herzfeld et al. 1994).*

Herzfeld *et al.* (1993) also presented a contour map of the region, and reported that the main portion of the Amery Ice Shelf was in the range 80-130 m (above the WGS-84 ellipsoid). A distinct change in surface slope was detected along a wavy line around the 100 m contour. This spanned the Budd *et al.* (1982) grounding line, and so was taken as confirmation that this was the grounding zone. Downstream from this line were local areas of higher elevation, which Herzfeld *et al.* (1993), like Zwally *et al.* (1987), attributed to partial grounding. The contours became more closely spaced and complex further south, suggesting increased surface roughness and topographic variation, due to the grounding of the ice. Herzfeld *et al.* (1993) reported that the surface elevations of the Lambert-Amery in the shear zones along the ice shelf edge were apparently lower than the main surface by 50 m. They added that this was 20-40 m greater than the difference measured during the ANARE 1968 survey (Budd *et al.* 1982). Herzfeld *et al.* (1993) concluded that the additional apparent elevation decrease was a result of altimeter 'snagging', caused by the instrument continuing to range to the ice shelf just after crossing the break in slope at the margins, before regaining track on the grounded ice.

Lingle *et al.* (1994) used Geosat data (1987-89) in conjunction with Seasat data (1978) to measure the change in elevation on the Lower Lambert Glacier (70.4 to 72.1°S) between the two epochs. They divided the Geosat data into 3-month blocks, the winter block coinciding with the 3 month operation of Seasat, and computed elevation differences between the two satellites using crossover analysis. Only crossovers from the same season were used to eliminate any seasonal biases. Lingle *et al.* (1994) estimated the bias between Seasat and Geosat from crossover differences over sea-ice in Prydz Bay, which they assumed to be constant every winter. They filtered the data to reduce the effects of random noise, and estimated that the elevations had increased at a rate of 31 ± 10 mm a^{-1} between 1978 and 1987-89. With no pre-filtering, Lingle *et al.* (1994) obtained a rate increased of 43 ± 53 mm a^{-1}. An independent crossover analysis using unfiltered data yielded a rate of increase of 73 ± 8 mm a^{-1}. With no inter-satellite bias accounted for, but instead the Seasat and Geosat orbits adjusted to a common ocean surface, an elevation increase of 83 ± 9 mm a^{-1} was obtained. Lingle *et al.* (1994) concluded that increasing elevations on the lower Lambert Glacier could be a result of the positive net mass budget over the entire drainage basin calculated by Allison (1979). Allison's (1979) mass budget estimate amounted to a thickening rate of 210 ± 190 mm a^{-1} for the Lambert Glacier system. Alternatively the Lambert Glacier may be thickening at its lowest part, and thinning upstream in a redistribution of mass following a surge, however the incomplete coverage of the Lambert-Amery system by both Seasat and Geosat meant that this could not be quantified (Lingle *et al.* 1994).

Herzfeld *et al.* (1994) completed their own comparative study using Seasat and Geosat data. The Geosat data were again divided into 3-month blocks and only the winter blocks were used, to reduce seasonal biases. Herzfeld *et al.* (1994) interpolated the Seasat data and the Geosat data using kriging, with a semivariogram computed for the region of interest (the region from 71°S to 72°S, which contained the supposed grounding zone). The result was two independent 3-km DEMs: one for 1978 (Seasat) and the other for 1987-89 (Geosat). The earlier epoch DEM had a smoother appearance since the Seasat data were sparser. Herzfeld *et al.* (1994)

interpreted the break in slope around the 100 m contour, as the grounding line. They showed that this feature had advanced by approximately 10 km between 1978 and 1987-89. They noted that this was consistent with the mean increase of the surface height reported by Lingle *et al.* (1994).

2.3.2 Satellite imagery

Visible and infra-red images provide very useful qualitative information on glacial systems. Swithinbank (1988) presented an overview of features of the Lambert-Amery system seen in Landsat imagery, using 25 images from 1972-74 to produce a mosaic that covered its entire complex system of tributary ice streams, superimposed with elevation contours from the Australian Division of National Mapping (map sheet SS40-42, 1973). He identified surface flowlines of the main Lambert Glacier, the presence of scattered meltwater lakes and rivers on the glacier, and pointed out a wavy strip of ice rumples that flowed to the west of Clemence Massif (latitude ~-72°12'S) that appeared to contain large areas of freely floating ice shelf. He also located several ice dolines which possibly imply floating ice: one doline was 30-km south east of Beaver Lake, another 35-km east of Mount Meredith (latitude ~-71°09'S) and two near Robertson Nunatak (latitude ~-71°54'S). Swithinbank (1988) pointed out the crevassed zone originating at the confluence of the Charybdis Glacier, and another originating at Gillock Island, both of which were previously noted by Brooks *et al.* (1983).

Hambrey and Dowdeswell (1994) investigated the flow regime of the Lambert-Amery system by analysing Landsat imagery, to assess whether it was cyclically surging or following a constant flow pattern. They used three digitally enhanced Landsat MSS images from 1973 and 1974, dividing the system into 8 major flow units from west to east, to infer flow dynamics from the pattern of ice structures. A map illustrating the location of the flow units is shown in Figure 2.7.

Hambrey and Dowdeswell (1994) noted features in the Landsat images near Clemence Massif (around 400 km from the ice shelf front) that provided evidence that the ice was floating there. This was around 120 km further south than the proposed grounding line position (Budd *et al.* 1982) which had been assumed (and

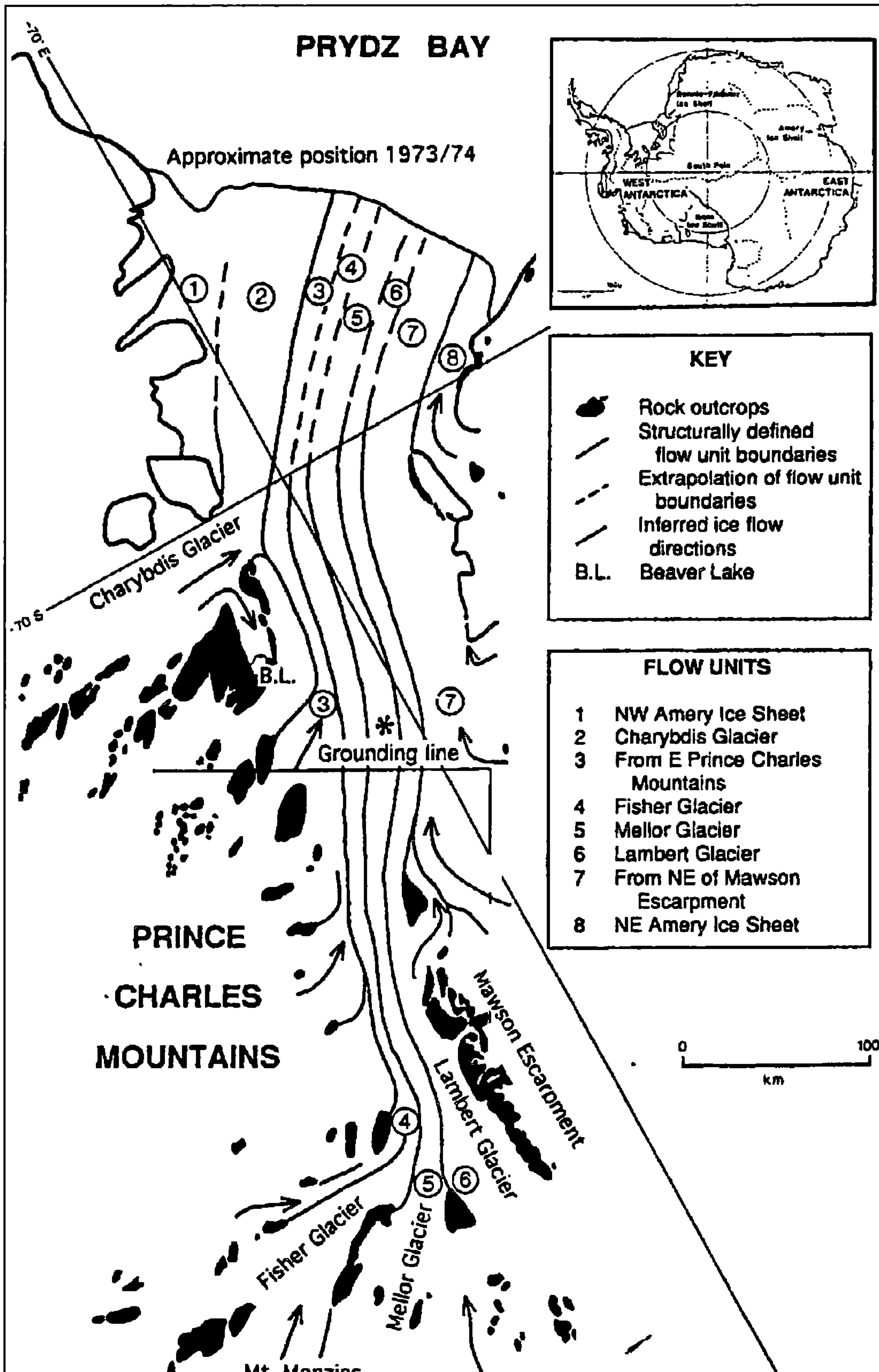

***Figure 2.7** Major flow units of the Lambert-Amery system derived from Landsat images. Taken from Hambrey and Dowdeswell 1994.*

often was thought to have been confirmed) during previous remote sensing studies in the region (e.g. Partington *et al.* 1987; Herzfeld *et al.* 1994). Hambrey and Dowdeswell (1994) analysed the structure of the Lambert-Amery system from the Landsat imagery, and reported the presence of longitudinal, undeformed flowlines, medial moraines and crevasse patterns that did not indicate any surging behaviour. They concluded that the flow regime had remained constant over a period of the order of 1000 years, despite any changes in ice thickness and mass balance that may have occurred.

2.4 Chapter summary

This chapter has outlined the existing knowledge of the glaciology of the Lambert-Amery system, based on previous fieldwork and remote sensing studies. It has showed that, despite the many studies carried out in the region, detailed knowledge of the surface structure and features is limited to localised areas of the system.

There is a limited amount of high quality elevation data, restricted by problems such as; inadequate coverage of satellite radar altimetry; large separation between neighbouring tracks and the use of different reference frames. There has also only been a limited amount of field-work in recent years on the ice shelf, the major surveying period for the region being in the 1960s and early 1970s.

The lack of accurate, extensive surface elevation and surface property information represents a significant gap in the knowledge of the structure of the Lambert-Amery system. Both the mass budget of the system and the exact location of the boundary between grounded and floating ice remain uncertain (Table 2.4). When considering the size of this portion of Antarctica and the importance of the drainage basin in terms of the total mass balance of Antarctica, this is an unsatisfactory situation.

It is clear that more topographic information is needed for the Lambert-Amery system. Accurate, detailed surface topographic mapping is an essential part of understanding the structure of the system, for modelling the dynamics of the system and subsequently for assessing its response to any climate change. This thesis will apply ERS satellite altimeter data to a study of the Lambert–Amery system, to obtain such information. Chapter 3 describes the ERS altimeter instrument, and the processing techniques required to extract accurate information over ice-covered regions.

TABLE 2.4 SOME UNCERTAIN PARAMETERS OF THE LAMBERT-AMERY SYSTEM

Parameter	***State of knowledge***	***Method***	***Comments***
Grounding zone location	*Located at the change in slope close to T4* *(Budd et al. 1982, Partington et al. 1987; Lingle et al. 1994)*	*Surface elevation profiles (ground survey and satellite altimetry)*	*Satellite imagery evidence suggests it is further south than reported*
Mass budget	*Slightly positive (Allison 1979)*	*Mass flux calculations*	*Based on sparse observations*
Basal melting and freezing	*Freezing occurs towards the front of the shelf (Budd et al. 1982; Wakahama and Budd 1976; Morgan 1972)*	*Ice core at G1, strain and mass flux calculations (Budd et al. 1982)*	*Exact distribution unknown*

Chapter 3 The ERS radar altimeters: operating principles and processing of data collected over ice

3.1 Introduction

The current state of knowledge of the Lambert-Amery system is limited (see Chapter 2), suggesting a need for further studies in the region. Detailed topographic mapping of most of the glacier - ice shelf systems of Antarctica (as far as 82°S) is now possible using data from the radar altimeters on board the European Space Agency's (ESA) Earth Remote Sensing (ERS) satellites. It is expected that such topographic information will improve the knowledge of the Lambert-Amery system.

The ERS altimeters are more suited to ice sheet mapping than their predecessors (Geosat and Seasat) for three main reasons. Firstly, they cover much more of the Antarctic ice sheet, since Geosat and Seasat only extended to 72.12°S. Secondly, higher accuracy orbits are available (Scharroo and Visser 1998) and, thirdly, they incorporate a specialised 'ice mode' for improved tracking over ice (Rapley *et al.* 1985). Altimeter data collected over ice need to be carefully processed in order to optimise the information content, because of the complex surfaces and scattering mechanisms involved (Bamber 1994). To interpret altimeter data correctly, it is vital that problems unique to altimetry over non-ocean surfaces be addressed. The aim of this chapter is to outline these problems and describe the processing methods that have been developed to overcome them.

3.2 ERS satellite phases

The first ERS satellite, ERS-1, was launched on 17 July 1991. Its counterpart, ERS-2, was launched on 21 April 1995 (ESA/ESRIN 1997a). The satellites are at an altitude of 782 km, and follow a sun-synchronous, near-polar orbit, inclined at an angle of 98.52° to the equator (Vass and Handoll 1991). This provides an almost global coverage, between latitudes 82°S and 82°N. The density of ground tracks depends on the repeat period of the orbit. ERS-1 has operated with three different repeat periods: 3, 35 and 168 days (Table 3.1).

TABLE 3.1 *PURPOSE, ORBITAL REPEAT PERIODS AND DATES OF THE ERS-1 SATELLITE PHASES.*

Phase	***Purpose***	***Repeat (days)***	***Dates***
A	*Commissioning Phase*	*3*	*25 Jul 91 - 10 Dec 91*
B	*1st Ice Phase*	*3*	*28 Dec 91 - 30 Mar 92*
-	*Roll Tilt Mode Campaign*	-	*4 Apr 92 - 13 Apr 92*
C	*1st Multidisciplinary Phase*	*35*	*14 Apr 92 - 21 Dec 93*
D	*2nd Ice Phase*	*3*	*23 Dec 93 – 10 Apr 94*
E	*1st Geodetic Phase*	*168*	*10 Apr 94 – 28 Sep 94*
F	*2nd Geodetic Phase*	*168*	*28 Sep 94 – 21 Mar 95*
G	*2nd Multidisciplinary Phase*	*35*	*21 Mar 95 – 5 Jun 96*

On 29 April 1995, ERS-2 joined ERS-1, to start the 'Tandem Mission'.
Information accessed from ESA/ESRIN World Wide Web pages ESA/ESRIN (1997b)

The orbital periods of ERS-1 were chosen for different applications. The 3-day repeat period (Phases B and D, the 'Ice' phases) were intended to give frequent repeat coverage of the Baltic Sea ice zones during the northern hemisphere winter (Vass and Handoll 1991). A 35-day repeat period was used for the 'Multidisciplinary' phases (Phases C and G of ERS-1 and Phase A of ERS-2). This repeat period optimised coverage for Synthetic Aperture Radar (SAR) imagery (Vass and Handoll 1991). The 168-day 'Geodetic' phases (Phases E and F) provided a high density of altimeter tracks, intended for gravity field and ocean surface mapping (Battrick 1993). This dense spacing is ideal for detailed topographic mapping (e.g. Bamber and Bindschadler 1997).

ERS-2 has only operated in a 35-day repeat orbit (Phase A). In this orbit, ERS-2 exactly followed ERS-1, in the so-called 'Tandem Mission' (ESA/ESRIN 1997b). This provided duplicate coverage with 24-hours between observations.

In this thesis, radar altimeter data are used from each orbit configuration of ERS-1. Data from Phases E, F and G of ERS-1 and Phase A of ERS-2 were validated with GPS measurements collected during Amery Ice Shelf survey (Chapters 4 and 5). The 35-day repeat period had an adjacent track spacing of ~25 km at 71°S (the Amery Ice Shelf) and provided repeat tracks, allowing repeatability analyses on the Amery Ice Shelf (Chapter 5). Phases E and F had a track spacing of 2-3 km at 71°S, ideal for mapping purposes. These high-density data were used to map the surface topography of the Lambert-Amery system (Chapter 5).

The short repeat period of 3 days for Phases B and D meant that the track spacing was around 300 km at 71°S (the latitude at the centre of the Amery Ice Shelf). Only one of the passes crossed the Amery Ice Shelf, but multiple repititions facilitated the monitoring of the development of a surface melt feature on the ice shelf (Chapter 8).

3.3 Radar altimeter operating principles

The satellite radar altimeter is a downward-looking, active microwave instrument with a simple operating principle. It operates by transmitting a short radar pulse vertically towards the surface, and receiving the reflected pulse. The time interval between transmission of the pulse and reception of the reflected pulse, together with the shape of the return pulse contain information about the surface with which the radiation interacts (Rapley *et al.* 1987).

In this section, a brief summary is given of the relevant and important features of altimeter operation, especially related to operation over the ice sheets and ice shelves.

3.3.1 Altimeter range measurement

Figure 3.1 illustrates the basic principle of satellite radar altimetry. The altimeter measures the time delay *(T)* taken for a radar pulse to travel to the surface and back again. The range *(R)* from the satellite to the surface is determined from the time delay from the following equation:

$$R = \frac{cT}{2} \qquad (3.1)$$

where c is the propagation velocity of electromagnetic waves in free space.

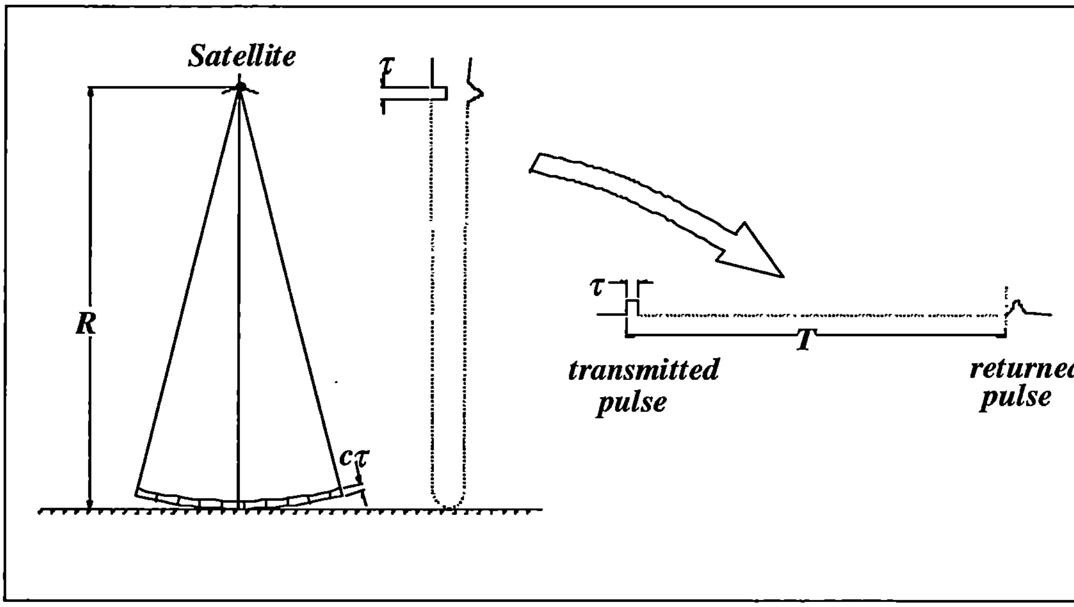

Figure 3.1 *Principle of satellite radar altimetry, in both the time dimension (left) and the distance dimension (right). Taken from Rapley (1990).*

Precise range measurements are achieved by using a short duration pulse. If the orbital altitude *(A)* of the satellite is known, the range can be converted to a surface elevation *(h)* above the reference ellipsoid. The equation is:

$$\mathrm{h}(\varphi,\lambda,t) = \mathrm{A}(\varphi,\lambda,t) - R(\varphi,\lambda,t) \qquad (3.2)$$

where A is satellite altitude

R is range from satellite to a point $P(\varphi,\lambda)$ on the Earth's surface at a time t.

The geometry of this situation is illustrated in Figure 3.2. As the satellite moves in its orbit, the altimeter measurements describe ellipsoidal height profiles *(h)* of the surface topography of the Earth. The orbital altitude at which the altimeter is placed is chosen such that the effects of atmospheric drag and the higher order components of the Earth's gravitational field are minimised (Rapley 1990). These influence the accuracy with which the satellite ephemerides can be determined from satellite tracking data. The altitude must also be within a certain range in order to meet constraints on transmitter power and the required signal-to-noise ratio of the return (Rapley 1990).

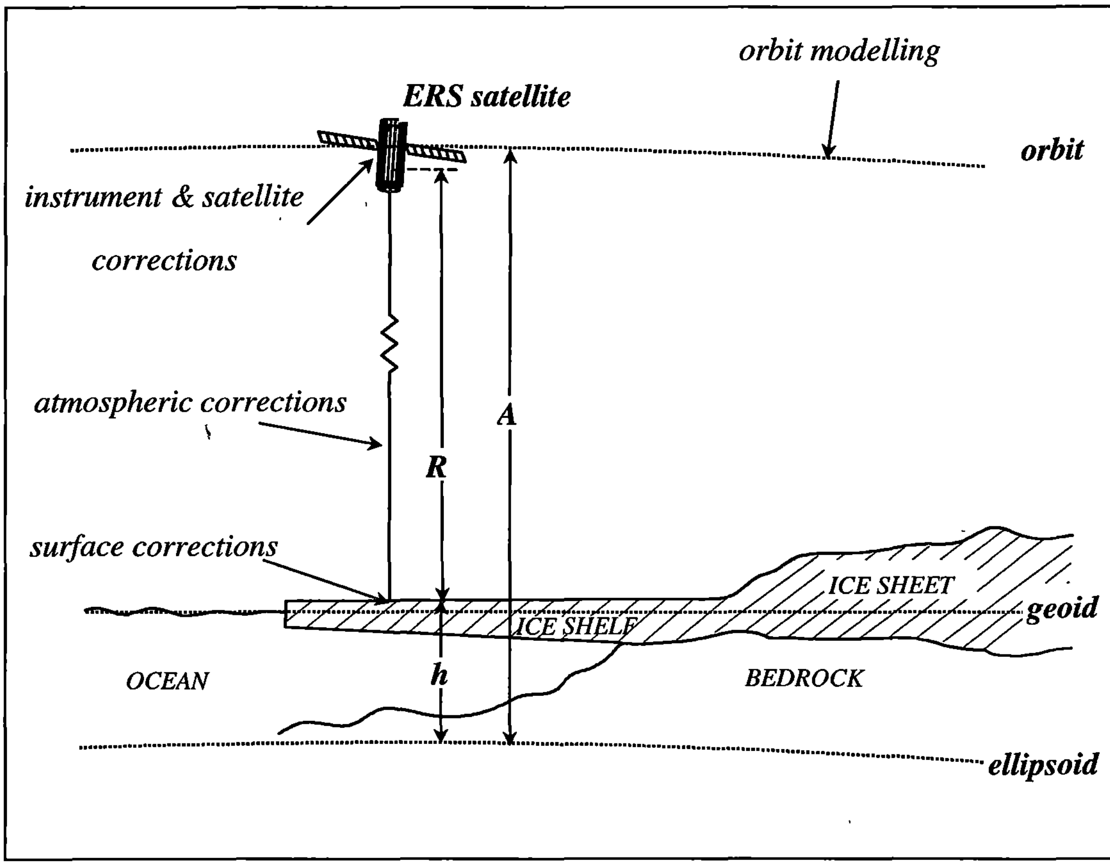

Figure 3.2 *Schematic diagram illustrating the determination of an ellipsoidal height (h) from an altimetric range measurement (R) over an ice shelf. Adapted from Partington (1988).*

3.3.2 Altimeter waveforms

When the transmitted radar pulse reaches the surface, the energy is scattered in various directions, and some will be reflected back in the direction of the radar (Ulaby *et al.* 1982). The shape of the reflected pulse (the 'waveform') is a result of this interaction, and is governed by the geometry and the scattering properties of the surface that it hits, as well as the instrument's antenna pattern (Rapley *et al.* 1987).

Ideal altimeter waveform

A good understanding of what the altimeter waveform represents is obtained by considering how it would look when the surface is 'ideal'. That is, the surface has uniform roughness (perfectly rough, or 'Lambertian'), is horizontally planar (no surface slope or curvature), and reflects the entire radiation incident on it (i.e. no absorption). A set of schematic diagrams of altimeter pulse interaction with such a surface is shown in Figure 3.3.

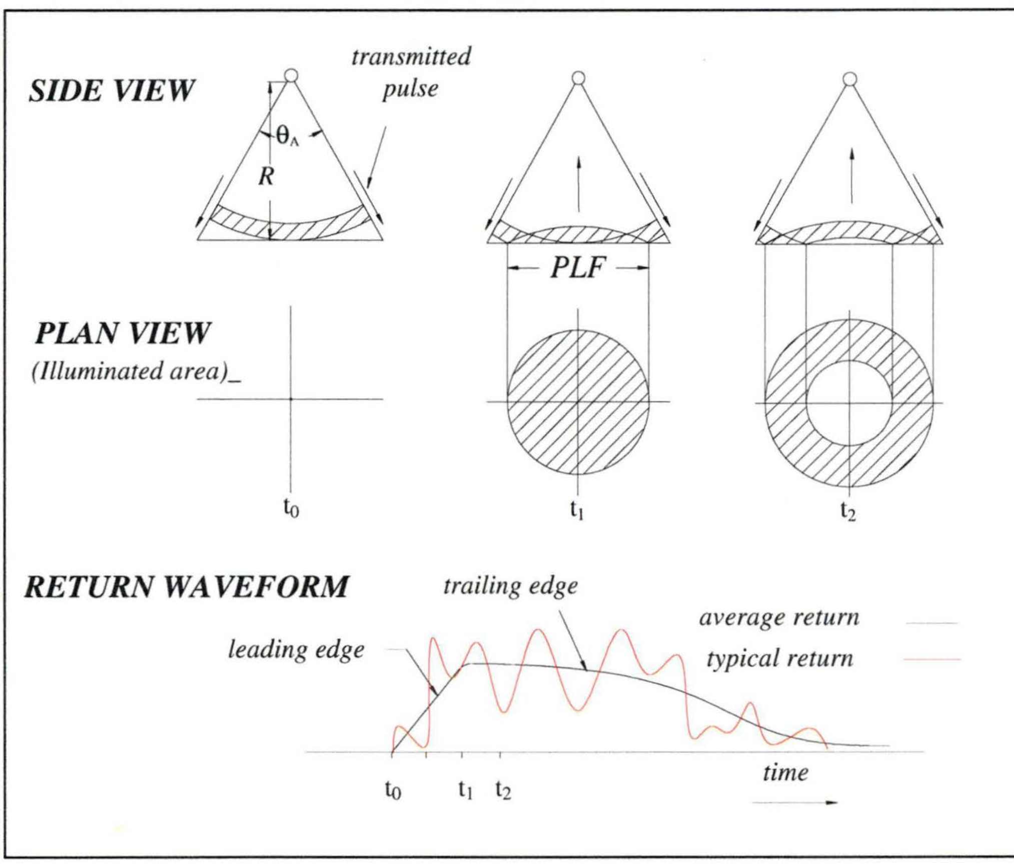

Figure 3.3 *The evolution with time of a surface scattered altimeter waveform from a flat, uniformly rough (Lambertian) surface. The pulse is transmitted at* $t = 0$*, and the front and back of the pulse intercept the surface at* $t = t_0$ *and* $t = t_1$ *respectively. The area of the footprint on the ground at* $t = t_1$ *is the pulse limited footprint (PLF). The figure is described in detail in the text. Taken from Ridley and Partington (1988).*

If the pulse is transmitted at time $t = 0$, the reference times t_0 and t_1, used in Figure 3.3 and the following text, are given by:

$$t_o = 2\frac{R}{c} \tag{3.3}$$

$$t_1 = t_0 + \tau \tag{3.4}$$

where R is the range to the closest point on the surface (see Figure 3.3)

τ is the pulse duration (see Figure 3.1).

The following is a description of the formation of the altimeter return pulse with time (Ridley and Partington 1988):

$\boldsymbol{0 < t < t_0}$ The radar altimeter pulse propagates towards the surface as part of an expanding spherical shell. The area of the sphere that can be received on the ground is defined by the antenna beam-width (θ_A in Figure 3.3).

$\boldsymbol{t = t_0}$ At the instant when the incident radar pulse first meets the surface it illuminates a point, and a reflected signal begins to return to the satellite.

$\boldsymbol{t_0 < t < t_1}$ The point becomes the centre of a disc whose area increases with time.

$\boldsymbol{t = t_1}$ The back of the shell reaches the centre of the circle and an annulus is formed, whose radius continues to increase whilst maintaining a constant area, until it reaches the edge of the radar beam.

The returned power received back at the satellite is proportional to the illuminated area (Rapley *et al.* 1987). The return power envelope grows rapidly between t_0 and t_1, until the back of the pulse reaches the surface at t_1, after which it remains constant. In reality, at t_1 it begins to attenuate, due to reduction of off-nadir scattering by the altimeter's antenna pattern, (Ridley and Partington 1988).

There are two types of altimeter operation: 'pulse-limited' and 'beam-limited' (Rapley 1990). This mode of altimeter operation is pulse-limited, because the illuminated area over a flat surface is determined by the effective duration of the transmitted pulse (PLF in Figure 3.3). In this mode, the leading edge of the pulse has not extended to the limit of the antenna beam by the time the back of the pulse has hit the ground (Moore and Williams 1957). In beam-limited operation the antenna beam width determines the footprint size (Rapley 1990). The period $t_0 < t < t_1$ is critical, as it contains the waveform leading edge, which corresponds to the initial interaction of the pulse with the surface (Ridley and Partington 1988). The maximum area of the surface corresponding to the leading edge of the waveform is the 'pulse-limited footprint'. The area and diameter of the pulse-limited footprint on the ground are determined by the pulse-width (τ). For the ideal surface, the pulse-limited footprint has an area (A_f) and diameter (D_f) of:

$$A_f = \pi R c \tau \tag{3.5}$$

$$D_f = 2\sqrt{R c \tau} \tag{3.6}$$

For the ERS altimeters, $\tau = 3.03$ ns and R ~800 km (Levrini *et al.* 1984). Therefore, the area and diameter of the ERS pulse-limited footprint over an ideal surface are ~2.3 km^2 and 1.7 km respectively.

Real altimeter waveforms

Radar altimeter waveforms from real surfaces differ considerably from that shown in Figure 3.3. When the microwave pulse intercepts the surface, some of the energy will be scattered, some transmitted through the surface layer, and the rest reflected back in the direction of the radar. The varying magnitudes of these components are governed by the surface geometry (roughness) and physical properties of the surface (Bamber 1994). The first reflections are returned from scattering elements closest to the spacecraft, while those from elements at more distant locations are received successively later. Information about the surface is therefore contained in the envelope of the returned energy intensity, i.e. the waveform of the returned pulse. The leading edge of the waveform corresponds to the initial interaction with the surface. In theory, several surface geophysical parameters can be deconvolved from the waveform (Ridley and Partington 1988; Chapter 8).

i. Waveforms over the ocean

When a radar altimeter operates over the ocean, the scattering is almost exclusively from the surface. When surface roughness is present, such as ocean waves, scattering from the wave crests precedes that from the troughs as the pulse-front propagates downward (Guzkowska *et al.* 1990). This has the effect of increasing the effective area within which the scattering elements appear to be simultaneously illuminated, broadening the rise time of the return, and widening the waveform leading edge. The width of the leading edge is related to the height of the ocean waves, and the pulse-limited footprint diameter D_f (given in Equation 3.6 for a flat surface) becomes:

$$D_f = 2\sqrt{c\tau' h} \tag{3.7}$$

where

$$\tau' = \left\{ \tau^2 + \left(4\frac{\sigma_s}{c}\ln 2 \right)^2 \right\}^{1/2} \tag{3.8}$$

where σ_s is the root-mean-square wave-height.

For the ERS altimeters, if the RMS wave-height increases from zero to 5 m, the diameter of the pulse limited footprint increases from 1.7 to 7 km (Rapley 1990).

Over the ocean, the slope of the waveform leading edge is used to estimate a parameter called significant wave-height (Martin *et al.* 1983). The mean range to the pulse-limited footprint is obtained by measuring to the range position corresponding to the point on the leading edge of the waveform that has half of the total received power.

An approximation for an altimeter return from the ocean can be made, by assuming that the mean surface is horizontal and planar, with a large number of scattering elements distributed normally about the mean surface (Moore and Williams 1957) Moore and Williams (1957) showed that for near-vertical incidence, the *mean* pulse-limited altimeter return power as a function of delay time is described by the convolution of two terms.

$$P_R(t) = P_T(t) * P_S(t) \tag{3.9}$$

where $P_R(t)$ is the power received back at the altimeter

$P_T(t)$ is the transmitted pulse profile

$P_S(t)$ is a function that includes the effect of the antenna gain, and the range distribution and backscattering properties of the surface scattering elements.

The Brown model for ocean returns

Brown (1977) developed a closed integral solution to describe surface scattering from the ocean, based on physical optics theory. He assumed that the illuminated surface was horizontal and planar, with a large number of scattering elements that were normally distributed in height. Brown (1977) approximated the transmitted pulse shape, the altimeter antenna pattern, and the range distribution of surface scattering elements with Gaussian functions. The scattering elements were assumed to return equal power, so that the term $P_S(t)$ in Equation 3.9 could be written as the convolution of two separate terms: one that described the 'average flat surface impulse response', and the other that represented the range distribution of the surface scattering elements. The expression for the returned power became a triple convolution (Brown 1977):

$$P_R(t) = P_T(t) * q(t) * P_{fs}(t) \tag{3.10}$$

where $P_{fs}(t)$ is the 'average flat surface impulse response' i.e. the average back-scattered power from a mean flat surface which has a low surface roughness but the same backscattering cross section per unit scattering area (σ_0) as the true surface

$q(t)$ is the delay time distribution of the surface scattering elements with range distribution $Q(R)$ (so that $q(t) = \dfrac{2 \cdot Q(R)}{c}$).

For a pulse-limited altimeter, $P_{fs}(t)$ is a step function with an exponential decay that expresses the attenuation of the return pulse shape by the antenna. Figure 3.4 illustrates the Brown (1977) model for a pulse-limited altimeter.

The shape of the waveform leading edge is the integral of the range distribution of surface scatterers (Rapley *et al.* 1987). The mean surface elevation and roughness are derived from the leading edge; measurements are made to the illuminated circle, the instant before it becomes an annulus $(t = t_1)$ (Rapley *et al.* 1987).

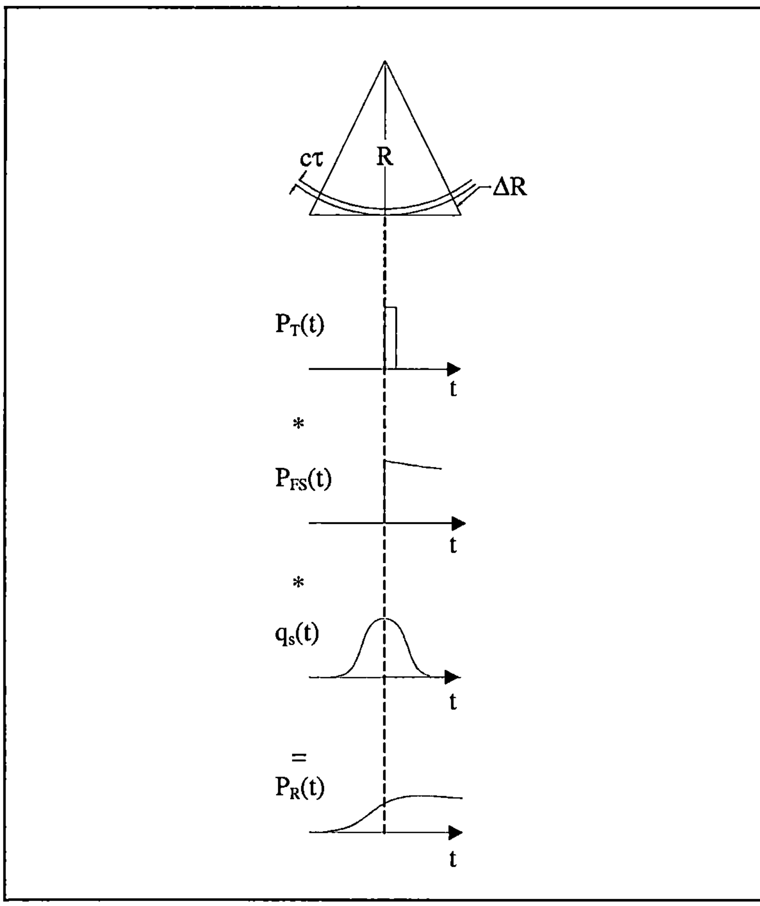

Figure 3.4 *The Brown (1977) model for the mean return from a pulse-limited altimeter from a planar, diffuse surface. The return power envelope is a convolution of the transmitted pulse, $P_T(t)$, the flat surface impulse response, $P_{fs}(t)$ and the delay time distribution of surface scatterers ($q(t) = Q(R) \times 2/c$). Taken from Partington (1988).*

ii. Waveforms over ice

The assumptions made in the Brown (1977) model are generally violated over ice sheets. Surface topography varies on a wide range of spatial scales and a Gaussian distribution can no longer be used to approximate the height distribution of surface scattering elements (Brown 1977). The response of the altimeter over an ice-covered surface is considerably more complex than over an ocean (Martin *et al.* 1983). Ice-covered regions have irregular surfaces that undulate with wavelengths of the order of 5-15 km, which is of the same order of size as the altimeter pulse-limited footprint over ice (McIntyre 1986). The presence of any kind of topographic feature in the pulse-limited footprint will distort the leading edge (Martin *et al.* 1983).

During the initial pulse interaction, the altimeter simultaneously views many randomly distributed scattering elements (Bamber 1994; Figure 3.5). Scattering

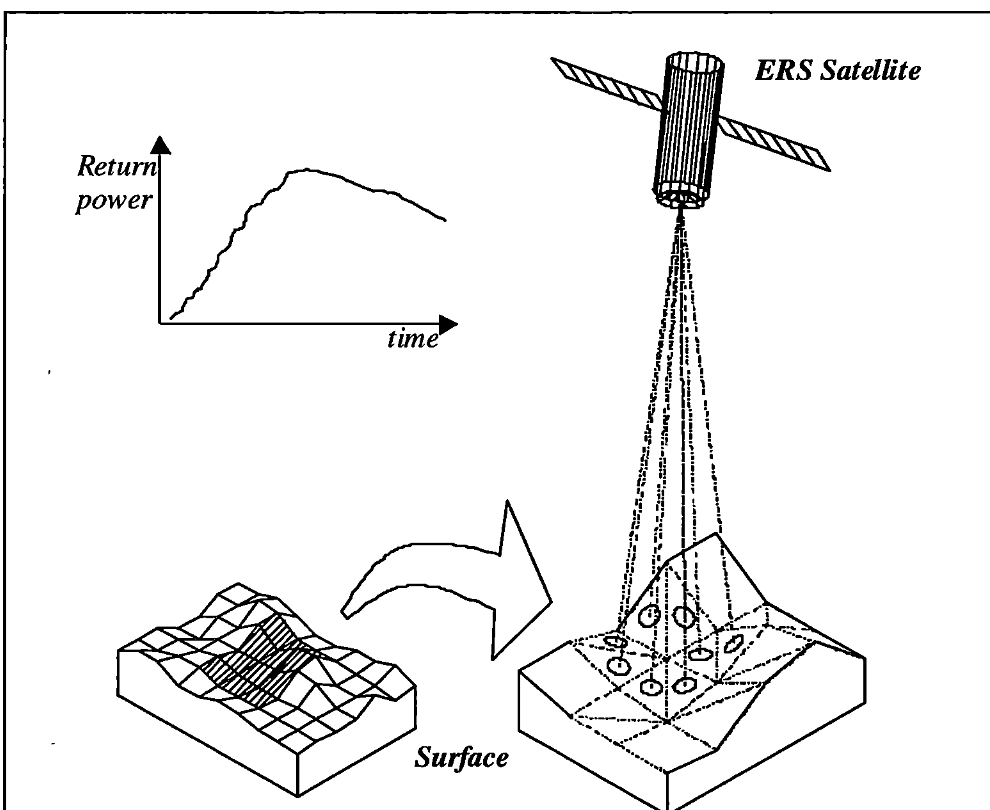

Figure 3.5 *Schematic drawing demonstrating the concept that many randomly oriented scattering elements are simultaneously illuminated by the altimeter beam over an ice surface. Also shown (inset) is a typical return power curve. Adapted from Bamber (1994).*

elements at different locations within the footprint, and with different elevations, may be at the same range from the satellite; therefore they will contribute to the same point on the return waveform. The amount of returned power from each surface element depends on its individual 'backscattering coefficient' and its angle to the incident beam (Bamber 1994). The total reflected power received back at the radar, depends on the total backscattering coefficient of the illuminated surface *(σ_0)*. Variations in σ_o can arise due to changes in surface properties (e.g. moisture content and surface roughness; see Chapter 8). Variations in σ_o and surface topography across the footprint result in a complex leading edge shape, which is often difficult to interpret (Wingham *et al.* 1993b; Bamber 1994). These problems are being investigated by applying techniques of seismic waveform migration to the altimeter waveforms in three dimensions (e.g. Wingham *et al.* 1993a; Wingham 1995).

Altimeter waveform averaging and recording

The ERS altimeters have a Pulse Repetition Frequency of 1020 Hz (Vass and Handoll 1991); i.e. they transmit approximately one pulse per millisecond. Individual altimeter return-pulse echoes are affected greatly by speckle, or Rayleigh noise, due to random interference of the coherent transmitted radiation across the footprint (Partington *et al.* 1987). To reduce this effect, the ERS altimeter sums 50 individual waveforms (Francis 1984), to form an average recorded waveform at ~20 Hz, which is the quantity telemetered to the ground and used in the range measurement. This improves the signal to noise ratio, so that the required range precision criteria is met (Rapley 1990).

Only a finite sample of each averaged return waveform is recorded, over a finite time interval. This time interval is equivalent to a range interval of 28.6 m, called the 'range window', which is quantised into 64 equal range intervals, or 'range bins' (Rapley *et al.* 1985). The quantity recorded in the waveform is equivalent to a histogram of average return pulse energy as a function of time (Martin *et al.* 1983).

3.3.3 Altimeter waveform tracking

The ERS tracking device is programmed to position the range window such that it contains the leading edge of the waveform. It does this by predicting the arrival time of the waveform based on previous measurements. In ocean-mode, measurements are made assuming the shape of the average return waveforms conform to the Brown (1977) surface-scattering model (Francis 1990). The tracking device uses a Sub-optimal Maximum Likelihood Estimator (SMLE) algorithm (Levrini *et al.* 1984). This statistical estimation technique uses a simplified version of the Brown (1977) model. The tracking point is the half-peak power point on the leading edge of the waveform, and the tracking device positions the centre of its range window at the predicted position from the SMLE.

For an ideal ocean surface, the tracking device will position the centre of the range window at the half peak power point on the leading edge (Ridley and Partington 1988). The range telemetered by the satellite is measured to the centre of the range window. Over much of the ocean surface, this is the true range. Over ice, however this is not the case (Cudlip *et al.* 1994b). When the ERS altimeters operate in ocean mode over ice, the following situations occur:

i) The shapes of the received pulses do not conform to the Brown (1977) model; and

ii) The surface topography changes rapidly.

These are two distinct problems, both of which make it difficult for the tracking device to predict the trend in the surface slope based on the most recent few measurements. This makes it difficult to position the range window correctly (Griffiths *et al.* 1984). Over ice, the leading edge of the waveform will either be offset from the tracking point, or not sampled at all. The first situation is corrected for by a post-processing procedure called 'retracking' (Martin *et al.* 1983; Section 3.5.1). The second situation is known as 'loss-of-lock'. Gaps in altimeter data collected over the ice sheets are caused by the tracking loop failing to keep up with changes in time delay caused by some of the rapid changes in surface height (Scott *et al.* 1994).

To improve altimeter tracking over ice, the ERS altimeters incorporate a second tracking mode, 'ice mode', in addition to the ocean mode (Francis 1984). To account for the problems encountered over ice, the ice mode tracker differs from the ocean mode tracker in two ways:

i) Waveforms are tracked using an algorithm which ensures that the centre-of-gravity of the recorded portion of the waveform is contained in the range window (Wingham *et al.* 1986); and

ii) An increased dynamic range is used, which increases the duration of the range window by a factor of four (Vass and Handoll 1991).

The centre-of-gravity position is used for tracking over ice because it is unique, therefore there is no ambiguity in the definition of the tracking point (Francis 1984). Furthermore, it is independent of the waveform shape (Griffiths *et al.* 1984). The centre-of-gravity tracker will usually maintain the leading edge in the range window. However, this tracker will introduce a bias depending on the waveform shape, because the centre of gravity of a waveform has no physical meaning (Griffiths *et al.* 1984). The waveform data therefore must be retracked. The wider range window permits a greater rate of range change to be tracked successfully, but results in a coarser resolution (Figure 3.6).

ERS-1 waveforms have 64 range bins of width 0.455 m in ocean mode and 1.82 m in ice mode (Rapley *et al.* 1985); therefore the total width of the range window is 28.8 m and 116.48 m for ocean and ice mode respectively. The instrument will maintain tracking up to a range acceleration of +/- 0.6 m s^{-2} in ocean mode and +/- 2.4 m s^{-2} in ice mode (Francis 1990).

To demonstrate the difference between ocean and ice modes, waveform sequences from two consecutive ERS-1 tracks across the Amery Ice Shelf were examined (Figure 3.6). These sequences were extracted from Cycle 3 (ocean mode) and Cycle 4 (ice mode) of ERS-1's Phase D along Track 013 (January 1994). Waveforms with the same number (from 1 to 20) correspond to similar locations on the ground. For each waveform, the y-axis represents power and the x-axis represents time. The effect on the waveform shape of increasing the bin width in ice

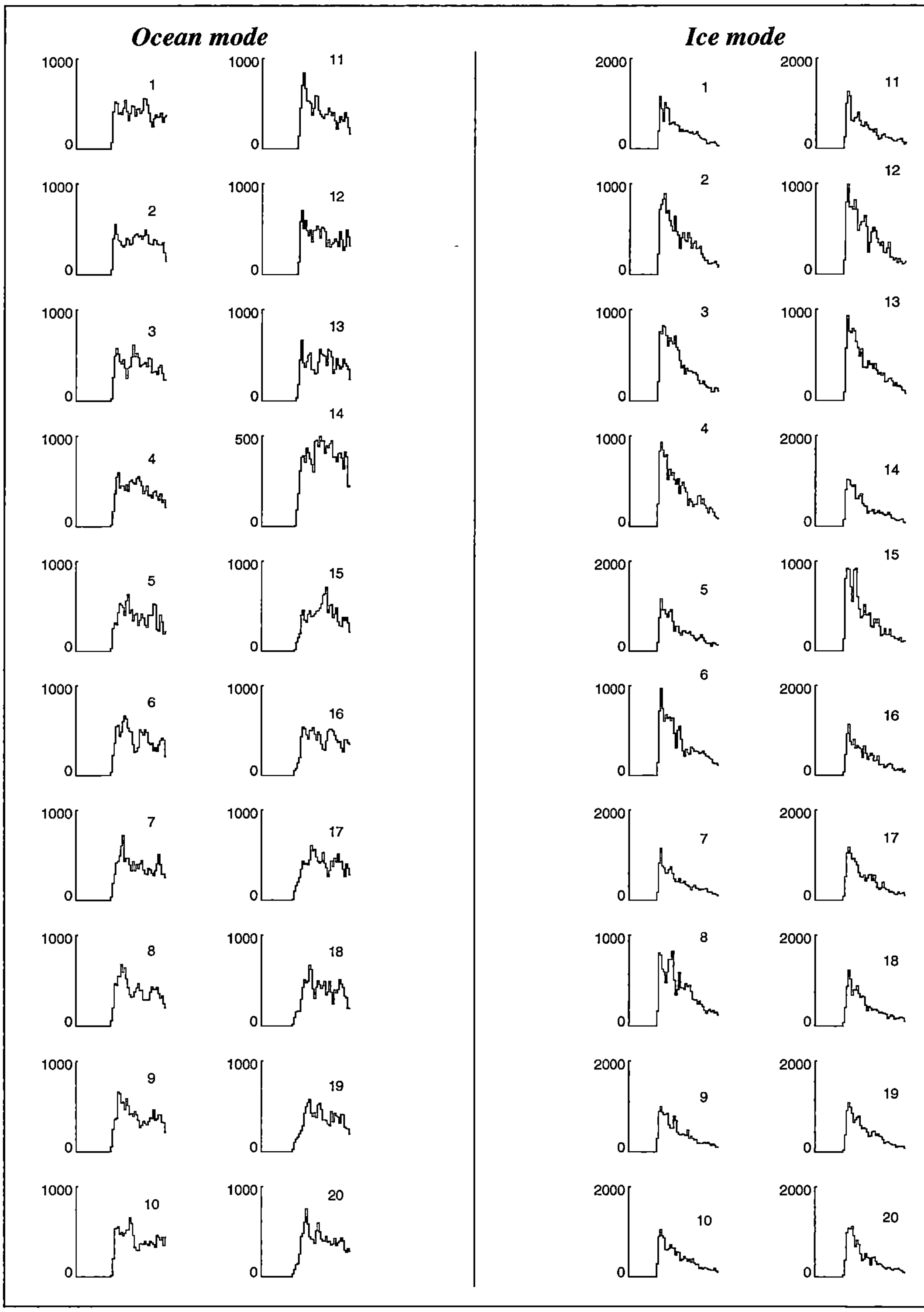

Figure 3.6 *Two sequences of ERS waveforms from consecutive repeats of a 3-day repeat track across the Amery Ice Shelf. The left sequence is in ocean mode and the right sequence in ice mode. Waveforms are numbered from 1 to 20, sequentially in time. Waveforms with the same number in each sequence are from approximately the same ground location.*

mode can be clearly seen. Since the ice mode waveforms are sampled more coarsely, they appear to be compressed. In addition, the ice mode waveforms have a more abrupt leading edge.

The ERS tracker is switched between ocean and ice mode under command from the ground (Scott *et al.* 1994). In the early stages of the ERS-1 mission (Phases B, C and D) the mode change occurred at the boundaries of the grounded ice. Furthermore, ice mode was only used for every alternate cycle during these phases. Later, during Phases E, F and G and for ERS-2, the ice edge was defined by the outer margin of the ice shelves, and ice mode was used for all cycles. Because of these mode changes, only a limited amount of ocean mode data exists over Antarctic ice shelves. Most of the data over the Lambert-Amery system used in this thesis were collected in ice mode. This is unfortunate, since around half of the grounded part of Antarctica that ERS-1 covers is free of undulations, as are the ice shelves (Scott *et al.* 1994). Data collected from these regions exhibit 'ocean-like' returns and ocean mode allows better sampling of the surface, leading to higher precision. Repeat track analysis carried out over these regions by Scott *et al.* (1994) demonstrated that the height precision was 0.28 m in ocean mode and 0.49 m in ice mode.

3.4 Errors in altimeter height measurements

Many corrections are needed to correct the time delay *(T)* measured by a satellite radar altimeter (Figure 3.1), to a range measurement (Guzkowska *et al.* 1990; Cudlip *et al.* 1994a). These corrections can be split into:

i) 'standard' altimeter corrections, which apply to altimeter data collected over all surface types; and

ii) 'ice' corrections, applicable to altimeter data collected over ice sheets and ice shelves.

Table 3.2 summarises the major sources of height errors and biases (both 'standard' and 'ice') in satellite altimeter data collected over ice sheets and ice shelves. Where possible the approximate magnitude and remaining error after correction are given.

TABLE 3.2 MAJOR SOURCES OF HEIGHT BIASES AND ERRORS, THEIR APPROXIMATE MAGNITUDES (IN METRES) AND RESIDUALS AFTER CORRECTION, IN SATELLITE RADAR ALTIMETER DATA COLLECTED OVER A) ALL SURFACES AND B) ICE SHEETS AND ICE SHELVES.

Bias/error	***Magnitude (m)***	***Residual after correction (m)***
a) 'Standard' biases/errors for all surfaces		
Instrumental errors	*~1.25*	*<0.01*
Satellite corrections	*~4.8*	*<0.08*
Propagation delays	*~2.3*	*~0.05*
Surface corrections (ocean and Earth tides)	*1-2*	*<0.11*
Radial orbit error	$\pm$ *0.3*	*<0.09*★
b) 'Ice' biases/errors for ice sheets and ice shelves		
Non-acceptable waveform shape	*N/A*	*waveforms removed through nested filtering*
Tracker error	$\pm$ *~20*	*up to 0.4*
Surface bias	*0 to 0.25*	*cannot be corrected for*
Surface penetration	*< 2**	*unknown*
Slope-induced error	*30 m for 0.5° slope*	*depends on local data density and surface topography*
Seasonal variation	*< 0.30 (Yi et al. 1997)*	*unknown*
Tide (ice shelves only)	*1-2*	*depends on model used and response of ice shelf*

Table compiled by author, from information reported in Cudlip *et al.* (1994a) and Guzkowska *et al.* (1990), except for those entries marked by ★ and * which are taken from Scharroo and Visser (1998) and Ridley and Bamber (1995) respectively.

'Standard' altimeter errors and their corrections are discussed in this Section 3.4.1. 'Ice' biases and errors are addressed in Section 3.4.2, and the various techniques developed for their correction are discussed in Section 3.5.

3.4.1 Standard altimeter corrections

Corrections supplied with the ERS-1 waveform data records are 'standard' corrections (Table 3.2). These standard corrections are generated at UK Earth Observation Data Centre (EODC) before the Waveform Advanced Product (WAP) data are released, with the exception of the orbit error (Cudlip and Milnes 1994). The standard corrections are described below.

Instrument corrections

These corrections (listed in Table 3.2) are dependent on the mode of operation of the altimeter instrument, and relate to internal hardware design, software processing delays and deterioration of electronic components (Cudlip *et al.* 1994a).

Satellite corrections

There are two main satellite-induced range corrections (Cudlip and Milnes 1994) which are listed below.

Doppler correction

The Doppler correction is required to account for the possible Doppler shift resulting from any relative vertical component of the satellite velocity, which is interpreted by the altimeter as a range offset (Cudlip and Milnes 1994).

Centre-of-gravity offset

The centre-of-gravity offset corrects for the distance between the range-measurement reference point on the altimeter (the aperture plane of the altimeter antenna) and the reference point for the spacecraft altitude provided in the orbit ephemerides (spacecraft's centre-of-gravity). The centre-of-gravity position changes throughout the mission as fuel is consumed, and a new offset value is used after each orbital update manoeuvre (Cudlip and Milnes 1994).

Atmospheric corrections

The atmospheric corrections account for the retardation of the radar pulse by the atmosphere through which it propagates (Cudlip *et al.* 1994a). Essentially, they convert the measured 'optical distance' travelled by the pulse into a true physical distance. Various algorithms have been adopted to compute these corrections (Cudlip *et al.* 1994a). However, these algorithms are generally not appropriate in the polar regions, and so the atmospheric corrections provided with the ESA ERS altimeter data are not accurate over Antarctica.

A solution to this problem is to use *in situ* atmospheric observations to derive regional atmospheric corrections. There are several sources of atmospheric observations for the Lambert-Amery system. Along the Lambert Glacier traverse route there are six Automatic Weather Stations (AWS) that continually measure surface temperature, surface pressure and wind speed (Chapter 2). Meteorological data are also available from the Australian Antarctic stations, Davis and Mawson (see Figure 1.2 for station locations). Tropospheric moisture content and temperature information are available from balloon-sondes launched from these stations. One other parameter that can be measured *in situ* is the 'Total Electron Content' (TEC) of the ionosphere, which is needed to compute the ionospheric correction. This can be derived from measurements collected by dual frequency GPS receivers (at Davis and Mawson).

Dry tropospheric correction

The dry tropospheric range correction (ΔR_{dry}) takes into account the delay in transmission time for the radar pulse through the atmosphere imposed by the presence of non-polar gases in the troposphere (oxygen, nitrogen *etc.*) (Cudlip *et al.* 1994a). Its calculation requires knowledge of the total mass of the air column, estimated from the surface air pressure.

ΔR_{dry} (in metres) is derived from the following equation (Cudlip *et al.* 1994a):

$$\Delta R_{dry} = \frac{2.277\times10^{-3}\left(1+0.00265cos(2\varphi)\right)}{P_0} \qquad (3.11)$$

where P_0 is the surface pressure in hPa

φ is the latitude.

From Equation 3.11, it can be seen that a discrepancy as small as 20 hPa in the pressure will lead to a 5 cm error in this correction. In the ESA records, ΔR_{dry} is set to zero when the surface elevation is greater than 1800 m, which introduces a height error of about 1.8 m. This is unsatisfactory in the Lambert-Amery system, where much of the surface is at elevations greater than 1800 m.

The values for ΔR_{dry} used in this thesis were derived from observations of surface pressure collected at the Lambert Glacier Basin traverse AWS sites (LGB00, LGB10, LGB20, LGB35, LGB46 and LGB59; see Figure 2.5 for AWS locations). The mean correction at each AWS site was calculated for each month of 1994 (Figure 3.7a). It can be seen that the correction is relatively constant throughout the year and varies by less than 3 cm. Therefore, to a first approximation, the annual mean value can be used for the ΔR_{dry} value at each AWS site. It is assumed that this is a valid approximation over the entire Lambert Amery system.

To correct for ΔR_{dry} over the Lambert-Amery system, a simple surface pressure versus surface elevation relationship was derived. This was a linear relation, based on a least-squares line fit to the AWS data (see Figure 3.7b). To correct the altimeter data, the approximate surface elevation *(h)* of each point was derived from Equation 3.2, and used to calculate ΔR_{dry} using the following regression equation:

$$\Delta R_{dry} = 2.085 - \left(1.86 \times e^{-3}\right)h \qquad (3.12)$$

A constant value for ΔR_{dry} was used over the Amery Ice Shelf for the ERS-1 and -2 data collected during the Amery survey (see Chapter 4), used in the validation section of Chapter 5. This value was 2.23 m, derived from a mean surface pressure of 983 hPa, calculated from daily observations made throughout the Amery survey.

The difference between the ΔR_{dry} values used here and the values provided in the ESA ERS records were calculated. For the 168-day data over the Lambert-Amery (for the cases where the correction had not been set to zero) the mean difference between the derived values and the ESA values was -0.16 m. Over the Amery Ice Shelf only, using the ERS-1/2 data collected during the survey, the values were in close agreement. The mean value from the measurements was 2.23 m, compared with a mean value from the ESA records of 2.21 m.

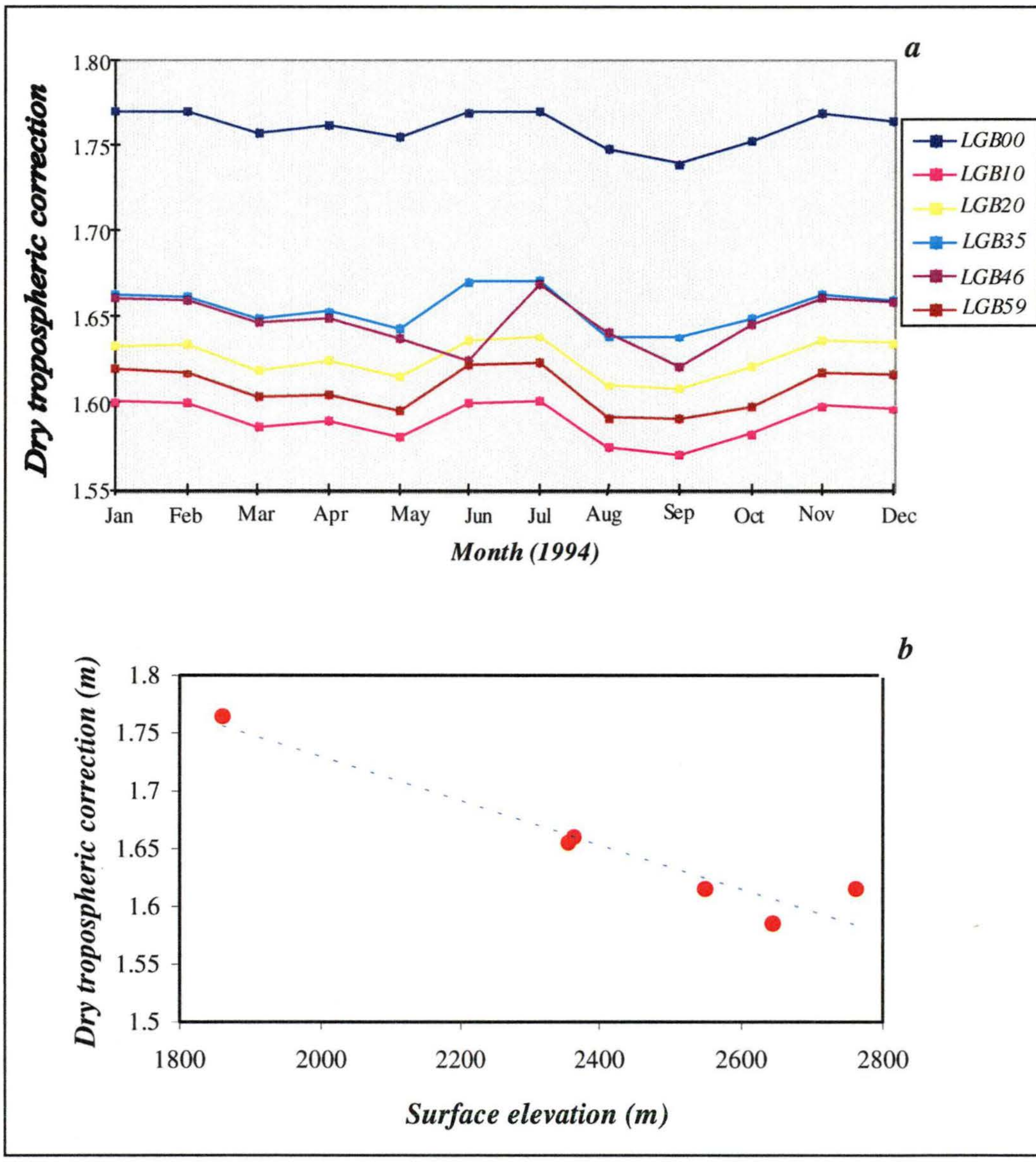

Figure 3.7 *a) Mean monthly dry tropospheric correction for 1994 at each Lambert Glacier AWS and b) mean annual (1994) dry tropospheric correction versus ellipsoidal surface elevation at each AWS. Data provided by Ian Allison, Antarctic CRC/Australian Antarctic Division.*

Wet tropospheric correction

The wet tropospheric range correction *(ΔR_{wet})* accounts for the effect of water vapour (polar gases) in the atmosphere (Cudlip *et al.* 1994a). ΔR_{wet} depends on the total integrated water vapour and surface air temperature. The correction is insignificant over the interior of Antarctica, where the air is so cold that the amount of water vapour it holds is small. However, close to the coast, especially during summer, relatively high values of moisture content can occur (Neil Adams, personal communication, 1997).

The correction (in metres) is calculated from the following formula (Cudlip *et al.* 1994a):

$$\Delta R_{wet} = -W * \left(2.584\times10^{-5} + 5.324\times10^{-2}\ln\left(1-\frac{32.5}{T}\right)\right) \qquad (3.13)$$

where W is the total integrated water vapour in kg m^{-2}

T is the surface air temperature in K

The value for ΔR_{wet} used in this thesis was a mean value derived from observations. Data from radio-sonde balloons launched at Davis and Mawson stations were used to estimate average monthly W values for 1994 over the region. These W values varied between zero and 21 kg m^{-2} (Neil Adams, personal communication, 1997).

Figure 3.8 shows the variation in ΔR_{wet} over this range of W values, with typical surface air temperatures for the Amery Ice Shelf. It can be seen that ΔR_{wet} varies from around 0.006 m to 0.16 m. The value used for ΔR_{wet} over the Lambert-Amery system was 0.10 m, compared with a mean value in the ERS records of 0.15 m.

Ionospheric correction

The ionospheric correction accounts for the delay in propagation of the radar pulse as a result of its interaction with free ions and electrons in the portion of the Earth's ionosphere between the satellite and the ground (i.e. between 70 km and 800 km). The ionisation is caused by the action of Extreme Ultra-Violet and X-band solar radiation on the gas molecules and atoms present at these altitudes (Hoffmann-Wellenhof *et al.* 1993). The degree of ionisation depends on the temperature and density of the gas molecules, and the solar radiation intensity. Therefore, it varies with time of day, with season, with geographical location and with the solar cycle.

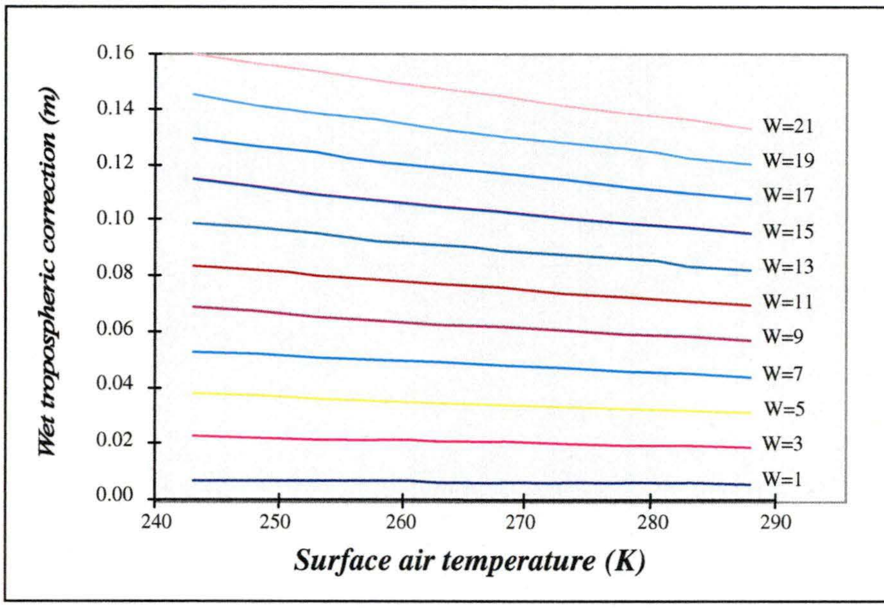

Figure 3.8 *Wet tropospheric correction values for typical total integrated water vapour and surface temperature values in the Lambert-Amery system. Meteorological data provided by Neil Adams, Antarctic CRC/Bureau of Meteorology.*

The refractive index of the ionospheric layer depends on the column-averaged density of free electrons, the total electron content (TEC), measured in TEC units (TECU, where 1 TECU = 10^{16} m^{-2}). The ionospheric delay correction, in metres, is calculated using the following expression (Cudlip *et al.* 1994a):

$$\Delta R_{ion} = 0.403\frac{E}{f^2} \qquad (3.14)$$

where E is the TEC in TECU

f is the frequency of the altimeter signal (13.8 GHz for ERS).

The ESA records contain a value of TEC derived from the sunspot number, and use a series of look-up tables containing monthly mean values of TEC. The 'International Reference Ionosphere' TEC model data is supplied by the Department of Physics at the University of Leicester, and the sunspot numbers from the World Data Centre at the Rutherford Appleton Laboratories. The models are known to be poor in

Antarctica where the ionosphere is subject to unpredictable disturbances during periods of high solar activity (Wyn Cudlip, personal communication, 1996). At high-latitudes, magnetospheric sub-storms, resulting from the interaction of the solar winds with the magnetosphere, are common. This leads to significant increases in TEC for up to several days, over horizontal scales of several tens of kilometres north-south and several hundreds of kilometres east-west. However, at the ERS altimeter frequency (13.8 GHz), a 30% increase in TEC (typically about $6 \times 10^{16}\ m^{-3}$) would only affect the ionospheric range correction by about 0.05 m (Equation 3.13).

Values of TEC are best obtained by direct measurements using a dual frequency microwave instrument, from the differential delay in transmission times of the two frequencies. ESA intended that the Precise Range And Range Rate Equipment (PRARE) (Hartl 1984), a dual frequency microwave ranging system on board ERS-1, would provide TEC measurements along the line of site from the ground station to the satellite. Unfortunately, PRARE failed and provided no data (Battrick 1993).

Dual frequency GPS measurements can also be used to compute TEC, along the line of sight from receiver to satellite (Goodwin *et al.* 1995). The correction process involves constructing a TEC shell, and then calculating the TEC along the propagation path from ERS to the ground. This was done for GPS data collected at Mawson, and the results have been used to estimate values for the Lambert-Amery basin station (Peter Morgan, personal communication, 1997). Based on these results, the ionospheric correction used for the Lambert-Amery system was a mean value of 0.09 m, compared with a mean value of 0.11 m in the ESA records over the region.

Surface corrections

The main range corrections associated with the surface are due to the action of Earth tides and, on free-floating parts of the ice sheets, ocean tides. These can be corrected for to derive ranges relative to a 'tide-free' surface.

Solid-Earth tide

This correction accounts for the Sun and Moon tidal effect on the solid Earth. It is calculated using a gravitational potential model. ESA applied a correction based on the NOAA Geosat code using Cartwright-Tayler-Edden tables with modifications (including Love numbers) as recommended by the TOPEX/Poseidon tides subcommittee (Cudlip *et al.* 1994a).

Ocean tide correction

A correction for ocean tides is required over the free-floating parts (ice shelves and glacier tongues) of the Antarctic ice sheet, which undergo vertical motion in response to ocean tides (Holdsworth 1977). The ocean tide corrections in the ESA data record are valid for the open ocean only. Therefore, a special treatment of this correction is required over ice shelves.

Each surface height profile described by an altimeter over an ice shelf can be thought of as a 'snap-shot' of the instantaneous ice shelf surface at the observing epoch. For any point on the ice shelf surface, the height h_t above the ellipsoid is made up of the tide-free height component (h_0) and the temporal tidal height component (Δh_{tide}) i.e. $h_t = h_0 + \Delta h_{tide}$. To compare heights measured at different epochs it is necessary to remove the tidal height component and use the 'tide-free' height component.

For this thesis, a tide model for predicting tides at Beaver Lake (the Beaver Lake Tide model (BLTM)) is available from the National Tidal Facility (NTF), Australia (Marion Tait, personal communication, 1996). Results presented in Chapter 4 indicate that the BLTM can be used as a proxy model to correct ERS altimeter heights to a tide free datum on the Amery Ice Shelf. Look-up tables of predicted tidal values were obtained from the NTF.

To subtract the BLTM value from the Amery Ice Shelf ERS heights, a mask was used which (approximately) defined the extent of the ice shelf. The mask was generated from the Slopes Database (Appendix B). For each ERS pass over the Amery Ice Shelf, the Universal Time of the first record that fell within the Amery Ice Shelf mask for that pass was used to find the tide value from the BLTM look-up table. The BLTM value was the same for all measurements along a pass across the Amery Ice Shelf, because the ERS satellites only took a few seconds to cross the

Amery Ice Shelf. The BLTM value was subtracted from the relocated ellipsoidal height measurement for each point within the Amery Ice Shelf mask.

Orbit error

The ephemerides used for the spacecraft location in the ESA ERS records were subject to certain errors. The orbits for both ERS-1/2 have been improved through post-processing and orbit refinement modelling by a group at the Delft Institute for Earth Oriented Research (DEOS), University of Delft, as outlined in Scharroo and Visser (1998). These orbits were down-loaded from the DEOS World Wide Web site (DEOS 1997). The radial precision of the DEOS orbits is approximately 90 mm Scharroo and Visser (1998).

The purpose of a new orbit is to provide an improved WGS-84 position for the ERS spacecraft at a given time. The information provided with the DEOS orbits is Universal Time (UT), and the latitude, longitude and altitude of the spacecraft (DEOS 1997). For each altimeter measurement, the UT was used to find the new position for the spacecraft from the DEOS orbits. The ESA values for latitude, longitude and altitude of the spacecraft were then replaced with the interpolated DEOS values.

3.4.2 Errors and biases in ice waveforms

The main problem encountered in processing altimeter data collected over non-ocean surfaces is in locating the point on the waveform echo that corresponds to the mean surface height. This difficulty arises because non-ocean surfaces are generally complex and inhomogeneous, as described in Section 3.3. Over these surfaces there are variations in topography, surface properties, geometric roughness and surface backscattering coefficients across the altimeter footprint. This introduces several errors and biases into altimeter waveforms collected over ice sheets and ice shelves. This section discusses these 'ice' errors and biases.

Table 3.2 listed several 'ice' errors and biases unique to satellite altimetry over ice sheets and ice shelves. These errors are:

- Non-uniform waveform shape
- Tracker error
- Surface bias
- Surface penetration bias
- Slope induced error

These errors must be corrected for using specially developed processing techniques. The various techniques that have been developed to remove them, and results of published evaluations of these techniques, are discussed in Section 3.5.

Waveform shape

The ERS Waveform Advanced Product (WAP) records contain waveforms that have passed the ESA testing algorithms for each ERS orbit (Cudlip and Milnes 1994). Over the Antarctic continent, there are many invalid waveforms present, which would yield erroneous range measurements if retained. Examples include waveforms that contain no leading edge (due to loss-of-lock) and waveforms that are too complex to interpret (Partington 1988). The WAP data must be filtered so that such waveforms are not used in the final altimeter data set.

In this thesis, filters were developed to identify invalid ERS waveforms over the ice sheet. The filters, outlined in Appendix A, searched for the following:

i) No leading edge in the range window

ii) Complex waveform shape

iii) Quasi-specular waveform shape

iv) Anomalous backscatter value.

These filters were applied using nested algorithms: i.e. waveforms passing one filter were used as input to the next filter (in the order i) to iv) above).

Tracker error

The range measurement supplied in the ERS data records is derived from the time delay between the transmission of the pulse to the mid-point of the range window (tracking point). When the ERS altimeters operate in ocean mode over the oceans, the leading edge of the waveform is generally located at the tracking point, therefore the time delay is measured to the true surface. However, over more complex surfaces, the ocean mode tracker cannot maintain the leading edge of the waveform at the centre of the range window. Furthermore, the ice mode tracker was not designed to keep the leading edge of the waveform centred at the tracking point (Section 3.3.3). In either case, the leading edge of the waveform will be offset from the tracking point, resulting in an error in the range (Martin *et al.* 1983; Figure 3.9).

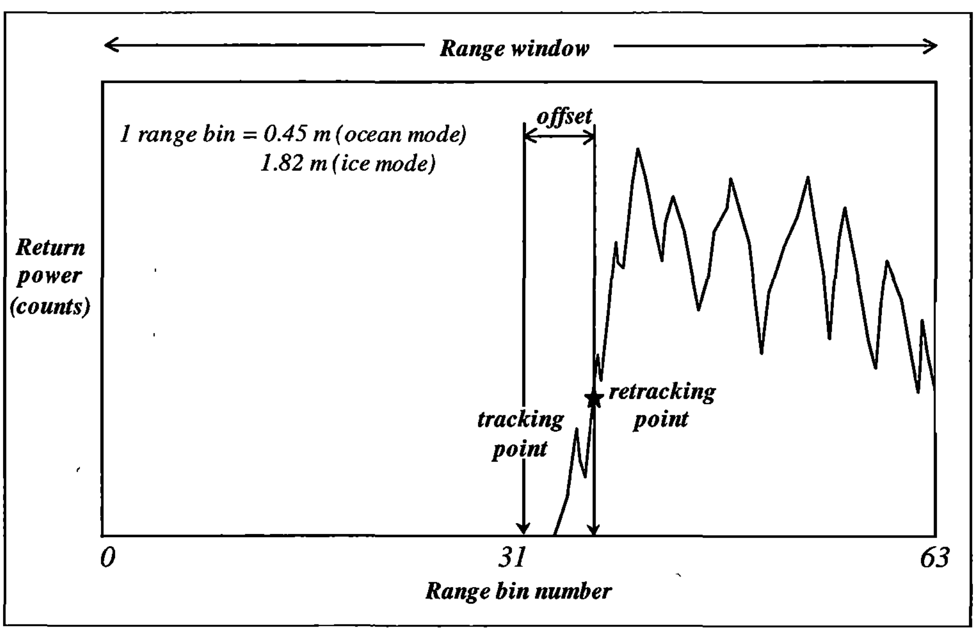

Figure 3.9 *Typical altimeter waveform from ice, showing the offset of the waveform leading edge from the tracking point. This offset is equal to the number of bins between the leading edge and the tracking point. Adapted from Davis (1997).*

Estimation of the true range to the reflecting surface can be obtained by determining the offset (in range bins) of the leading edge from the mid-point of the range window, on a waveform by waveform basis. This procedure of re-measuring the range to the surface, given the telemetered range and the recorded waveform, is known as 'retracking' (Martin *et al.* 1983).

Retracking corrections over the ice sheets can be up to several metres (Martin *et al.* 1983). Failure to retrack can result in false apparent surface features, and can overlook real features (Martin *et al.* 1983). For a retracking algorithm to be useful for mass balance studies, it must produce a repeatable surface height measurement (Davis 1997). A requirement for the selection of a retracking algorithm is therefore that it is consistent in selecting a retracking point on the waveform leading edge (i.e. that it is robust for small variations in waveforms), so that no further bias is introduced into the elevation estimate.

Surface bias

After retracking, a bias will remain in the surface height estimate, known as the 'surface bias'. The surface bias is the offset between the chosen retracking point on the leading edge, and the location on the waveform of the true mean surface. Estimation of the size of this bias (up to 25 cm) depends on the true surface geometry, the geometric roughness distribution and also variations in backscatter characteristic of surface facets. Since its calculation requires an exact description of the surface, the surface bias is difficult to remove.

Surface penetration bias

Over much of the Antarctic plateau, not all of the incident radiation is scattered at the surface (Ridley and Partington 1988). Some of it penetrates the surface firn layer, leading to 'volume scattering' from within the layer and reflections from sub-surface layers and ice lenses (Figure 3.10). This increases the path length of the reflected radiation, and therefore its travel-time back to the satellite, resulting in the waveform having a different shape to that if only surface scattering occurred.

Surface penetration can cause elevation errors of up to 3.3 m (Ridley and Partington 1988).

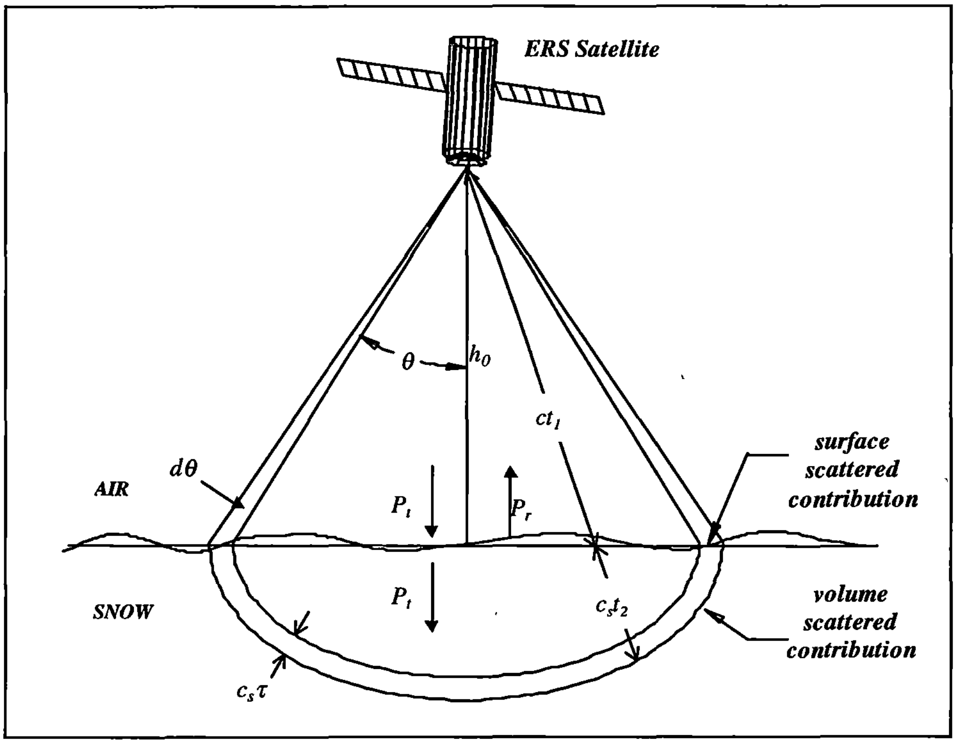

Figure 3.10 *Schematic diagram illustrating the process of volume scattering. The altimeter pulse penetrates into the surface layer and subsequently undergoes scattering within the layer. Adapted from Davis and Moore (1993).*

Slope-induced error

A further problem with altimetry over non-ocean surfaces results from the effect of larger scale topography. The satellite altimeter range measurement is made to the closest point on the surface within its 'beam-limited' footprint (Brenner *et al.* 1983). When the reflecting surface is tilted with respect to the ellipsoid, this point will not be at the sub-satellite point (nadir), but at a point displaced up-slope from nadir along the direction of maximum slope (Brenner *et al.* 1983). The range measurement that is provided in the altimeter data records does not correspond to the nadir position, and an offset must be applied either to the range measurement or to the coordinates provided in the ERS-1 data set, or both. The difference in the position of the nearest point compared to that at nadir is proportional to the magnitude of the slope, and is displaced along the direction of the maximum gradient within the footprint. Over sloping regions of Antarctica, this is by far the largest error encountered in altimetry.

It is known as the 'slope-induced error' (Brenner *et al.* 1983) and, to a certain extent, can be corrected for by adopting a slope correction technique.

3.5 Processing techniques over ice sheets and ice shelves

This section discusses the various techniques that have been developed to correct for the errors and biases discussed in Section 3.4.2, to estimate mean surface height from altimeter waveforms collected over ice. Retracking techniques are discussed first, followed by slope-induced error correction techniques. Results of previous studies using the various techniques are also presented.

3.5.1 Retracking techniques

Several retracking algorithms have been successfully implemented and tested by different altimeter research groups (e.g. Martin *et al.* 1983, Wingham *et al.* 1986, Davis 1993b, Davis 1997).

The main retracking algorithms that have been developed are:

i) β-parameter retracking algorithm (Martin *et al.* 1983)

ii) leading edge threshold detector using the OCOG algorithm (Wingham *et al.* 1986; Bamber 1994)

iii) surface and volume retracking algorithm (Davis 1993b).

These retracking techniques are discussed below, followed by a critical comparison of the techniques.

β-parameter retracking algorithm

This was the first documented ice sheet retracking method, and was developed at the National Aeronautics and Space Administration (NASA) by Martin *et al.* (1983). The β-parameter algorithm uses a theoretical model based on the Brown (1977) model, and fits a 5 or 9-parameter function to the altimeter waveform (Figure 3.11).

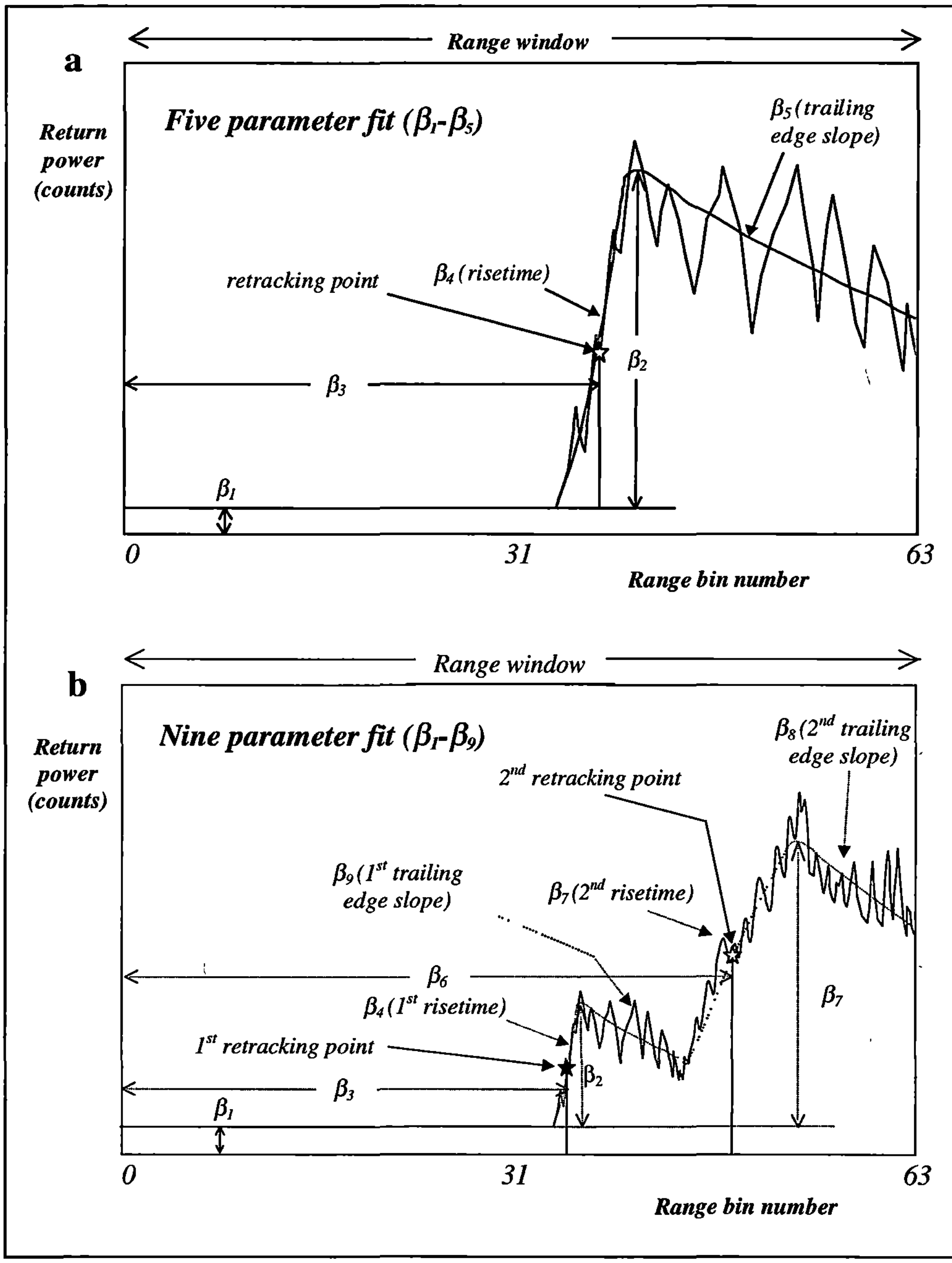

***Figure 3.11** β-parameter fitting using a) a 5 parameter (single ramped) model and b) a 9 parameter (double ramped) model.*

The 5-parameter model (Figure 3.11a) is used for 'simple' waveform shapes that have a single leading edge. One of the parameters *(β_3)* defines the position of the waveform leading edge, which is then used to correct the altimeter measurement. The 9-parameter model (Figure 3.11b) is used for 'complex' waveforms, which have two leading edges. This type of return is observed when there are two main reflecting surfaces at different ranges contributing to the power in the range window.

In this case, two of the parameters *(β_3 and β_6)* define the leading edges, providing two range corrections.

The β-algorithm first classifies each individual return waveform as being 'simple' or 'complex', and then fits the relevant model to the waveform to find the leading edge. A disadvantage of the β- parameter algorithm is that it has difficulty fitting to the waveforms when they contain topographic-induced distortions (Rapley *et al.* 1990).

Offset Centre-of-Gravity (OCOG) threshold retracker

The Offset Centre-of-Gravity (OCOG) threshold retracker uses a power threshold based on the waveform shape to determine a retracking point on the waveform leading edge (Bamber 1994). An estimate of the waveform amplitude is made and used to threshold retrack the leading edge at a specified percentage value. The waveform amplitude is determined using the OCOG algorithm, a technique first described by Wingham *et al.* (1986) to improve tracking over topographic surfaces for ERS-1 (ice mode). A threshold retracker using the OCOG algorithm is currently used by ESA.

The waveform amplitude *(A)* is determined by computing a rectangular box whose centre-of-gravity and area are the same as the waveform itself. The amplitude is twice the amplitude of the centre of gravity of the waveform. That is (Wingham *et al.* 1986):

$$A = 2\frac{\sum 0.5 p_n^{\,2}}{\sum p_n} \qquad (3.15)$$

where p_n is the power in the n^{th} range bin, and the summation is over all range bins.

In practice, the square of the waveform power *(p_n^2)* is used to calculate A (Rapley *et al.* 1987). This reduces the effect of the low value bins at the front of the waveform. For ERS-1 the first few bins of each waveform data are aliased, due to the problem of Fourier wraparound (Jeffrey Ridley, personal communication, 1998) therefore these bins are left out of the summation.

With these modifications, Equation 3.15 becomes:

$$A = \sqrt{\frac{\sum_{5}^{64} p_n^{\ 4}}{\sum_{5}^{64} p_n^{\ 2}}} \tag{3.16}$$

The OCOG method is illustrated in Figure 3.12. The retracker uses a threshold value, $T_{x\%}$, a pre-defined percentage *(x%)* of *A*. The first bin on the leading edge with a value exceeding $T_{x\%}$ is determined. Linear interpolation between this bin and the preceding bin provides the location of the retrack point on the leading edge.

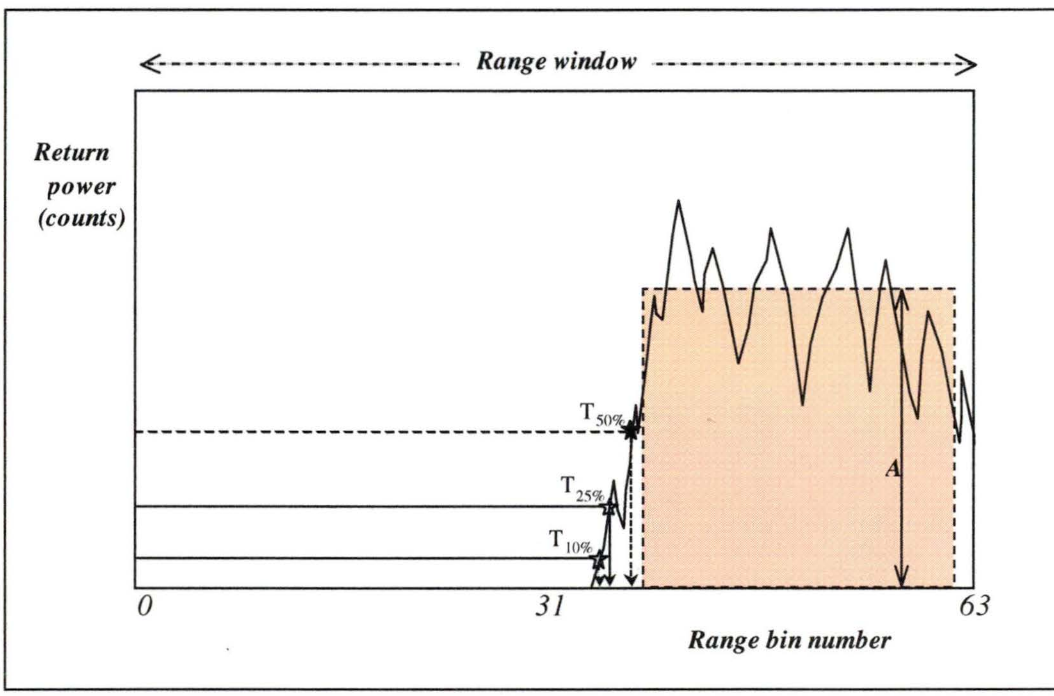

Figure 3.12 *Schematic diagram illustrating OCOG method. The amplitude (A) is twice the height of the vertical position of the waveform centre of gravity. The diagram illustrates three different threshold values on the leading edge (10%, 25% and 50% of A). Adapted from Rapley et al. (1987).*

Various values have been adopted for the percentage value, usually 25% or 50% (Bamber 1994). For returns from the ocean, the 50% value generally coincides with the mean surface.

A disadvantage of the OCOG threshold retracker is that because the OCOG algorithm is an empirical technique, and not based on a physical model, the retrack position on the leading edge can be sensitive to variations in surface properties (Ridley *et al.* 1989). Despite this, it has been shown to perform well (see 'Comparison of retracking techniques').

Surface and volume retracking algorithm

The combined surface and volume scattering retracking algorithm was developed by Davis (1993b) to account for the effect of surface penetration of the radar pulse (see Figure 3.10). Neither the OCOG threshold technique nor the β-parameter model can account for this effect, as it requires a theoretical model for the return power envelope, based on both the surface and the volume scattered contributions.

When the energy from the expanding spherical shell hits the surface, the incident power density is divided into a reflected component and transmitted component. The reflected component is dependent on the power-transmission coefficient at the surface, whilst the transmitted component is proportional to the relative complex dielectric constant at the surface. The transmitted radar power at a certain depth is attenuated through scattering and absorption by particles within the volume of the layer. The backscattered power is further attenuated as it propagates back up through the layer on its way to the surface, where it is transmitted back across the surface boundary and received back at the altimeter.

Ridley and Partington (1988) developed an integral model to describe the altimeter return waveform, accounting for both the surface and the volume scattering components, based on radiative transfer theory. Davis and Moore (1993) built upon this work by developing a closed (non-integral) expression to describe the average return power envelope received by the altimeter that results from volume scattering. Davis (1993b) combined the Davis and Moore (1993) volume scattering model with the Brown (1977) model for surface scattering, and utilised the combined model in a retracking algorithm. Both the model and retracking algorithm are discussed below.

Davis and Moore (1993) volume scattering model

Davis and Moore (1993) made the following assumptions:

- The surface is ideal, and homogeneous across the footprint
- The height distribution of the surface scattering elements and the altimeter antenna pattern can be represented by Gaussian functions
- There is only one surface layer, which is homogeneous, composed of dry, spherical ice particles and air, the material properties varying linearly with depth.
- There is no multiple scattering
- The angles θ are small

The expression for the total volume-scattered portion of the term was derived by integration. Each point on the expanding spherical pulse has a penetration depth that is determined by its angular distance from nadir *(θ)* (see Figure 3.10). The equation for the differential power received back at the altimeter from a differential volume is derived using spherical coordinates and by considering the radiative transfer equations for a given penetration depth.

Davis and Moore (1993) simplified the derivation by converting to t'', the two-way incremental ranging time given by:

$$t'' = t - t_0$$

where t_0 is the time of initial intersection of the pulse with the surface i.e. $t_o = 2\frac{h}{c}$.

By integrating over all angles θ, from nadir to the edge of the shell volume, where $0 < \theta < \cos^{-1}(t_o/t)$, Davis and Moore (1993) obtained the following expression:

$$dP_{vol} = A'\left\{\exp\left(\frac{-2t''}{t_0\beta^2}\right) - \exp(-2k_e c_s t'')\right\} \qquad (3.17)$$

which is valid only for ranges *below* the ice surface (i.e. t'' > zero, or $t > t_0$) where volume scattering actually contributes to the received power.

Davis and Moore (1993) integrated Equation 3.17, to obtain an expression for the returned power due to volume scattering. This was done by calculating a convolution integral, between the impulse response dP_{vol}/dt'' and the transmitted pulse profile $P_T(t)$ (assumed to be Gaussian). The resulting expression was rewritten as a tabulated integral, and the following closed expression for the received power due to volume scattering, $P_{vol}(t'')$, obtained:

$$P_{vol}(t'') = A''\left\{\exp\left(\frac{\beta_\tau^{\ 2}}{t_0^{\ 2}\beta^4} - \frac{2t''}{t_0\beta^2}\right) - \exp\left(\beta_t^{\ 2}k_e^{\ 2}c_s^{\ 2} - 2k_e c_s t''\right)\right\} \qquad (3.18)$$

where t'' is the two-way incremental ranging time

A'' is an amplitude given by $A'' = \sqrt{\pi}\,\beta_\tau A'$

β_τ is the pulse-width constant

k_e is the extinction coefficient of the surface layer

c_s is the speed of propagation of electromagnetic radiation in the surface layer

The extinction coefficient (k_e) is the sum of the absorption coefficient k_a and the scattering coefficient k_s. Davis and Moore (1993) noted that the constants in the argument of the first exponent in Equation 3.18 were determined by the design characteristics of the altimeter, whilst those in the second term were determined by the physical properties of the surface layer.

Surface scattering model

The Brown (1977) model for ocean returns has already been discussed. The model assumes that the height distribution of scattering elements can be approximated by a Gaussian function, and that only surface scattering occurs. The Brown (1977) surface scattering model P_{surf} in terms of the two-way incremental ranging time t'' is:

$$\begin{aligned} P_{surf}(t'') &= 0.5P_{fs}(0)\left\{1 + \operatorname{erf}(t''/\sqrt{2}\sigma_c)\right\} && \text{for } t'' < 0 \\ &= 0.5P_{fs}(t'')\left\{1 + \operatorname{erf}(t''/\sqrt{2}\sigma_c)\right\} && \text{for } t'' \geq 0 \end{aligned} \qquad (3.19)$$

The parameters in Equation 3.19 are described by equations related to both the properties of the surface and of the altimeter. These are:

- **$P_{fs}(t'')$:** the flat-surface impulse response, given by

$$P_{fs}(t'') = \exp\left(\frac{-4ct''}{\gamma R}\right) \tag{3.20}$$

where c is the speed of propagation of electromagnetic radiation in vacuo

γ is the one-way beam-width coefficient of the antenna given by

$$\gamma = \frac{2\sin^2(\theta_{3db}/2)}{\ln 0.5} \tag{3.21}$$

where θ_{3db} is the half power beam width of the antenna pattern

R is the satellite range

- **erf:** the error function:

$$erf(x) = \frac{2}{\sqrt{\pi}}\int_0^x e^{-t^2}\,dt \tag{3.22}$$

- **σ_c:** a parameter given by:

$$\sigma_c = \sqrt{\sigma^2{}_p + \left(2\frac{\sigma_s}{c}\right)^2} \tag{3.23}$$

where σ_p is related to the pulse width τ by $\sigma_p = 0.425\ \tau$

σ_s is the RMS surface roughness

Combined model

The expression for the total returned power is obtained by summing of the surface and volume scattering components. By writing the surface and volume scattering models in terms of the two-way incremental ranging time t'', the combined surface and volume-scattering model can be written:

$$P_{total} = P_{surf}(t'') + KP_{vol}(t'') \tag{3.24}$$

where $P_{surf}(t'')$ is the surface-scattering component (Equation 3.19)

$P_{vol}(t'')$ is the volume-scattering component (Equation 3.18)

K is the volume scattering coefficient

Davis and Moore (1993) fitted their combined model to averaged Geosat altimeter waveforms collected from three different regions of the Antarctic and Greenland ice sheets. They demonstrated that variations in waveform shape result from changes in near-surface properties, leading to differing relative amounts of surface and volume scattered power. Davis and Moore (1993) classified the return waveforms into three categories: purely surface scattered; purely volume scattered; and a combination of surface and volume scattered. They found that volume scattering contributes considerably to the total return power for the majority of the East Antarctic plateau waveforms.

The physical parameters that control the modelled altimeter waveform shape are (Davis and Moore 1993):

i) surface roughness (σ_s);

ii) volume scattering coefficient (K); and

iii) extinction coefficient (k_e).

σ_s controls the leading edge width when surface scattering occurs. K controls the relative contribution of the volume-scattered power to the total received power. k_e controls the rate at which the return power increases when volume scattering occurs. Larger values of k_e lead to a more rapid rise in the return power i.e. a steeper leading edge.

Figure 3.13 illustrates the evolution with time of the individual components of the return power when both the surface and volume scattering processes take place.

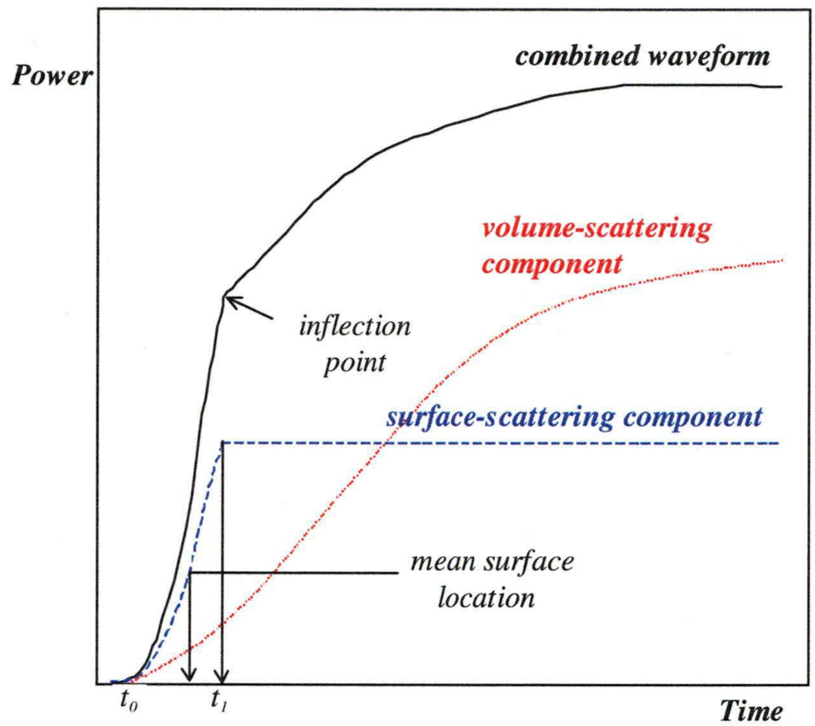

Figure 3.13 *Surface- and volume-scattering components of an ideal modelled ice sheet return. When both surface and volume scattering are present, the total power is a combination of their individual contributions. Between t_0 and t_1, both contributions increase with time, and the waveform gradient is steep. Surface scattering becomes constant at t_1, but volume scattering continues to increase. This produces a 'notch' or point of inflection in the waveform, which can be used to locate the mean surface. Taken from Ridley and Partington (1988).*

During surface scattering, for the period between the initial point of interaction (t_0) until the back of the pulse reaches the surface (t_1), the area contributing to the returned power increases with time (see Figure 3.3). As the volume of snow contributing to the return immediately after t_0 is small, surface scattering dominates, and the waveform shape closely follows the Brown (1977) model. Volume scattering becomes increasingly significant as the volume of snow contributing to the return power increases. For the period from t_0 to t_1, an initial sharp rise in the return power occurs, corresponding to a linear increase in both the surface area and the sampled volume. Once the illuminated surface area becomes constant, surface scattering no longer increases, however volume scattering continues to increase, so the return power also continues to increase, but at a slower rate. This causes an inflection point on the return power curve at t_1 (the time when the back of the pulse reaches the surface, Figure 3.3). Beyond the inflection point, the return is determined by the bulk properties of the snow, which define the scattering and absorption processes (Ridley and Partington 1988).

In the surface and volume-scattering retracking algorithm (Davis 1993a; hereafter referred to as the 'S/V algorithm'), the Davis and Moore (1993) model is fitted individually to each observed waveform. The observed radar surface is matched to the model radar surface, and the real surface location (n') calculated. n' is output as a correction to the half-power point on the leading edge of the surface-scattering component of the combined waveform. By locating the inflection point on the waveform, the mean surface can be estimated. The S/V algorithm returns five model parameters (Table 3.3).

TABLE 3.3 THE PARAMETERS RETURNED BY THE DAVIS (1993B) SURFACE- AND VOLUME-SCATTERING RETRACKING ALGORITHM.

Parameter	***Symbol***
RMS surface roughness	σ_s
Mean surface location	n'
Peak amplitude	A_m
Volume scattering coefficient	K
Extinction coefficient	k_e

There is a slight difference in the representation of the Davis and Moore (1993) model in the S/V algorithm, because the S/V algorithm only requires the *ratio* of the surface-scattered component to the volume-scattered component. Therefore, the absolute power need not be calculated, and the multiplication constants can be omitted from both the surface and volume scattering equations in the S/V algorithm. Normalisation constants ensure that the quantities $\{P_{surf} + P_{vol}\}$ and P_{vol} range from 0 to 1, so that K represents the true proportion of volume scattering (Davis 1993a).

The S/V algorithm is a non-linear model and uses an iterative least-squares process to fit the model to the observed waveform. The critical step is the estimation of the initial estimates for the least squares fitting process. Even when fitting the model to a waveform generated within the program, the algorithm does not return exactly the original input parameters (Curt Davis, personal communication, 1994). For this reason, in their paper applying the model to Geosat waveforms from Greenland, Davis and Zwally (1993) averaged output parameters from 100 input waveforms.

The S/V model can encounter problems when estimating the initial conditions for the fit. These conditions have to be established such that the fit converges. Application of the S/V model can be problematic since the surface and volume scattering models both describe the *mean* received power, whereas real waveforms fluctuate about this mean due to noise. This occurs despite the fact that each waveform is itself an average of many individual return pulses (50 for ERS). Although this averaging increases the signal-to-noise ratio to an acceptable level for signal processing, there is still some noise present (Griffiths *et al.* 1984,Wingham *et al.* 1986).

A version of the S/V algorithm (Davis 1993b), written for the retracking of Geosat data, was made available by Curt Davis for this project. The S/V algorithm (Davis 1993b) computes its initial estimates for k_e and K by generating many thousands of theoretical waveforms from a wide range of typical parameter values, with surface roughness held constant at 0.3 m (Davis 1993b). It determines the gradients of the leading edge and the plateau for each waveform, and stores them within a large four-dimensional 'look-up' table, together with the values for k_e and K. The real input waveform is first smoothed, and estimates for its leading edge and plateau gradients are determined. Initial estimates for k_e and K are found by matching these values with values in the 'look-up' table (Davis 1993b).

The initial estimate for mean surface location is the range bin corresponding to the maximum slope, and the initial estimate for surface roughness is determined from the leading edge width (Davis 1993b). The initial estimate for the waveform amplitude is simply the maximum power. An upper limit is set on the number of iterations to perform in the least-squares process. If the least-squares process has not converged after this number of iterations, the model parameters are not returned.

The S/V algorithm (Davis 1993b) was modified for ERS-1 data. Figure 3.14 shows a typical S/V algorithm model fit to an ERS-1 waveform from the Amery Ice Shelf. The application of the (modified) S/V algorithm to ERS-1 data is discussed further in Chapter 8. It will be shown that the algorithm only works well for ocean mode data (Figure 8.1). Since this project uses mainly ice mode data, the S/V model was not used here as a retracker.

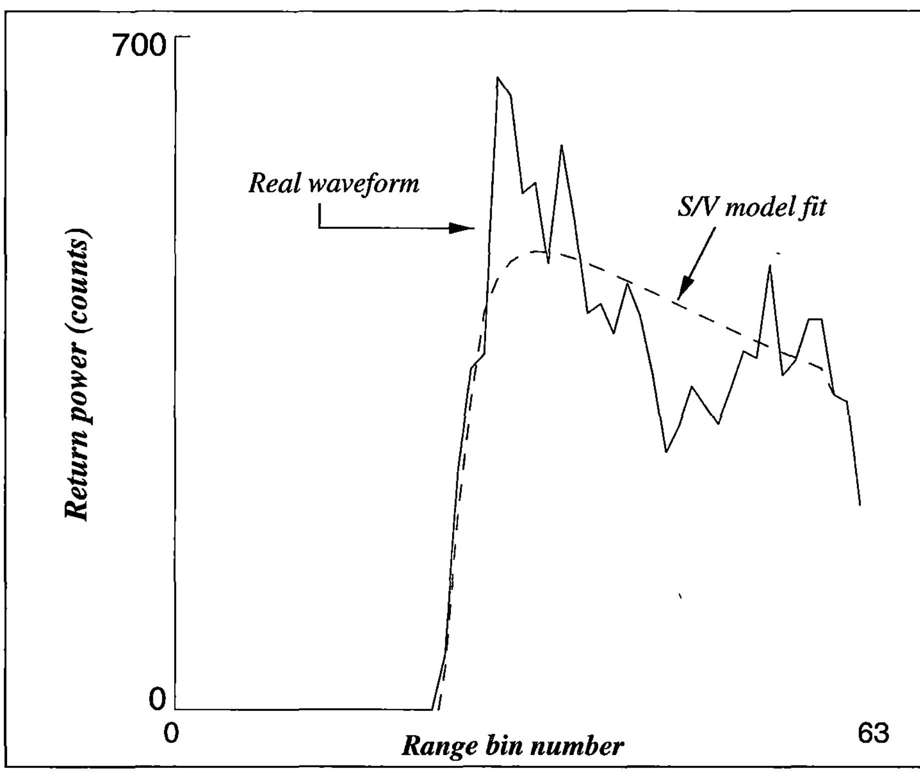

Figure 3.14 *Model waveform from the modified S/V algorithm fitted to an ERS waveform.*

Comparison of retracking techniques

Several authors have reported on the varying performances of retracking algorithms for different radar altimeters over the Antarctic and Greenland ice sheets (e.g. Bamber 1994; Davis 1995 and 1996; and Leeuwenburgh *et al.* 1996). Bamber (1994) tested the OCOG threshold retracker against the β-parameter retracker, using two repeats of Seasat altimeter data across Antarctica. He found that the standard deviation of the differences in elevations produced between the two repeat tracks was

1.28 m for the β-parameter retracker; 0.96 m for the OCOG threshold retracker using the 25% threshold (OCOG 25%); and 1.22 m for the OCOG threshold retracker using the 50% threshold (OCOG 50%). Over the Amery Ice Shelf, the respective differences were 0.66 m, 0.40 m and 0.40 m. Bamber (1994) concluded that OCOG 25% values were the least noisy. He confirmed this result by simulating several hundred ERS-1 waveforms for a flat, Lambertian surface with varying significant wave heights. He calculated the standard deviation of the retrack error, using the OCOG 25% and OCOG 50% values, and found it to be considerably lower for the OCOG 25% values, even at large values of significant wave height.

Davis (1995) used retracked heights from four different retracking algorithms (OCOG 25%, β-parameter, S/V and a simple threshold) to compare the performance of each one. He used the standard deviation of the height differences at crossovers for each of the retrackers as a measure of the algorithm's consistency in locating the retracking point. Using Seasat altimeter data, he found that the crossover differences were 0.79 m for the β-parameter algorithm and 0.51 m for all remaining three algorithms. Using Geosat data from the same time-period as the Seasat data, the corresponding differences were 1.34 m and 1.09 to 1.13 m. Using Geosat data for the entire 18 months, the differences increased slightly to 1.36 m for the β-parameter algorithm, and 1.14 to 1.15 m for the other three. This analysis showed that the empirical algorithms produced heights that were as repeatable as those from the theoretical S/V model, and more repeatable than those from the β-parameter model.

Davis (1996) estimated the repeatability of the surface elevations derived from Seasat and Geosat waveform data using the β-parameter, OCOG 25% and the S/V retracking algorithms. He used only data from a period when no elevation change was expected to occur. Davis (1996) calculated surface elevations using all three retrackers, analysed the height differences at several thousand crossover points on the Greenland and Antarctic ice sheets, for retrackers. Over Antarctica, he found that the standard deviations of the differences at 3868 crossover points of Seasat were 0.76 m for β-parameter, 0.58 m for OCOG 25% and 0.56 m for S/V. He attributed the larger errors in the β-parameter model to the fact that a mixing of the 5 parameter and 9 parameter models could be occurring at the four closest waveforms to a crossover point. This would yield a height discrepancy, since the two models produce different retracking corrections (Figure 3.10a and b). Davis (1996) found that, on average, the surface elevations from the OCOG 25% values were higher than the S/V-derived elevations, and the β-parameter heights were consistently lower than the S/V elevations.

Leeuwenburgh *et al.* (1996) tested the performance of the β-parameter retracker and the threshold retracker using the OCOG 25% value, using crossover analyses based on 6 months of ERS-1 waveform data collected over Greenland in both ocean and ice tracking modes. They calculated RMS height differences at crossover locations from both the OCOG 25% retracked heights and the β-parameter retracked heights using i) all waveforms, and ii) only those waveforms classified as single ramped by the β-parameter model. They found that the RMS differences (Table 3.4) were consistently lower for the OCOG 25% values.

TABLE 3.4 RMS OF HEIGHT DIFFERENCES AT CROSSOVER LOCATIONS USING THE β-PARAMETER AND OCOG THRESHOLD RETRACKERS FOR I) ALL WAVEFORMS, AND II) ONLY THOSE WAVEFORMS CLASSIFIED AS SINGLE RAMPED BY THE β-PARAMETER MODEL LEEUWENBURGH ET AL. 1996.

	β-parameter		***OCOG 25%***	
	Ocean mode	*Ice mode*	*Ocean mode*	*Ice mode*
i)	*0.51 – 4.26*	*0.90 – 1.97*	*0.41 – 2.21*	*0.46 – 0.96*
ii)	*0.50 – 0.80*	*0.74 – 1.40*	*0.38 – 0.67*	*0.46 – 0.94*

In summary, many researchers have reported that threshold retracking using the OCOG 25% value produces better results than the β-parameter algorithm over ice-covered surfaces. Davis' own analyses (1995 and 1997) have shown that there is little difference in performance between threshold retracking using the OCOG 25% value and his S/V algorithm. Therefore, for practical purposes, the threshold retracking using the OCOG 25% value is the most preferred, as it is computationally simpler and easier to implement. A simple threshold retracker, described by Davis (1995 and 1997), was recently adopted by NASA, after it was found to be more robust than their original β-parameter technique (Davis 1995). Davis's threshold retracker is simpler than the OCOG threshold retracker, as the threshold used is simply a percentage of the maximum waveform amplitude. This retracker was developed specifically for the measurement of ice-sheet elevation *change*, as it produces a more repeatable retrack point than the β-parameter model (Davis 1995).

In this thesis, a threshold retracker using the OCOG algorithm is adopted for the retracking of the ERS waveforms collected over the Lambert-Amery system. On the Amery Ice Shelf retracking is performed to the 10%, 25% and 50% thresholds, and the results compared with GPS heights (Chapter 5).

3.5.2 Slope-induced error correction

An accurate, three dimensional, slope correction requires an *a priori* knowledge of the local cross-track slope at the sub-satellite point (Brenner *et al.* 1983). This presents a somewhat circular problem in that, in general over the Antarctic continent, the magnitude of the slope under the altimeter is not known *a priori*. An iterative approach is therefore required in order to reconstruct the real altimeter surface from the apparent surface. The best information available for computation of these slopes is provided by the non-slope-corrected ERS data themselves. A major problem with using this method for previous altimeter missions and for the early phases of ERS-1, was that there was little information across track (Brenner *et al.* 1983). At 71°S, the ERS 35-day repeat cycles have a track spacing of only 25 km. However, with the availability of the more densely spaced ERS-1 168-day phase data from its geodetic phases, more information across track is provided.

After the slope correction has been applied, the residual error is dependent on the uniformity of the slope and the accuracy with which the slope can be determined. For example, a 0.1° slope known to 5% accuracy results in a slope correction of 1.2 m with an uncertainty of 12 cm (Guzkowska *et al.* 1990)

There are three well-documented methods for correcting satellite altimeter data for slope-induced error (Brenner *et al.* 1983, Remy *et al.* 1989; and Cooper 1989). These three methods are illustrated in Figures 3.15.a-c, and discussed below.

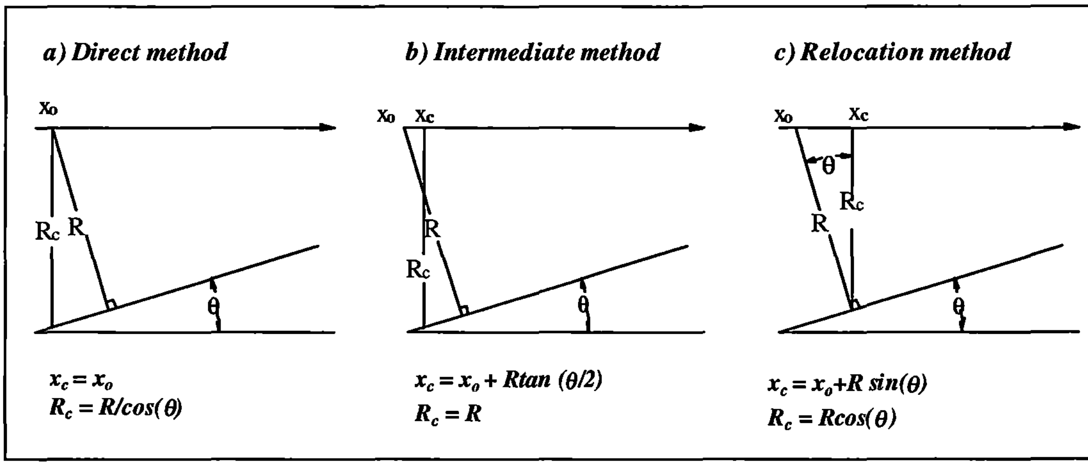

Figure 3.15 *Schematic diagrams of the three methods that have been suggested for correcting for slope-induced error a) direct method, corrects only the range, b) intermediate method, corrects both the range and the position, c) relocation method, corrects only the position. (Taken from Bamber 1994).*

Direct method

The direct method, suggested by Brenner *et al.* (1983), considers the slope error as a range error (Figure 3.15a). A corrected range to the nadir position is calculated using an estimate of the surface slope between the reflecting point and the nadir (Brenner *et al.* 1983). The method assumes that there is a constant slope (θ) between the near-range point and the nadir point, and the accuracy of the correction therefore depends on the relative size of errors caused by local deviations from the mean regional slope.

Intermediate method

Remy *et al.* (1989) introduced the intermediate method, which considers the slope error as a combination of a range error and a position error (Figure 3.15b). It calculates the position on the surface at which the measured range is correct. This position has a surface elevation that is higher than the nadir-point but lower than the near-range point (Remy *et al.* 1989). A constant slope is assumed between points.

Relocation method

The relocation method was described by both Brenner *et al.* (1983) and Cooper (1989). The method considers the slope error as a position error (Figure 3.15c). The method estimates the location of the near-range point corresponding to the range measurement, and calculates the correct elevation for that point from the measured range using the slope value at the near-range point (Brenner *et al.* 1983). The relocation method uses an estimate of the surface slope magnitude and direction at the measurement point, and uses this to determine the correction required to obtain the surface elevation at the point. In order to do this, both the range measurement and the satellite position must be corrected. An individual point (latitude φ, longitude λ) is relocated up-slope in a direction determined by the slope direction, by an amount proportional to the slope magnitude.

The relocation method was chosen for this thesis for three reasons. Firstly, it does not require any height information external to the altimeter dataset, and secondly local surface topographic variations on length scales of 1 km can be resolved (Cooper 1989). Finally, it also does not assume a constant surface slope between the nadir point and the reflecting point, as the direct and intermediate methods both do.

Relocation equations

The relocation method was first introduced by Brenner *et al.* (1983), and then modified by Cooper (1989), to account for satellite geometry and Earth curvature. Cooper (1989) provided a more rigorous set of equations than Brenner *et al.* (1983), based on a theoretical method of Harrison (1970) developed for deriving bedrock topography from radio echo sounding measurements over glaciers.

The geometry on which Cooper's (1989) equations are based is illustrated in Figure 3.16. The quantities in Figure 3.16 and the equations are:

- the surface slope magnitude θ (in a direction ϕ)
- the measured (retracked) range, R_m
- the corrected (relocated) range, R_c
- the distance from satellite to the centre of the Earth, R_s where

$$R_s = A + r_\alpha \tag{3.25}$$

where A is the satellite altitude (above the ellipsoid)

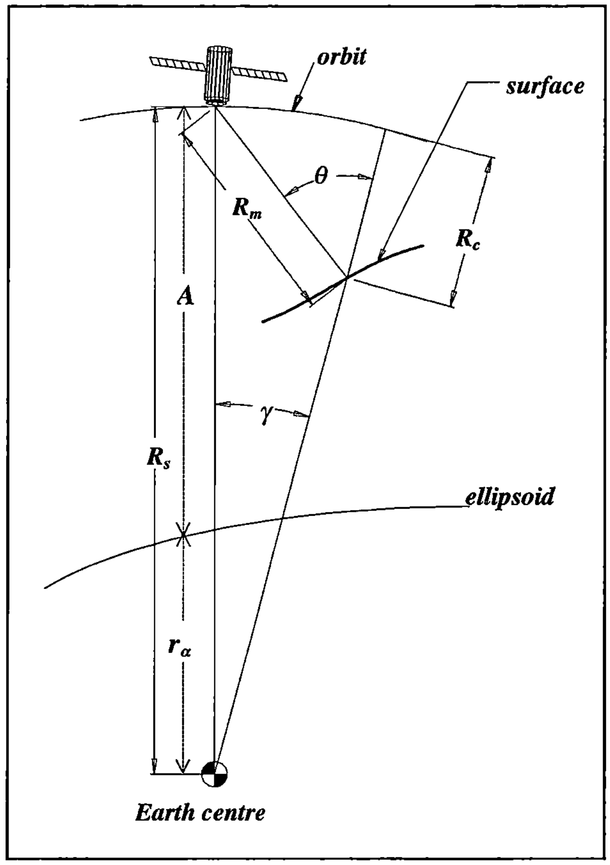

Figure 3.16 *Diagram illustrating geometry of the slope correction technique. Adapted from Cooper (1989).*

- the radius of curvature of the ellipsoid at the sub-satellite point r_α (latitude φ, longitude λ) in the direction ϕ, given by:

$$r_\alpha = \frac{\rho \nu}{\nu \cos^2(\phi) + \rho \sin^2(\phi)} \qquad (3.26)$$

where ν and ρ are the radii of curvature in the east-west and north-south directions, respectively

$$\nu = \frac{a}{\left(1 - e^2 \sin^2 \varphi\right)^{1/2}} \quad \text{and} \quad \rho = \frac{a(1-e^2)}{(1 - e^2 \sin^2 \varphi)^{3/2}} \qquad (3.27)$$

where a is the semi-major axis of the ellipsoid

e is the eccentricity

- the angle subtended at the centre of the Earth between the spacecraft and the point, γ, given by:

$$\gamma = \sin^{-1}\left(\frac{R_c \sin(\theta)}{R_s}\right) \tag{3.28}$$

Using this notation, the corrected range R_c to the relocated point is given by:

$$R_c = R_s \frac{\sin(\theta - \gamma)}{\sin(\theta)} - r_\alpha \tag{3.29}$$

The distance *(d)* from the original point on the Earth's surface to the relocated point is given by:

$$\mathrm{d} = \gamma\, \mathrm{r}_\alpha \tag{3.30}$$

The relocated latitude *(φ)* and longitude *(λ)* values are obtained by applying the corrections $\Delta\varphi$ and $\Delta\lambda$ respectively. These corrections can be derived from *d* using Gauss's mid-latitude formulae (Bomford 1911):

$$\Delta\varphi = \frac{d\cos\theta}{\rho} \qquad \Delta\lambda = \frac{d\sin\theta}{v\cos\varphi} \tag{3.31}$$

Cooper (1989) tested his relocation equations on modelled ice sheet data only. He concluded that the largest problem with the method was the poor estimation of surface slope by the altimeter in regions of high relief. Cooper and Hinton (1996) tested the procedure using real altimeter data from the Geosat geodetic mission, collected over the Wilkins Ice Shelf, Antarctica. He concluded that the technique works well for apparent slopes between zero and 0.6°. He found it particularly effective over the low slopes of ice shelves.

The relocation method was adopted by Bamber (1994), who defined a mean height for the grid corners, and performed a linear interpolation from the grid corners to get the grid cell slope. Bamber (1994) noted that the scheme failed for slopes greater than 0.7°, where the return became severely attenuated.

The relocation algorithm developed as part of this project used *a priori* slope information from the ERS-1 Slopes Database for the Lambert-Amery system (see Appendix B). This database was derived from the ERS-1 168-day dataset (Phases E and F), and was generated on a polar stereographic grid with a cell size of 10 km. For each cell that contained at least three points, a slope magnitude (θ) and direction (ϕ) was computed by fitting a plane to the points in that cell. To relocate an individual altimeter dataset, the slopes database was opened, the geodetic coordinates of each point were converted into polar stereographic coordinates and bi-linear interpolation was used to find the slope magnitude and direction for that point. The position and elevation of the point were then updated using Equations 3.25 to 3.31.

It is evident from the results of Cooper and Hinton (1996) and Bamber (1994) that the relocation technique performs optimally over regions where the topography is uniform. In some parts of the Lambert-Amery system, the terrain is steeply-sloped and non-uniform (Appendix B). In these regions, there will be some difficulty in correcting the data for slope error using this technique.

3.6 Data quality assessment

This chapter has demonstrated how post-processing of satellite radar altimeter data can be carried out to produce optimum height measurements over ice covered surfaces. After all corrections have been applied, the internal consistency of the altimeter data can be determined by comparing surface heights along repeated tracks (Scott *et al.* 1994), and at crossover locations (e.g. Brooks *et al.* 1978, Zwally *et al.* 1983). To assess the quality of the absolute measurement and to determine how well the altimeter profile represents the true surface, an independently surveyed reference surface is required (e.g. Schenke *et al.* 1993, Cefalo *et al.* 1994). These 'internal' and 'external' data validation methods are discussed briefly below.

3.6.1 Internal data validation

Since the ERS satellites operate in repeating orbit cycles, the ERS altimeters make measurements along approximately the same ground track. By comparing altimeter heights along track for successive repeats, the 'repeatability' of the altimeter data can be determined, in areas of low variability (i.e. areas with stable surface properties and low accumulation). Selected close repeat tracks can be used to assess repeatability of the measurements. By resampling the altimeter data onto a 'reference' ground track so that measurement locations coincide at a fixed location, the differences in heights at repeat points can be found. As the ERS ground tracks only repeat to about $\pm$ 1km (Vass and Handoll 1991), this technique does not work for all repeats. Furthermore, this technique can only be used with data from the 3-day and the 35-day repeat orbits. Ground tracks were not repeated for the 168-day cycles.

Orbit crossover analysis is a well-documented method for determining the repeatability of the altimeter measurement (Brooks *et al.* 1978; Zwally *et al.* 1983). The nature of the satellite orbit results in a regular, predictable mesh of intersection points between ascending and descending ground tracks. Crossover analysis is simply the technique of comparing the altimeter height at each intersection point of the ascending track with the descending track. This is done by locating the two altimeter measurements on either side of the intersection point, and interpolating to find the height at that point. In this way, a set of crossover differences can be constructed. When the altimeter measurements are close together in time, the crossover differences can be used to determine the error in the measurement.

3.6.2 External data validation

Two issues must be considered when inter-comparing satellite radar altimeter data with data from other sources: the consistency of the coordinate systems and the consistency of the measurement (i.e. that the height measurements represent the same thing).

Consistency of coordinate systems

The geodetic reference surface used for the ERS satellite orbits computed by DEOS is the World Geodetic System 1984 (WGS-84) ellipsoid. This is also the same reference surface used in GPS surveying. Brooks *et al.* (1983) used the ANARE 1968 optical levelling data to compare with their Seasat altimetric DEM (Chapter 2). This is not ideal, as levelling surveys are made relative to the geoid, not the ellipsoid, and the geoid-ellipsoid separation is not well known in this region (Chapter 6).

Consistency of the measurement

Satellite altimeters have a wide footprint on the ground, from which they return a single averaged height measurement (Wingham 1995). This means that it is not strictly correct to directly compare surface elevations from altimetry with those determined from single point GPS measurements or other survey methods (Bamber 1994). This problem can partially be overcome by surveying a grid, so that a three-dimensional reference surface, or Digital Elevation Model (DEM; Appendix C), can be constructed. A reference surface for the ERS-1 altimeter was established on the Filchner-Ronne Ice Shelf in 1992 using kinematic GPS (Schenke *et al.* 1993).

3.7 Chapter summary

This chapter has introduced the principles of satellite radar altimetry. The errors and biases that affect the altimetry height measurement over ice were described, and the techniques used to overcome them discussed. Where more than one technique is available to perform the same task, a critique of each method was provided.

Once the radar altimeter data have been processed and their self-consistency checked through crossover solution, some form of 'ground truthing' is required, to assess their absolute quality. In Chapter 4, a GPS survey of the central Amery Ice Shelf, undertaken in the Austral spring of 1995, is described. This survey was designed to provide a reference surface for validating ERS data. In Chapter 5, a discussion of the processing of the ERS data, comparison of the resulting height with GPS heights on the Amery Ice Shelf and the subsequent construction of two DEMs for the Lambert-Amery system is given.

Chapter 4 The Amery Ice Shelf GPS survey

4.1 Introduction

In Chapter 3, the major height biases and errors in altimeter data collected over ice surfaces, and ways in which careful processing using specific techniques can eliminate them, were discussed. To assess the accuracy of the resulting height measurement, and determine how well the altimeter height profile represents the 'true' ice sheet surface, an independently determined surveyed surface is required. This is known as 'ground truthing'. To date, one of the major shortfalls in altimetry over ice is that there simply have not been enough high quality surveys (such as GPS surveys) on ice sheets to validate altimeter height measurements. This lack of validation data results from the fact that surveys are generally expensive to carry out, the regions often inaccessible and GPS data processing to sufficient accuracy is not straightforward.

The Amery Ice Shelf is located between the Australian stations of Davis and Mawson (Figure 1.2). The region has been a focus ANARE surveys since the early 1960s, when field parties travelled there over land (Chapter 2). Nowadays, the ice shelf is reached easily by helicopter from Davis in around four hours. Furthermore, using the technique of 'kinematic' GPS it is now possible to carry out efficient, precise and extensive surveys of the ice shelf surface. These types of GPS surveys are useful for altimeter height calibration. The aim of this chapter is to describe and present the results of a GPS survey carried out on the Amery Ice Shelf, designed to provide a height reference surface for the ERS–1 and ERS-2 altimeters.

This chapter consists of two main sections. The first provides a *brief* overview of the theory behind GPS, introducing static and kinematic GPS techniques and highlighting in particular the limitations of GPS surveying in Antarctica. The second section describes the Amery Ice Shelf GPS survey, including its aims and design and the methods used to process the data. The main results from the survey, which include results obtained in addition to the construction of the ground truth reference surface, are also presented. The comparison of the GPS heights collected on the Amery with ERS heights over the same region is presented in Chapter 5.

4.2 Overview of GPS surveying

Over the past decade, the development of the US Department of Defense's Global Positioning System (GPS), a satellite-based radio-navigation system, has completely transformed the science of geodetic surveying and positioning. Originally designed for military navigation purposes, the system first became available to civilian users in the early 1980s.

Since this thesis uses GPS only as a tool for altimeter data validation, a full explanation of GPS theory is not required here. Comprehensive descriptions of GPS can be found in Hoffmann-Wellenhof *et al.* (1993) and Strang and Borre (1997). However, some features of GPS surveying do need to be introduced, to explain how the Amery Ice Shelf survey was designed, and how the GPS data collected on the ice shelf were processed. This section presents an overview of the main concepts of GPS surveying, highlighting the problems faced by users of GPS in Antarctica.

4.2.1 GPS satellites and observations

The full GPS constellation consists of 28 satellites (24 active) that follow near-circular orbits at a nominal altitude of 20 200 km with an inclination of 55° to the Equator. The orbits are confined to six orbital planes, each of which is occupied by four satellites (Hoffmann-Wellenhof *et al.* 1993). The orbit inclination means that, at the high latitudes of Antarctic stations, the GPS satellites are at low elevations above the horizon, therefore an individual satellite will only remain in view for short observing periods.

GPS is based on the principle of satellite ranging, which obtains the unique position of a point in space from the intersection of three spheres, whose radii correspond to distances measured from the spacecraft (Strang and Borre 1997). Additional independent distances reduce the errors and improve the positioning. Each GPS satellite transmits two signals centred on two different 'carrier' frequencies in the L-band of the microwave region: L_1 (1575.42 MHz) and L_2 (1227.60 MHz) (Hoffmann-Wellenhof *et al.* 1993). GPS signals are usually modulated by two pseudo-random noise (PRN) ranging codes. The first is the Coarse/Acquisition (C/A) code, which acts on L_1 only, is unique for each satellite so that a GPS receiver can distinguish between each of the 24 satellites, and is used primarily to acquire the P-code. The second code, the Precise (P) code, acts on both L_1 and L_2 and is the principal navigation ranging code.

There are two fundamental observations that can be obtained from the GPS signal by a GPS receiver (Strang and Borre 1997):

i) The pseudorange (or code) ρ observation; and

ii) The carrier phase ϕ observation.

Pseudorange

If a signal is transmitted by a GPS satellite at GPS time t_0, and detected by the receiver at a later GPS time t_1, an accurate measurement of the time delay ($\Delta t = t_1 - t_0$) defines the travel time. This assumes perfect synchronisation between the two instrument clocks. This is not the case, as GPS receiver clocks (often quartz) are of a lower quality than satellite clocks (atomic). In reality, the respective offsets of both the satellite clock and the receiver clock from GPS time will bias the time delay. The incorrect (biased) time $\Delta t'$ multiplied by the speed of light provides what is known as a 'pseudorange' (ρ):

$$\rho = c\Delta t' \tag{4.1}$$

The receiver clock error may be estimated, and therefore eliminated, by obtaining pseudoranges from at least four different satellites. The measurement precision of the P-code pseudorange observation is around 0.3 m (Hoffmann-Wellenhof *et al.* 1993).

Carrier phase

The GPS receiver determines the instantaneous fractional phase difference between the carrier wave from a GPS satellite, and an internally generated carrier wave (Hoffmann-Wellenhof *et al.* 1993). This fractional phase difference represents the fractional part of the distance from the satellite to the receiver; the rest of the distance is a large integer number of whole wavelengths, which cannot be measured. This whole number of wavelengths, or whole multiple of 2π in the phase, is known as the 'ambiguity' (N) (where N is, in theory, an integer value). The total phase (ϕ_{total}) difference between the satellite to the receiver at initial lock-on is given by:

$$\phi_{total} = 2\pi N + \phi + \varepsilon \tag{4.2}$$

where N is the ambiguity

ϕ is the fraction that is measured $(0 < \phi < 2\pi)$

ε is a term containing all the errors introduced by clocks, propagation delays, satellite orbits and receiver noise.

ϕ_{total} can be thought of as an 'unwrapped' phase. The total number of cycles is given by the total phase divided by 2π. This number multiplied by the carrier wavelength, λ (which is 19.05 cm for L_1 and 24.45 cm for L_2) yields the range (Φ) in metres:

$$\Phi = \lambda\left(N + \frac{\phi}{2\pi} + \varepsilon\right) \tag{4.3}$$

Once the ambiguity value is determined for a satellite, it is known for as long as the receiver maintains lock on that satellite. Loss-of-lock will create a new ambiguity value. The measurement precision of the phase observation is approximately 0.1 radians (3 mm for L_1); much higher than that of the pseudorange observation (Tiberius and Jonge 1995a).

4.2.2 Errors and biases in GPS observations

There are many sources of errors and biases contained in both types of GPS observation (pseudorange and phase). These fall into three main categories (Hoffmann-Wellenhof *et al.* 1993):

i) satellite orbit errors and satellite clock biases; and

ii) signal propagation delays (due to the troposphere and ionosphere); and

iii) receiver clock errors.

These errors can be removed through elimination or through solution.

The principal elimination technique used in GPS processing is 'differencing'. If two receivers are both tracking a pair of satellites, a 'double difference' equation can be obtained (see Figure 4.1). A double difference combination is formed by calculating either:

i) a between-satellite difference, and differencing between receivers; or

ii) a between-receiver difference, and differencing between satellites.

Since between-satellite differencing removes receiver dependent biases, and between-receiver differencing removes most satellite dependent biases, the use of double difference technique essentially eliminates all biases (Strang and Borre 1997).

The 'double difference equation' for the phase observation is given by (Tiberius and Jonge 1995b):

$$\begin{aligned}\Phi_{dd} &= \lambda\left\{N_1^1 - N_2^1 - N_1^2 + N_2^2 + \frac{1}{2\pi}\left(\phi_1^1 - \phi_2^1 - \phi_1^2 + \phi_2^2\right)\right\} + \varepsilon_1^1 - \varepsilon_2^1 - \varepsilon_1^2 + \varepsilon_2^2 \\ &= \lambda N + \frac{\lambda}{2\pi}(\phi_1^1 - \phi_2^1 - \phi_1^2 + \phi_2^2) + \varepsilon \qquad (4.4)\end{aligned}$$

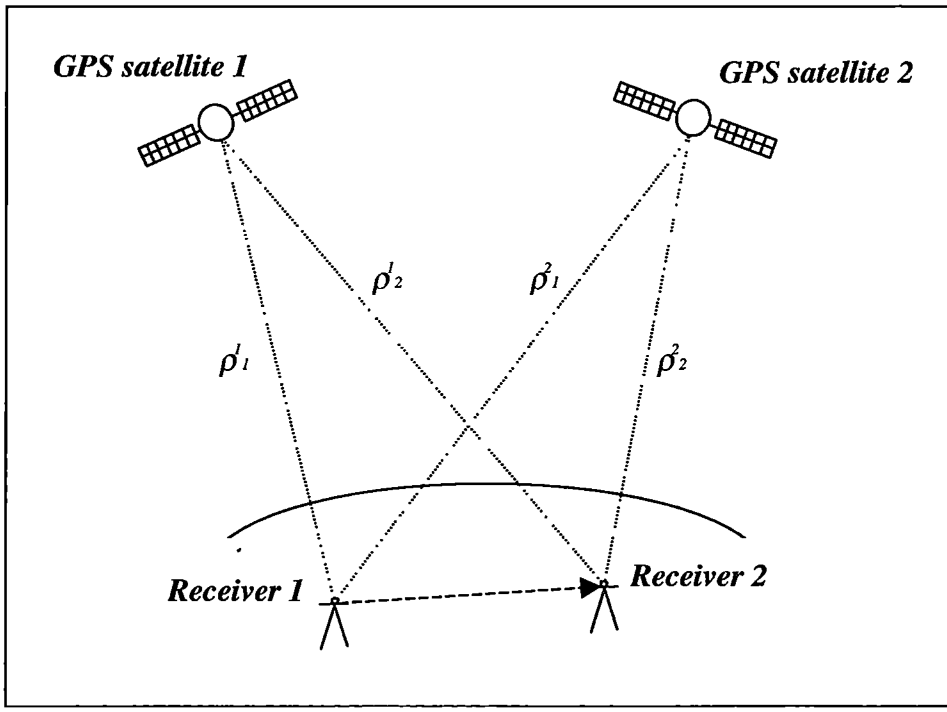

Figure 4.1 *A double difference combination $(\rho^1_1 - \rho^1_2) - (\rho^2_1 - \rho^2_2)$ made from simultaneous observations from two GPS satellites and two receivers. (Adapted from Tiberius and Jonge 1995b).*

where ϕ^i_j is the phase observation from satellite i at receiver j

N^i_j is the ambiguity value for satellite i and receiver j

ε^i_j is the error term for satellite i and receiver j

N is the total ambiguity value (linear combination)

ε is the net error term

The method used to process GPS data varies widely depending on the level of sophistication of the processing software. In 'proprietary' software packages, intended for small-scale surveys, many errors (such as tropospheric and ionospheric delays) are removed through differencing. More sophisticated packages eliminate these errors through solution, which requires a network of GPS stations.

Removal of ionospheric effects from GPS signal is particularly important in Antarctica, where ionospheric activity is high. The ionospheric correction has already been discussed with respect to the ERS satellite radar altimeter in Chapter 3. Since the GPS satellite transmit signals at a much lower frequency than the ERS altimeter (1227.60 and 1575.42 MHz for GPS, 13.8 GHz for ERS), the ionospheric delay is much greater for GPS (see Equation 3.14 in Chapter 3). In GPS processing, the standard approach to removing the ionospheric delay is through 'dispersion'. This technique combines the L_1 and L_2 phase observations into the 'ionosphere-free' linear phase combination (Bock *et al.* 1986) ,denoted as L_3.

4.2.3 Static GPS surveying

In a standard static GPS survey, two receivers are operated simultaneously at different locations for a period of time (Hoffmann-Wellenhof *et al.* 1993). The length of time required to obtain a reliable, precise solution generally increases with receiver separation, or 'baseline length'. Other factors affecting the quality of the solution include (Hoffmann-Wellenhof *et al.* 1993):

- the relative geometry of the satellites and the change in the geometry;
- the number of satellites available; and
- the ionospheric activity.

When baselines are comparatively short (< ~30 m), it can be assumed that the paths travelled by the GPS signal are the same at stations at either end of the baseline. In this case, many of the error terms at the receivers (primarily due to propagation effects) cancel out (i.e. in Equation 4.4, ε^1_1 is approximately equal to ε^1_2, and ε^2_1 is approximately equal to ε^2_2).

Longer baselines

When baselines are longer, the GPS signal received at each end of the baseline has passed through different parts of the troposphere and ionosphere, so the propagation values are different and no longer cancel. Long baselines are unavoidable in Antarctica, where the permanent GPS tracking sites are located on fixed rock points at habitated stations, and most GPS surveys are carried out up to several hundred kilometers from these stations. The central Amery Ice Shelf is around 350 km from both Davis and Mawson stations, where permanent GPS receivers are located. For the Amery survey, a temporary GPS station was located on rock at Beaver Lake, 60-100 km from the main survey area.

GPS processing over long baselines can be achieved by combining the GPS data at the unknown site with GPS data from a full network of remote stations with accurately known positions. Propagation errors are removed through modelling, whilst orbit errors, clock errors, and station coordinate errors are removed through solution. The addition of this capability into a GPS package increases the software size and complexity. GPS processing software capable of carrying out the more sophisticated type of static GPS processing include:

i) GAMIT/GLOBK, Massachusetts Institute of Technology (MIT)/Scripps Institute of Oceanography (SIO), (King and Bock 1994; Appendix D); and

ii) GIPSY, Jet Propulsion Laboratory (JPL), (Lichten 1990); and

iii) BERNESE, University of Berne, (Rothacher and Mervart 1996).

The GPS software used for processing the static GPS data from the Amery Ice Shelf survey was GAMIT/GLOBK, which is installed and used at the University of Tasmania.

GAMIT uses weighted least-squares algorithms to estimate the relative positions of a set of stations and satellite orbits (King and Bock 1994). The set of stations usually includes a well-spaced (with respect to the unknown sites) subset of permanent stations within a global network e.g. the International GPS Geodynamics Service (IGS) global tracking network (Mueller and Beutler 1992). The user can enforce different constraints on each station's coordinates in the solution. The known sites are generally tightly constrained and the unknown sites are loosely constrained. Once new coordinates are found for the unknown sites, the *a priori* coordinates can be updated, and the constraints tightened.

More complete descriptions of the GAMIT and GLOBK are given in Appendix D.

4.2.4 Kinematic GPS surveying

In kinematic GPS surveying, use is made of the same double difference equation (Equation 4.4) and phase observations as discussed in the static case. One receiver is used as a reference at a known location and operated in static mode, remaining stationary throughout the survey. Another receiver (preferably of the same type) is operated in kinematic mode and mounted on a moving platform. Simultaneous collection of data at identical sampling rates by each receiver allows accurate computation of the continuously changing baseline (Hoffmann-Wellenhof *et al.* 1993).

Kinematic GPS surveys usually operate over relatively short baselines (< 10 km), although there is much work being done to reliably extend this limit to baselines approaching 500 km or more (e.g. Colombo *et al.* (1995)). Over short baseline lengths, it is unlikely that there will be significant variation in ε_j' and hence cancellation of error is not a major problem. A more significant problem in kinematic surveying is the initial determination and maintenance of the ambiguities.

An 'initialisation' process is required to determine these ambiguities before the kinematic survey commences. Four methods are generally used, summarised as follows:

i) **Occupation of a known baseline.** This method involves occupation of a known baseline by the two antennae (obtained through precise static survey) for about 5 minutes before the roving receiver starts to move (Hoffmann-Wellenhof *et al.* 1993). On the moving ice streams and ice shelves of Antarctica, this method can be achieved by:

   - placing the initial and roving antennae at each end of a bar (of known length in a known orientation) mounted on a tripod during the initialisation; or
   - estimating the initial position of the ice station relative to a fixed rock station.

ii) **Reoccupation.** In this method, the roving antenna reoccupies its initial position at the end of the survey (Tiberius and Jonge 1995b). This is not generally suitable for ice streams and ice shelves, where the horizontal velocities are high and (on ice shelves) vertical displacements due to ocean tides occur. For example on the Amery Ice Shelf, where surface velocities can exceed 400 m a^{-1}, during a typical 2-4 hour survey, the initial station can move 10-20 cm horizontally and 0.5 m vertically.

iii) **Antenna swap.** This method involves occupation of a short (< 1 m) known baseline by the roving and base antennae. The antennae are then interchanged, which artificially changes the geometry and allows the ambiguities to be estimated (Hoffmann-Wellenhof *et al.* 1993). This method is suitable for a kinematic GPS survey on an ice stream or ice shelf.

iv) **Ambiguity search.** This method uses a search of the ambiguity value in a spatial volume (Han and Rizos 1995). This method, known as 'on-the fly' ambiguity resolution, is computationally intensive, but is an ideal approach for surveys on ice streams and ice shelves as the processing can restart even after a loss-of-lock.

After initialisation, the 'roving' antenna begins to move, commencing the kinematic part of the survey. The position of the moving station is estimated by a simple vector addition of the kinematic baseline to the known reference station position. This yields the coordinates of the roving antenna at each epoch of measure, typically every 1-5 seconds. A reference surface for satellite altimetry can be constructed by surveying a gridded pattern of GPS profiles.

The important point in kinematic surveying is that, once the ambiguity values are determined, they must be maintained throughout the survey. This value is often lost ('loss-of lock') when the satellite geometry changes, or if a cycle slip occurs. Loss-of-lock or cycle slips can occur due to obstructions or through rapid movement of the antenna. The former is unlikely on Antarctic ice shelves (apart from at the base camp); however, the latter can occur when crossing sastrugi. After a loss-of-lock event, the new ambiguity value can be established by 're-initialisation' (Hoffmann-Wellenhof *et al.* 1993).

Long range kinematic surveys

The problems of processing GPS data over long baselines have already been discussed for the static case (i.e. the error ε_j terms in Equation 4.4 no longer cancel). These problems are also encountered in the kinematic case. Long-range kinematic techniques need to employ more sophisticated modelling, to account for the greater variability on ε_j

A standard GPS processing technique for long baselines is the solution for a constant (real) number for the ambiguity, rather than an integer value. The procedure results in an 'ambiguity free solution', and is used in the Leica proprietary software SKI (Static KInematic). Other techniques involve the modelling of the ε_j' terms, and methods have been suggested for this (e.g. Colombo *et al.* 1995; Han and Rizos 1995).

4.2.5 GPS surveying in Antarctica

GPS was first used by ANARE in 1988, and several static GPS surveys were carried out on the Amery Ice Shelf and its surrounding glaciers between 1988 and 1991 (Allison 1991; Chapter 2). These GPS surveys used single frequency GPS receivers (1988-89) and dual GPS frequency receivers (1990-91) to determine ice flow velocities. Data from these surveys were noisy, due to a combination of high ionospheric activity and unsophisticated GPS receiver technology. Furthermore, the precision of global orbits was inadequate, primarily due to the lack of southern hemisphere tracking sites. Initial analysis of these data using proprietary processing software produced low quality positions (~1-10 m) (Ian Allison, personal communication, 1998). The level of precision (especially in height) and sparse coverage of the 1988-91 surveys meant that these data were inadequate for validating ERS altimeter heights on the Amery Ice Shelf.

To provide a suitable height reference for validation of the ERS heights, a specialised GPS survey was planned on the Amery Ice Shelf, for the austral spring of 1995. Other locations where ERS 'ground truthing' GPS surveys have taken place in Antarctica include the Filchner-Ronne Ice Shelf in 1992 (Schenke *et al.* 1993) and Dome C (Cefalo *et al.* 1993) in 1993. The Filchner-Ronne Ice Shelf survey described a 40 km by 40 km grid, while the Dome C survey employed radial techniques across selected features. Other examples of applications of GPS in Antarctica include static GPS measurement of the tidal response on the Hells Gate Ice Shelf (Bondesan 1994) and kinematic GPS measurement of the tidal flexure on the Rutford Ice Stream (Vaughan 1994 and 1995).

4.3 The Amery Ice Shelf GPS survey

4.3.1 Survey aims and design

Aims

The major goal of the Amery Ice Shelf survey was to obtain a 'ground-truthing' height reference surface for the ERS-1 and ERS-2 satellite radar altimeters. To achieve this goal, the survey was designed so that the resulting pattern of surveyed lines could describe a suitable three-dimensional model of the surface, against which the ERS heights could be validated.

There were three subsidiary aims of the Amery Ice Shelf survey:

i) to measure tidal motion at base camps on the Amery Ice Shelf;

ii) to measure instantaneous surface velocities at the base camps on the ice shelf, and compare these velocities with those determined from the 1968 and 1970 surveys; and

iii) to retrace the 1968 ANARE optical levelling line and compute any elevation changes along the line.

Design

To satisfy the aims described above, the Amery Ice Shelf survey was designed around the following considerations:

- **GPS provides only discrete positions.** To compare the GPS heights with the altimeter heights (averaged over a 5-10 km footprint), it would be necessary to generate a DEM of the survey region from the GPS data. Therefore, the survey was designed on a grid, composed of 24 x 10-km squares, to be surveyed using kinematic GPS (Figure 4.2). The 120 km x 20 km grid was centred on six temporary base camps (C2, C4, C6, C8, C10, and C12) along the centre line, at 20-km spacing. From each camp, the four surrounding squares were surveyed, which took 2-3 days.

- **Duration of each kinematic survey.** It was estimated that each 10-km x 10-km square would take approximately 4 hours to survey using skidoos. It was further estimated that over a 4-hour period the base station would move about 0.2 m horizontally and up to 0.5 m vertically. A GPS sampling interval of 5 seconds was chosen, and a nominal speed of 10 km per hour on the skidoo would generate a GPS sample point every ~14 m. This spatial density was considered sufficient to characterise dunes and other small-scale features in the ice shelf topography.

- **Profile measurement.** The measurement of profiles around each grid square was chosen such that all of the arms internal to the grid were traversed twice, in opposite directions with a maximum separation in time, and only the outer lines of the grid were covered by a single run (Figure 4.3). This meant that if a serious loss-of-lock were to occur late in a run (e.g. arm 4 in square A3 of Figure 4.3) it would be covered by a traverse from another square (arm 1 in square A1). The difference between the two repeated traverses would provide an upper limit for the height errors in the GPS data.

- **Location of fixed rock sites.** A base station was planned on rock next to Beaver Lake. This station provided a 'fixed' rock site, which would allow the conventional permanent GPS site approach to be used to determine the static positions of the base stations in GAMIT (see Appendix D).

- **Grid orientation.** The orientation of the grid was chosen such that its centre-line coincided with the 1968 ANARE optical traverse line, so that any change in elevation could be deduced.

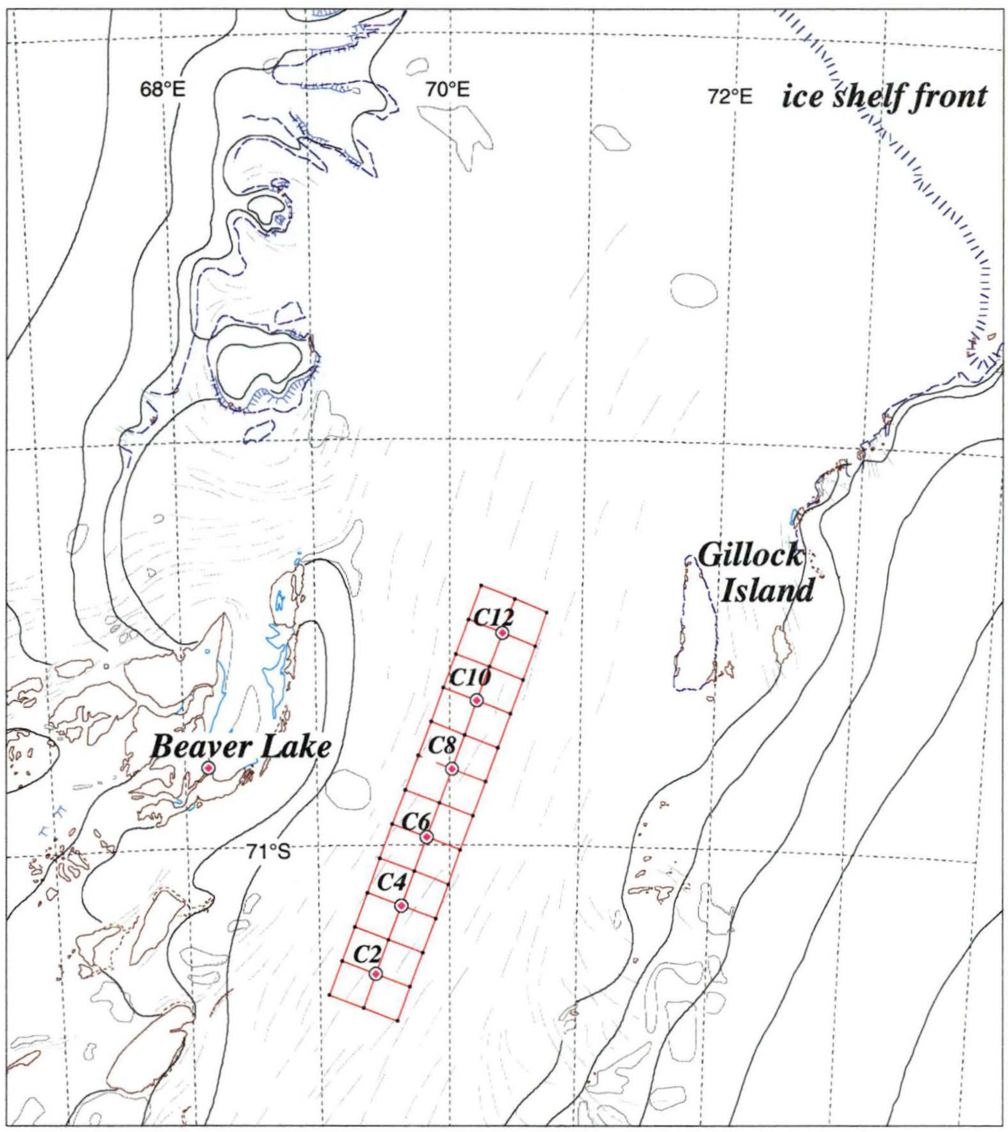

Figure 4.2 *Location map of the 120 x 20 km GPS survey grid on the Amery Ice Shelf. Longitudinal lines were named W (West), C (Centre), and East; transverse lines were numbered 1 to 13, giving each grid node a unique identification (e.g. E3). Temporary base camps for the kinematic and static survey were established at every second grid node along the centre-line (C2, C4, C6, C8, C10 and C12).*

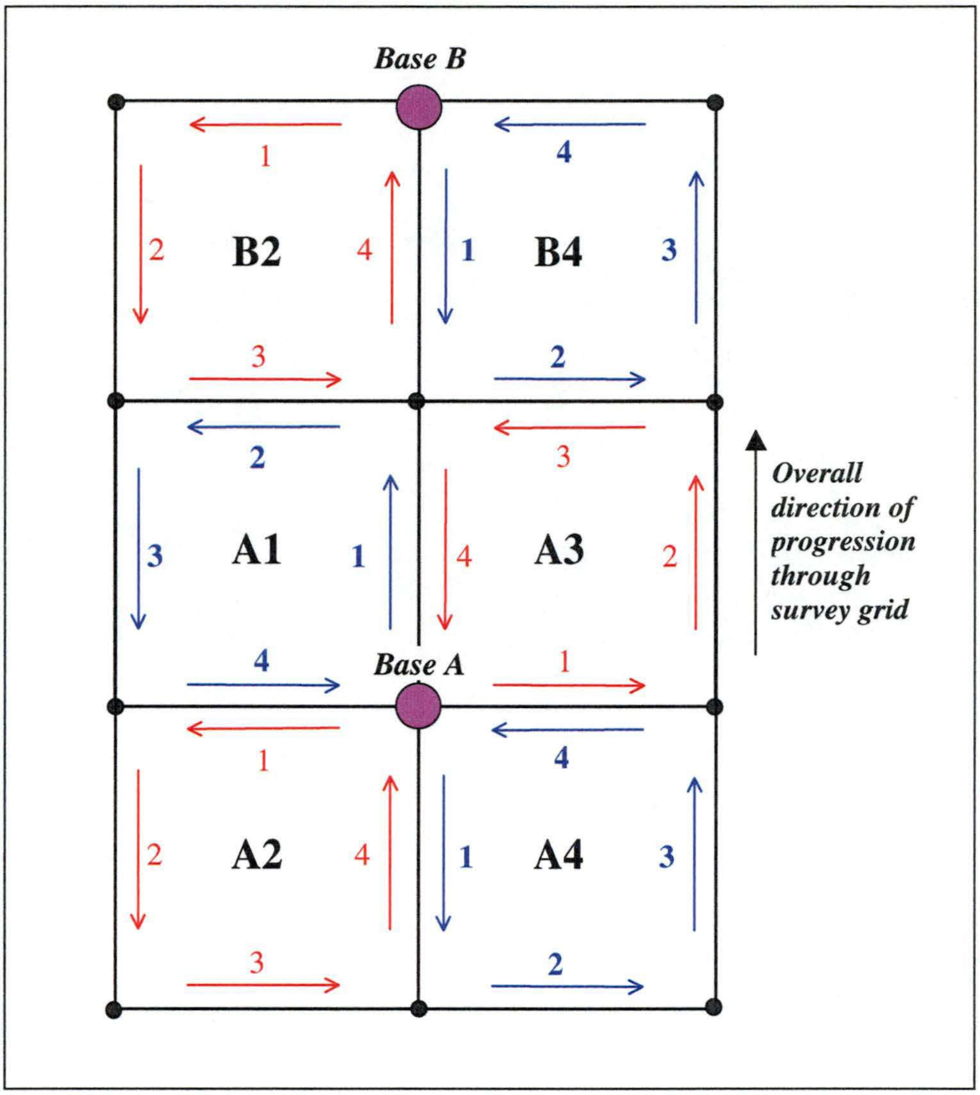

Figure 4.3 *Schematic diagram showing the order of surveying of squares from each base camp in the Amery Ice Shelf survey grid (A1-A2-A3-A4). With multiple base camps, this order of surveying of the squares lead to all internal arms being surveyed with a maximum separation in time (A1-A3-B2-B4).*

- **Time of survey.** The survey was scheduled for late spring to ensure that travel around the squares would not be impeded by melt-water and soft snow, which had been observed on the ice shelf during summer by previous ANARE expeditioners (Ian Allison, personal communication, 1995). This would have made access difficult, increasing the travel time and the probability of a loss-of-lock occurring during the kinematic survey, as well as increasing the expected movement of the base station.

- **Amount of static GPS data collected at camps.** Static GPS data could be collected at the temporary base camps both during and in between the kinematic surveys, which would cover a sufficient time span (2-3 days) to meet subsidiary aims i and ii. The sampling interval of the reference receiver could be increased from 5 to 30 seconds when no kinematic survey was taking place, which was sufficient for static processing. GPS tracking at these ice shelf reference camps did not have to be continuous unless a kinematic survey was in progress.

This survey design proved to be highly effective, and the entire survey was successfully completed in 22 days (25 October to 14 November 1995). The survey used three Leica 299 (dual frequency) Geodetic GPS receivers. One receiver was deployed on bedrock next to Beaver Lake to provide rock control, for both the static estimation of the base camps and long range kinematic observation for the survey grid. The other two receivers were deployed on the ice shelf, one serving as a local reference station at each base camp, and the other serving as a roving receiver for the kinematic survey.

The initialisation method used for the kinematic survey was the 'occupation of a known baseline'. During initialisation, the reference and roving antennae were mounted on a bar, which was 40 cm in length and oriented along the longitudinal axis of the survey grid (i.e. the approximate direction of ice flow) (Figure 4.4).

After initialisation, the roving antenna was moved carefully to a mount on the surveying skidoo, and driven around each 10-km square at approximately 10-15 km h^{-1}. At the end of the survey, the roving antenna was returned to its initialisation position on the bar.

4.3.3 Processing of GPS survey data

Processing of the GPS data from the Amery Ice Shelf survey was split into two major components: static and kinematic. Static processing was completed first, since this provided an accurate starting point on which the kinematic processing relied.

Static data processing

The static GPS data, collected at the Beaver Lake rock site and the six Amery Ice Shelf base camps, were processed using the GAMIT/GLOBK software (see Appendix D).

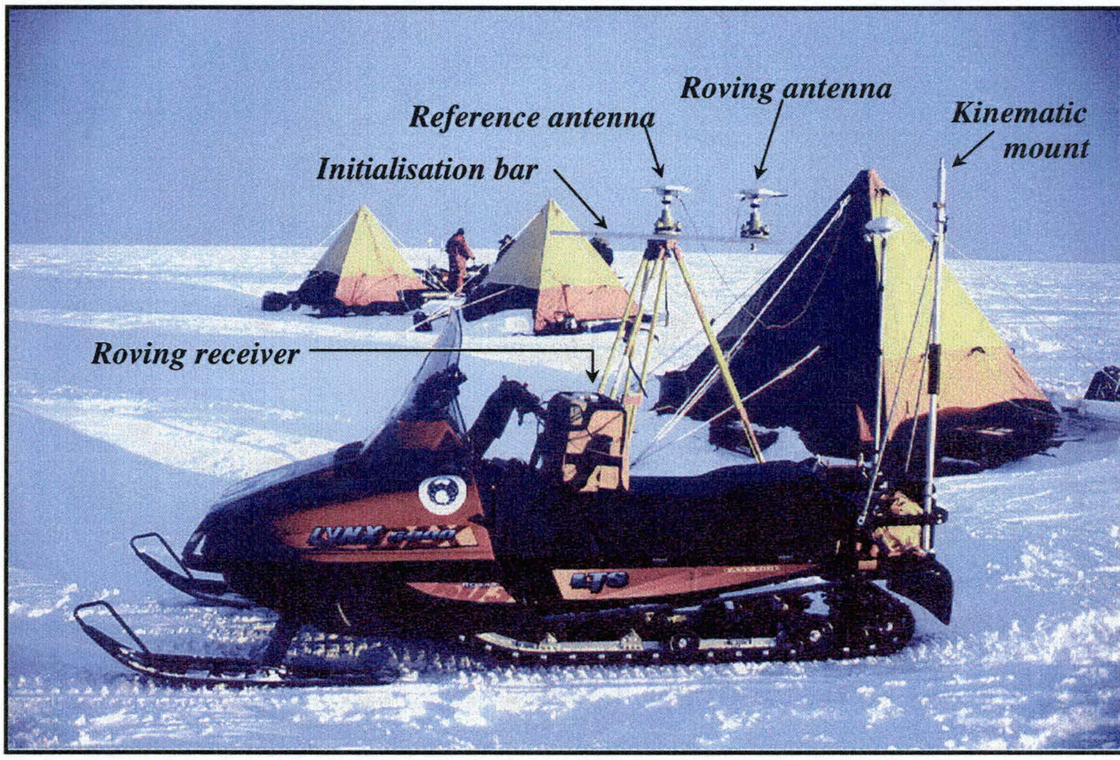

Figure 4.4 *Roving and reference antennae in place on the bar for the kinematic survey initialisation. After this baseline had been occupied for about 5 minutes, the roving antenna was moved to its position on the mount on the skidoo, and the kinematic part of the survey commenced.*

Since the camps were in constant motion with the ice shelf, the multiple-day GPS observations from each camp were divided into approximately 2-hour segments, to approximate a static solution. A period of 2 hours was chosen as a compromise between the lower limit on the amount of static data needed to acquire a good solution, and an upper limit on the amount of motion at the site. The splitting of the static data files was performed carefully. By manually examining the individual time-series from each GPS satellite, optimum start and finish times were chosen for each segment, to avoid introducing new ambiguity terms (Figure 4.5). The segments for each camp were named accordingly (e.g. at Camp C2 the first three segments were named C2A, C2B and C2C).

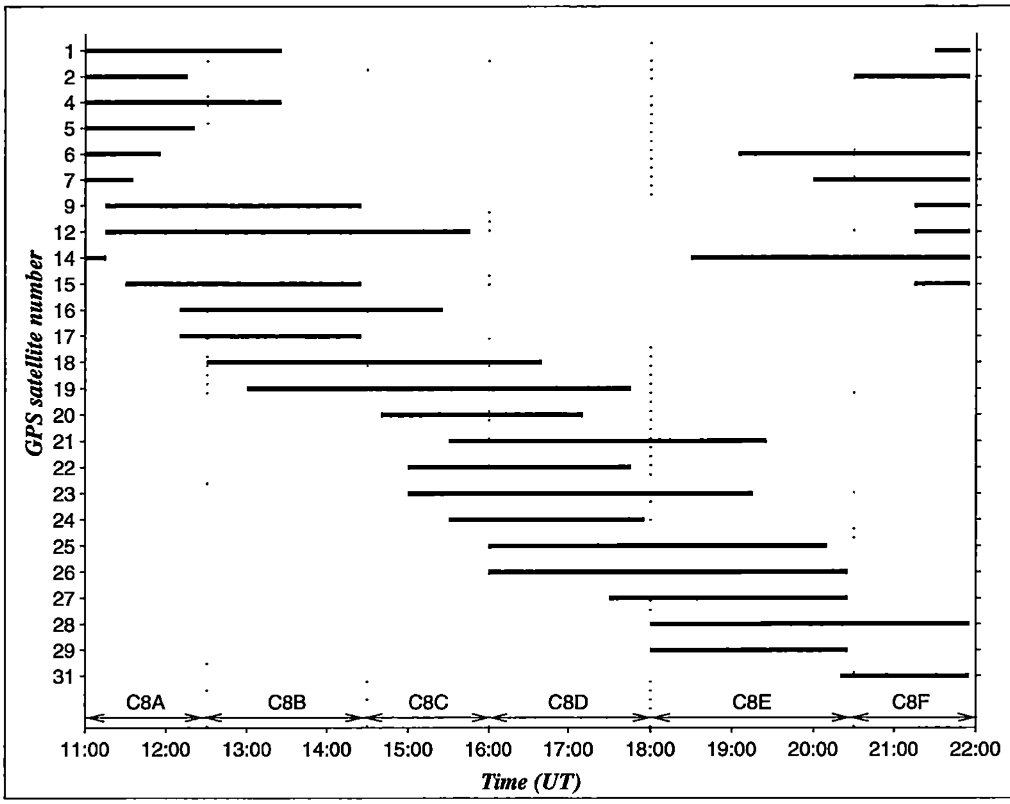

Figure 4.5 *Satellite time-series plot from C2 to illustrate the splitting of the static data files in order to minimise the introduction of new ambiguity terms for each segment (by rising and setting of satellites, loss-of-lock, etc).*

For each day of the Amery Ice Shelf campaign, the appropriate 2-hourly static segments from the camps were combined with other GPS data from Beaver Lake, Davis, Mawson and other global GPS tracking sites in GAMIT (see Appendix D). Figure 4.6 illustrates the location of the permanent GPS tracking sites in the portion of the Southern Hemisphere that was used in the GAMIT solutions. A precise 3-day orbit was used, which overcame the discontinuities associated with discrete 1-day orbits (Peter Morgan, personal communication, 1998). This technique produced an accurate coordinate for each 2-hour segment, which represented an averaged position over the 2-hour period.

The change in the average positions of successive 2-hour segments indicated the amount of motion at each camp. The effect of down-slope motion and firnification (Hulbe and Whillans 1994) was considered to be negligible, mostly due to the short time periods, but also due to the low slopes encountered on the ice shelf. This station movement was resolved into horizontal (N, E) and vertical (U) components, which closely represent surface ice flow velocity and tidal variation respectively.

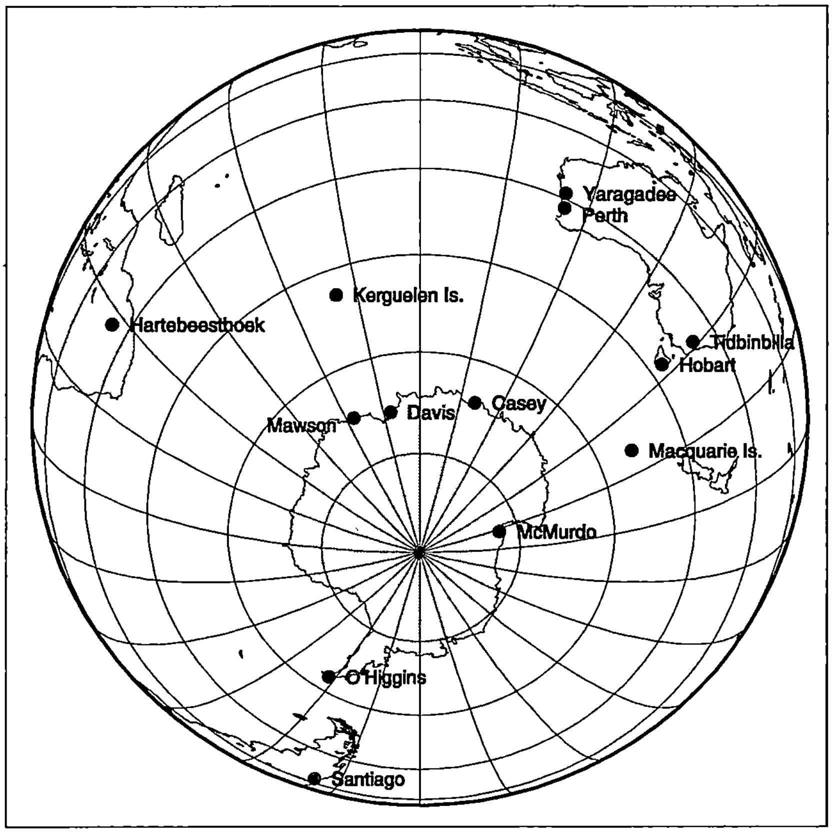

Figure 4.6 *Permanent GPS tracking stations in the portion of the southern hemisphere used to process the static GPS data from the Amery Ice Shelf GPS survey in GAMIT.*

Surface ice flow velocities (N, E)

The ice flow velocities at each camp were computed by fitting a regression line to the individual 2-hour (N, E) solutions. This fitting technique is illustrated in Fig 4.7 for camp C10. The resulting velocities at each camp increased from south to north, from 326.9 $\pm$ 0.5 ma^{-1} at C2 to 373.6 $\pm$ 4.6 ma^{-1} at C12 (Table 4.1).

Figure 4.8 shows the resulting velocities at each camp, together with velocities measured along the central flowline during the 1968-70 ANARE surveys (Budd *et al.* 1982; Figure 2.2). This comparison between the 1968-70 and 1995 results suggests that there have been no significant changes in ice flow velocities since 1968, given the error bars on the data. The estimated error on the 1968-70 velocities is 2.5% of the magnitude.

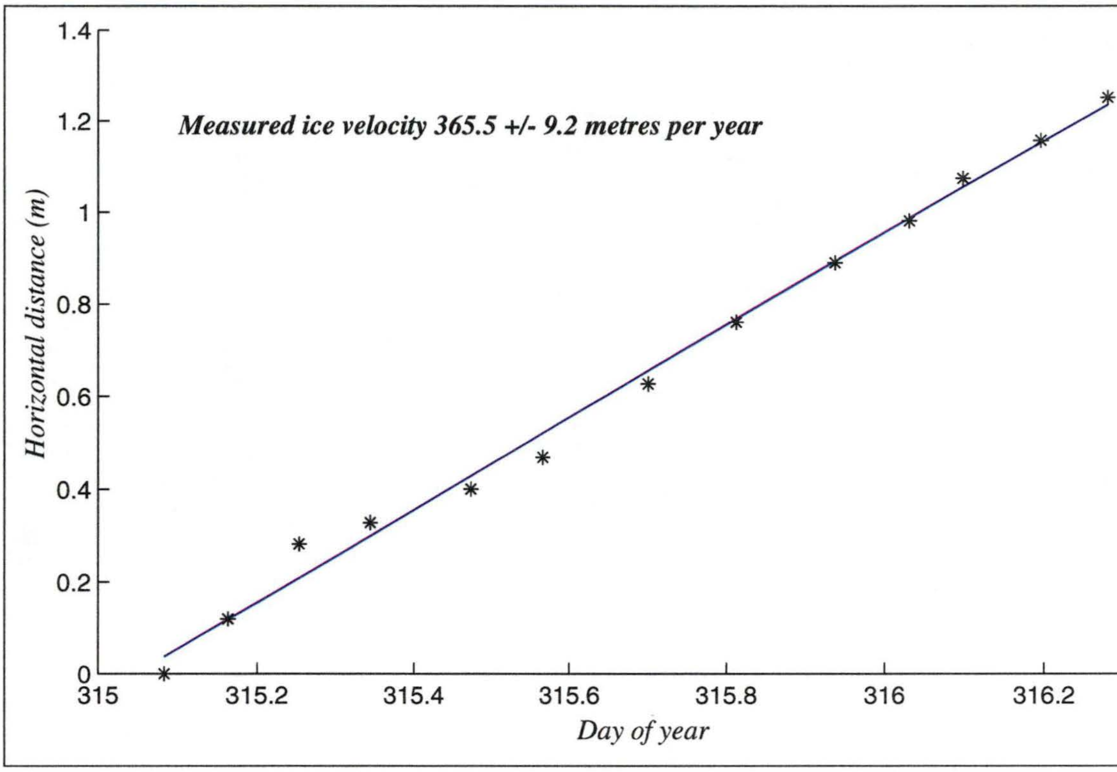

Figure 4.7 *Calculation of surface ice flow velocities at Amery base camp C10 from the 2-hourly static GPS positions.*

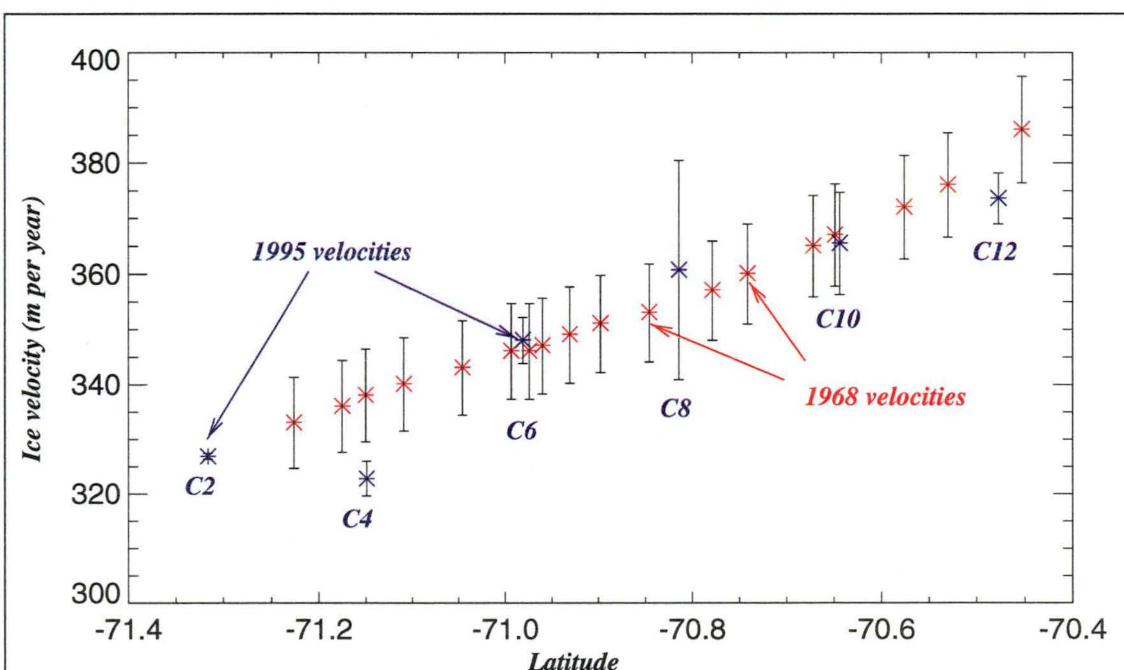

Figure 4.8 *Surface ice flow velocities at each Amery camp together with measured velocities along the central flowline from the ANARE surveys of 1968-70 (see Figure 2.2).*

TABLE 4.1 SURFACE ICE FLOW VELOCITIES AND RMS AT EACH CAMP, DERIVED FROM THE 2-HOURLY STATIC GPS SOLUTIONS USING WEIGHTED LINEAR REGRESSION.

Camp	Velocity($m\ a^{-1}$)	RMS ($m\ a^{-1}$)
C2	326.9	0.4
C4	322.8	3.2
C6	348.0	4.2
C8	360.7	19.8
C10	365.5	9.2
C12	373.6	4.6

The large RMS at C8 is a result of the tripod falling over in a blizzard.

Tidal variations (U)

A tide model, constructed from tide observations collected over a 22-day period during 1990-91 (Ward 1991) is available for Beaver Lake from the Australian National Tidal Facility (NTF) at Flinders University, South Australia (Marion Tait, personal communication, 1996). Figure 4.9 shows the variations in GPS heights against time for each of the Amery base camps, together with the predicted tide from the Beaver Lake Tide Model (BLTM). The average offset has been removed between the GPS heights and the BLTM values. It can be seen that the GPS-derived variations at the camps closely match the predicted BLTM variations. The RMS of the differences between the GPS heights and the interpolated predicted tidal heights are shown on each plot. The RMS values range from 0.01 m at C2 to 0.38 m at C10.

The GPS height variation at C4 does not match the BLTM predictions as closely as for the other camps (Figure 4.9). The BLTM values over the whole 22-day survey period are shown in Figure 4.10, together with the periods corresponding to each camp occupation. The tidal amplitudes range from about –380 mm to 1400 mm. It can be seen that the predicted tidal variation was lowest when C4 was occupied. This could explain the mismatch between GPS heights and the BLTM variations at this camp.

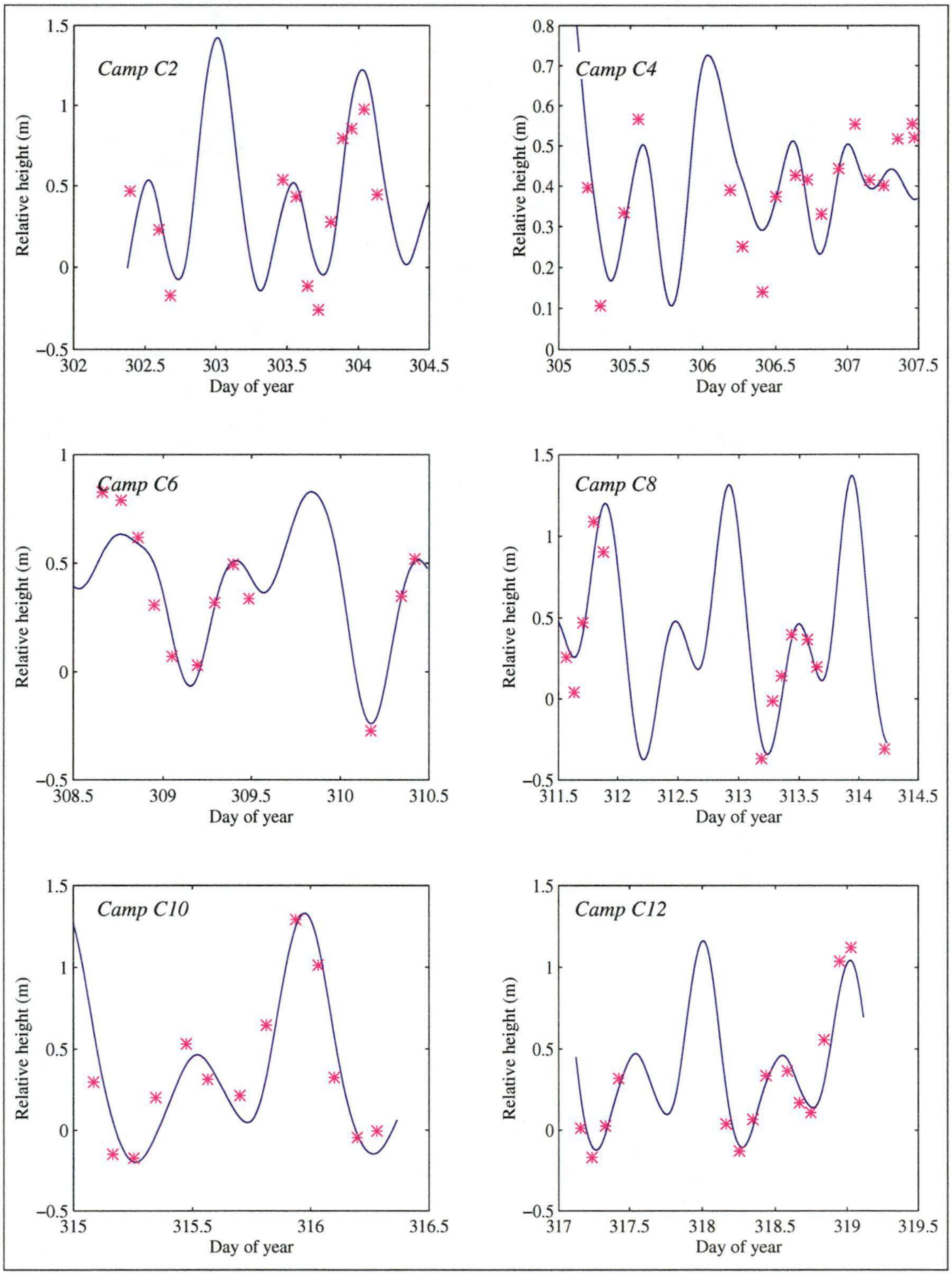

Figure 4.9 *Time series of the tide-induced vertical height variations (asterisks) determined from static GPS measurements the six Amery Ice Shelf base camps, together with the predicted tides for Beaver Lake (solid line). Time is plotted in day of year, where day 302 is 19 October 1995.*

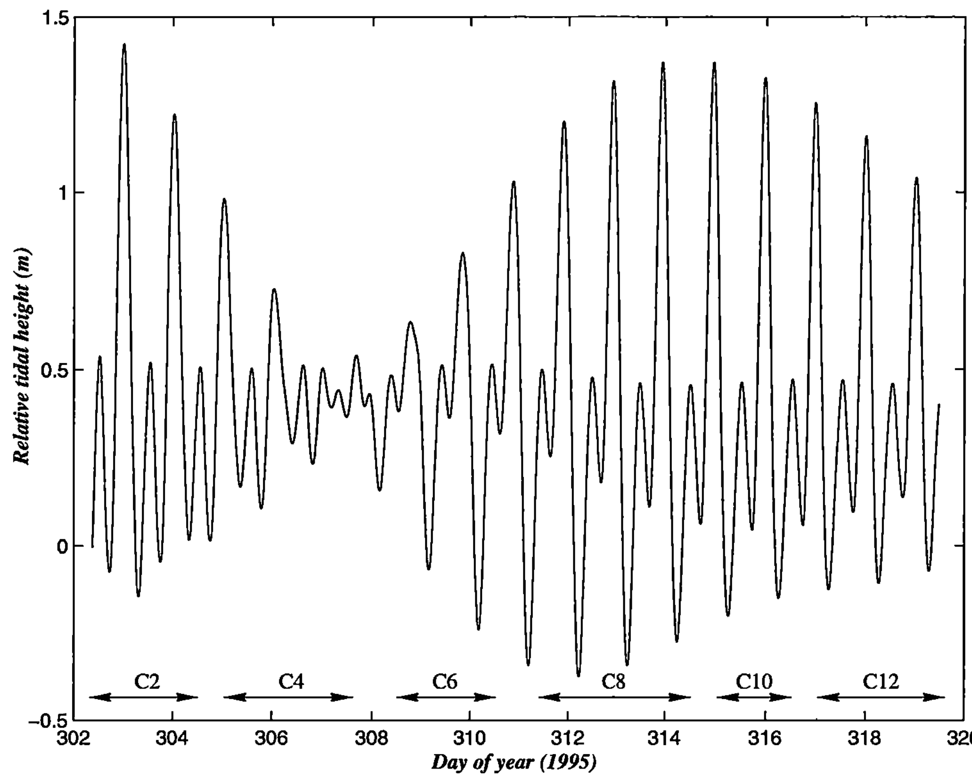

Figure 4.10 *Predicted tides for Beaver Lake from the BLTM for the entire period of the Amery ice Shelf GPS survey, with the epochs during which each camp was occupied.*

The close agreement between vertical height variations and the BLTM variations indicates that the BLTM is a good proxy for real tidal amplitude on the ice shelf. Furthermore, it indicates that the ice is freely floating at the base camps, hence the grounding zone of the Amery Ice Shelf is further south than Budd *et al.* (1982) reported.

Kinematic data processing

The kinematic GPS data were processed using Leica's Static KInematic (SKI) software. For the kinematic GPS processing around each square of the Amery Ice Shelf survey grid there were two options for the choice of the reference receiver:

i) the Amery Ice Shelf base camp; or

ii) the Beaver Lake rock site.

The first option was problematic, especially towards the end of a run around a 10-km square, since the base camps were in constant horizontal and vertical motion. The second option provided a more stable reference station since it was located on rock, but introduced problems associated with the GPS processing of longer baselines, as it was 60-100 km from the survey region. To minimise these effects, the data were processed using both options, and all of the results combined.

The components of the Amery Ice Shelf GPS survey, and the various tide corrections involved to produce a height relative to a tide-free surface, are represented schematically in Figure 4.11. The mean height difference between the Beaver Lake rock site and the ice shelf is indicated. The tidal variations at Beaver Lake and the ice shelf are considered the same. The initialisation epoch of the kinematic survey is t_0.

The different processing strategies for the two options of reference station are outlined below.

Amery Ice Shelf base camps

Using the receiver at the Amery Ice Shelf camp as a reference, initialisation was accomplished in SKI using the 'known baseline method'. The position of the starting point of the reference receiver was interpolated to high precision from the corresponding GAMIT 2-hourly static values. The positions along the kinematic traverse were then corrected for the effect of ocean tide using a two-stage process. The first correction subtracted a shift to account for the tidal height at the initialisation epoch (t_0), which brought the height of the ice station to a mean 'tide-free' surface (Figure 4.11). The second correction accounted for the changing tide over the 4-5 hour survey duration. This correction was necessary because, although there was negligible relative tidal motion between the reference station and the roving receiver, in SKI the coordinates at the reference station were held fixed at the initial position. Therefore, the change in tidal amplitude as the survey progresses had to be accounted for.

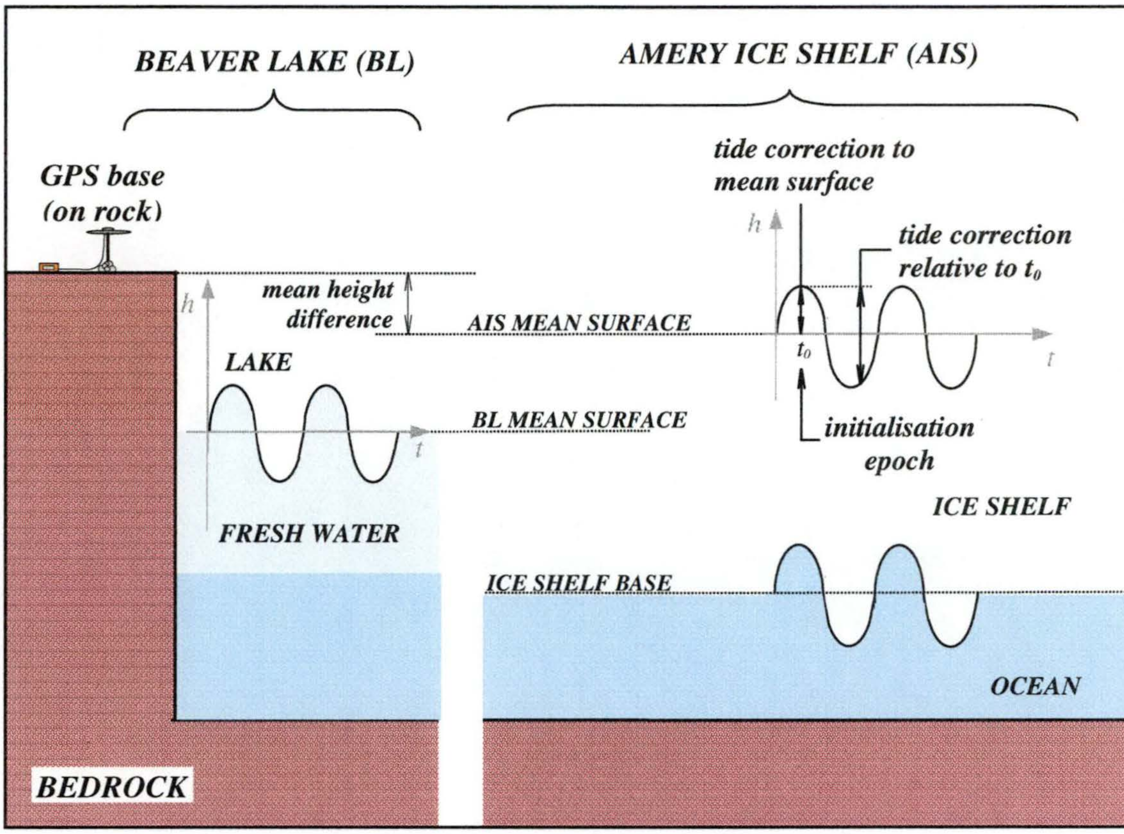

Figure 4.11 *Schematic diagram illustrating the components of the Amery Ice Shelf GPS survey and the various tide corrections involved to produce a height relative to a tide-free surface (Not to scale). In the kinematic survey, the initialisation epoch is t_0.*

Beaver Lake rock site

Using the Beaver Lake rock site as the reference station, initialisation was carried out in SKI using the known baseline technique. The positions along the kinematic traverse were determined from Beaver Lake to the instantaneous ice shelf surface. The ice shelf heights were corrected for tides using the BLTM, by applying a correction to the resulting heights, depending on the observation epoch, to bring them to the mean 'tide-free' surface (Figure 4.11).

Results

By processing the kinematic GPS data using the techniques described above, all kinematic GPS heights were referenced to the same 'tide-free' datum, using the BLTM value for the observing epoch. With the Amery base camps as the reference point, only

2 out of 24 squares of kinematic data were processed completely in SKI, and others could only be processed part-way round the square. With the Beaver Lake rock site as the reference point, 21 out of 24 squares were processed completely, although ambiguities were not resolved. The GPS closure, i.e. the RMS differences in the base camp station coordinates between the start and finish of the survey, was approximately 0.4 m in all three components (latitude, longitude, and height). A significant proportion of the horizontal (latitude and longitude) components was due to surface ice flow, which was approximately 0.2 m in 4 hours.

The combination of resulting height profiles from the two processing methods meant that each internal 10-km arm (surveyed twice) had up to four independent determinations. Comparison of these values provided an estimate of the repeatability of the GPS measurement and processing technique. The fact that many of the lines had multiple observations also meant that some interactive editing could be carried out on these lines. Individual profiles along a segment were graphically stacked and edited, and those data segments containing clear outliers were rejected.

Figure 4.12 presents repeat surface elevation profiles along a) the line from C11 to C12 and b) from C12 to C13. It can be seen that the profiles mostly repeat closely. Examples of segments containing outliers are seen in Figure 4.12b, between latitude -74.64 and -70.63 at latitude -70.58. In this case, the whole of Profile 2 (processed with respect to Beaver Lake) and the outliers at latitude -70.58 were removed.

Height differences between different profiles were calculated using a spline-fitting process to resample data on to the same measurement points. The mean of the residuals along the line from C12 to C13 was 0.0113 m. For the line C10 to C11 the mean of the residuals was 0.0884 m with all data left in, and 0.011 m, with all outliers removed.

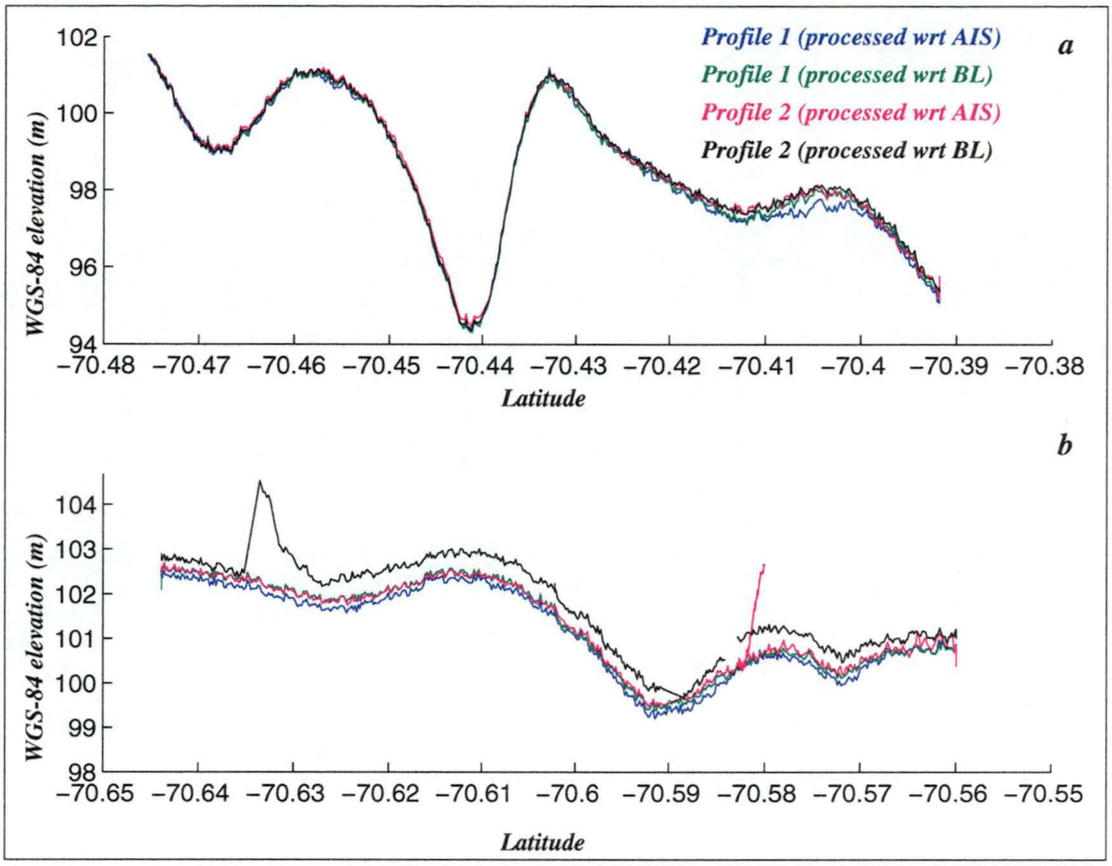

Figure 4.12 *Four independent determinations of the surface elevation profile along the 10-km lines from a) C12 to C13 and b) C10 to C11. Each line was surveyed twice, and the resulting data were processed both relative to the Beaver Lake rock site and relative to the Amery base camps, resulting in four independent surface profiles.*

4.3.4 Construction of GPS reference surface

A three-dimensional reference surface was created from the tide-corrected, kinematic GPS profiles. Since this reference surface was intended for validating the ERS altimeter heights, an appropriate coordinate convention had to be used. Therefore, the final coordinates from the individual kinematic profiles (φ, λ, and h on the WGS-84 ellipsoid) were transformed onto a polar stereographic projection (X, Y). For the Amery Ice Shelf, the conventional X-axis of the polar stereographic projection is closely aligned to the principal flow direction. This approximately corresponds to the longitudinal axis of the GPS survey grid (along the ice shelf).

Construction of a three-dimensional reference surface from the GPS survey grid was performed using kriging routine, with the GSLIB software (see Appendix C). The individual GPS points were used to generate directional semivariograms along the transverse (Y-axis; 0°) and longitudinal (X-axis; 90°) directions respectively.

The semivariograms are illustrated as solid lines in Figure 4.13, where direction 1 is transverse and direction 2 is longitudinal. It can be seen that the semivariograms for each direction are quite different. This is expected, since the height variation is much greater in the transverse (Y) direction, as this is perpendicular to the flowlines. This is where there is the greatest short-wavelength variation in height. In the longitudinal (X) direction, there is a broad-scale negative gradient from south to north, but the short-wavelength component exhibits much less variation. A fitting routine was used to fit a combination of a spherical and an exponential model to these anisotropic semivariograms (see Appendix C). These models, shown in Figure 4.13 as dashed lines, were used to calculate the parameters needed for the kriging, which are outlined in Appendix C.

The resulting interpolated GPS surface is illustrated in Figure 4.14. Since the kriging technique used a semivariogram to interpolate over 10-km squares, not all of the true features are present in the interpolated surface. Large-scale features observed in the semivariogram are preserved, but local small-scale features will not be represented. It can be seen from this plot that the GPS survey covered a variety of topographic features.

Towards the northern end of the survey, the topography is smooth, whereas in the southern end it is much more variable. Two flat-bottomed, longitudinal depressions are revealed (see Figure 8.16 for a better view of these features) approximately 3-km wide and about 5 m lower than the surrounding surface. These surface depressions carried meltwater in the 1993-94 summer season (Phillips 1998; Chapter 8) but were frozen over at the time of the 1995 survey.

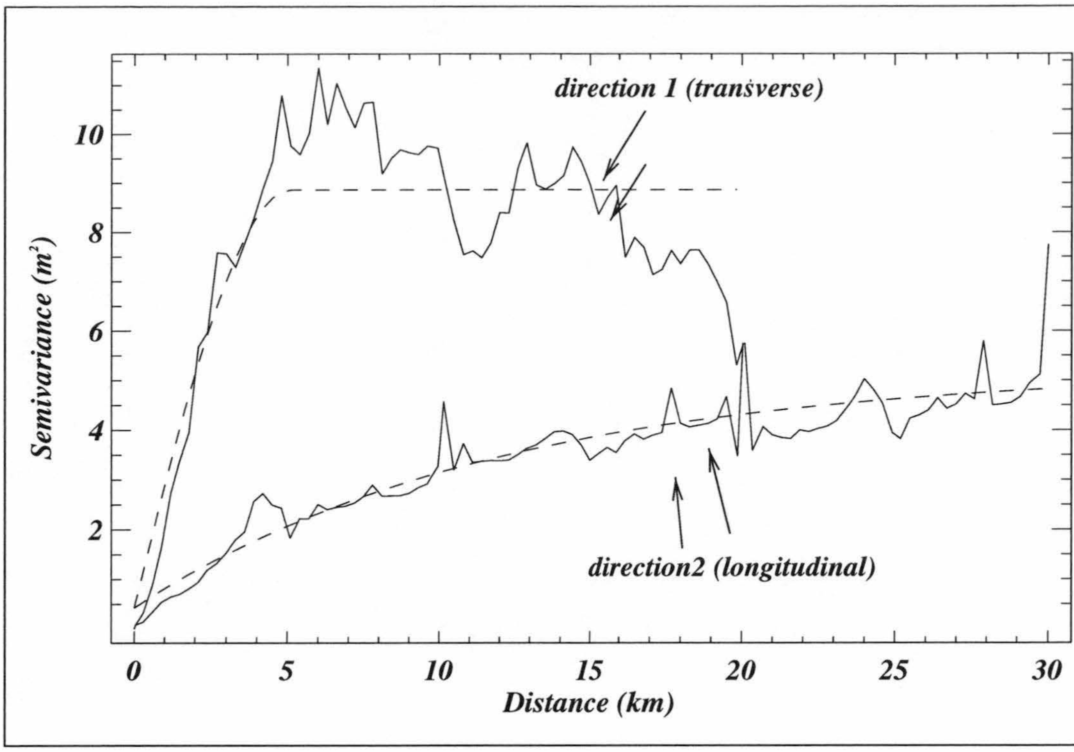

Figure 4.13 *Anisotropic semivariograms for kinematic GPS data over Amery Ice Shelf survey region. Fitted model (dashed line) is a linear combination of a spherical and an exponential function. Directions are along the polar stereographic Y and X axes.*

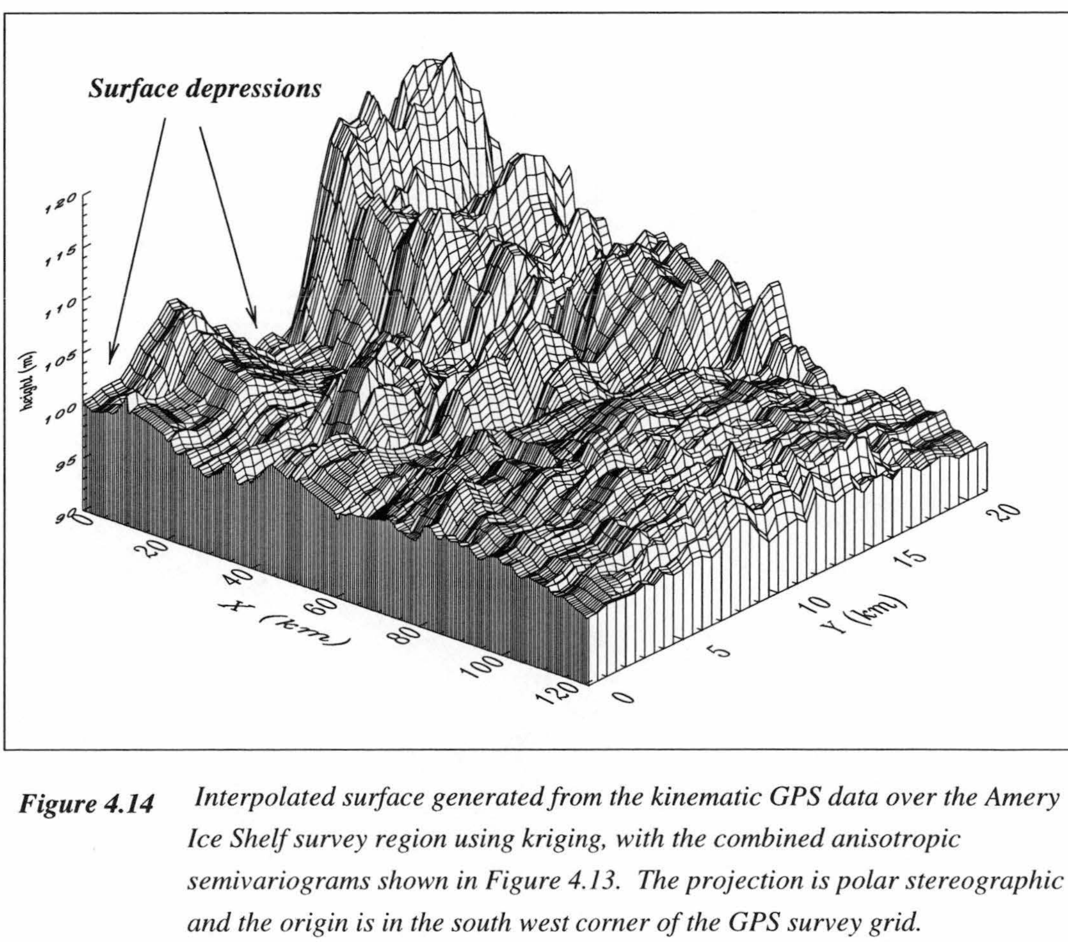

Figure 4.14 *Interpolated surface generated from the kinematic GPS data over the Amery Ice Shelf survey region using kriging, with the combined anisotropic semivariograms shown in Figure 4.13. The projection is polar stereographic and the origin is in the south west corner of the GPS survey grid.*

4.4 Chapter conclusions

The Amery Ice Shelf GPS survey was a successful GPS campaign that collected some invaluable static and kinematic GPS data. The multi-day static GPS observations collected at the six temporary camps on the Amery Ice Shelf were split into 2-hour segments and a three-dimensional position computed for each segment. The resulting station motion was resolved into local horizontal and vertical components, which represented surface ice flow velocities and tidal motion respectively.

The time series of the vertical variation in the GPS positions provided evidence of tidal motion at each camp, the southernmost camp (C2) being at latitude 71.3°S. This result indicates that the sub-ice cavity under the Amery Ice Shelf extends further south than Budd *et al.* (1982) reported. Furthermore, the vertical variations matched closely with predicted values in the Beaver Lake Tidal Model (BLTM), supplied by the NTF (Marion Tait, personal communication, 1996). This means that the Amery Ice Shelf is largely freely floating and that the BLTM can be used with confidence to transform the elevations of all points observed on the Amery Ice Shelf (both by GPS and altimetry) to a tide-free surface, therefore removing the tidal bias (see Chapter 3).

Comparison of the resulting horizontal ice flow velocities with ice velocities from the 1968 ANARE survey showed that there has been no significant change in surface ice flow velocities along the central flowline over this 27-year period. This suggests that there have been no substantial changes in the dynamics of the region over this period, which confirms that the new grounding line position does not represent a change with time, but is a redefinition based on more comprehensive data.

The kinematic component of the Amery Ice Shelf GPS survey provided an accurate set of densely sampled GPS heights over a 120-km by 20-km grid. These heights are referenced to the WGS-84 ellipsoid and therefore can be directly compared with the ERS heights. The positions have been transformed onto a polar stereographic projection and interpolated using kriging, which has provided a three-dimensional reference surface. Results of the comparison between the ERS and GPS heights and this reference surface are presented in Chapter 5.

Chapter 5

Validation of ERS heights and generation of Digital Elevation Models

5.1 Introduction

This chapter concentrates on the validation of the ERS height measurement and the subsequent generation of altimeter DEM products for the Lambert-Amery system.

The aims of this chapter are:

i) to describe the ERS waveform data processing and present the results;

ii) to describe the comparison between the ERS heights with the GPS heights collected during the Amery Ice Shelf survey; and

iii) to generate DEMs for the Lambert-Amery system.

The first section of this chapter presents the results of applying the processing techniques described in Chapter 3 to the ERS-1 168-day dataset over the Lambert-Amery system. It also discusses the comparison of altimeter-derived heights from the 35 and 168 day phases with GPS heights collected during the Amery Ice Shelf surveys (Chapter 4). The comparison of ERS and GPS height measurements in the survey region provides a localised indication of the quality of the derived ERS height measurement. The second section describes the generation of two DEMs for the Lambert-Amery system. The first is a high-resolution (1-km) product for the Amery Ice Shelf only (AIS-DEM), and the second is a 5-km product for the entire Lambert-Amery system (LAS-DEM). Both products are presented and their main features discussed. The AIS-DEM is compared qualitatively with a detailed cumulated AVHRR image of the same region (Ted Scambos, personal communication, 1998). The accuracy of the LAS-DEM is estimated by comparing its elevations with GPS height measurements collected during the Lambert Glacier traverse (see Chapter 2).

5.2 Altimeter data processing and data quality assessment

5.2.1 Altimeter data processing

The data processing steps required to produce an ellipsoidal height measurement from satellite altimeter data were discussed in detail in Chapter 3. These steps are summarised in a flow chart in Figure 5.1.

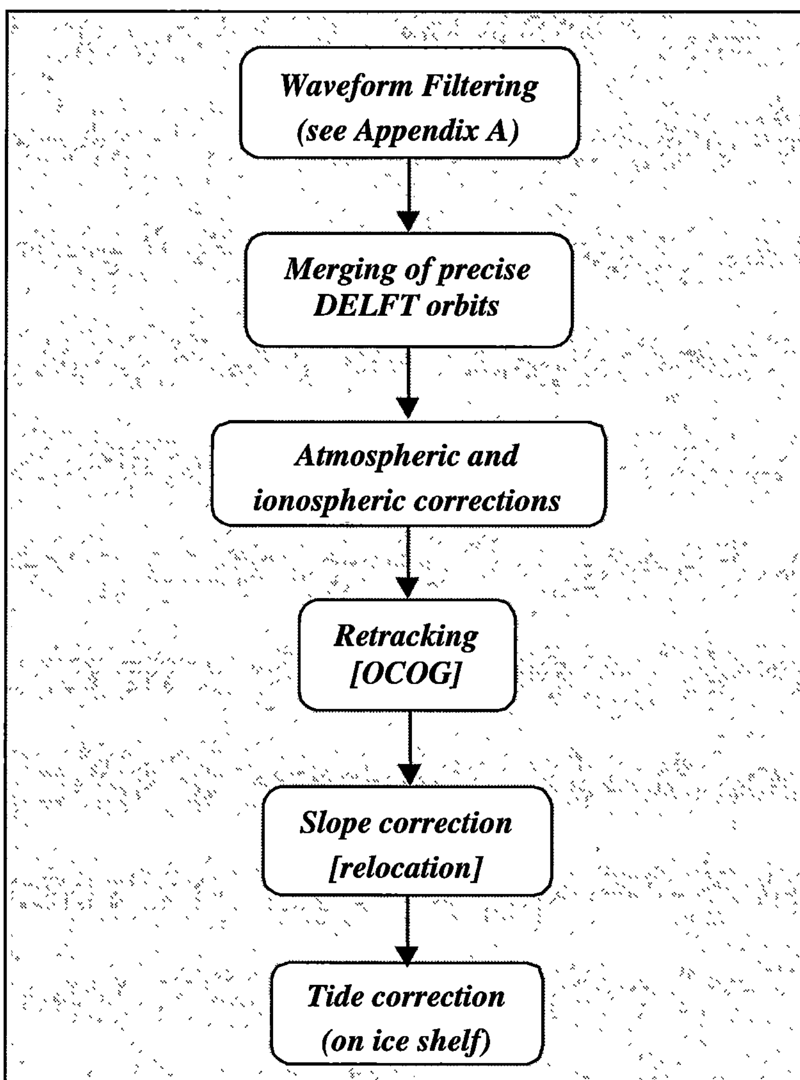

Figure 5.1 *Flow chart of processing steps applied to ERS altimeter data. See Chapter 3 for specific processing techniques (in square parentheses).*

The ERS altimeter data used here are from the 35-day repeat Tandem Mission (Phase G of ERS-1 and Phase A of ERS-2) and the 168-day repeat geodetic mission (Phases E and F of ERS-1). Although the 35-day repeat data were used in the validation analysis, they were not used to generate the DEM products. Therefore, when bulk processing statistics are presented in this chapter they correspond to the 168-day dataset only.

Most of these data were in the Waveform Advanced Product (WAP) V2.0 format obtained from ESA, with the exception of some cycles used for Chapter 7 which were provided by Mullard Space Science Laboratory in their own ERS Altimeter (EA) format. All of these data had already undergone substantial low-level processing (Level 1.0) and higher level processing (Levels 1.5 and 2.0) at the UK Earth Observation Data Centre (EODC), described in detail in Cudlip and Milnes (1994).

All of the ERS data used in this chapter were processed using the steps shown in Figure 5.1. For the 168-day phases of ERS-1, the filtering process removed 5.8% of the original waveforms, reducing the number of altimeter data points over the Lambert–Amery system from 11 x 10^6 to 10.35 x 10^6. A location map of all filtered waveforms over the Lambert-Amery system is shown in Figure 5.2. It can be seen that most of these waveforms arose from regions of changing surface topography and steep slopes, either in mountainous regions or around the ice sheet periphery. This is because the altimeter tracking-loop could not keep track of the surface in these regions. The specular filter eliminated the majority of returns from sea-ice, together with some other occurrences that arose from the smooth, flat surfaces of meltwater and refrozen meltwater. These were located in the ablation zone of the Lambert-Amery system, and where meltstreams had been present in surface depressions on the ice shelf itself (Phillips 1998; Chapter 8).

Retracking was carried out using the OCOG technique (Chapter 3), and all data were retracked to the 10, 25 and 50% thresholds. This was so that the optimum retracking threshold could be determined through comparison with the GPS data (see next section).

Atmospheric corrections based on *in situ* observations were carried out for the Lambert-Amery system as described in Chapter 3.

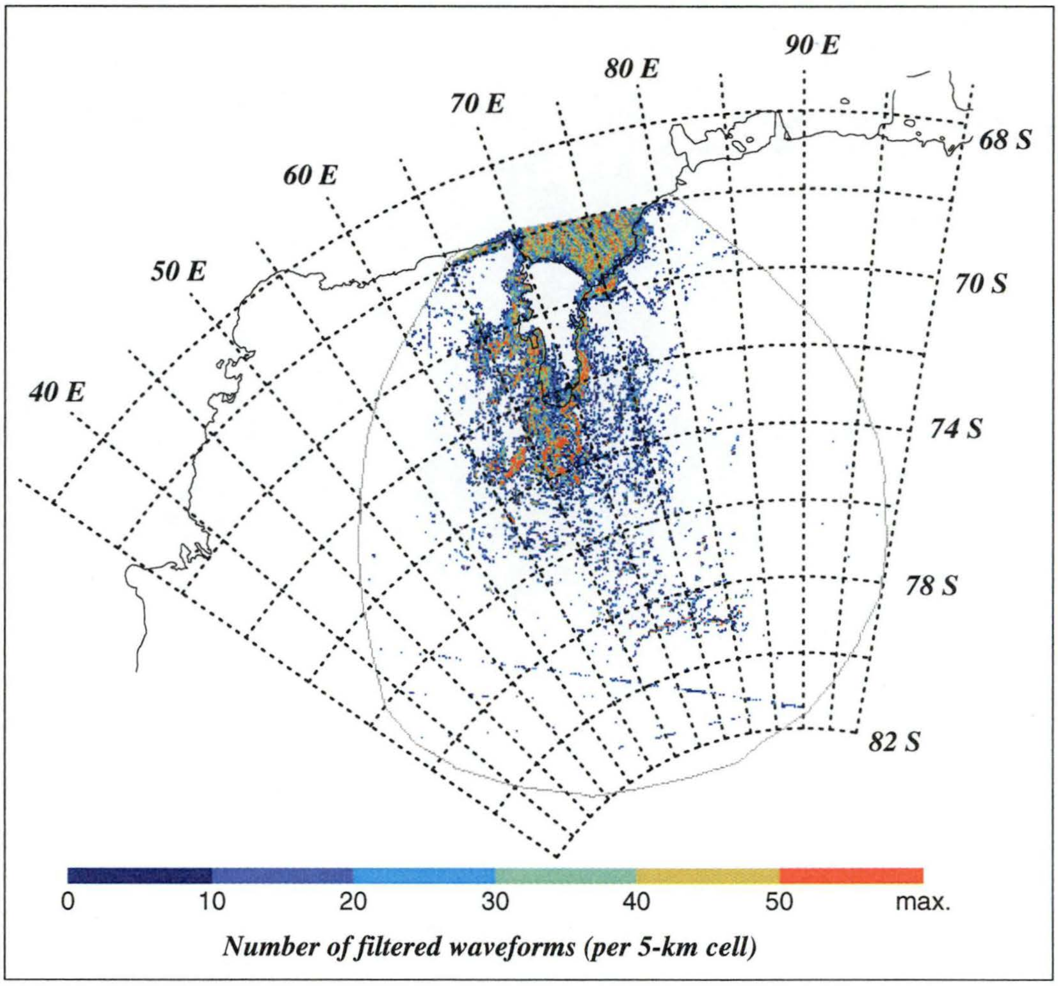

Figure 5.2 *Location of waveforms filtered from the 168-day dataset, over the Lambert-Amery system by applying the filters outlined in Appendix A.*

Internal data validation by crossover solutions

After passing the 168-day data through the filters, a preliminary crossover analysis was carried out and some large crossover values were found. Individual tracks were examined more closely and it was found that there were 16 orbits containing bad height values. These orbits (numbers 14415, 14770, 15134, 15394, 15468, 15469, 15651, 16549, 16723, 17681, 17762, 17769, 17850, 18814, 18901 and 19098) were all removed from the 168-day dataset.

Crossover analyses (see Chapter 3) were applied before and after data processing, to assess the improvement to the data integrity introduced by the processing scheme.

Height differences at orbit intersections are independent of slope correction, because the magnitude of the slope-induced error is dependent only on the local surface slope, which is the same at coincident locations. Histograms of crossover differences over the Lambert Glacier – Amery Ice Shelf system for the 168-day data, before and after all of the processing steps of Figure 5.1 (except for relocation) had been completed, are shown in Figure 5.3. Before processing, the mean of the height differences at the crossovers was 0.80 $\pm$ 15.60 m; after processing this reduced to 0.08 $\pm$ 1.99 m. These histograms show that the internal consistency of the height measurement improves considerably after processing.

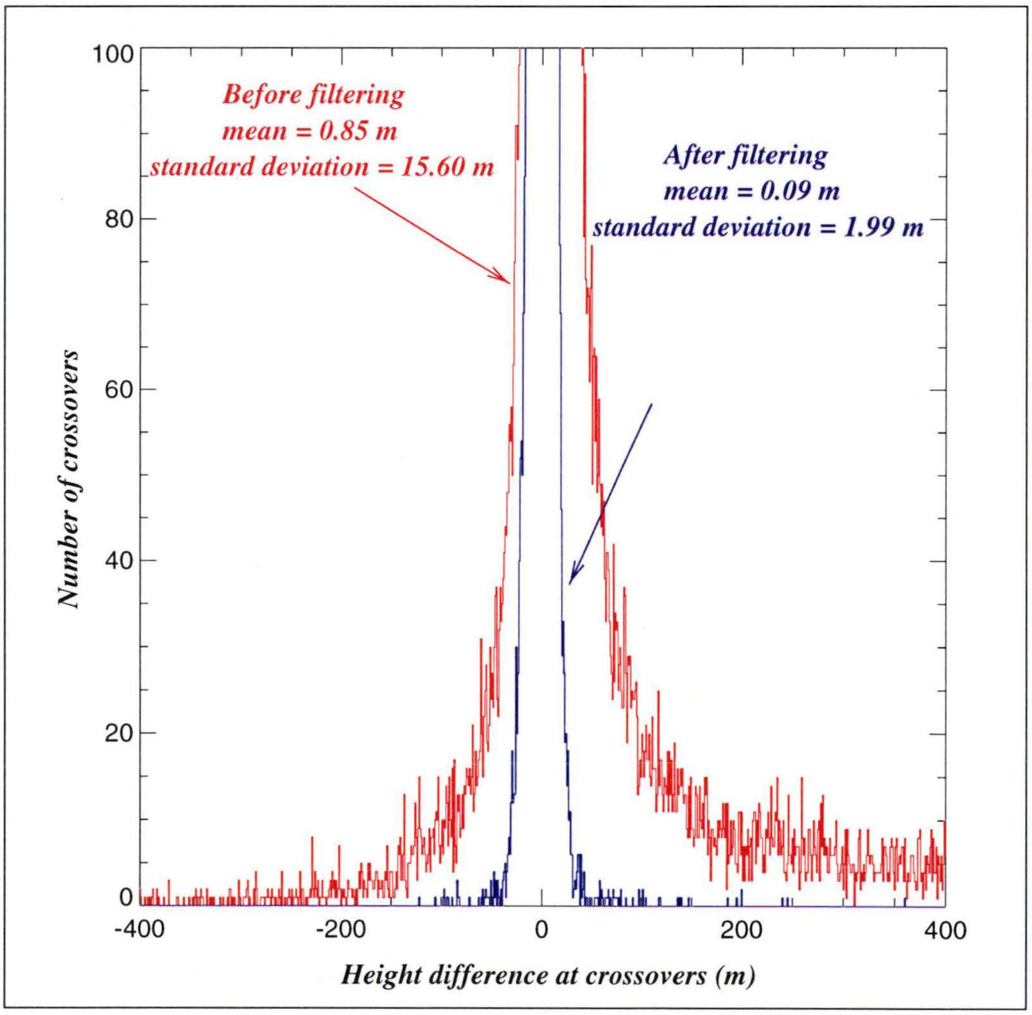

Figure 5.3 *Histogram of height differences at altimeter crossovers before and after processing of the 168-day data over the Lambert–Amery system.*

5.2.2 Inter-comparison of ERS and GPS altimeter heights on the Amery Ice Shelf

The results of a GPS survey carried out on the Amery Ice Shelf in the austral spring of 1995 were presented and discussed in Chapter 4. The Amery Ice Shelf survey provided ground-truth ellipsoidal height measurements that could be directly compared with those from the ERS-1 and ERS-2 satellite radar altimeters. A 120-km by 20-km survey grid composed of twenty-four 10-km squares was established on the ice shelf using kinematic GPS techniques. Static GPS measurements of the tidal-induced elevation variation at each of the survey base stations closely matched the predicted tidal signal for Beaver Lake. The kinematic GPS data were corrected for this tidal displacement, and interpolated using kriging to produce a 'tide-free' ice shelf validation surface.

The ERS data used to validate the altimeter height measurement over the survey region were from various phases. The Tandem Mission was operating at the time of the survey; Figure 5.4 illustrates the location of the five ERS satellite ground tracks from this mission that coincide with the GPS survey grid on the ice shelf. This comparison uses one repeat cycle of ERS-1 and two repeat cycles of ERS-2 that were available from October and November 1995, all in ice mode. Table 5.1 lists the dates of these repeat tracks. The advantage of using data from the same time as the survey is that any temporal height bias will be minimised. Such biases could have arisen from seasonal variations in penetration depth of the radar signal resulting from changes in surface properties of the ice shelf (Ridley and Partington 1988; Yi *et al.* 1997).

Data from the 168-day repeat geodetic mission (Phases E and F of ERS-1) were also used here for comparison with the GPS data. Although the geodetic phase did not coincide in time with the survey, its 168-day repeat period did mean that the density of tracks was much greater, allowing many more measurement points for inter-comparison. During the geodetic phase, adjacent ground tracks had a spacing of 2-3 km over the survey region, compared to ~30 km for the 35-day repeat data. There were forty-eight ERS-1 satellite tracks from the geodetic phase that crossed the GPS survey grid, all in ice mode, compared to fifteen from the 35-day repeat.

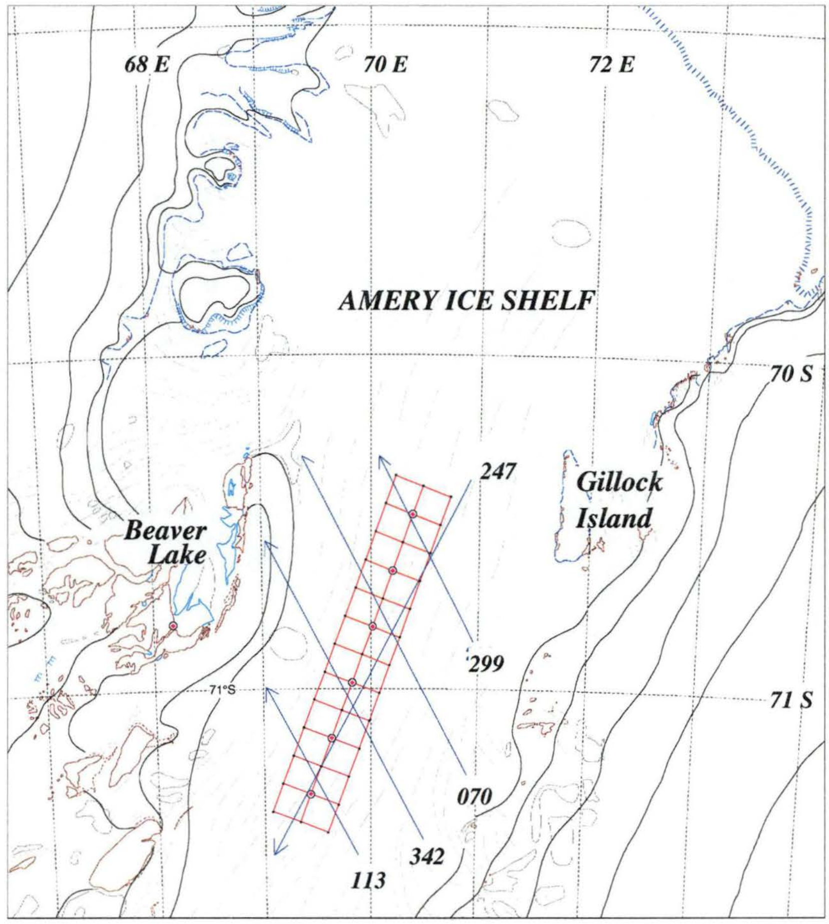

Figure 5.4 *Location of survey grid and 35-day repeat ERS altimeter ground tracks on the Amery Ice Shelf. Arrows on ERS tracks indicate the direction of satellite motion.*

TABLE 5.1 *TRACK NUMBER, DIRECTION AND DATE OF EACH REPEAT, FOR 35-DAY REPEAT ERS TRACKS THAT CROSSED THE GPS GRID, ABOUT THE SAME TIME AS THE SURVEY.*

TRACK	**DIRECTION**	**DATES (1995)**
070	ASCENDING	6 AND 7 OCTOBER, 11 NOVEMBER
113	ASCENDING	9 AND 10 OCTOBER, 14 NOVEMBER
247	DESCENDING	19 AND 20 OCTOBER, 24 NOVEMBER
299	ASCENDING	22 AND 23 OCTOBER, 27 NOVEMBER
342	ASCENDING	25 AND 26 OCTOBER, 30 NOVEMBER

In this analysis, three methods were used for inter-comparison. The first was a direct comparison of height values at the intersecting points of the ERS tracks and the GPS survey grid, which provides an indication of the accuracy of the individual altimeter heights. The second method was a comparison of the GPS surface sampled along the ERS ground tracks, which indicates how realistically the altimeter is representing the surveyed surface. The third method was a direct comparison of the two interpolated surfaces, which reveals any differences in the resulting shape of each surface.

The map projection used for the GPS surface was a polar stereographic projection (Chapter 4). On the Amery Ice Shelf, the X-axis of this projection is approximately along the main ice flow direction, and the Y-axis is across the shelf. The coordinates of all ERS data and GPS data were transformed onto this projection for the comparisons carried out here. The heights were all in metres relative to the WGS 84 ellipsoid.

Direct comparison at intersecting points

This comparison looked at differences between the ERS altimeter heights and the GPS heights at intersecting points of the ERS tracks with the GPS survey. There were eighty-three such intersecting points for the 35-day ERS-1/2 tracks and two-hundred-and-sixteen for the 168-day ERS-1 tracks. There were three repeats along each 35-day ground track, which lead to clusters of ERS intersection points. For the 168-day tracks, the ERS intersection points were well distributed over the whole survey region.

At each intersection point of the ERS tracks with the GPS grid, the values of the altimeter and GPS heights were obtained. Linear interpolation was used between measurements either side of an intersection, to derive a height value at the exact point of intersection. For the altimeter heights, only measurements that were separated along track by less than 600 m were used in the interpolation. Three different altimeter height values were used, corresponding to the 10%, 25% and 50% OCOG retracked values (see Chapter 3).

Histograms of the height differences at intersecting points are illustrated in Figure 5.5, for the 10%, 25% and 50% OCOG retracked heights. The left set of histograms corresponds to the 35-day data, and the right set to the 168-day data. Statistics for these distributions are shown in Table 5.2.

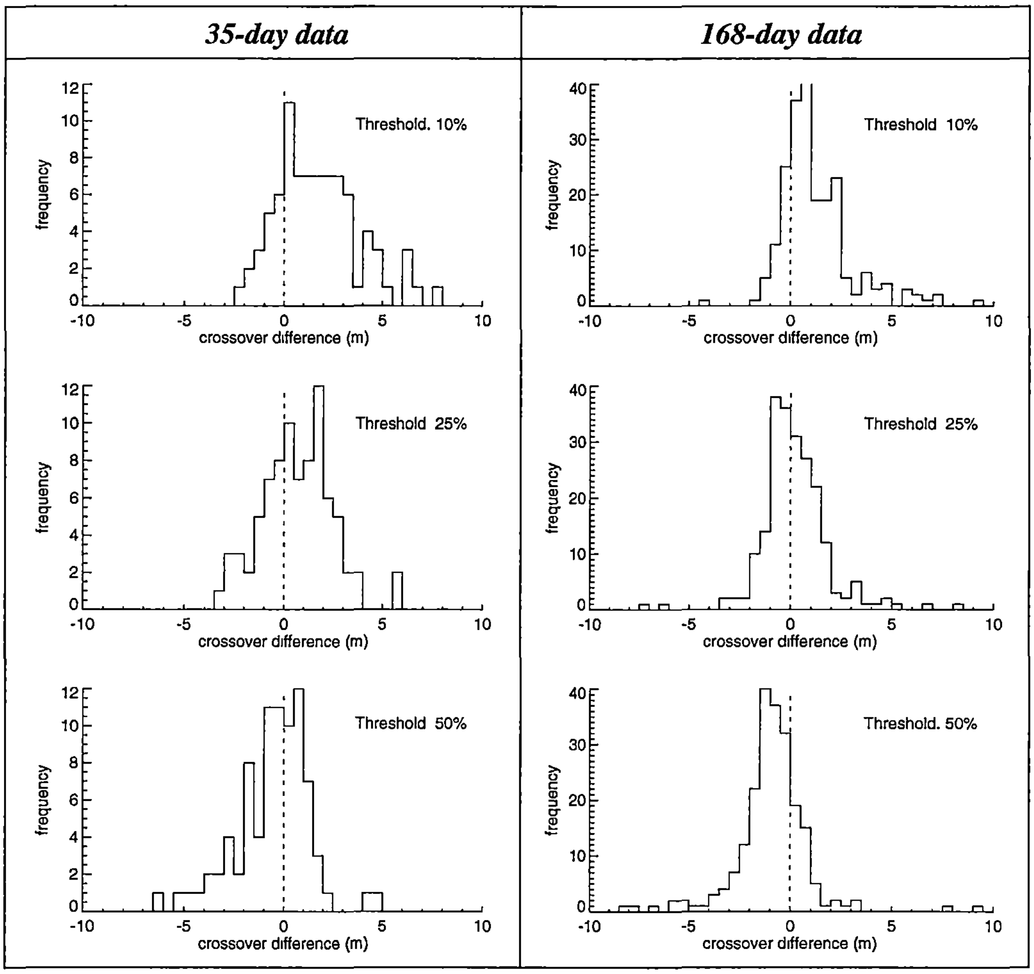

Figure 5.5 *Histograms of height differences for a) the 35-day data and b) the 168-day data. Height differences are h_{ERS}-h_{GPS}.*

TABLE 5.2 *MEAN AND RMS OF THE HEIGHT DIFFERENCES (H_{ERS}-H_{GPS}) AT THE INTERSECTING POINTS OF THE 35-DAY AND 168-DAY ERS TRACKS AND THE GPS SURVEY.*

	35-day (83 points)		***168-day (216 points)***	
Threshold	***Mean (m)***	***RMS(m)***	***Mean (m)***	***RMS (m)***
10%	*1.2 ± 0.2*	*2.0*	*1.0 ± 0.1*	*1.8*
25%	*0.2 ± 0.2*	*1.7*	*0.0 ± 0.1*	*1.7*
50%	*-1.0 ± 0.2*	*2.3*	*-1.3 ± 0.2*	*2.3*

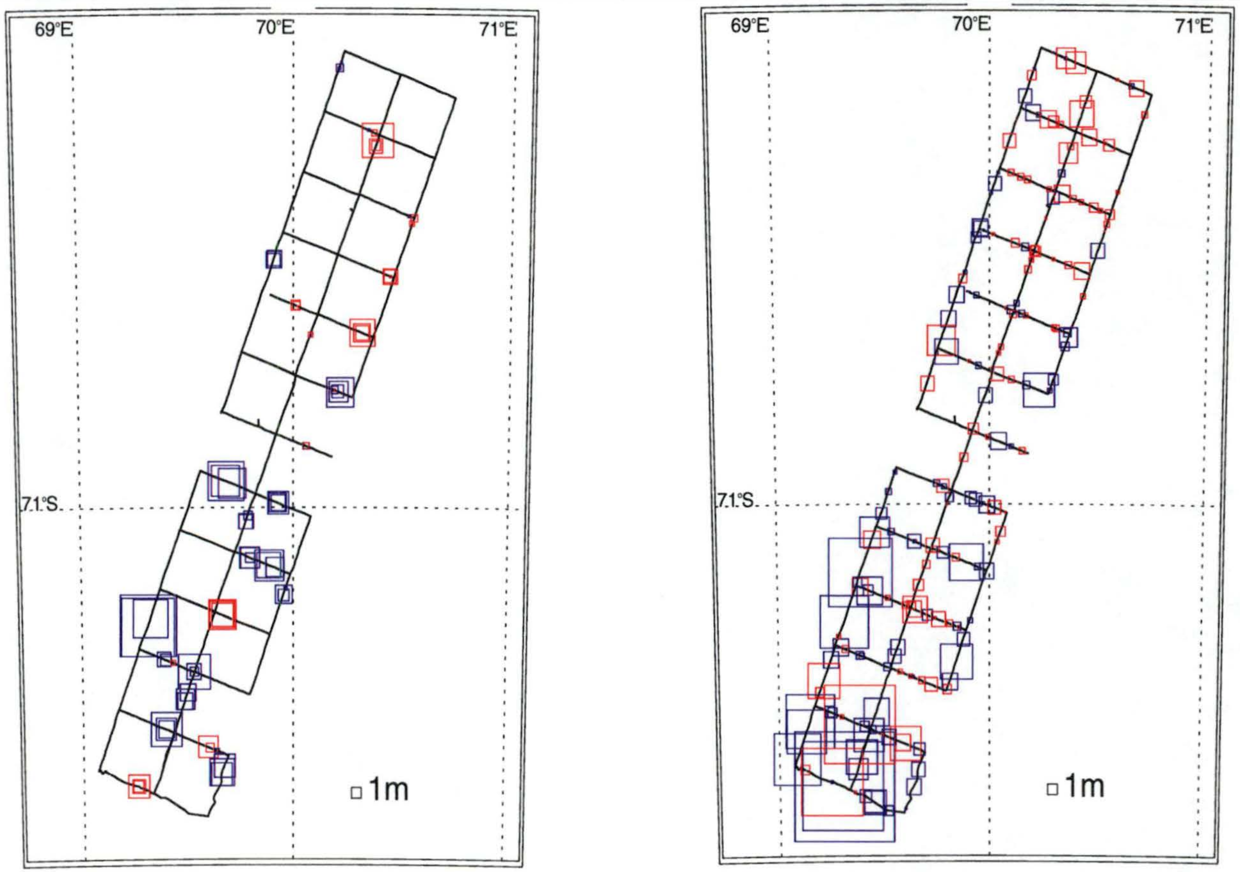

Figure 5.6 *Spatial distribution of height differences at intersecting points of the GPS survey grid and the 35-day ERS tracks (left plot) and 168-day tracks (right plot). Each square represents a height difference (ERS-GPS) and is scaled according to the magnitude of the difference (inset square represents 1 m). Positive differences are blue while negative differences are red.*

These results show that the ERS height value resulting from retracking to the 25% OCOG threshold produces the closest overall agreement with the GPS data. Figure 5.6 illustrates the spatial distribution of these differences for the 35-day dataset (left plot) and the 168-day dataset (right plot) at the 25% OCOG threshold.

The plots in Figure 5.6 show that the height differences are greater in the southwestern region of the survey. Indeed, when considering only the intersecting points that lie in the northern part of the survey region (i.e. north of latitude 71°S), the RMS height difference for the 168-day data at the 25% threshold reduces from 1.7 m to 0.9 m. The similarity of the statistics for the 35-day (same time as the survey) and 168-day datasets suggests the temporal height bias in the ERS altimeter heights over the Amery Ice Shelf is small.

Comparison of surface-height profiles

The GPS reference surface generated using kriging on a 0.5-km grid over the survey region was presented in Figure 4.14. To give an indication of how realistically the altimeter was representing the 'true' surface, altimeter height profiles across the survey region were compared with profiles derived from the GPS surface. All three passes of the 35-day phase ERS data were used for this comparison (two ERS-2 and one ERS-1).

For the comparison with altimeter heights, the GPS data were interpolated using kriging, with a cell size of 2 km, the approximate diameter of the altimeter pulse-limited footprint. For each altimeter measurement, the coincident GPS height measurement was interpolated from the GPS surface grid. In this way, a GPS height profile was generated for each ERS ground track, at coincident locations.

The resulting height profiles along each of the five 35-day ERS tracks (Tracks 299, 070, 342, 113 and 247) are shown in Figure 5.7. The profiles, using the 25% threshold, are plotted against distance in kilometres along the ground track, with the direction of satellite travel from left to right. Only one repeat of each ERS track has been shown, because the tracks repeat very closely. Although the tracks crossed refrozen meltstreams, there was no evidence of snagging. This is likely to be because a layer of snow was present on top of the refrozen meltstreams at the time of the overpasses. The presence of this snow layer, observed in shallow snow pits dug during the Amery survey, made the refrozen melt features appear rough to the radar altimeter, resulting in a diffuse return.

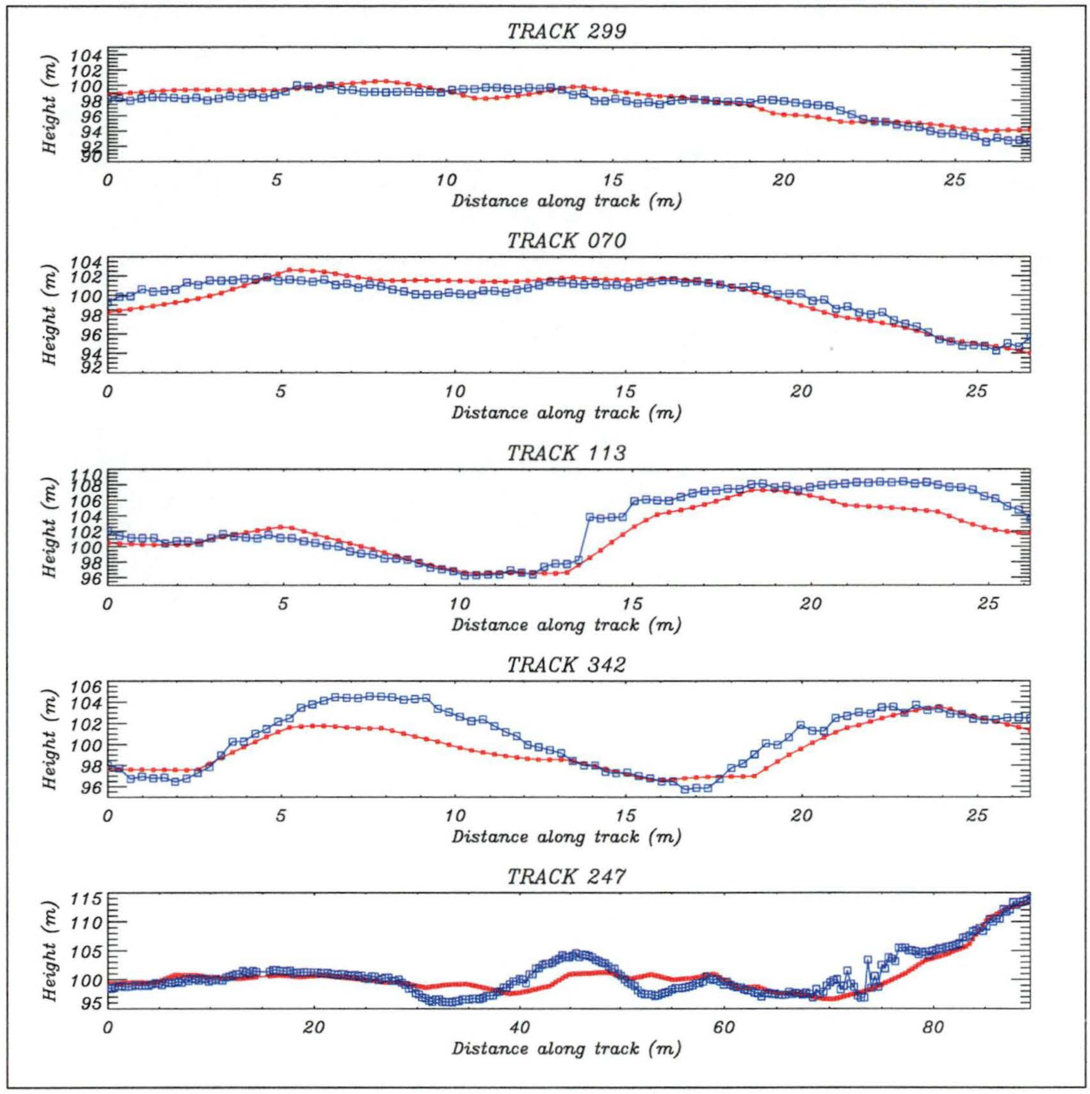

Figure 5.7 *ERS (25% retracked) and GPS surface height profiles along the five 35-day ERS tracks (Tracks 299, 070, 342, 113 and 247). The open squares represent ERS heights and the smaller solid squares the GPS surface height at each ERS measurement location.*

Along Tracks 299 and 070, the altimeter encounters relatively little topographic variation, and the tracker manages to follow the surface reasonably well. Along Track 113, however, the topography is more variable, and the tracker clearly has problems following the surface. This demonstrates a limitation of the radar altimeter instrument over rough surfaces. For example, the small, 3-m surface bump at 5 km is under-estimated using the 25% threshold, and the 10-m rise at 20 km is detected as soon as it comes into the pulse-limited footprint. Along Track 342 the altimeter encounters similar problems, although they are less severe. Along Track 247, there is good agreement between altimeter heights and GPS heights over much of the surface. The surface bump in the altimeter profile at 45 km is almost certainly a real feature. However, it is most likely located to one side of the ERS ground track, and therefore not present in the sampled GPS profile.

The mean and RMS of the differences between the ERS altimeter heights (h_{ERS}) and the interpolated GPS heights (h_{GPS}) along a track were calculated, to give an estimation of accuracy for that track. Table 5.3 displays the mean and RMS errors using the 25% threshold value for each track. All three repeat cycles have been combined here. Note that the ascending tracks are listed from north to south (refer to the map in Figure 5.4), so the topography becomes more variable moving down the table.

TABLE 5.3 MEAN AND RMS HEIGHT DIFFERENCES (H_{ERS}-H_{GPS}) AT THE 25% RETRACK THRESHOLD FOR EACH 35-DAY ERS GROUND TRACK. ALL THREE REPEAT CYCLES OF THE ERS DATA HAVE BEEN COMBINED.

	Track	Mean (m)	RMS (m)
Ascending	299	-0.4	1.1
	070	-0.2	1.1
	342	1.0	1.6
	113	1.0	1.9
Descending	247	0.3	1.8

Comparison of interpolated surfaces

A three-dimensional reference surface was created from the geodetic phase ERS-1 altimeter data. In a similar manner to the GPS data described in Chapter 4, these data were converted into polar stereographic X and Y coordinates, and interpolated onto a 1-km grid using kriging (see Appendix C). An anisotropic semivariogram was computed from the ERS data using the GSLIB software package. The directions used for the semivariogram corresponded to the angles made by the altimeter tracks, along which the data density is greatest. In the polar stereographic projection used here, 0° is along the Y-axis and 90° is along the X-axis. Direction 1 corresponds to the descending track direction (108.6°) and Direction 2 to the ascending track direction (41.4°).

The semivariograms for the ERS data are illustrated in Figure 5.8. Comparing these results with the semivariogram for the same region generated from the GPS data (Figure 4.13) it can be seen that the shapes are quite different. This can be explained by the different directions used in the semivariogram calculations. The directions used for the GPS semivariograms were 0° and 90°. In the survey region, the maximum variation in topography is across the flowlines and surface depressions, approximately along the Y-axis (0°), whilst the minimum variation in topography is along these features, approximately along the X-axis (90°). The semivariograms for the GPS data were therefore created along directions that contained the extremes of the possible topographic variation. However, in the ERS semivariograms the directions were 41.4° and 108.6°. The variability of height with distance is larger along 41.4° than it is along 0°, and smaller along 108.6° than it is along 90°. Therefore, the lines of the semivariogram plots for the ERS data fall in between those for the GPS data.

Like the GPS semivariogram shown in Figure 4.13, the fitted model is also a nested structure, which is a linear combination of a spherical and an exponential function. Note that, for direction 2, the model does not fit well to the semivariogram at large distances (> 20 km). This is of no concern here since the search radius used for the kriging is only 15 km.

Using these semivariogram parameters, an interpolated surface was generated from the altimeter data using kriging (Appendix C). The altimeter surface (Figure 5.9) is similar in structure to the GPS surface over the same region (Figure 4.14), although it is smoother and most of the features appear broader. This is to be expected, because the altimeter measures a mean surface height over the area of the pulse-limited footprint, and also tends to 'see' high features early, as seen in Track 113 (Figure 5.7).

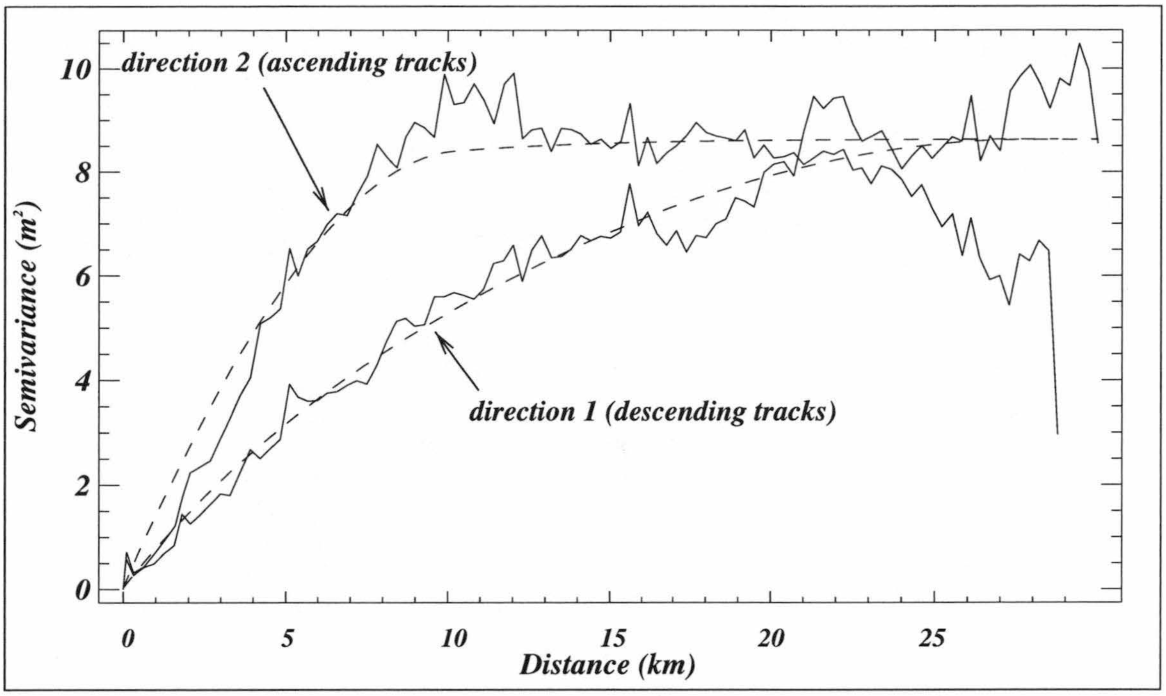

Figure 5.8 *Anisotropic semivariograms for ERS-1 168-day data over the Amery Ice Shelf survey region. Fitted model (dashed line) is a linear combination of a spherical and an exponential function. Directions are along descending tracks and ascending. tracks. (Compare with Figure 4.13 for GPS data over the same region).*

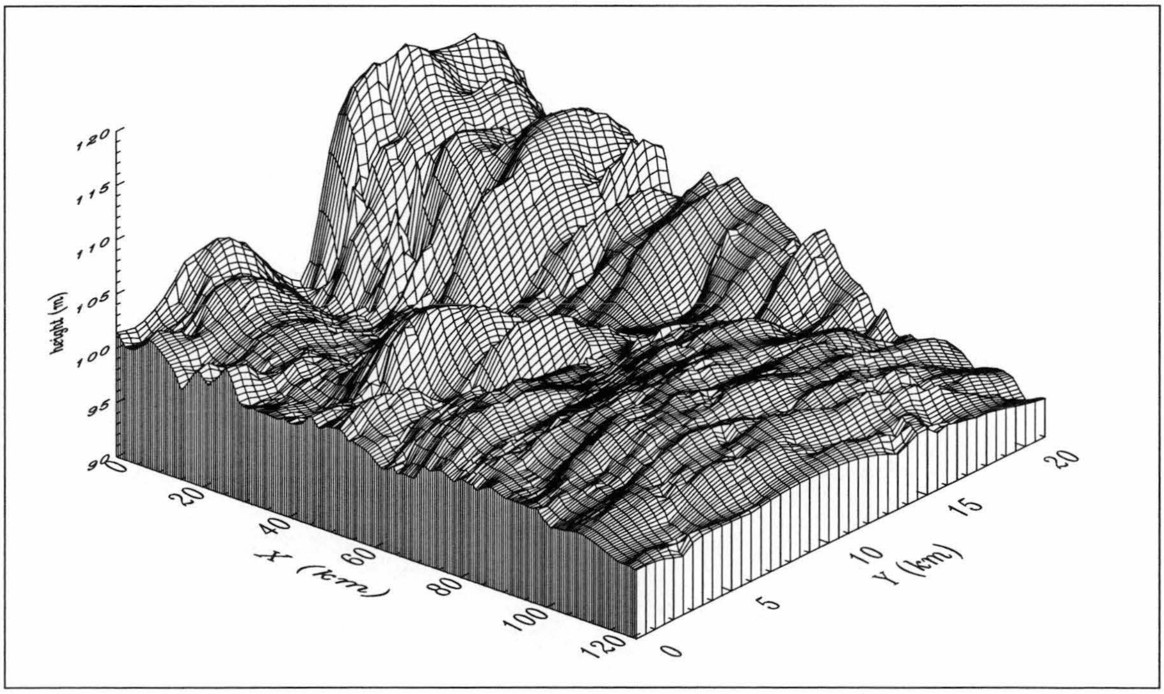

Figure 5.9 *Interpolated surface generated from the ERS-1 168-day data over the Amery Ice Shelf survey region using kriging, with a combined anisotropic semivariogram (Figure 5.8). The projection is polar stereographic and the origin is in the SW corner of the GPS survey grid. (Compare with Figure 4.14).*

Discussion on observed height differences

Differences between the ERS altimeter-derived heights and the GPS-derived heights can arise from a number of possible sources. The combined RMS error remaining in the altimeter height measurements after merging in the precise orbits (~90 mm), correcting for propagation delays (~15 mm) and tidal motion (~50 mm) is ~104 mm. The RMS error introduced by the OCOG retracking method is 0.49 m per waveform in ice mode (Scott *et al.* 1994), which amounts to ~80 mm for the 35-day dataset (83 intersections), and ~50 mm for the 168-day dataset (216 intersections). The potential remaining sources of bias are:

- ***Electromagnetic bias:*** the shape of the altimeter waveform received by a radar altimeter is dependent on the properties of the surface with which the pulse interacts, and will be distorted to a varying degree, depending on inhomogeneities on the surface (see Chapter 3). No simple retracker can account for these non-uniform waveforms, and techniques such as waveform migration (Wingham *et al.* 1993) are being developed to cope with this problem.

- ***Surface penetration:*** this problem has been approached by Davis (1993) in his surface and volume retracking program (Chapter 3). However, this algorithm does not work well for ice mode, where there is a wider range window and the waveforms are more coarsely sampled (see Chapter 8).

5.3 Generation of DEM products

The results of the comparison of ERS heights with GPS heights on the Amery Ice Shelf provided validation for the ERS altimeter heights in this region. This meant that Digital Elevation Models (DEMs) for the region could be generated with confidence that the data were at least reliable over the survey region.

Two DEMs were generated for this study (Table 5.4):

i) a 1-km DEM of the Amery Ice Shelf only (AIS-DEM); and

ii) a 5-km DEM of the entire Lambert Amery system (LAS-DEM.

Further GPS data were available at the Lambert Glacier traverse sites, from a similar epoch to the ERS-1 data (1994-95) for comparison with the LAS-DEM.

TABLE 5.4 MAIN CHARACTERISTICS OF THE TWO ERS-1 ALTIMETER DEM PRODUCTS GENERATED FOR THE LAMBERT-AMERY SYSTEM.

Region	***Method***	***Grid (km)***	***Map projection***
Amery Ice Shelf only (AIS-DEM)	*Kriging*	*1*	*Polar stereographic*
Lambert Amery system (LAS-DEM)	*Averaging*	*5*	*Polar stereographic*

The reason for using averaging for the LAS-DEM is explained in Section 5.3.2.

For both products, all of the data from the geodetic phases (Phase E and F) of ERS-1 were used. The two geodetic phases, when combined, consisted of 4945 orbits collected between April 1994 and March 1995 (orbit numbers 14302 – 19247), 2445 of which passed over the Lambert Glacier Basin data extraction region. The low repeat frequency (168 days) meant that the spatial sampling density was very high (2-3 km), providing very detailed surface topographic mapping.

Previous DEMs of the region used data that were much less spatially dense (Herzfeld *et al.* 1993; Figure 2.5). Although their DEM was produced on a 3-km grid, the input Geosat data only had a track spacing of ~30 km, therefore topographic features were poorly sampled. The region was also covered by a 20-km DEM for the whole of Antarctica generated from ERS-1 35-day Fast Delivery data (Bamber 1994a). Recently, Bamber and Bindschadler (1997) presented an improved 5 km DEM for Antarctica generated from the same ERS-1 geodetic phases used here. This DEM was generated using a similar technique to that of the LAS-DEM described below, and even at this spatial resolution the level of detail was such that large-scale flow features and undulations were clearly seen on the Ross Ice Shelf.

The first part of this section describes the techniques used to create the fine resolution 1-km AIS-DEM. Plots of the resulting surface are presented and discussed. One of these plots is compared with a cumulated AVHRR image provided by Ted Scambos of the National Snow and Ice Data Centre (NSIDC). The second part describes the generation of the 5-km LAS-DEM and presents plots of the DEM, pointing out its limitations. To assess the accuracy of the LAS-DEM, height values are derived at the Lambert Glacier Traverse stations by interpolation, and compared to the measured GPS heights.

5.3.1 Amery Ice Shelf (AIS) DEM (1 km)

Production of AIS-DEM

A preliminary DEM for the whole Amery Ice Shelf (generated by averaging the entire 168-day ERS-1 data on a 5-km grid) showed that the topography varied widely along the length of the shelf. Therefore, it was decided to generate the AIS-DEM using four overlapping transverse sections. It was assumed that the semivariogram for each section would yield a good representation of the true height variation within that section. The sections were numbered in order from North to South; therefore AIS1 corresponded to the front section of the Amery Ice Shelf and AIS4 to the transition zone with the Lambert Glacier. The size of each section is shown in Table 5.5 below, and their locations are indicated on the contour plot in Figure 5.13.

To ensure that data were from the ice shelf only, the floating ice shelf mask used for the tide correction (Chapter 3) was used to extract only the data lying within the mask. However, since the mask was created from the 10-km ERS Slopes Database (Appendix B), it is only an approximate indicator of the floating ice shelf extent, and there would be some regional discrepancy at the 1-km scale.

TABLE 5.5 *GRID DIMENSIONS (KM) FOR EACH SECTION OF THE AIS-DEM.*

Section	***Grid dimensions (km)***		***No of cells in overlap***
	X	***Y***	
AIS1	*185*	*192*	
AIS2	*212*	*171*	*32*
AIS3	*93*	*115*	*32*
AIS4	*144*	*85*	*42*

The sections AIS1 to AIS4 are shown in Figure 5.14.

Semivariograms for each of the four sections AIS1-AIS4 were computed using the GAMV2 program in GSLIB (Appendix C), and modelled using standard least-squares fitting routines. The computed semivariograms for each of the four sections are shown in Figure 5.10 (solid lines), together with their model fits (dashed lines).

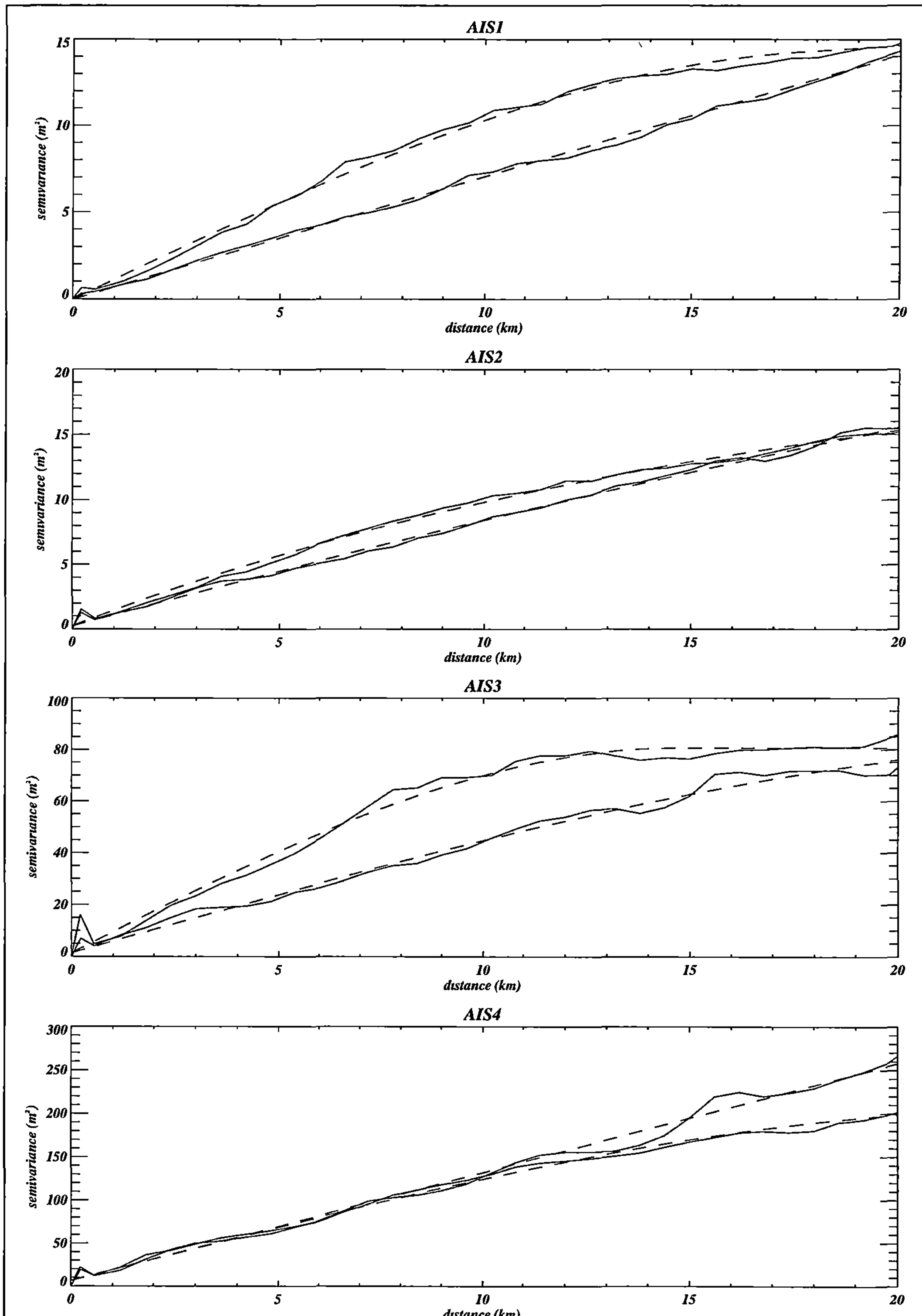

Figure 5.10 *Computed (solid line) and modelled (dashed line) semivariograms for the sections AIS1 to AIS4. The sections are numbered from North to South i.e. AIS1 is the front section of the Amery Ice Shelf and AIS4 is in the transition zone with the Lambert Glacier (see Figure 5.14 for locations).*

It can be seen that the semivariance of the data is greatest in section AIS4, which is to be expected since the data are noisier here due to the more variable topography.

The resulting semivariograms for each of the four sections were used in the KTB3D (kriging) program within the GSLIB software (see Appendix C). Each region was interpolated separately on a 1-km grid. Comparison of the surfaces in their overlapping regions provided an indication of the accuracy of the kriging technique. Three-dimensional plots of the height differences for the three overlapping regions are shown in Figure 5.11. The mean and RMS of the height differences at each grid node are written on each plot. It can be seen that, as expected, most of the discrepancies occur at the grid edges.

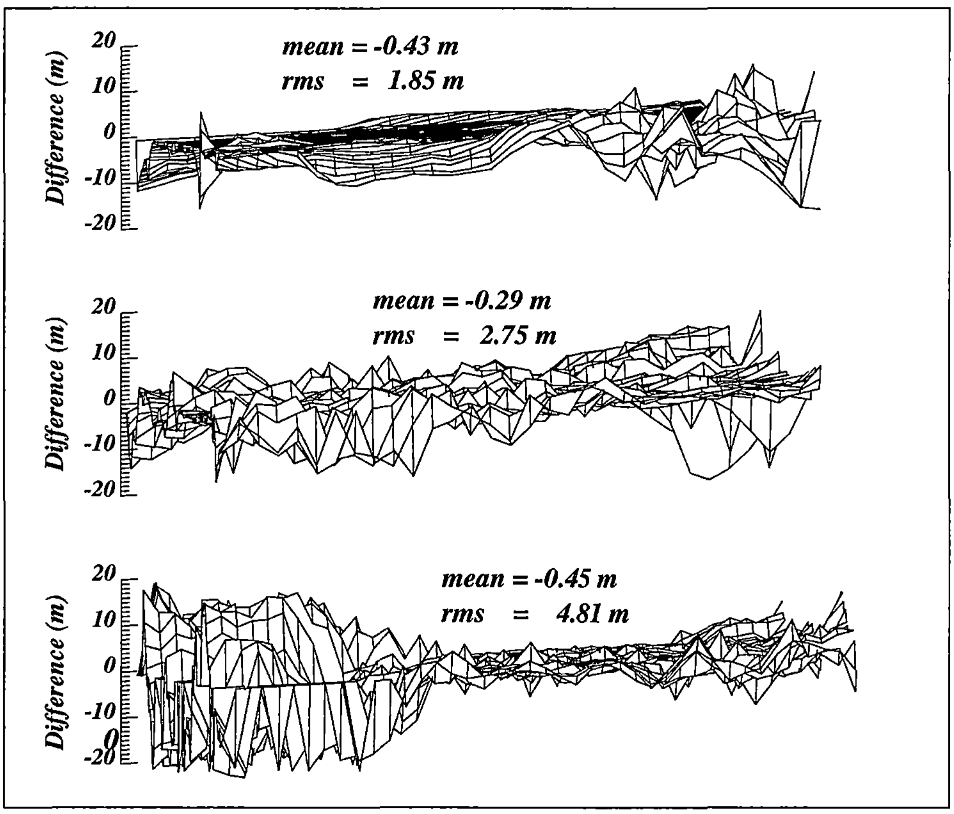

Figure 5.11 *Height differences between grids at each of the three overlapping portions between the four sections of the Amery Ice Shelf. Height differences are North minus South (i.e. AIS1 minus AIS2, etc.).*

The four sections (AIS1-AIS4) were combined to form the final AIS-DEM. So that the AIS-DEM was continuous across the three regions that contained overlapping sections, a distance-weighted averaging technique was used in these regions. In the overlaps, each cell was assigned a height equal to the distance-weighted average of the two heights from each contributing section. The x value of each cell was used to calculate the distance of that cell from the start of the overlap.

The distance-weighted averaging process is illustrated in Figure 5.12. Consider an overlap of three cells between two grids (MAP1 and MAP2). For any arbitrary cell within the overlap O(i, j), the distance-weighted average height value, h_{ij}, is:

$$h_{ij} = \frac{X - dx}{X} h_{MAP1} + \frac{dx}{X} h_{MAP2}$$

where h_{MAP1} is the height value of cell O(i, j) in MAP1

h_{MAP2} is the height value of cell O(i, j) in MAP2

dx is the number of cells in the X-direction between cell O(i,j) and the last non-overlapping cell of MAP1

X is the number of cells in the X-direction between the last non-overlapping cell of MAP1, and the first non-overlapping cell of MAP2.

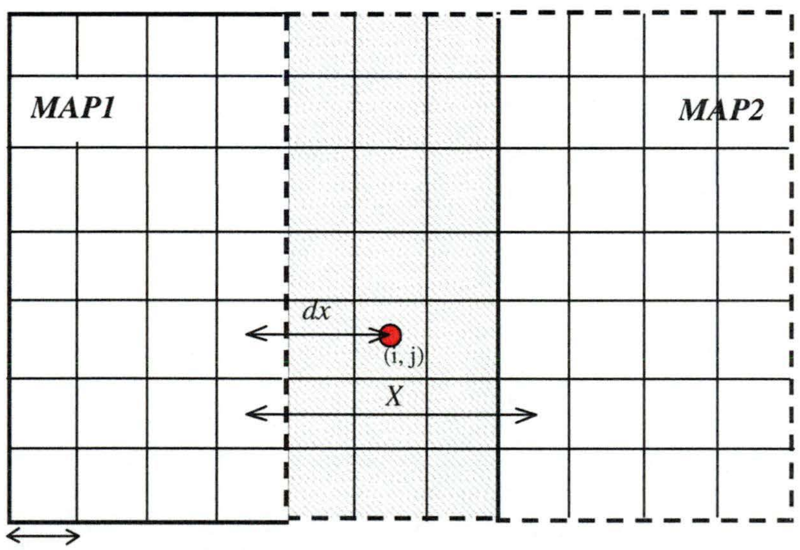

Figure 5.12 *Schematic diagram illustrating the distance-weighted average technique used to join the overlapping sections of the AIS-DEM. In this example, the overlap is three cells wide. In the overlap, the height value of any cell (i, j) is weighted according to its distance in the X-direction from the cell at the edge of the overlap.*

When $dx = 0$, MAP2 has no influence on the cell height (the cell is at one edge of the overlap) and when $dx = X$, MAP1 has no influence on the cell height (the cell height is at the other edge of the overlap). When $dx = \frac{X}{2}$ (the middle of the overlap) the cell value is the average of the values from each section.

The resulting AIS-DEM, created by merging the four independent segments, is shown in Figure 5.13 (perspective view) and Figure 5.14 (contour plot). In Figure 5.14, the locations of four AIS sections are indicated.

Discussion of AIS-DEM surface features

The shaded surface plot of the AIS-DEM (Figure 5.13) exhibits a high level of structural detail. Through comparison of this new DEM with the previous 3-km DEM available for the region (Herzfeld *et al.* 1993; Figure 2.6), it can be seen that there is a significant improvement in resolution, both horizontally and vertically. This is because the input Geosat data for the Herzfeld DEM only had a track spacing of ~30 km (around 10 grid cells of the AIS-DEM), so topographic features were poorly sampled. The distance between the ERS-1 tracks on the Amery track spacing is only about 2.5 km, providing improved sampling of topographic features.

A feature to note in the AIS-DEM is that a faint striated pattern is evident on the surface, corresponding in location with the individual altimeter tracks. This arises from a combination of the exactitude of the kriging technique, and the fact that the directions chosen for the semivariograms were along the altimeter tracks, and not along and perpendicular to the flowlines.

To see whether the semivariogram could be improved, in order to remove the striated pattern, a new semivariogram was calculated for AIS1 elevations approximately along and perpendicular to the flowlines (at angles 0° and 90°). The new semivariogram was isotropic. This is most likely because features of a similar wavelength occur both along (crevasse fields and rifts) and across (flowlines and surface depressions) the flow direction, so the elevations have a similar semivariance in both directions. Since the data sampling density is greatest along the descending/ascending directions, the best DEM is realised using those directions for the semivariogram.

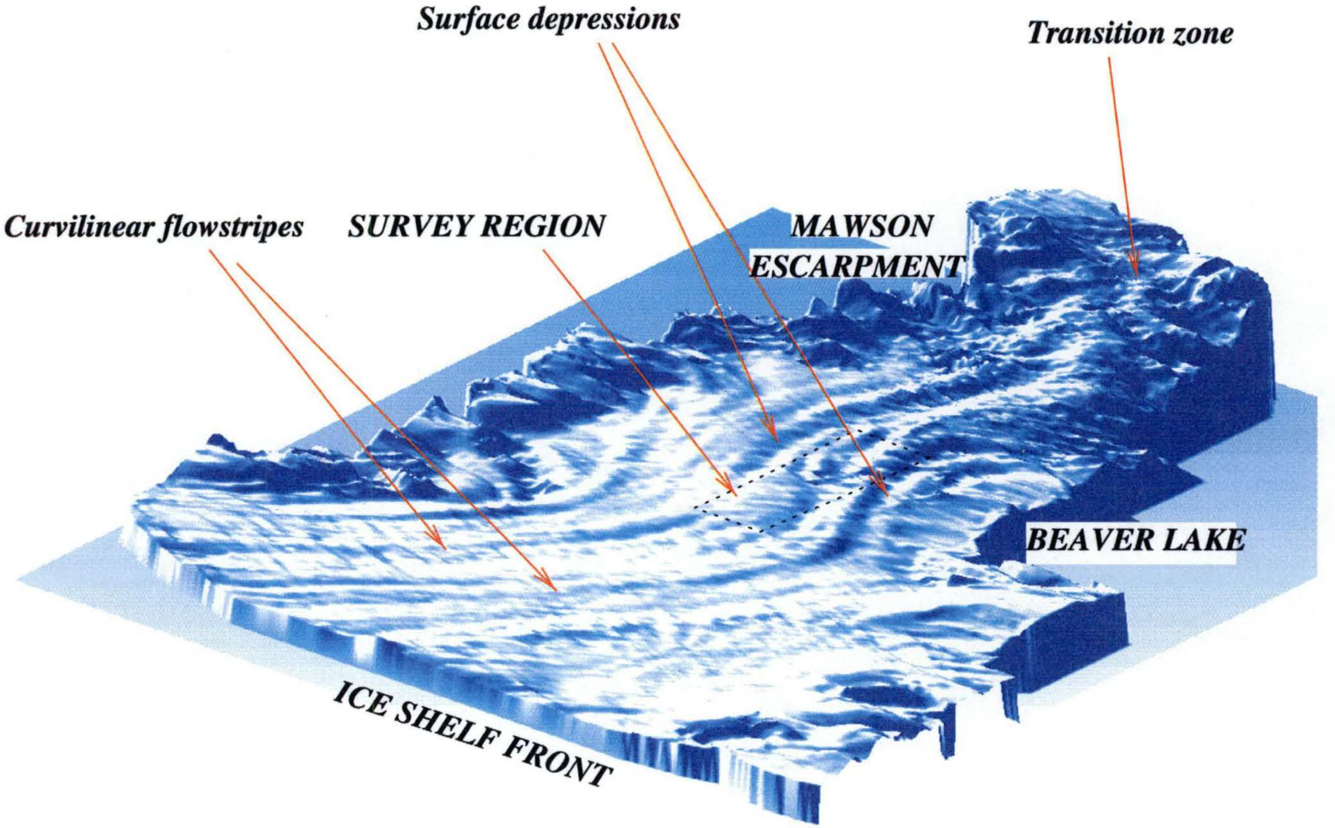

Figure 5.13*Perspective view of the AIS-DEM, generated on a 1-km grid using kriging. The main features are indicated, and are discussed in the main text.*

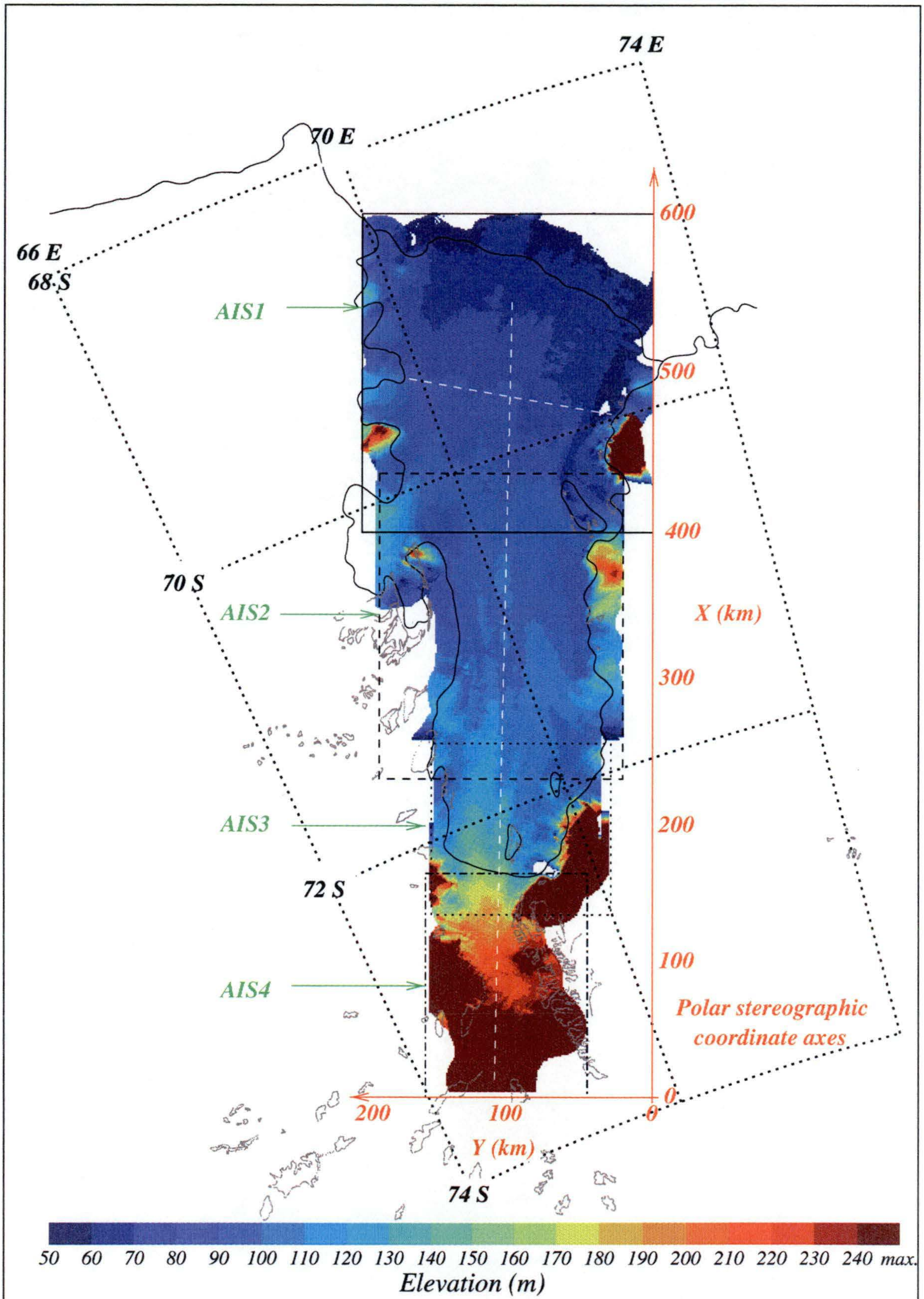

Figure 5.14 *Contour plot of the AIS-DEM, showing the four sections AIS1-4. The location of the surface profiles shown in Figure 5.15 are indicated as white dashed lines.*

To demonstrate the topographic variations parallel and perpendicular to the flowlines, surface elevations from the AIS-DEM were extracted along lines oriented approximately in these directions. The locations of these lines are shown in Figure 5.14.

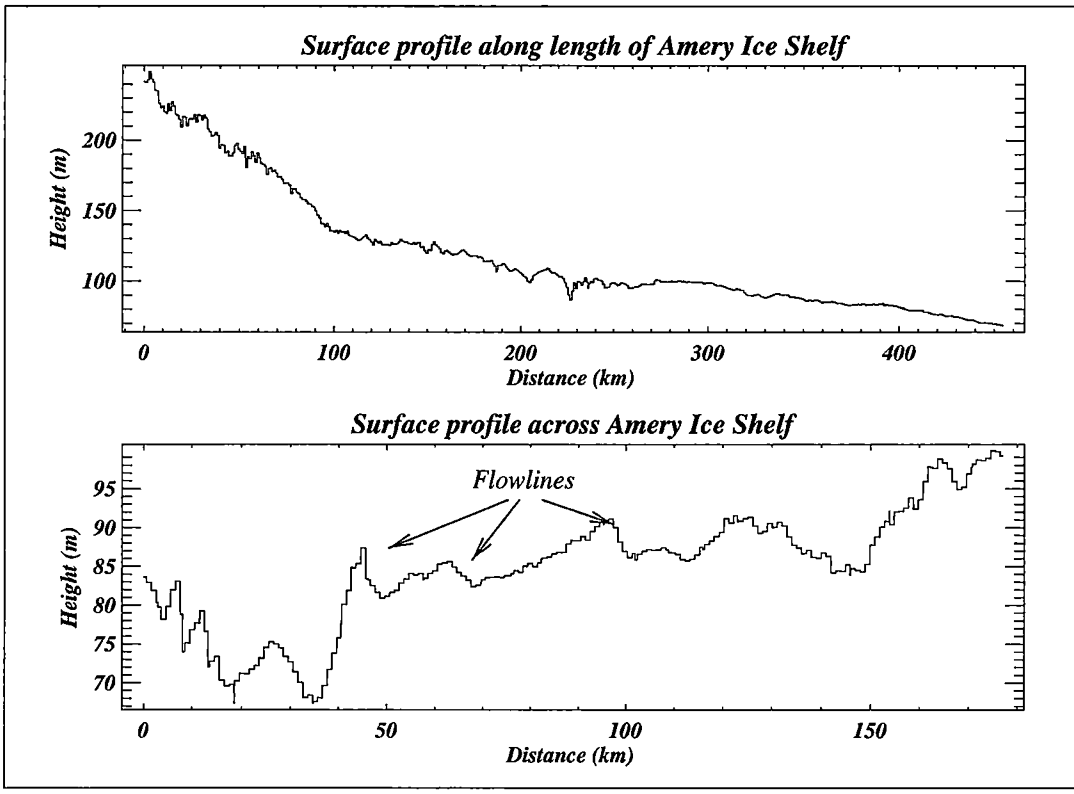

Figure 5.15 *Surface elevation profiles a) along the ice shelf from south to north b) across the ice shelf from east to west. The locations of these lines are shown on the contour plot in Figure 5.14.*

The main surface features seen in the surface presented in Figure 5.13 are discussed below:

Flowlines

Easily discernible are longitudinal (oriented approximately along the X-axis) linear features that are parallel to the broad scale ice flow direction, and are present across the entire surface of the ice shelf. These are the main flow features of the shelf, arising from the Lambert Glacier and other tributary glaciers such as the Charybdis Glacier. The mapping of ice shelf surface features, such as flowlines and meltstreams, provides insight into the structure of the ice shelf. For an ice shelf in steady state, the tangent at a point in a flowline coincides with the horizontal component of the velocity vector at the point. The features contain information about the flow regime of the Amery Ice Shelf and the ice streams that feed it. Longitudinal variations in these features characterise non-steady state flow and may contain information on historical variations of the flow (Bamber and Bindschadler 1997; Hambrey and Dowdeswell 1994).

Surface features have previously been mapped from satellite imagery on the Filchner, Ronne and Ross Ice Shelves (Crabtree and Doake 1980; Casassa and Brecher 1993). Flowline patterns observable in Landsat MSS data have been studied on the Amery Ice Shelf (Hambrey and Dowdeswell 1994; Figure 2.7). Large ice sheet features like flow lines, ice streams and crevasse patterns are more pronounced in certain wavelength bands due to photometric effects on the surface slopes: low sun elevation angles provide enhancement to subtle surface topographic features that would not otherwise be easily detected (Massom 1991). Visible wavelength remote sensing instruments respond to contrasts in surface properties between different flow bands as well as slope variations (Hambrey and Dowdeswell 1994), as do near infra-red instruments. However, mapping of surface features using imagery does not provide quantitative information of their structure. An elevation profile approximately across the flowlines towards the ice shelf front is shown in Figure 5.15b. Elevation maxima occur in the middle of flow bands corresponding to distinct ice streams. These peaks are parallel to each other along the ice shelf, which is why these features are so prominent in the DEM.

Grounding zone

The region corresponding to AIS4, in the south of the AIS-DEM is the transition region of the Lambert Glacier Amery Ice Shelf system, or the grounding zone. This region has a much greater surface slope than the remainder of the ice shelf. Blue ice and variable surface topography result in noisier altimeter data and the surface appears rougher. The abrupt change in slope seen in Landsat imagery and documented by Hambrey and Dowdeswell (1994) is also seen here.

Surface depressions and flat regions

In the middle section of the ice shelf, in the vicinity of the survey region, distinct surface depressions are revealed in the AIS-DEM, which are known to carry surface water during periods of melting (Phillips 1998; Chapter 8). Other features revealed in the DEM are regions where the ice shelf surface slopes are very small and the topography is very flat (eastern section, front section). Here the accuracy of the altimeter data is at its highest, therefore these features are real.

Qualitative comparison of AIS-DEM with AVHRR image

Figure 5.16 presents an AVHRR cumulated image of the Amery Ice Shelf created and supplied by Ted Scambos of the NSIDC. This image is generated from six individual AVHRR images using data cumulation (Scambos *et al.* 1998). The AVHRR images were acquired at the High Resolution Picture Transmission (HRPT) facility at Casey station between 30 January and 7 March 1996. This is less than a year after the end of the ERS-1 geodetic mission, from which the AIS-DEM is derived. The acquisition times for each image are between 09:14 and 10:00 GMT. The pixel size of the resulting image is 200 m, and the estimated spatial resolution is 750 m. The image is on a polar stereographic projection on the WGS-84 ellipsoid, with a coarse terrain correction applied using USGS 5' global DEM (ETOP05) (Ted Scambos, personal communication 1998). The sun azimuth varies between 318.05 and 330.42°, while the elevation angle varies from 21.26 to 34.7°.

To directly compare the structure in the altimeter DEM with the AVHRR image, an 'image' view of the Amery Ice Shelf DEM was created (Figure 5.17). This was achieved by plotting the surface with the look-angle directly above, and the illumination angle similar to the mean illumination angle of the six AVHRR images. Looking at the AVHRR image and the AIS-DEM 'image' simultaneously, it can be seen that similar surface features are discernible in each image.

The most obvious features in each image are the flowlines themselves. The flowline pattern is similar in each image. There is a distinct flow divide that separates the ice from the Charybdis Glacier and that from the North Prince Charles Mountains (flow bands 2 and 3 in Figure 2.7). This occurs because the ice originating in the Charybdis Glacier is moving slower than the ice in the adjacent flow sector, which has been inferred from GPS measurements (Allison 1991). The flow divide (shear margin) is characterised by rifts aligned perpendicular to the flow direction and contained within a narrow band. This type of structure has been referred to as 'ladder-like' (Merry and Whillans 1993).

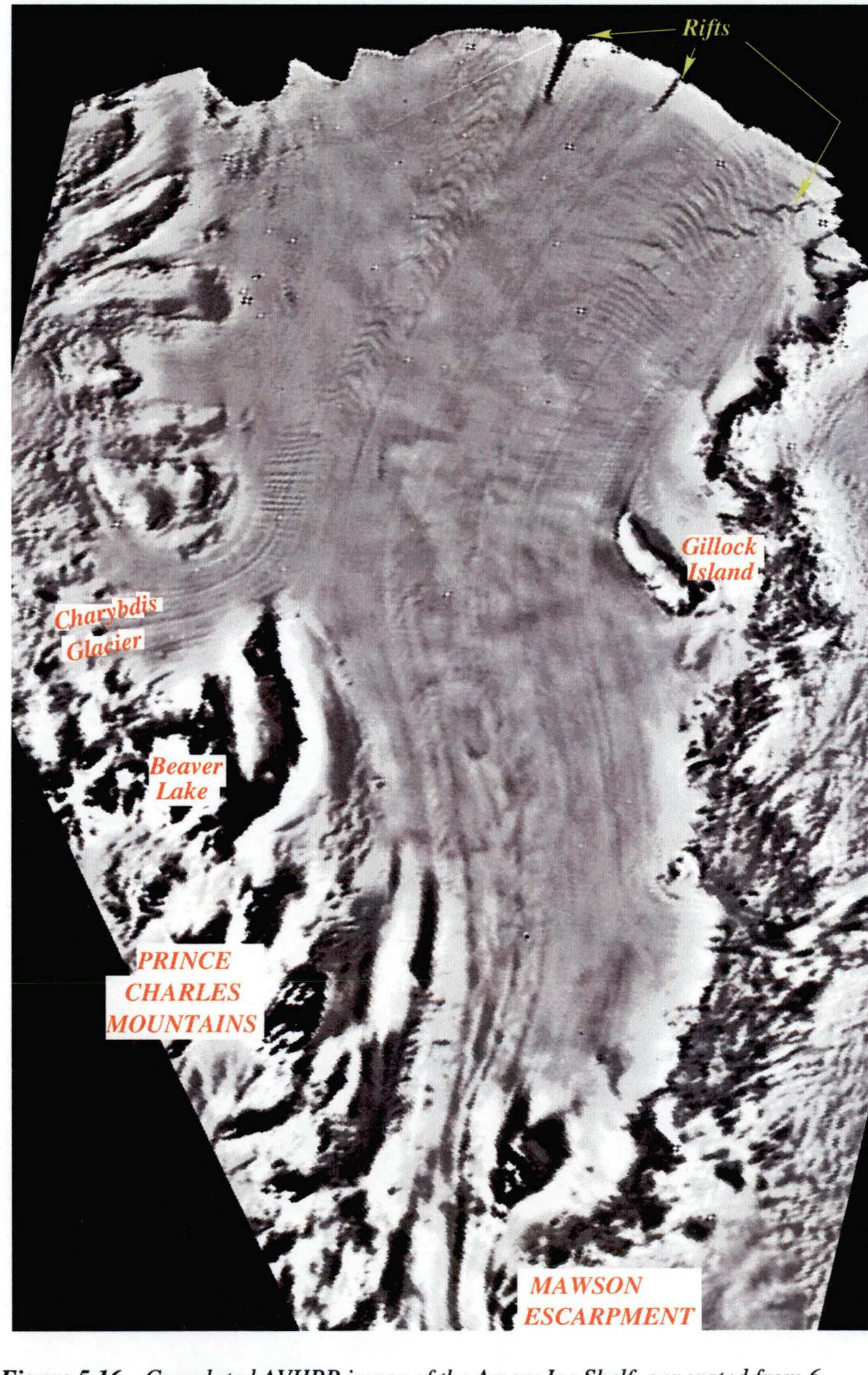

Figure 5.16 *Cumulated AVHRR image of the Amery Ice Shelf, generated from 6 scenes collected between 30 January and 7 March 1996 at Casey station. Image provided by Ted Scambos of the NSIDC, Colarado.*

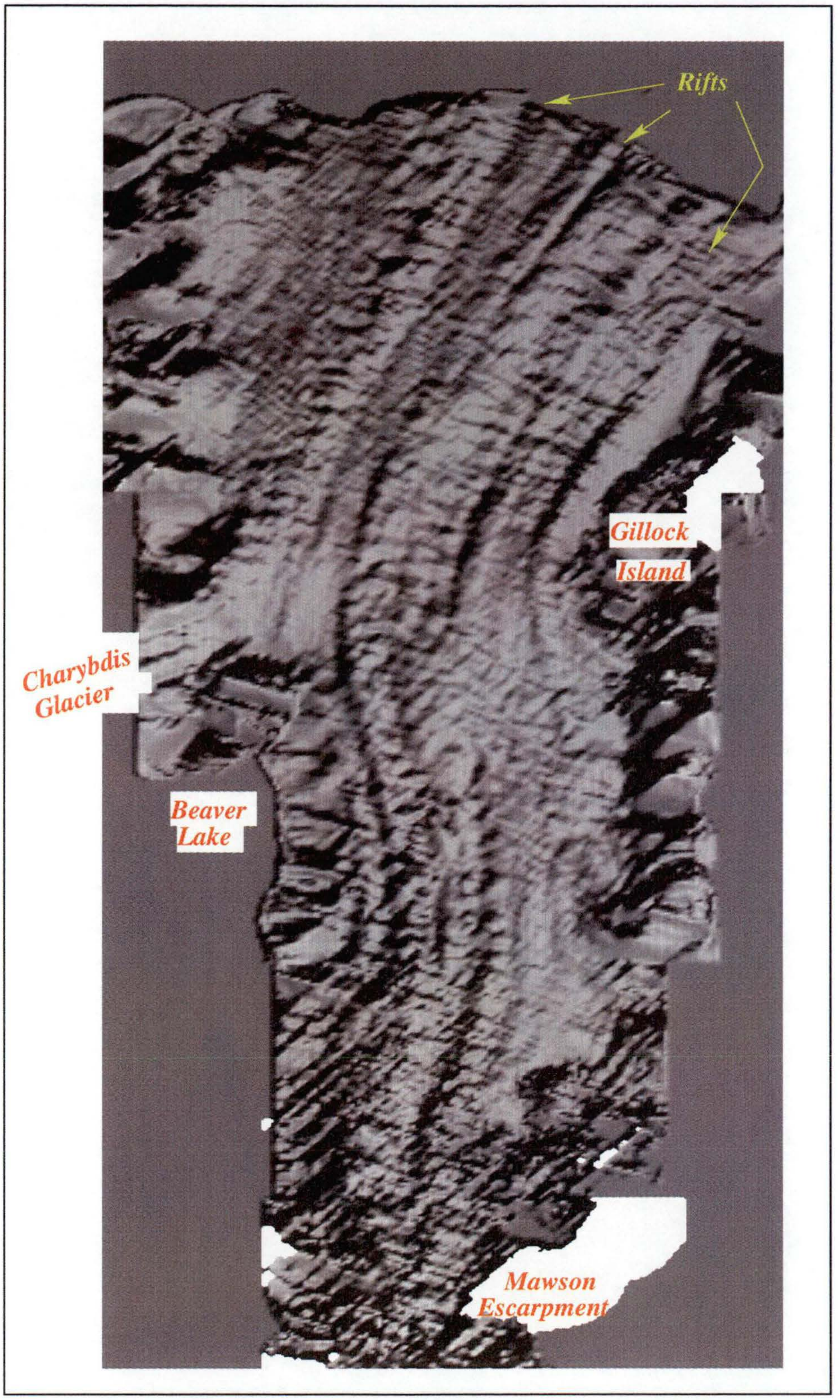

Figure 5.17 *Plan view of the AIS-DEM. The position of the light source has been chosen such that it represents the mean of the angles of illumination in the six AVHRR scenes that make up Figure 5.16.*

There are two distinct lines, approximately 20 km and 15 km long respectively, at the ice front, parallel to the flow in the middle of the ice shelf front. These features have formed where three distinct flow bands have separated due to divergence of the flow, leaving longitudinal rifts. There are further rifts at the eastern edge of the ice front, where there are also crevasse bands. These rifts indicate possible calving lines, along which icebergs may calve in the future.

5.3.2 Lambert Glacier Basin DEM (5 km)

A second DEM was generated from the ERS-1 data, on a 5-km grid over the entire Lambert Glacier drainage basin. To compare DEM production techniques, a small test region was chosen, which lay within the limits 71 to 72°S latitude and 76 to 81°E longitude. This region lies on the eastern side of the Lambert Amery system. Using the same technique described for the survey region, and for the four sections of the AIS-DEM, an anisotropic semivariogram was calculated over the test region and a surface generated for the region on a 5-km grid using kriging. The resulting surface is illustrated in Figure 5.18a. Figure 5.18b illustrates a second surface over the test region derived using a simple averaging technique. The value at each grid cell centre is the mean value of all the geodetic phase ERS heights that lie within that 5-km cell. It can be seen that, apart from at the edges the surfaces are very similar. The mean and RMS of the height differences at each grid node are 3.77 ± 11.2 m (kriging minus averaging), which includes some of the edge effects from the kriging (seen in Figure 5.18a). This provides a justification for using the simpler averaging method over the kriging technique. The advantage of the averaging method is that it is fast to implement computationally, whilst the kriging method is computationally intense. To grid the entire Lambert Amery system using kriging would require dividing the region into many different segments of similar topographic characteristics, and would take substantial computing time, which for generating a 5-km broad scale topographic map, is not warranted. Given that the chosen size of the grid cells is twice that of the track spacing, no extra structural detail is provided using the kriging technique. This is not true at finer resolutions and averaging would clearly not have been suitable for the 1-km Amery Ice Shelf DEM.

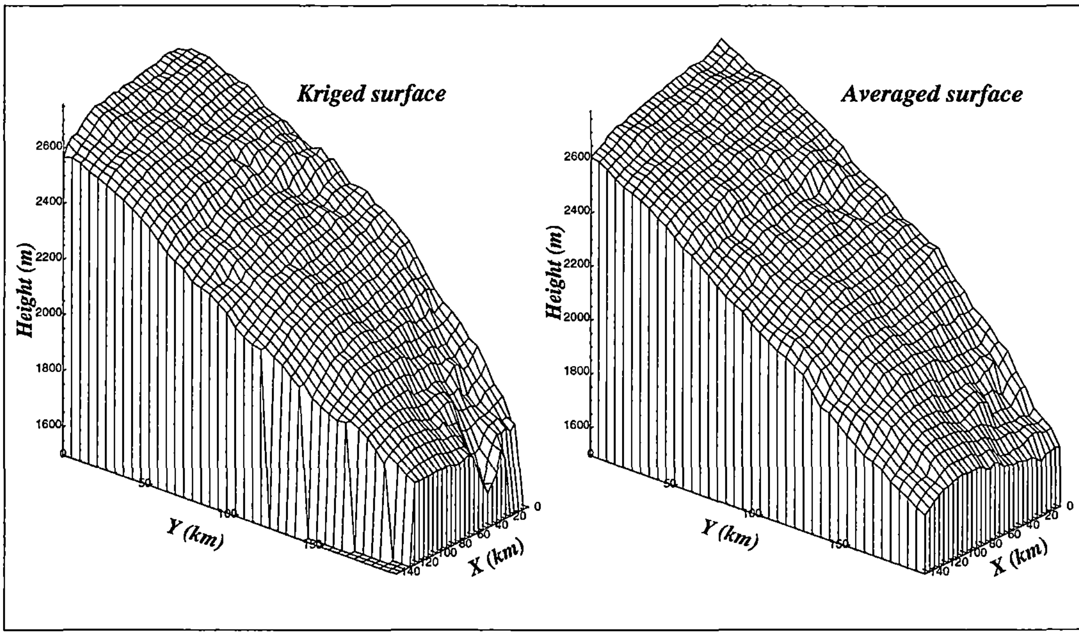

Figure 5.18 *Surface plots of a 160 x 140 km region on the eastern side of the Lambert Amery sytem, generated from ERS altimeter data on a 5-km grid using a) kriging with anisotropic semivariogram b) averaging all data points in a cell.*

The Lambert Glacier DEM was therefore generated using a simple averaging technique. Each 5-km cell of the LAS-DEM was assigned a mean height value, calculated from all of the height lying in that cell. The variance and the number of observations were also recorded (see Figure 5.20). Figure 5.19 is a shaded surface plot of the LAS-DEM, oriented to look up the Amery Ice Shelf and Lambert Glacier. A contour plot of the LAS-DEM is shown in Figure 5.20.

The top plot of Figure 5.21 illustrates the variance of the height measurements that make up the average height value for each cell of the LAS-DEM. As expected, the greatest variances occur in regions of greater slope variability (compare with the Slopes Database shown in Appendix B). In regions where the variances are small, slopes are generally very small, and this occurs on the ice shelf and on the plateau. The density of altimeter points per cell (after filtering) is illustrated in the bottom plot of Figure 5.21. Note that there are no data around the perimeter of the Amery Ice Shelf, nor over mountainous regions and rock outcrops, or along coastal margins with large slopes. Comparison of this plot with that in Figure 5.2 shows that most of the data from these null data regions have been filtered out, due to poor altimeter tracking.

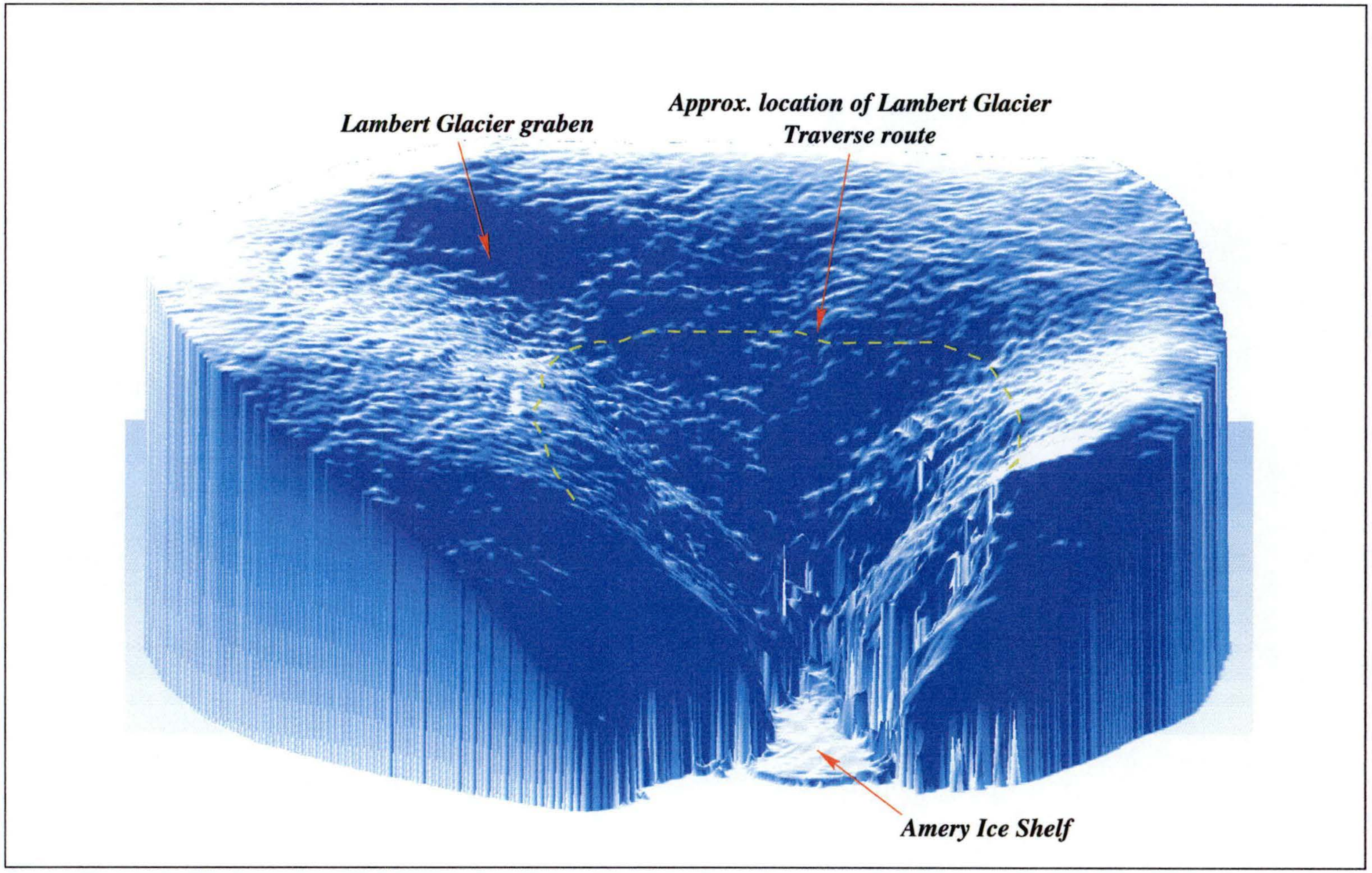

Figure 5.19 *Shaded surface representation of the LAS-DEM. The vertical lines at the coast and near the ice shelf edge are a result of no altimeter data here (value set to zero) Some of the flowlines of the Amery Ice Shelf are discernible even at this resolution. The approximate location of the Lambert Glacier traverse route is indicated.*

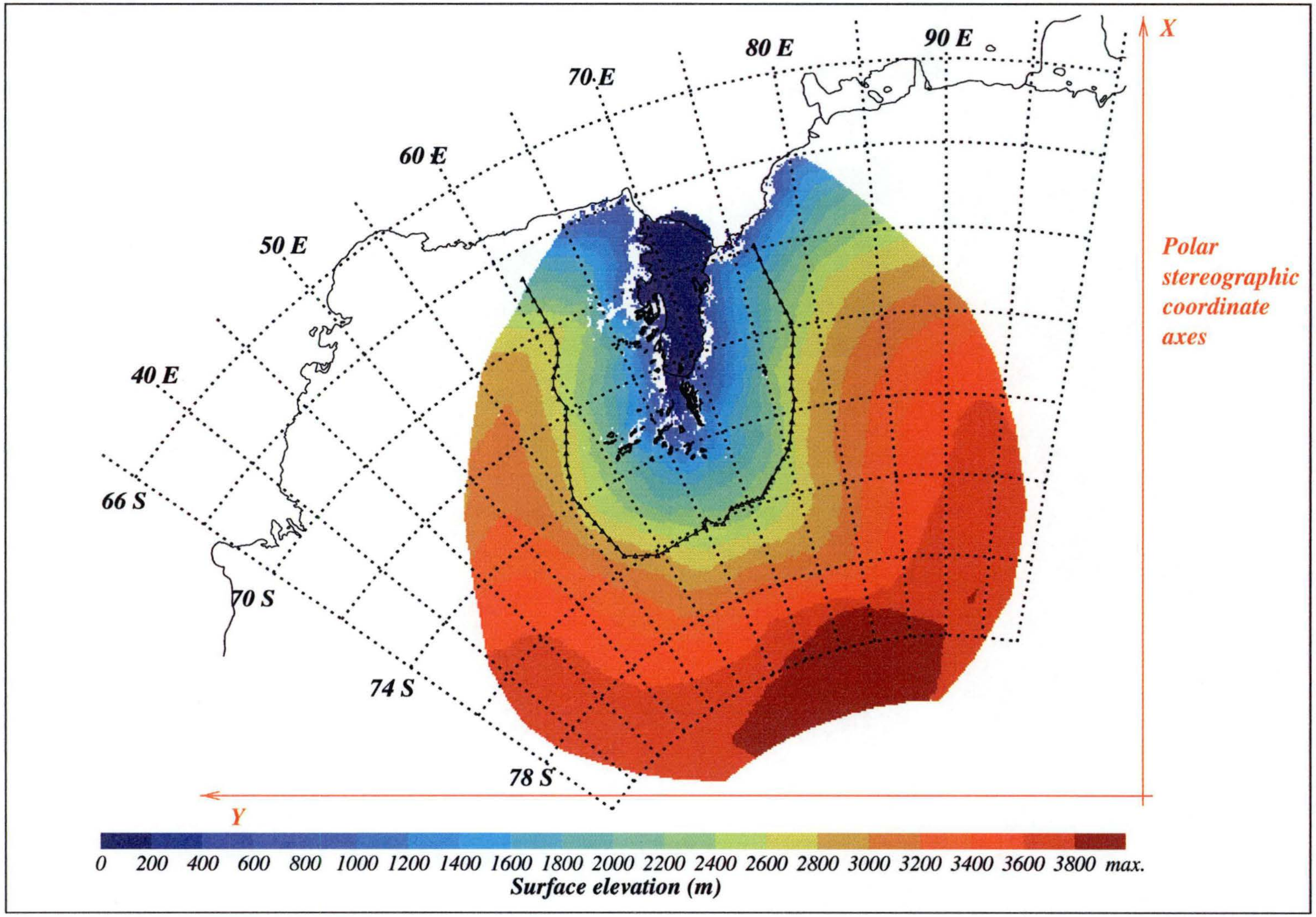

Figure 5.20 *Colour contour plot of the LAS-DEM, generated on a 5-km grid using averaging. Also shown are the axes of the polar stereographic projection used throughout this thesis, and the locations of the LGB traverse stations.*

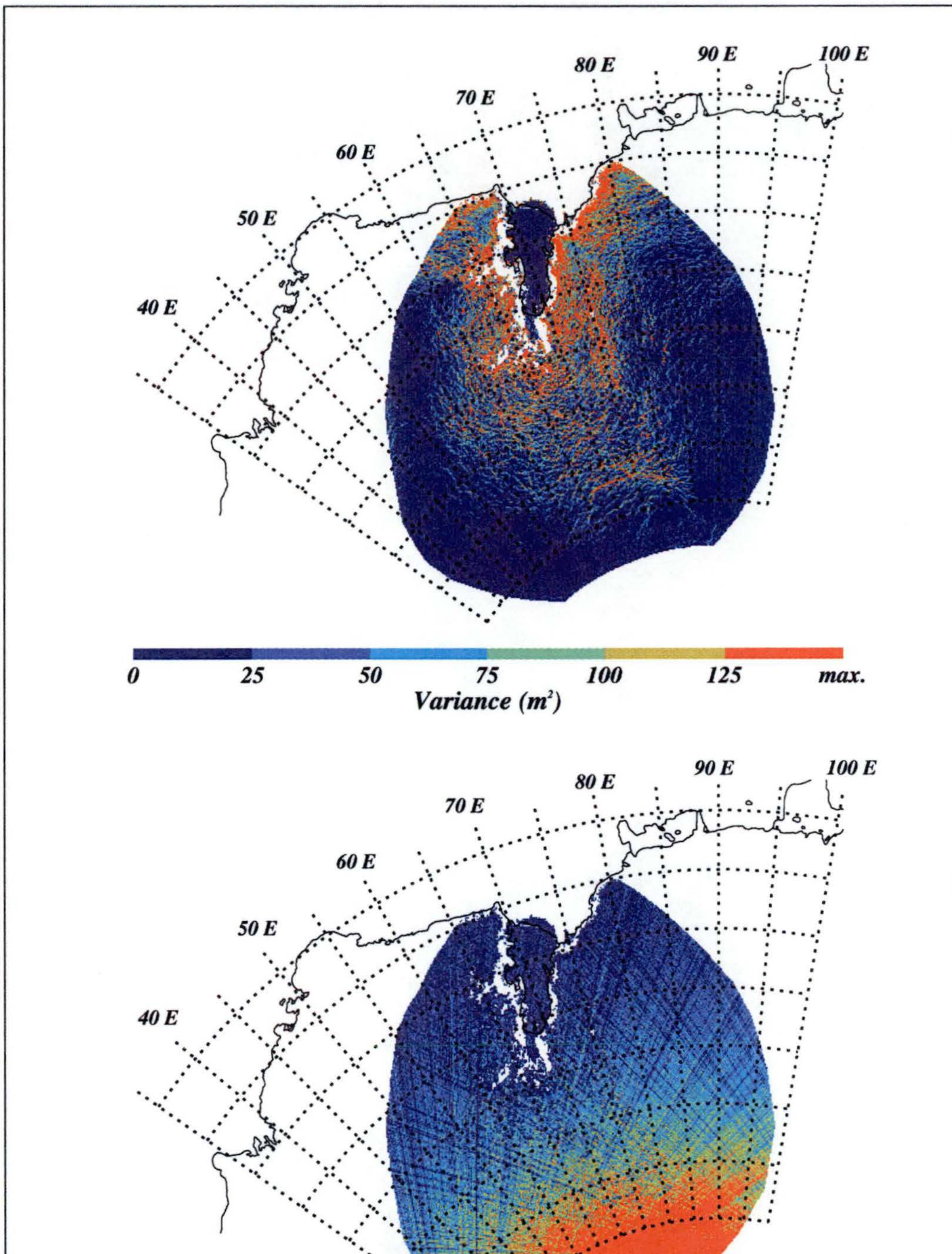

Figure 5.21 *Spatial distribution of the variance (top plot) and the number (bottom plot) of ERS height measurements within each 5-km grid cell of the LAS-DEM*

Discussion of LAS-DEM

The shaded surface representation of the LAS-DEM reveals a great deal of surface detail. The delineation of the basin can be clearly seen from the location of the ridges. The relatively steep slopes of the Lambert graben (observed in RES measurements during the LGB traverse) can also be seen. The approximate location of the Lambert Glacier Traverse is shown.

The vertical lines around the periphery of the ice shelf and the coast are an artefact corresponding to cells with no data (compare with Figure 5.2) where the height values have been set to zero.

Comparison of DEM with Lambert Glacier traverse GPS data

Further height validation for the ERS altimeters in the Lambert-Amery system is provided by the GPS data collected at sites along the Lambert Glacier Traverse (Chapter 2). Static GPS data from the 1994-95 Lambert Glacier Traverse have recently been re-computed within the GAMIT software (Manson *et al.* 1998). These elevations are from approximately the same epoch as the ERS-1 heights, and they are relative to the WGS-84 ellipsoid, i.e., the same reference frame as the ERS heights. Although these heights were only spot heights and therefore not directly comparable with the altimeter heights, the difference between the interpolated height values from the DEM and the GPS height value at each LGB site, provides an indication of the accuracy of the DEM. There were 73 stations along the Lambert Glacier traverse route (see Figure 2.5). Using their WGS-84 positions, the corresponding elevation of the LAS-DEM for each station was determined using bilinear interpolation.

Figure 5.22a illustrates the variation in height along the traverse at each of the stations. The red line is the height profile interpolated from the LAS-DEM, and the blue line is the height profile from the GPS positions. Good agreement can be seen between the LAS-DEM heights and the Lambert Traverse GPS height. Figure 5.22b illustrates the differences in height along the traverse, with error bars corresponding to the standard deviation of the ERS-1 height measurements contributing to the average height of each 5-km cell. These differences have a mean of 17.3 m and an RMS of 20.3 m.

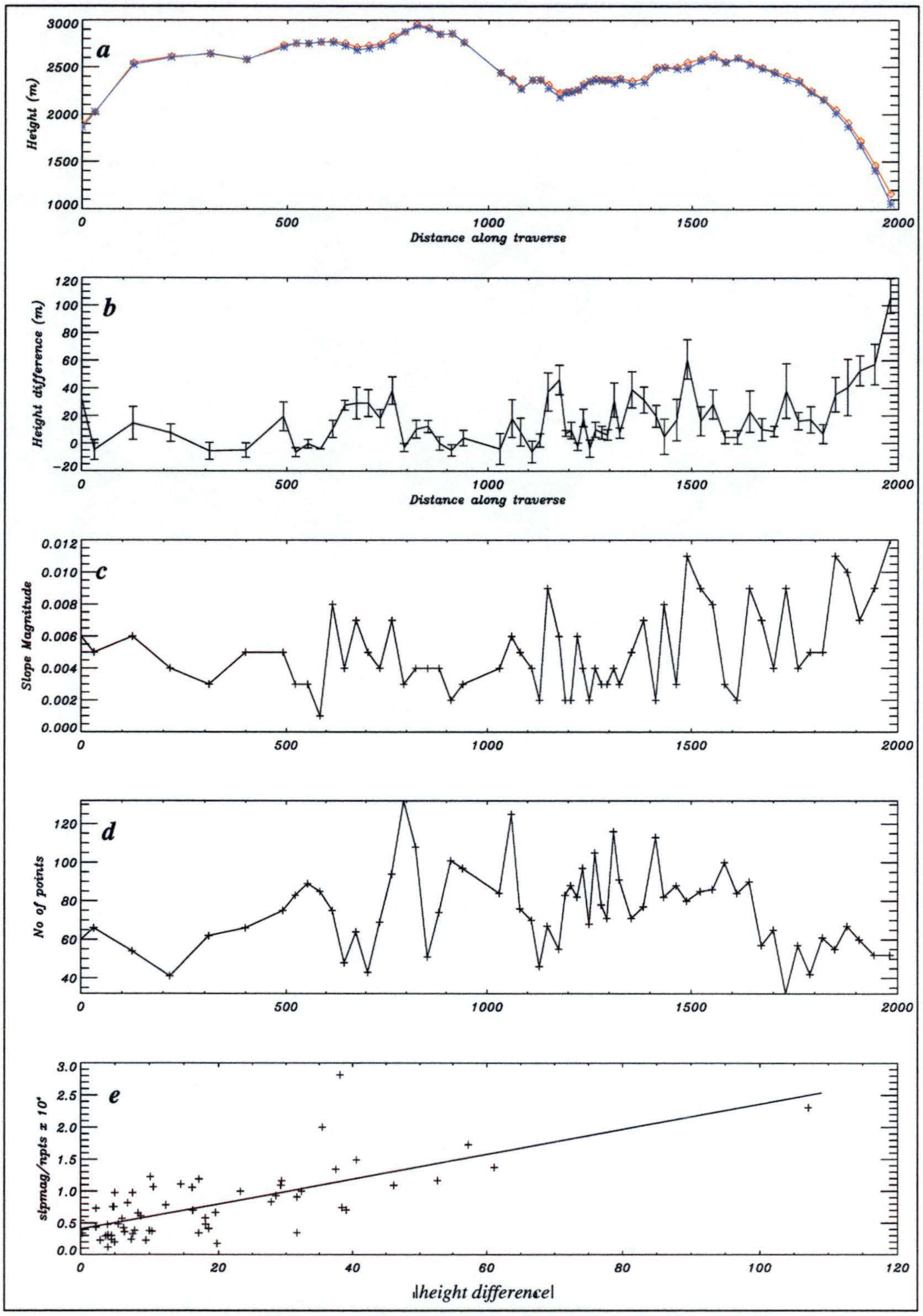

Figure 5.22 *a) Comparison of interpolated elevations from LAS-DEM (red) with GPS elevations (blue) along the Lambert Glacier traverse*
b) height differences (ERS - GPS)
c) Slope magnitude for LAS-DEM cell
d) Number of points per LAS-DEM cell
e) Slope magnitude divided by number of cells vs |height difference|.

The observed height differences can be explained by looking at the slope magnitude of each cell and the number of points per cell. Figures 5.22c and d illustrate the variation in these parameters around the Lambert Glacier Traverse route. The relationship between slope magnitude, number of points per cell and the absolute value of the height difference is shown in Figure 5.22e. The quantity (slope magnitude/number of points) appears correlated with the height difference, suggesting that the main sources of discrepancy are topography variations and poorer altimeter sampling of the surface.

5.4 Chapter conclusions

This chapter aimed to verify ERS satellite altimeter-derived heights with those collected on the ground using GPS surveying, and to generate DEM's for the Lambert – Amery system. Comparison of ERS heights from the Amery Ice Shelf GPS survey region with GPS heights collected during the Amery Ice Shelf survey (October - November 1995), showed that the ERS altimeters reproduced the surface topography of the ice shelf. In the surveyed region, height values closely matched those obtained through GPS techniques, especially where the surface topography was smooth. Using the 25% threshold in the OCOG algorithm, the mean and RMS height difference at the intersecting points of the ERS-1 geodetic phase tracks with the GPS survey is 0.0 m and 1.7 m, respectively. The spatial distribution of the height differences is highly correlated with the topographic variations evident in an interpolated surface generated from the GPS data.

The total combined RMS error remaining in the altimeter height measurements after merging in the precise orbits, correcting for propagation delays, tidal motion and tracking error is at most 0.13 m. When considering the GPS closure error of 0.4 m, this does not fully account for the RMS height differences obtained. The only remaining sources of discrepancy are biases arising from terrain effects and, to a lesser extent, surface-layer penetration. An *a priori* knowledge of the surface topography would be required to extract more accurate height information from satellite altimetry over ice regions. The GPS survey provided an accurate ground-truthing reference surface for the ERS altimeters due to the large survey area and the high precision of the GPS coordinates.

Using the validated ERS data, a high-resolution (1-km) DEM was made of the ice shelf using kriging (AIS-DEM) and a lower resolution (5 km), DEM made for the entire Lambert Amery system using averaging (LAS-DEM). Structural features were well represented in the AIS-DEM that have previously only been observed in visible or near infra-red satellite imagery. This has provided quantitative information on the nature of such features on the Amery Ice Shelf.

The 5-km LAS-DEM contained less detail due to its lower resolution and the averaging technique used in its generation, but nevertheless provided an extensive surface topographic map of the Lambert Glacier Basin. The map contains a great deal of information that can be used for modelling studies and will contribute significantly to mass balance studies of the region (see Chapter 7).

The results of this chapter have confirmed that the ERS-1 altimeter has provided unprecedented information on surface topography of the ice-covered regions of Antarctica, and in particular the Lambert Glacier-Amery Ice Shelf region. Not only are the maps constructed from data that are extremely dense, but they are also known to be highly accurate over the ice shelf and around the traverse route. This type of information is essential for gaining knowledge of the mass budget and dynamics of the system, and for monitoring its behaviour in the long-term in a possible response to any climatic changes.

In Chapters 6 and 7, two very different glaciological applications are presented of such satellite altimeter DEMs. In Chapter 6, the 1-km AIS-DEM is used in hydrostatic calculations, along with ice thickness information, to locate regions of grounding and varying ice densities, which is important not only for mass balance/dynamic studies but also for sub-ice shelf circulation studies (basal melting/refreezing). In Chapter 7, the 5-km LAS-DEM is used in balance flux calculations, along with accumulation information, to estimate the state of balance of the system, through comparison with observations made along the Lambert Glacier traverse route.

Chapter 6 Applications of the Amery Ice Shelf Digital Elevation Model

6.1 Introduction

In Chapter 5, the construction of a high resolution, accurate DEM for the Amery Ice Shelf region (AIS-DEM) was discussed. The AIS-DEM contained unprecedented detail, yielding quantitative information about the structure of the Amery Ice Shelf and locating many surface features previously observed only in satellite imagery, such as flowlines and meltstreams. The AIS-DEM not only provides an accurate height reference surface against which to monitor any future elevation change on the shelf, but also can be utilised immediately to provide further insight into the structure of the ice shelf.

This chapter describes the application of the AIS-DEM, in combination with ice thickness data to obtain information on two parameters of the Amery Ice Shelf that are susceptible to change under an altered climate. The first is the location of the grounding zone, and the second is the amount of melt and freezing that occurs under the shelf.

6.2. Climate-sensitive parameters of the Amery Ice Shelf

Two parameters of the Amery Ice Shelf that are sensitive to climate are:

i) the location of the grounding zone; and

ii) the amount of melting and freezing at the ice shelf base.

The first part of this section discusses previous studies of the grounding zone. The second part of the section describes the mechanism behind the melt and freezing processes. It also discusses ways in which the amounts of melting and freezing have been estimated in the past.

6.2.1 The grounding zone

The location of the grounding zone of the Lambert Glacier-Amery Ice Shelf system has been a subject of recent uncertainty (see Chapters 2 and 4). As discussed in Chapter 2, Hambrey and Dowdeswell (1994) proposed that, from features seen in satellite imagery, there were regions of the system close to Cumpston Massif (~73°S) where the ice appeared to be still floating. This region is approximately 200 km south of the location previously reported by Budd *et al.* 1982 (71.2°S). In Chapter 4, static GPS results from the 1995 Amery Ice Shelf GPS survey were presented, which implied that the ice shelf is influenced by tides as far south as 71.2°S, 11 km further south than the location of the grounding line proposed by Budd *et al.* (1982). More recently, the presence of a tidal signal in static GPS measurements made further south in the 1997-98 season has confirmed that the ice shelf is floating at 72.5°S (Andrew Ruddell, personal communication, 1998).

6.2.2 Basal melting and freezing

The oceanography underneath an ice shelf is unique, since the ocean water contained in the sub-ice shelf cavity is insulated from the atmosphere, yet connected with the water on the continental shelf by a thermohaline circulation system (Williams *et al.* 1998a; Figure 6.1). This circulation system causes melting and freezing at the ice shelf base (Jacobs *et al.* 1992; Jenkins and Bombosch 1995).

The thermohaline circulation system under an ice shelf is initiated by the formation of high salinity shelf water (HSSW) resulting from the rejection of brine during the growth of sea-ice on the ocean surface off the front of the ice shelf during winter (Jenkins and Bombosch 1995). This relatively high density water sinks to the bottom of the water column, and follows the backward slope of the continental shelf, eventually penetrating under the ice shelf. HSSW comes into contact with the base of the ice shelf deep in the sub-ice shelf cavity. The HSSW is able to melt the basal layers as its freezing point is depressed, due to increased pressure (Jenkins and Bombosch 1995). This melt forms cold, fresh, low density ice shelf water (ISW) which migrates towards the ice front, rising along the inclined base of the ice shelf. As the ISW rises, the freezing point depression decreases. At a critical depth, the ISW becomes supercooled (i.e. the temperature of the ISW is less than the freezing point temperature), and it refreezes onto the base of the ice shelf (Jenkins and Bombosch 1995).

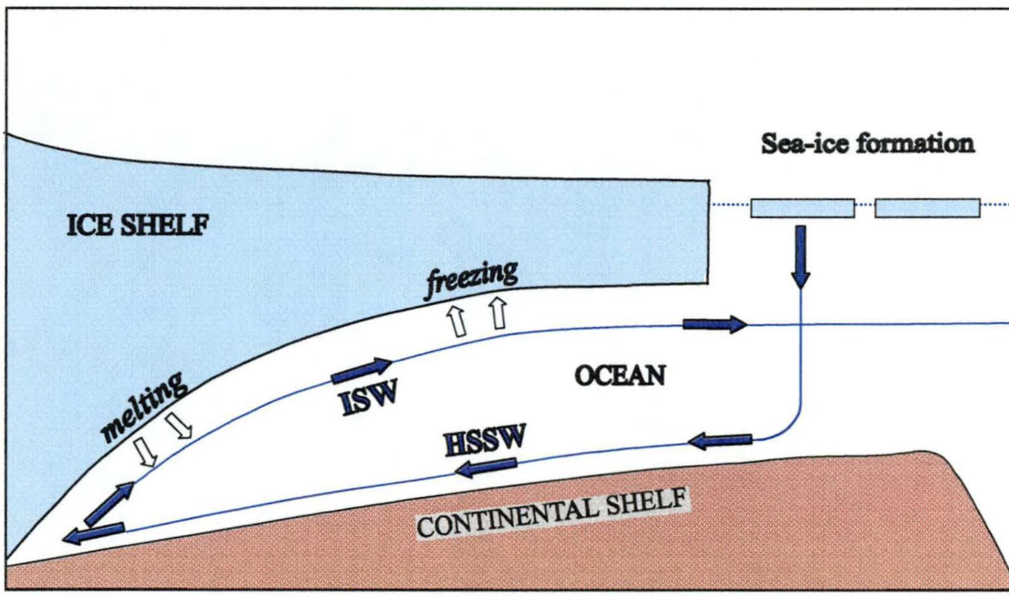

Figure 6.1 *Schematic diagram of the thermohaline ocean circulation in the deep cavity below an ice shelf. Winter production of sea-ice in front of the ice shelf leads to the formation of dense High Salinity Shelf Water (HSSW) which drops to the ocean floor. The HSSW penetrates the sub-ice shelf cavity, where depression of the freezing point enables it to cause melting at the base of the ice shelf near the grounding line, forming Ice Shelf Water (ISW). The ISW rises along the gradient of the ice shelf base until it becomes supercooled, when it freezes on the base of the shelf. Adapted from Jacobs et al. (1992) and Jenkins and Bombosch (1995).*

Basal melting and freezing processes redistribute ice under the ice shelf, and therefore affect the dynamics of the shelf. The amounts of melting and freezing make a significant contribution to the ice shelf mass budget (Jacobs *et al.* 1996). The total amount of ice melted and accreted at the base of the ice shelf is intimately linked with ocean temperatures. Warming of the oceans, or change in ocean circulation near Antarctica, could lead to shifts in the distribution of basal melting and refreezing (Nicholls 1997; Williams *et al.* 1998b). Another factor affecting the redistribution is the vertical mixing of the water column by tide action, which brings the warmer HSSW water at the bottom of the water column into contact with the ice (MacAyeal 1984). The spatial distribution of marine ice accretion under an ice shelf could be a sensitive indicator of climatic conditions.

A spot value of 158 m for the thickness of the marine ice layer under the Amery Ice Shelf has been inferred from bore-hole measurements at G1, located towards the ice shelf front (Morgan 1972; Chapter 2). Using this result and mass flux calculations, Budd *et al.* (1982) proposed the existence of a basal marine ice layer over the entire length of the shelf, along the flowline through G1. To determine what conditions could lead to this amount of accretion, Hellmer and Jacobs (1992) applied a two-dimensional thermohaline circulation model to the sub-ice cavity under the Amery Ice Shelf. They used the sub-ice cavity shape and ice composition derived by Budd *et al.* (1982) (Figure 2.4) as an input to their model, and varied the cavity shape in an attempt to match the amount of accretion observed at G1. None of their model simulations could reproduce this amount; a maximum of 10 m being obtained from a channel flow simulation. Hellmer and Jacobs (1992) concluded that the G1 core may have been taken from a location where a basal crevasse had filled with marine ice, and pointed out the need for additional direct measurements under and in front of the ice shelf.

6.3 Contribution of the AIS-DEM to knowledge of ice shelf parameters

The ERS-1 altimeter data used to construct the AIS-DEM was extracted to encompass all of the ice in the Lambert-Amery system that was thought to be floating. This was done so that the AIS-DEM could be used to further investigate the extent of the floating ice, by combining the elevation information with ice thickness information and a simple density model, through hydrostatic calculations.

This first half of this section describes the relationship between surface elevation and ice thickness for a body that is in hydrostatic equilibrium (hydrostatic calculations) and its significance in ice shelf studies. Where the ice is floating, the ratio of its surface elevation to its thickness depends on the column-averaged densities of the ice and water. It follows that if the surface elevation, ice thickness and density at a point on an ice mass are known, the hydrostatic relation can be used to determine whether the ice mass is floating at that point. The second half of this section describes the ice thickness dataset for the Amery Ice Shelf that was used in this project.

6.3.1 Hydrostatic equations

The relationship between the surface elevation of a floating ice shelf and its thickness is derived from Archimedes' Principle, which states that any body immersed in a fluid experiences an upthrust force whose magnitude is equal to the weight of fluid displaced (Kinsky 1992). In the case of a floating body, there is no resultant force and the upthrust force is equal to the weight of the body.

From this principle, the following relationship emerges between surface elevation and ice thickness for ice floating on sea-water:

$$H = \frac{Z(\rho_w - \rho_i)}{\rho_w} \qquad (6.1)$$

where H is the orthometric surface elevation (relative to the geoid)

Z is the ice thickness

ρ_w is the column-averaged density of the sea-water

ρ_i is the column-averaged density of the ice.

Equation 6.1 can be used to determine when the surface elevation is in hydrostatic balance with the ice thickness. If accurate surface elevation and ice thickness data are available for a glacier-ice shelf system, and both the ice and water densities are known, Equation 6.1 can be applied, to define where the ice is floating. Conversely, in regions where the ice is known to be floating, Equation 6.1 can be used to derive the column-averaged ice density, ρ_i.

If the column-averaged densities ρ_w and ρ_i are both known, Equation 6.1 can be used to define a hydrostatic height anomaly term, which is the difference between the measured orthometric height ($\overline{H}$) and that derived from the ice thickness assuming hydrostatic equilibrium in (Equation 6.1), *(H)*. The hydrostatic height anomaly ($\Delta h'$) is given by:

$$\Delta h' = \overline{H} - \frac{Z(\rho_i - \rho_w)}{\rho_w} \qquad (6.2)$$

This is a useful term, since it can be used to define the extent of the floating ice (ie. the limits of the region where Equation 6.1 is satisfied) over an ice mass. Where the ice is floating, $\Delta h'$ will be close to zero. $\Delta h'$ will be non-zero where the ice is grounded and if there are errors in either the height or thickness measurement.

A common error in ice thickness measurement can occur over ice shelves when the measuring technique is radar sounding, and a marine ice layer is present at the ice shelf base. Marine ice contains brine cells that increase the dielectric absorption of the ice. The radar sounder may only detect the interface between this layer and the overlying continental ice (Jenkins and Doake 1991; Vaughan *et al.* 1995). Seismic sounding is often more reliable when marine ice is present, although this technique is limited to regions accessible by ground transport. Furthermore, where basal freezing occurs there can be a layer of ice slush at the ice shelf base, therefore the ice-ocean interface may be unresolvable from the seismic echoes (Vaughan *et al.* 1995).

As mentioned above, derivation of the hydrostatic height anomaly requires knowledge of the column-averaged ice density. This can be obtained, in the first instance, from a suitable density model. However, there can be variations in column-averaged ice densities over an ice shelf which arise from processes including differences in densification rate of the firn layer, related primarily to the accumulation rate and temperature (Ian Allison, personal communication, 1998).

6.3.2 Ice thickness dataset

The ice thickness data used for the hydrostatic calculations in this chapter were obtained with an airborne radar or Radio Echo Sounder (RES). The Soviet Polar Marine Geological Research Expedition (PMGRE) collected a large amount of RES data in the Lambert-Amery system along a dense pattern of flight lines over 5 field seasons between 1985 and 1995 (Sergey Popov, personal communication, 1998). Sergey Popov and Valery Masalov of the PMGRE provided these data for this project.

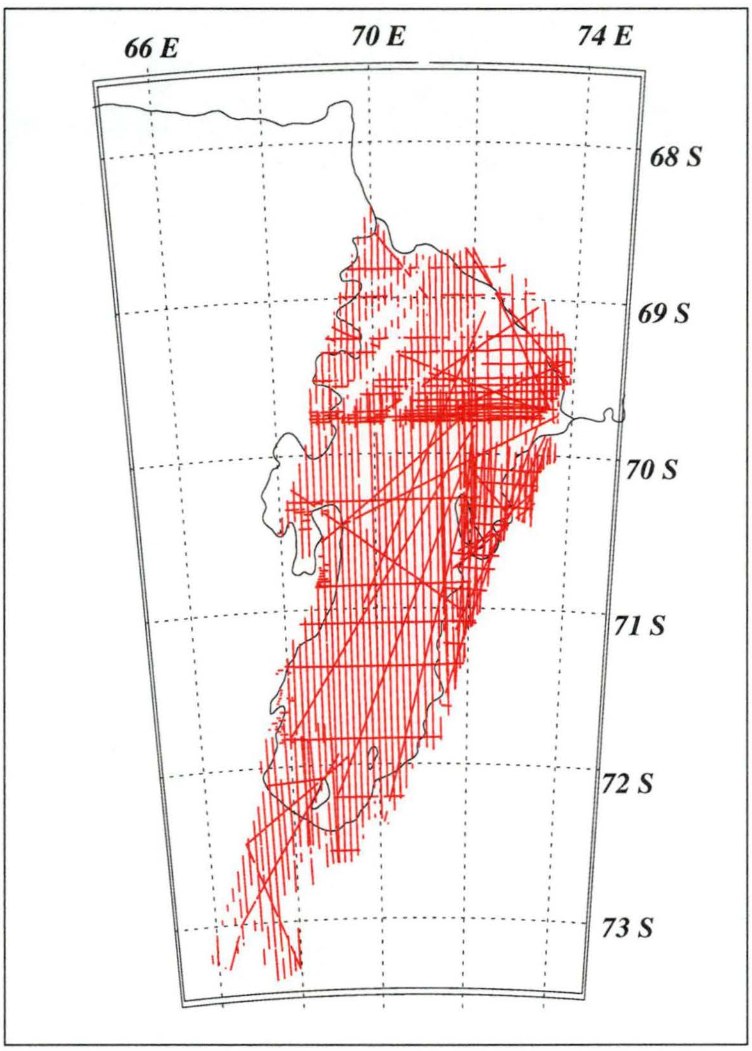

Figure 6.2 *Spatial distribution of PMGRE ice thickness measurements over the Amery Ice Shelf, provided by Sergey Popov, Soviet Polar Marine Geological Research Expedition (PMGRE).*

To investigate the relationship between surface elevation and ice thickness over the AIS-DEM, RES data coinciding in location with the AIS-DEM are required. This was achieved by generating a mask to define the region covered by the AIS-DEM, and using this mask to extract those data from the PMGRE data set that corresponded in location with the AIS-DEM. The resulting spatial distribution of RES data across the ice shelf is illustrated in Figure 6.2.

Figure 6.2 shows that there are several localised regions, on the western half of the ice shelf towards the ice front, where there are missing data. In these regions there was no resolvable basal echo detected by the radar. This can occur when there is a layer of marine ice present underneath the ice shelf (Vaughan *et al.* 1995). The internal consistency of the PMGRE RES data was computed using a modified version of the altimeter crossover algorithm (Glenn Hyland, personal communication, 1998). The results of this comparison showed that the differences at intersecting profiles of RES data across the ice shelf had a mean of 15.3 m and a RMS error of 53.4 m.

6.4 Application of the AIS-DEM to determine ice shelf parameters

This section presents the results of the application of the AIS-DEM. The first section describes the preparation of the three datasets required for the hydrostatic calculations whilst the second presents the results of the calculations. These will be discussed (in the context of their contribution to the knowledge of parameters of the Amery Ice Shelf discussed in Section 6.2) in the next section.

6.4.1 Preparation of datasets

The three datasets required for these calculations were surface elevation (relative to mean sea-level), ice thickness, and density. The AIS-DEM is on a polar stereographic projection and composed of 615 x 199 cells each of size 1-km (Figure 5.14). To perform these calculations as array operations, the datasets were all defined on the same polar stereographic grid.

Surface elevation

The surface elevations provided in the AIS-DEM are relative to the WGS-84 ellipsoid. For the hydrostatic calculations, surface elevations must be relative to mean sea level or the geoid. Using the latitude and longitude value of each grid cell, the value of the geoid from the EGM-96 (International Geoid Service 1997) model was interpolated, and subtracted from the ellipsoidal elevation. The resulting height was relative to mean sea level and could be used in the hydrostatic calculations.

Ice thickness

So that the RES data and the AIS-DEM could be directly compared, the RES data were gridded onto exactly the same (615 x 199) 1-km grid as the AIS-DEM. Gridding of the RES data was carried out using kriging (see Appendix C) with an isotropic semivariogram. This resulted in a near-continuous ice thickness map for the whole ice shelf. Since the spatial distribution of the RES data was only about 5 km (Figure 6.2), some artefacts may be introduced as a result of the kriging process. Some of the cells within this map had null values, because no data were found within the search radius used in the kriging (see Figure 6.4).

Column-averaged density

The hydrostatic calculations require *a priori* knowledge of the column-averaged density over the ice shelf. A simple model was constructed for the Amery Ice Shelf by interpolating surface elevations and ice thicknesses from the AIS-DEM and the Russian ice thickness map along a line. For extra simplicity, the line was chosen to be parallel to the X-axis of the AIS-DEM, and to pass through the cell that contained G1, where the density is known. The derived density profile could be subject to error, due to errors in either the surface elevation or the ice thickness measurements, or errors introduced through the kriging process. These errors were assumed to be constant along the profile. A straight line was fitted to the profile, and a bias (equal to 43.1 kg m^{-3}) added, so that the density at G1 matched the observed density (890 kg m^{-3}). The linear profile was then extended over the whole DEM, resulting in a linear density model (Figure 6.3).

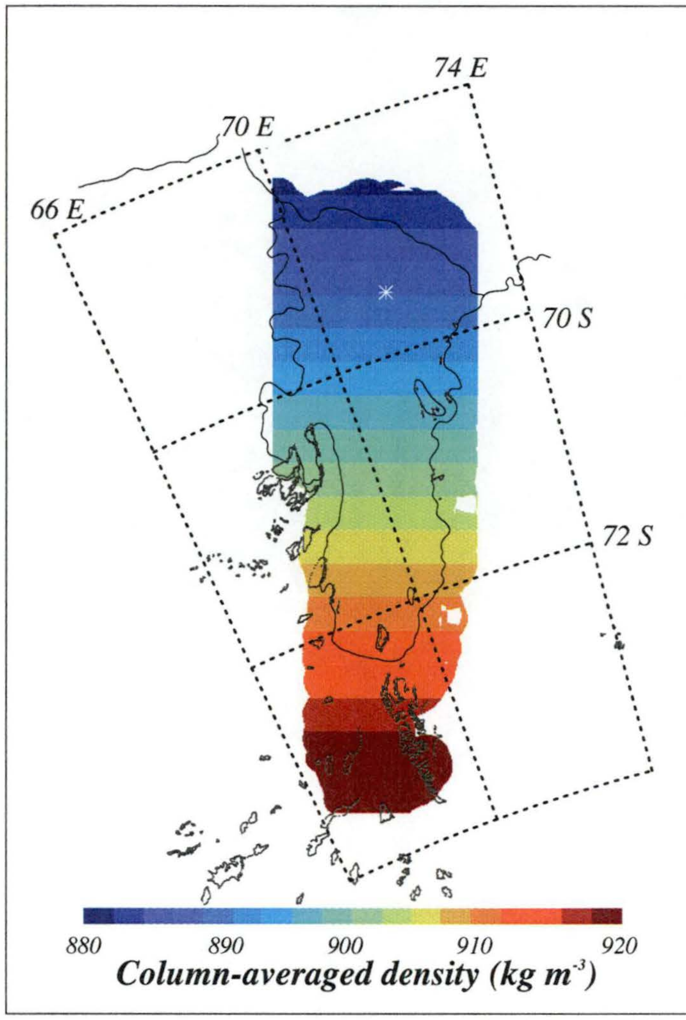

Figure 6.3 *Simple linear model for the column-averaged ice density of the Amery Ice Shelf, used in the hydrostatic calculations. The model is derived from observed elevations and ice thickness data, and a bias added so that the density at G1 was equal to the observed value of 890 kg m^{-3}.*

6.4.2 Hydrostatic calculations and results

Once the RES data and the density model were on the same grid as the AIS-DEM, it was straightforward to perform the hydrostatic calculation at each grid node. The results of calculations are outlined below.

Height anomaly term $\Delta h'$

The height anomaly term is given by Equation 6.2. It is the difference between the observed surface elevation (given by the AIS-DEM) and the theoretical surface elevation derived from the observed thickness, assuming hydrostatic equilibrium. The value of this term for each grid node of the AIS-DEM was calculated from the surface elevation, the ice thickness value (from the RES grid), the column-averaged density (from the density model) and an estimated water density. The value used for the estimated water density was 1027 kg m^{-3} derived from *in situ* profiles collected at the ice shelf front using Conductivity, Temperature and Depth (CTD) instruments (Nathan Bindoff, personal communication, 1998). The spatial distribution of the derived hydrostatic height anomaly term is shown in Figure 6.4.

Where the observed surface elevation and the inverted surface elevation are approximately equal (within the measurement errors) indicates floating ice, and the hydrostatic height anomaly term will be close to zero. From Figure 6.4, it can be seen this condition is true over the whole of the Amery Ice Shelf, and that it also extends upstream close to Mawson Escarpment, into the narrow trunk of the Lambert Glacier. The southernmost point of the region where the hydrostatic condition holds is 72.6°S.

There are two distinct regions where the hydrostatic condition does not hold and the values of the hydrostatic height anomaly term are positive. The first of these regions is around the margins of the floating ice of the Amery Ice Shelf, resulting from the fact that the ice is grounded and therefore hydrostatic equilibrium does not apply. This region defines the boundary of the grounded portion of the Lambert-Amery system. The second region where there are anomalous values is on the western side of the ice shelf, towards the ice front, where the height anomaly is up to 26 m. It is suggested that this difference is due to the presence of a marine ice layer accreted onto the ice shelf base. If this is the case, the reflected RES echo arises from the interface between continental ice and higher salinity marine ice, and not from the bottom of the ice shelf (Figure 6.5). The presence of a marine ice layer would also explain why many of the echoes are lost here (see Figure 6.2).

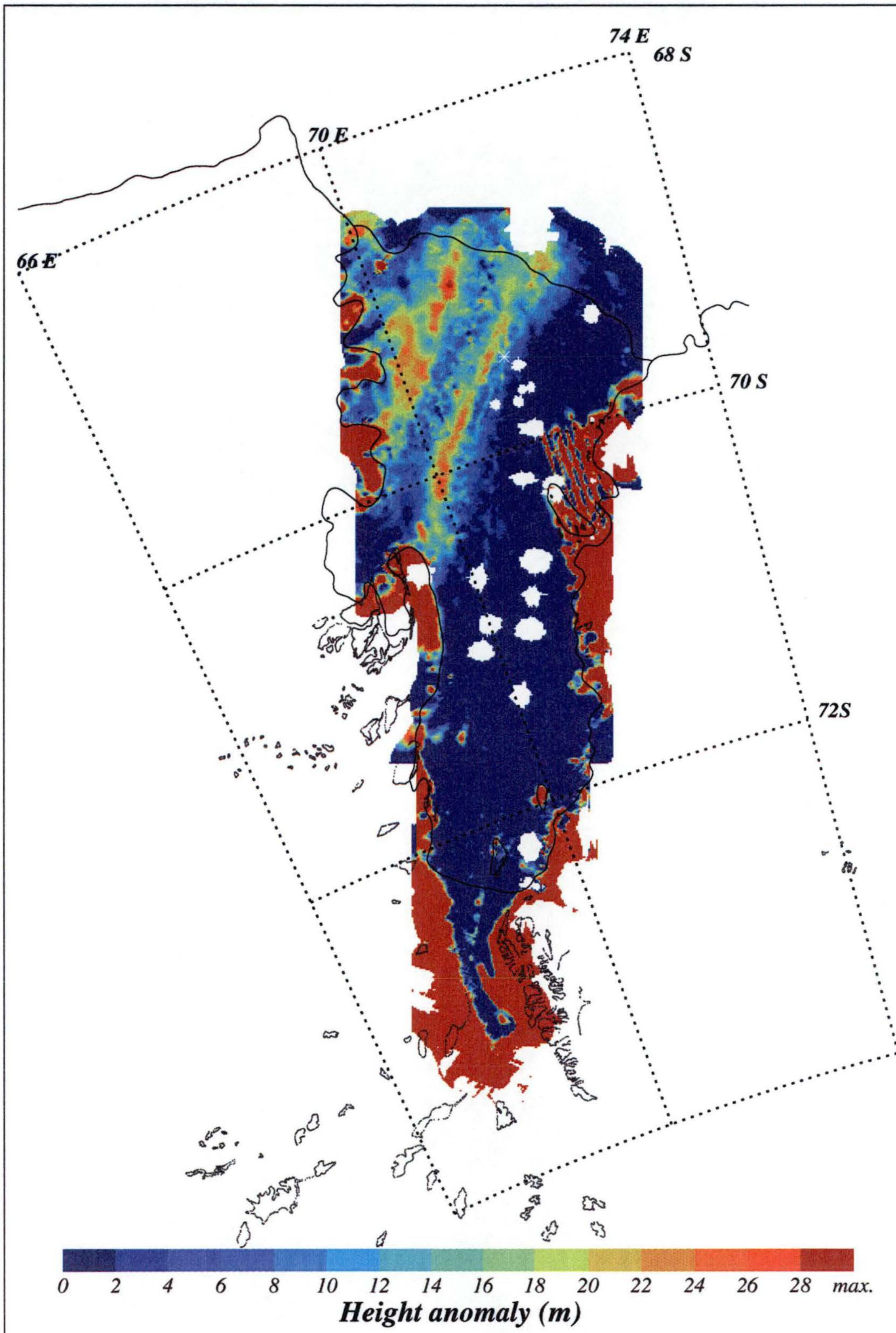

Figure 6.4 *Spatial distribution of the hydrostatic height anomaly calculated from Equation 6.2 using the elevations of the AIS-DEM, ice thicknesses from the RES data and a simple density model (Figure 6.3).*

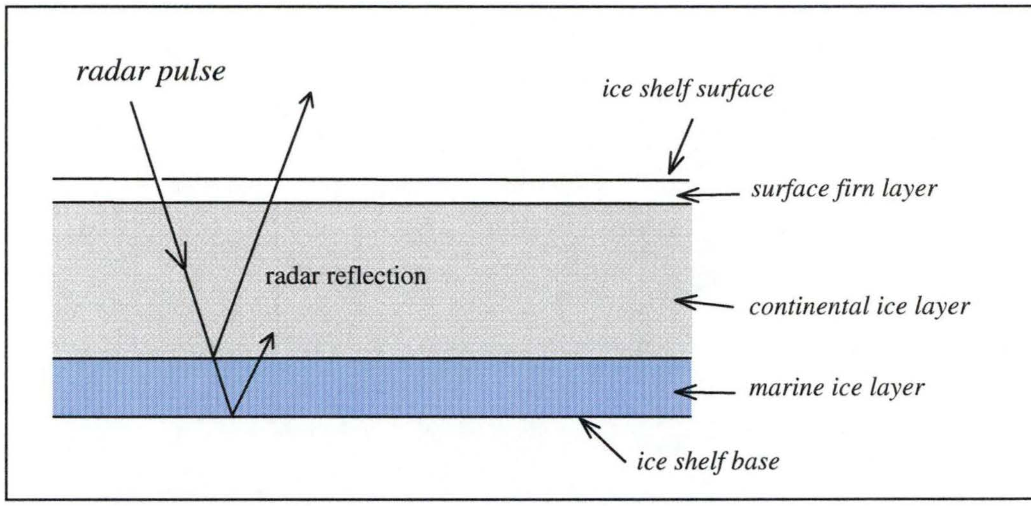

Figure 6.5 *Schematic diagram of a longitudinal section through an ice shelf where basal refreezing occurs, resulting in more than one sharp reflecting interface in the radar path.*

Thickness of marine ice layer

The thickness of the marine ice layer was estimated using the measured orthometric heights $(\overline{H})$ from the AIS-DEM, the measured thicknesses $(\overline{Z})$ from the RES data and the simple density model (Figure 6.3). The 'theoretical' thickness (Z) required to support the observed surface elevation $(\overline{H})$ under hydrostatic equilibrium was calculated from the AIS-DEM using Equation 6.1. This 'theoretical' thickness represents the sum of the measured thickness $(\overline{Z})$ and the marine ice layer thickness (Z_{mi}) (see Figure 6.5). That is:

$$Z = \overline{Z} + Z_{mi}$$

Therefore, subtracting the ice thickness map derived from the RES data from that derived from the AIS-DEM provides an estimation of the thickness of the marine ice layer, Z_{mi}. The result of this calculation over the AIS-DEM is shown in Figure 6.6.

It can be seen from this map that the inferred thickness of the marine ice underneath the ice shelf is up to 200 m. The distribution of the layer is oriented along distinct ridges in the ice shelf draft, and confined to the western side of the ice shelf.

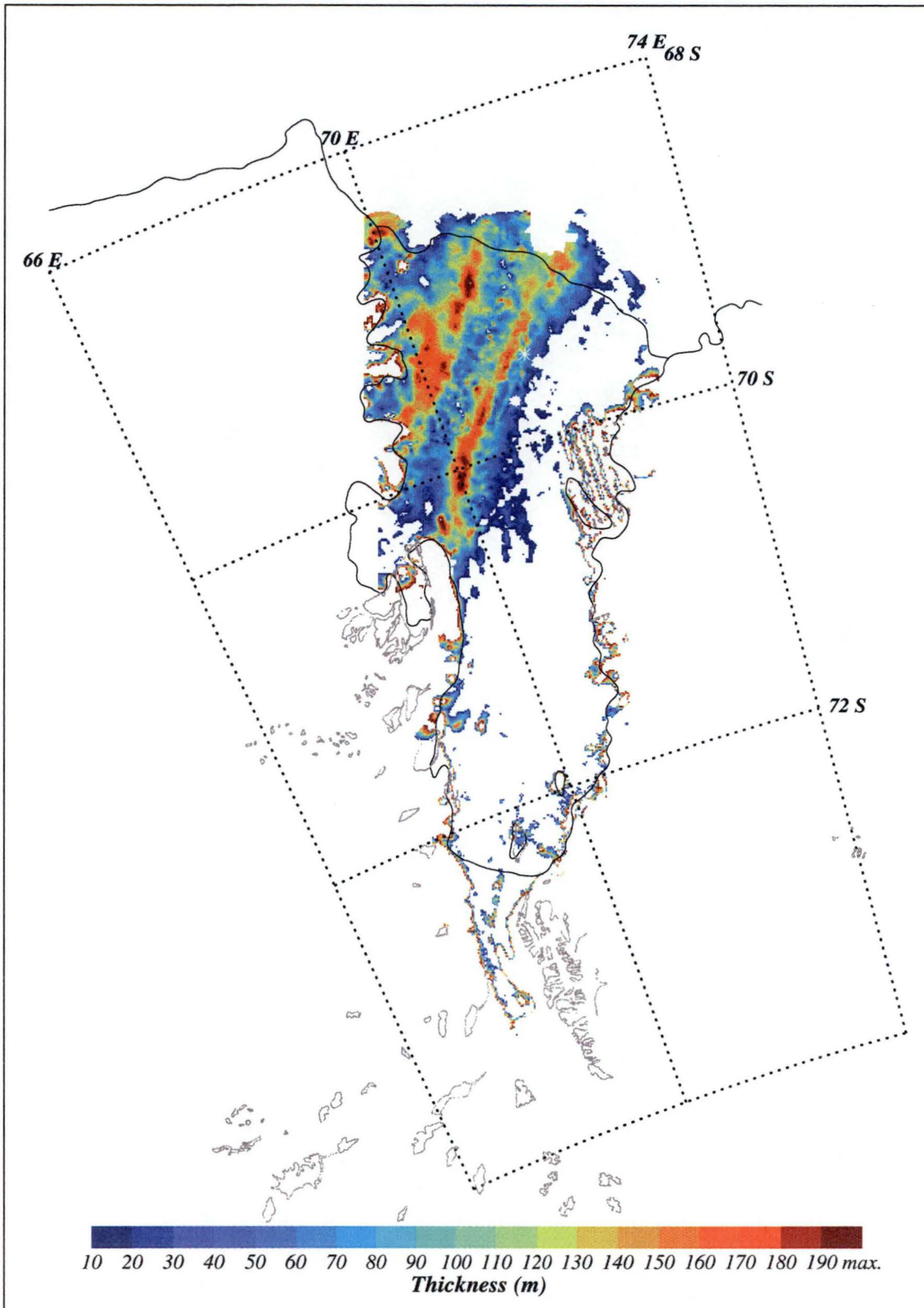

Figure 6.6 *Spatial distribution of the thickness of the accreted marine ice layer calculated from Equation 6.1 using the elevations of the AIS-DEM, ice thicknesses from the RES data and a simple density model (Figure 6.3).*

From this distribution, the estimate for the thickness of the marine ice layer at G1 is 110 m. The location of the 1968 G1 borehole is marked by a star in Figure 6.6. The thickness of the marine ice layer at G1 was inferred to be 158 m (see Chapter 2; Budd *et al.* 1982). The technique used here to infer the marine ice layer thickness is subject to several errors, due to the inherent errors in the measurements and the assumptions made in the calculations. The WGS-84 ellipsoidal elevations of the AIS-DEM were converted to orthometric heights using a global geoid model. Lack of gravity measurements on the Antarctic ice sheet means that the global models are the least reliable there, and errors in the geoid may be up to 3 or 4 m (Richard Coleman, personal communication, 1998). Combined with the RMS error of 1.7 m obtained for the Amery Ice Shelf heights (Chapter 5), this could lead to an error of around 4.28 m in the orthometric elevation value. The crossover analysis for the Russian ice thickness measurements revealed an internal consistency of mean 15.3 m and RMS 53.4 m. Errors in radar sounding data result from uncertainties in the speed of radio waves in ice, the uncertainty of the correct firn correction and limitations of the digitising techniques (Vaughan *et al.* 1995). There are also errors in the density model applied to the ice shelf, since the model is only an approximation, but this is a minor contributor to the total error. Combining all these errors the estimated marine ice layer thickness using this technique is around 55 m. This means that the estimate for the marine ice thickness at G1 from this study is 110 m $\pm$ 55 m. Therefore, to within the errors, the thickness of the marine ice derived in this chapter is consistent with the results of the ice core borehole drilled at G1.

Estimated density

For the regions known to be floating (Figure 6.4) and free of any marine ice accretion (Figure 6.6), the column-averaged ice density was calculated from Equation 6.1. The spatial distribution of the column-averaged ice density is shown in Figure 6.7. On the broad scale, the average ice density reveals a gradual transition from high values in the south (approximately 930 kg m^{-1}) to lower values in the north (approximately 890 kg m^{-3}). This is consistent with increasing firnification rates that occur with the increasing snow accumulation from south to north on the ice shelf.

The estimate for the density is subject to errors in the orthometric height data (4.28 m) and the ice thickness data (53 m). Using the principle of propagation of errors (Bevington 1969), the RMS error in the density estimate amounts to around 14 kg m^{-3}. Thus, the value for the maximum ice density in the south of the ice shelf becomes 930 $\pm$ 14 kg m^{-3}. The maximum density of continental ice is 917 kg m^{-3} (Paterson 1994). This implies that, to within the errors, the derived density values are physically realistic.

6.5 Discussion

6.5.1 Location of the grounding zone

The grounding zone of the Amery Ice Shelf has been redefined. From the map shown in Figure 6.4, the southernmost point of the Amery Ice Shelf is 72.6°S. This is approximately 150 km upstream of the grounding zone proposed by Budd et al. (1982). From this new definition, a new estimate of the area of the Amery Ice Shelf (for the 1994-95 epoch) emerges. This area is approximately 69 092 km^2.

The method adopted here to locate the grounding zone was that of hydrostatic inversion. The point that this method computes is known as the 'hydrostatic point' (H) which is slightly different to the true grounding line (G) (Vaughan 1994; see Figure 6.8). Two further points that are associated with the grounding zone are F, the limit of flexure (or the hinge line) and I, the point of gradient change. On Rutford Ice Stream, the horizontal distance between the limit of flexing and the hydrostatic point is around 2 km, approximately one ice thickness (Vaughan 1994). The limit of flexing can be detected by tiltmeter measurements (Stephenson *et al.* 1979), static GPS methods (Chapter 4), kinematic GPS methods (Vaughan 1994) and satellite radar interferometry (Rignot 1998). Satellite altimetry and satellite imagery methods can be used to detect the change in gradient, I. A Landsat satellite image over the grounding zone of the Amery Ice Shelf is illustrated in Figure 6.9. It can be seen that the line defining the change in slope in the satellite image has a similar shape to the shape of the grounding zone defined in Figure 6.4. Static GPS measurements, collected at ice stations located between Mount Stinear and Mawson Escarpment (as far as 72.5°S) during the 1997-98 summer revealed

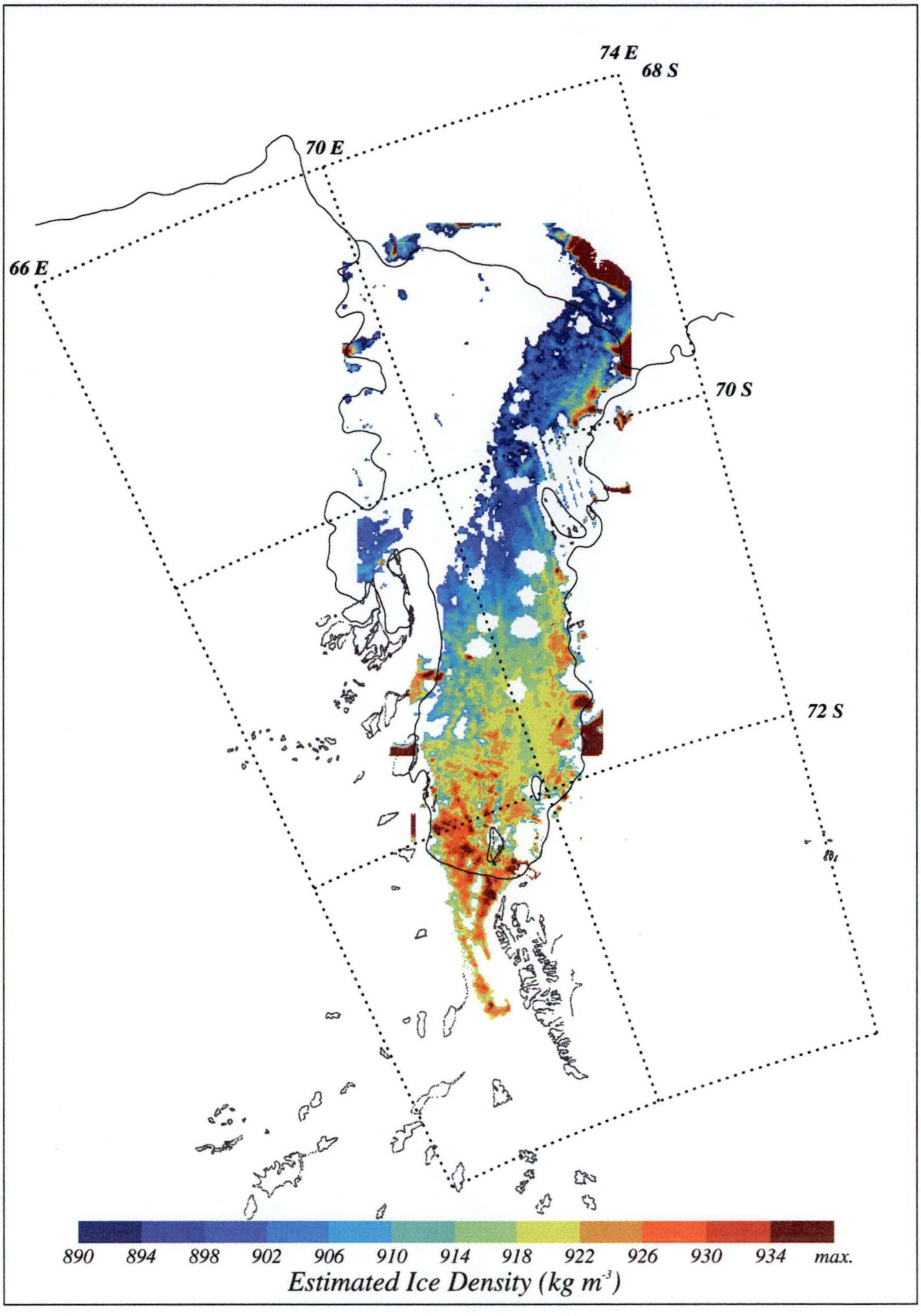

Figure 6.7 *Spatial distribution of the of the estimated column-averaged ice density calculated from Equation 6.1 using the elevations of the AIS-DEM and ice thicknesses from the RES data, for the part of the ice shelf thought to be marine ice free.*

a tidal signature of ~1 m (Andrew Ruddell, personal communication, 1998), confirming that the flexing point is located upstream of these stations.

Budd *et al.* (1982) interpreted the change in slope around the 100-m elevation contour (near T4) on the Amery Ice Shelf as the grounding zone (Chapter 2). The redefinition of the grounding zone presented here has implications for previous studies of the region. Partington *et al.* (1987) reported they had located the change in slope, and therefore mapped the position of the grounding zone. Herzfeld *et al.* (1994) also used the change in slope around the 100-m contour as the grounding zone, finding it had advanced by approximately 10 km between 1978 and 1989. This was consistent with a mean increase of surface height on the Lambert Glacier described by Lingle *et al.* (1994). These results were all obtained using Seasat data, whose southernmost extent was 72.12°S. According to the new location of the grounding zone, Seasat did not cover the Lambert Glacier.

The new definition of the grounding zone also affects the sub-ice shelf modelling outputs (Hellmer and Jacobs 1992) and mass budget calculations (Allison 1979). Hellmer and Jacobs (1992) were not able to reproduce the amount of marine ice observed at G1. With the new definition of the sub-ice shelf cavity, their model may well be able to match the amount of marine ice observed at G1. Allison (1979) estimated the mass budget of the Lambert Amery system (Chapter 2). For this study, the Budd *et al.* (1992) definition of the grounding zone was used. In the region south of T4, Allison (1979) only accounted for ablation at the surface, as this was thought to be the trunk of the Lambert Glacier, and did not account for basal melting. Allison (1979) inferred that the system was in positive mass budget. With the new definition of the grounding zone, basal melting must also be a contributor to the mass budget equation in the region in the south of the Amery Ice Shelf.

Accurately defining the location of the grounding zone is a significant contribution to the knowledge of the Lambert-Amery system as a whole. The grounding zone marks the extent of the floating ice, and is the point downstream of which the ice is in direct contact with the ocean. Its position is sensitive to changes in ice thickness and sea level (Vaughan 1994). Changes in global air temperatures could lead to changes in ocean

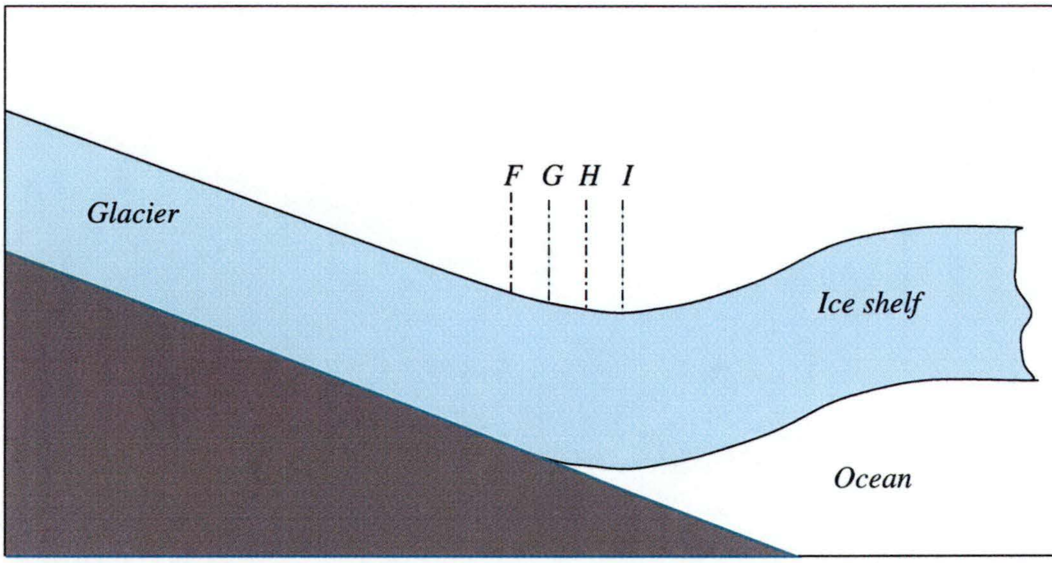

Figure 6.8 *Schematic representation of features of the grounding zone. F is the 'limit of flexure'; G is the 'grounding line'; H is the hydrostatic point; and I is the location of the change in slope. From Vaughan (1994).*

Figure 6.9 *Band 4 Thematic Mapper image from Landsat 4 (Path 127, Row 112) the Lambert-Amery grounding zone; acquired 08 March 1988.*

temperatures and in sea level, which in turn could change the position of the Lambert-Amery grounding zone. Systematic measurement of the dynamics and morphology of individual ice-streams in the vicinity of their grounding zones is one way of monitoring climate change. However, to do this a baseline must be established against which to monitor change.

6.5.2 Melting and freezing

The derived spatial distribution of marine ice layer thickness implies that the oceanic circulation under the Amery Ice Shelf is clockwise. The flow enters from the eastern side, and leaves on the western side, depositing ice on the base of the ice shelf. The clockwise pattern is consistent with results of recent paleoclimate work, which has studied the spatial pattern of deposition from sediments collected in Prydz Bay (Domack *et al.* in press). This means that the circulation shown in Figure 6.1 is only a one-dimensional representation of the real sub-ice shelf circulation.

The inferred distribution of basal freezing reported here is consistent with the melting-freezing pattern obtained through applying a three-dimensional ice shelf circulation model to the sub-ice shelf cavity (Williams *et al.* 1998b). Williams *et al.* (1998b) concluded that steep gradients in the ice shelf base can cause high rates of freezing, since they can accelerate the rising of the supercooled water. They estimated that the amount of basal refreezing under present conditions was 3.6 Gta^{-1}, which was exceeded by melting, resulting in a net loss of 7.8 Gta^{-1}. The effects of ocean warming on the circulation under the Amery Ice Shelf were also investigated, by raising the ocean temperature at the ice front in uniform intervals up to 1°C. The freezing rate decreased to 3.0 Gta^{-1}, and the net melt to 34.6 Gta^{-1}, after an ocean warming of 1°C illustrating the sensitivity to temperature of these quantities. Using their melting and freezing rates combined with ice velocities for the shelf, Williams *et al.* (1998b) accumulated ice along a flowline passing approximately through G1. They could not accumulate the amount of marine ice observed at G1, attributing the discrepancy to uncertainties in the ice shelf draft and submarine topography. Since they did not have access to the Russian RES data used in this project, their ice shelf draft was derived from less densely sampled ANARE RES data collected during 1988-90, so this could well be the case.

The amount of melting and refreezing influences the dynamics and grounding zone location of an ice shelf (Jacobs *et al.* 1992) therefore these two parameters are intrinsically linked. The distribution of basal melting and refreezing under an ice shelf is sensitive to underlying oceanic conditions (see Figure 6.1). Therefore quantification of the amount of marine ice accreted under the Amery Ice Shelf is an important result in terms of ice shelf monitoring to detect climate change. Subsequent studies of this kind will determine whether the distribution and thickness of the marine ice layer has changed over the time between observations.

A point to note is that the method used to estimate the thickness of the marine ice layer relies implicitly on the fact that the signal in the RES data originates from the interface between the marine ice layer and the continental ice layer. It also assumes that if a marine ice layer is present then the RES echo always originates from that interface. If there are regions containing marine ice where the RES data also detected the true base, then these regions would be not be picked up using this technique.

6.6 Chapter conclusions

This chapter has described the application of accurate, extensive surface elevation information over an ice shelf, and has resulted in the determination of some important glaciological parameters for the Amery Ice Shelf. The elevations of the high-resolution 1-km ERS-derived DEM of the Amery Ice Shelf (AIS-DEM) were combined with ice thickness data, using a simple density model and a hydrostatic relation, to derive the height required for hydrostatic equilibrium. This computed height was subtracted from the observed heights to yield a hydrostatic height anomaly term.

Where the hydrostatic height anomaly term is close to zero (within the measurement errors) indicates floating ice. This condition occurred over most of the Amery Ice Shelf and continued well upstream, into the trunk of the Lambert Glacier. Significantly positive values of this term occur around the margins of the floating ice, resulting from the fact that the ice is grounded in these regions, defining the grounded portion of the system. The shape of the grounding line at its southernmost point is consistent with that of the line marking a steep change in slope on a Landsat image of the region. This confirms that the Amery Ice Shelf extends much further south than the widely accepted position proposed by Budd *et al.* (1982). The fact that the ice is floating further south than Budd *et al.* (1982) proposed was also inferred from tidal signatures in time series of static GPS on the shelf between 71.2°S and 72.5°S in the 1995-96 and 1997-98 ANARE seasons (Chapter 4; Andrew Ruddell, personal communication 1998).

A region in the northwest quadrant of the shelf displays anomolously positive values of the hydrostatic height anomaly term. The ice is known to be floating here and the anomaly is attributed to the presence of a marine ice layer accreted to the base of the shelf. In this region the reflected radar echo was from the interface between continental ice and higher salinity marine ice, and not from the base of the ice shelf. The hydrostatic relation was used to calculate the theoretical thickness required to support the observed surface elevation, using a simple density model. The difference between the theoretical ice thickness and the observed ice thickness quantifies the thickness of the marine ice layer underneath the ice shelf. The results of this calculation indicate that the thickness of the marine ice underneath the ice shelf is up to 200 m, and the distribution of the layer is oriented along distinct ridges in ice shelf draft, and confined to the western side of the ice shelf. This pattern implies that the oceanic circulation under the Amery Ice Shelf is clockwise. The flow enters from the eastern side, melting ice from the base of the ice shelf, and leaves on the western side, depositing ice on the base. This circulation pattern is consistent with consistent with results from paleoclimate work reported by (Domack *et al.* in press). It is also consistent with the melting/refreezing pattern obtained through applying a three-dimensional model of ice shelf circulation to the sub ice shelf cavity (Williams *et al.* 1998b). The thickness of the marine ice is consistent with the results from the ice core borehole drilled at G1 in 1968.

The implied average ice density was calculated over the ice shelf from the hydrostatic equation in regions that were freely floating and where no marine ice was present. This revealed a gradual transition from high values in the south (approximately 930 kg m^{-3}) to lower values in the north (approximately 890 kg m^{-3}), which is consistent with increasingly lower firnification rates that occur with the increasingly greater snow accumulation from south to north on the ice shelf.

The results of this chapter have been shown to be consistent with ***in situ*** and model results and demonstrate the important contribution of the satellite altimeter instrument to ice shelf studies. The reference surface provided by the AIS-DEM will be used in conjunction with height measurements from future altimeter missions to provide ongoing monitoring of elevation change on the Amery Ice Shelf.

Chapter 7

Applications of the Lambert-Amery system Digital Elevation Model

7.1 Introduction

In Chapter 6, the high-resolution AIS-DEM was successfully used to delineate the grounding zone of the Amery Ice Shelf, and to estimate the amount of marine ice accreted onto the base of the shelf. The second DEM presented in Chapter 5 (the LAS-DEM) had a lower spatial resolution and therefore contained less structure than the AIS-DEM. Nevertheless, the LAS-DEM provided surface slope information for the entire Lambert-Amery system, which can be used to provide further insight into the glaciology of the region. Two important parameters that can be estimated from surface slope information over the grounded part of the Antarctic ice sheet are flowline trajectories and balance fluxes, both parameters being important for mass budget studies.

This chapter describes applications of the LAS-DEM, demonstrating the value of surface elevation information over the ice sheets. For grounded ice, the surface slope, spatially averaged over distances of 10 to 20 ice thicknesses, defines the ice flow direction (Budd 1968). Therefore, knowledge of the topography of the Lambert-Amery system provides information on the direction of ice velocities in the system. The LAS-DEM is used to calculate ice flow trajectories, which are used to define the boundaries of the major components of the drainage basin. By combining the LAS-DEM with an accumulation distribution, balance fluxes are computed. Comparison of balance fluxes with observed fluxes provides information on the state of balance of the Lambert-Amery system.

The next section (Section 7.2) includes a review of previous mass budget estimates for the region, and a discussion of two ways that the LAS-DEM can directly contribute to this knowledge, through flowline determination and balance flux calculations. Section 7.3 describes these two applications of the LAS-DEM and presents the results.

7.2 The mass budget of the Lambert-Amery system

7.2.1 Previous measurement

The total mass budget of the Antarctic ice sheet is an important climatic variable, since any significant deviation from a balanced state would directly influence global sea level (Meier 1993). However, the determination of this quantity is no simple task, primarily due to the sheer size of the ice sheet. The sparsity of *in situ* surface velocity, ice thickness and surface accumulation measurements and insufficient knowledge of the surface velocity factor (i.e. the ratio of the surface velocity to column-averaged velocity) all add to the complexity of this task. Despite these difficulties, significant contributions have been made in this area and many authors have attempted to estimate the mass budget of the entire ice sheet from observations, e.g. Jacobs *et al.* (1992); Bentley and Giovinetto (1991). Other authors have restricted their studies to more manageable scales by studying outlet glaciers or individual drainage basins, e.g. Shimizu et al. (1978); Whillans and Bindschadler (1988). These 'localised' studies provide useful information on the response of an individual drainage system to any regional changes in climate.

Allison (1979) estimated the mass budget of the Lambert Glacier Drainage Basin (LGDB), a section of the Lambert-Amery system, from survey data (see Chapter 2). The LGDB is enclosed entirely within the Lambert-Amery system, and is the part of the system that drains through the major ice streams entering the rear of the Amery Ice Shelf (see Figure 2.4). It does not include any ice that originates from the part of the Lambert-Amery system to the west or east of the Amery Ice Shelf. Allison (1979) estimated mass fluxes for the system, obtaining an influx of 60 Gta^{-1} for the interior portion of the basin (equivalent to an average net accumulation over the basin of 55 $kg\,m^{-2}a^{-1}$) and an outflow into the main channel of the Lambert Glacier of 30 Gta^{-1}. This yielded an overall positive imbalance for the interior of 30 Gta^{-1}. For the Lambert Glacier system, Allison (1979) estimated mass losses at 18 Gta^{-1} (7 Gta^{-1} through ablation and 11 Gta^{-1} via outflow into the Amery Ice Shelf), yielding a positive mass budget of 12 Gta^{-1}. These estimates are equivalent to a surface rise of 0.03 m water equivalent per year averaged over the interior basin and 0.04 m water equivalent averaged over the total drainage basin. Throughout Allison's (1979) calculations, estimates of mass input terms were minimised and those of loss terms were maximised.

Bentley and Giovinetto (1991) made estimates of the imbalance of several drainage basins, including the Lambert-Amery system, as part of continent wide studies. Surface mass input data was previously calculated by Giovinetto and Bentley (1985) using data from the 1968-70 ANARE surveys (Budd *et al.* 1982) and McIntyre's (McIntyre 1985a) interpretation of surface accumulation which followed Allison's (1979) study. For the 1991 study, this surface mass input data was slightly modified to allow for Allison's (1979) original interpretation of a positive accumulation rate over an extensive region in the interior. For the grounded ice, Bentley and Giovinetto (1991) obtained a positive mass imbalance of 39 Gt a^{-1} (78%) for the entire LGDB system. This compares with Allison's (1979) imbalance of 42 Gta^{-1} for the entire system (30 Gta^{-1} for the interior plus 12 Gta^{-1} for the Lambert Glacier system).

7.2.2 Contribution of LAS-DEM to mass budget studies

A direct way to determine the state of balance of the Antarctic ice sheet is to accurately measure its surface elevation at repeated sampling intervals. For this kind of information to be obtained quantitatively using satellite altimeter-derived surface elevations, a long period (10-20 years) of repeat observations is required (Rapley *et al.* 1985). Previous attempts to do this for the Lambert-Amery system used crossover analysis between Seasat and Geosat data, e.g. Lingle *et al.* (1994); Herzfeld *et al.* (1994), (see Chapter 2). These studies were affected by problems associated with maintaining consistent reference frames over long time periods, which was difficult at the time of Seasat and Geosat (1975-1985).

The LAS-DEM is composed of satellite altimeter data collected between April 1994-March 1995, and has been verified with GPS heights in the WGS-84 reference frame. It can therefore be used in the future as a reference surface against which to compare DEMs from a later epoch (say post-2004) to detect any major changes that may have taken place in the system over this decade.

Although in isolation it cannot provide direct, extensive mass budget information for the Lambert-Amery region, the LAS-DEM can make a useful contribution to mass budget studies since it contains highly accurate and detailed surface slope information. For the grounded part of a glacier system, the direction of the maximum surface slope, averaged over a horizontal scale of 10 to 20 ice thicknesses, determines the direction of ice flow (Budd 1968). Therefore, the LAS-DEM provides glaciologically interesting information on the Lambert-Amery system that cannot be provided by other means. Estimates of ice flow direction can be obtained in regions where there are no *in situ* observations and no flow features are seen in satellite imagery. In particular, two useful quantities that can be derived from slope information are flowline trajectories and balance fluxes. These quantities are discussed below.

Flowlines

'Flowlines' are an important concept in glaciology, since they provide insight into the shape of the 'flow field' within a glacier system. Flowlines in a glacier system are analogous to streamlines in fluid mechanics. They are the surface projection of the path that an individual ice particle would take in moving through the system (which includes a vertical component). The tangent at a point on a flowline coincides with the direction of the velocity vector at the point. Every point in a glacier system is on a unique flowline. If the system is in steady state, this information can be used to construct the flow field.

All of the ice that flows through a section transverse to the flow field originates from the up-slope catchment area that is bounded by the two flowlines that pass through the points on either end of the section (see Figure 7.1). This is useful since it means that calculation of flowlines allows the selection of particular flowlines delineating catchments. The amount of ice flux through a transverse section is equal to the accumulation integrated over the area of the catchment. Therefore, given an accumulation distribution, the input mass component can be estimated for each section.

Flowlines can be determined from a DEM that has been smoothed on an appropriate spatial scale. The LAS-DEM extends slightly further than the Lambert-Amery system boundary (see Chapter 5 and Appendix B). Calculation of flowlines from a smoothed version of the LAS-DEM can therefore be used to define the extent of the system (to ~5 km), a useful precursor to any mass budget estimate for the Lambert-Amery system. The results of this work will be presented in the Section 7.3.2.

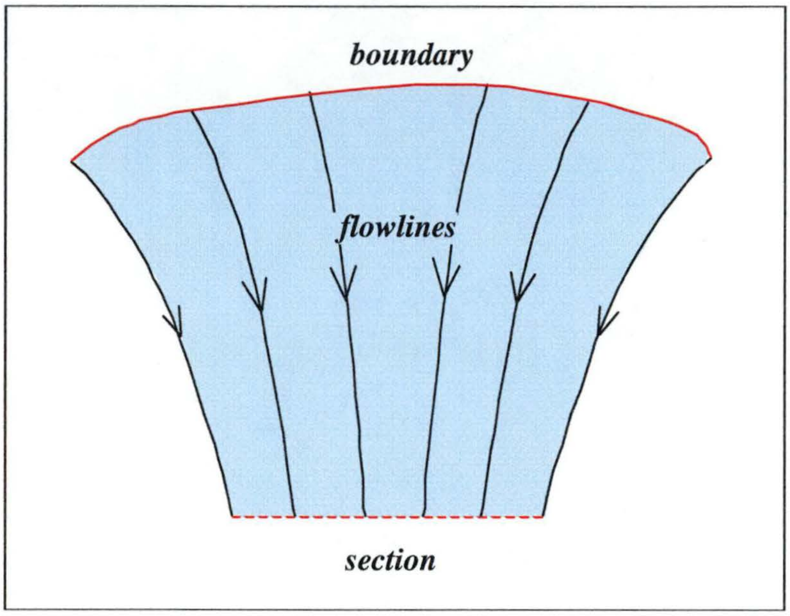

Figure 7.1 *Simple schematic diagram of flowlines (plan view), illustrating the concept that flowlines delimit the extent of a glacier system.*

Balance fluxes

The 'balance flux distribution' is another useful quantity that can be calculated from knowledge of the surface slopes for a glacier system, combined with the spatial distribution of ice accumulation rate (the 'accumulation distribution') in the system. The balance flux distribution is the hypothetical distribution of mass flux that would exist if the system were in steady state, under a given accumulation distribution.

Since knowledge of the overall state of balance of the Antarctic ice sheet is ultimately sought, it may seem strange to calculate a quantity that would keep the system in balance. However, balance flux calculations can provide information towards this result. For example, comparison of calculated balance fluxes with observed fluxes can give an indication of the state of balance of a glacier system. For the Lambert-Amery system, *in situ* observations of surface ice velocities and ice thickness are available at the LGB traverse sites (Figure 2.5), and at Allison's (1979) sites GL1-GL11 (see Figure 2.4). These observations allow the calculation of local ice fluxes at these locations.

Another significant point about comparing balance fluxes with observed fluxes is that it provides an indication of the quality of the accumulation distribution used to calculate the balance fluxes. Since accumulation is still a large source of uncertainty in any mass balance estimate, this can be useful.

7.3 Application of the LAS-DEM to mass budget studies

This section presents the results obtained by applying the LAS-DEM to determine the two quantities described in the previous section for the Lambert-Amery system, and is divided into three subsections. The first sub-section describes the preparation of the 5-km LAS-DEM for these applications. The second sub-section describes and presents the determination of ice flow trajectories that delineate the Lambert-Amery system. Flowlines are calculated to delimit the extent of the basin and ascertain the flow field for the system. The final sub-section discusses the computation of the balance flux distribution, including a description of the accumulation distributions available for the region. The balance fluxes are derived for the system, using several different accumulation distributions. The results of comparing the derived balance fluxes with *in situ* measurements made in the Lambert-Amery system are presented and discussed.

7.3.1 Preparation of the LAS-DEM

Smoothing

The shaded surface plot of the LAS-DEM (Figure 5.19), at a horizontal resolution of 5 km, shows many fine scale details of the surface topography of the ice sheet and provides detailed information on the shape and structure of the Lambert-Amery system. Since it is the large-scale 'average' surface slope that defines ice flow direction, the topography on the 5 km horizontal scale is inappropriate for ice flow studies. Therefore, the LAS-DEM must be spatially smoothed for ice flow studies. The average ice thickness along the LGB traverse, from RES measurements, is around 2120 m (Higham *et al.* 1995). Hence, the appropriate range for smoothing the surface information along the traverse is between 20 and 40 km.

For this work, the LAS-DEM was smoothed on two horizontal scales: 15 and 35-km. A simple, 'moving area' averaging scheme was used for this. Each cell was assigned the average value of itself and the appropriate number of surrounding 5-km cells (8 for 15-km and 48 for 35-km). This scheme has the advantage that it maintains the high spatial resolution of the LAS-DEM yet incorporates the appropriate scale slope information applicable to ice flow.

Polishing

In regions of positive accumulation, an ice sheet in steady state can have no surface hollows or regions that are exactly flat. Flowline computation and balance flux calculations do not allow any surface hollows or regions that are exactly flat in the DEM. A data preparation step that ensures that there are no such occurrences is referred to as elevation 'polishing' (Roland Warner, personal communication, 1998). During the polishing step, the DEM is checked for local hollows and exactly flat gradient regions. Local hollows in the DEM are filled in, such that no site has a local minimum. Flat spots are given a slight slope by adding a small quantity to the elevation.

Integration of rocks

Bedrock protrusions (e.g. rock outcrops and mountains) obstruct the ice flow, such that the ice flows around them. The flowline pattern around such obstructions is evident in satellite imagery of the ice sheet (Swithinbank *et al.* 1988). If accurate balance fluxes are required downstream of such a feature, an elevation value greater than that of the surrounding ice sheet should be placed in the DEM at these locations, to simulate an obstruction. The ERS altimeter lost lock over most rock outcrops (see Figures 5.20 and 5.21) and no data are present in these regions. Extra information (such as georeferenced satellite imagery) is required for this step, to locate the rock features. In this study, since the balance fluxes used in comparison with observed fluxes are *upstream* of the major rock features (the LGB traverse and the GL line) this step is not required. However, it must be noted that the estimated balance fluxes entering the Amery Ice Shelf itself will not be strictly correct.

7.3.2 Flowline trajectories

Processing

To determine flowlines for the Lambert-Amery system the following steps were first carried out:

i) smoothing of the LAS-DEM at the 15 and 35-km spatial scales;

ii) polishing of the LAS-DEM; and

iii) determination of the direction of maximum downward surface slope (slope aspect) by comparing each cell with its 8 neighbours.

These preliminary steps resulted in a new database that contained the (polar stereographic) X- and Y-components of the maximum surface slope direction, which provided a description of the unit-vector tangents to the ice flow trajectories for the Lambert-Amery system. This array of normalised streamline vectors was used as input into a flowline computation algorithm, written in MATLAB code.

The flowline algorithm solves the differential equation that relates the unit tangent ($\hat{\underline{t}}$) at a point on the curve $\underline{x}$(s), described in terms of the distance (s) along the curve, to the field of normalised flow directions. This equation is:

$$\frac{d\underline{x}}{ds} = \pm\hat{\underline{t}}(\underline{x}(s)) \qquad (7.1)$$

which is solved by simple forward Euler stepping, up or downstream. Using a pre-defined step-size, the initial point is moved a distance *(Δs)* up or down-slope, i.e.:

$$\underline{x}(s+\Delta s) = x(s) + \Delta s\hat{\underline{t}}(x(s)) \qquad (7.2)$$

In the next step, the unit tangent to the flow field at the new point is found by interpolation in the array of tangent vectors and the process is repeated. This continues until a pre-defined number of steps have been made, when the algorithm terminates.

The flowline algorithm can be operated down-slope or up-slope. The stepping scheme used in the flowline algorithm is sensitive to whether flowlines are converging or diverging. Since flowlines in the Lambert-Amery system converge downstream, the down-slope mode is preferred, especially into the rear of the Amery Ice Shelf, near the grounding zone. Here the flowlines become very close together and have a spacing of less than one grid cell (5 km). The spatial resolution is insufficient to resolve adjacent flowlines in this region, and separation of their paths up-slope is difficult. Towards the perimeter of the system, however, the flowlines become more spread out and the up-slope routine can be used.

For the Lambert-Amery computation, flowlines were calculated by combining the up-slope and the down-slope results. Both calculations were started at the coordinates of points located along a line *just inside* the perimeter of the Lambert-Amery system. The resulting up-slope and down-slope flowlines from each point were joined, to create one continuous flowline through each initial point.

Results

Figure 7.2 illustrates flowlines for the Lambert-Amery system calculated using the method described above. A selection of the flowlines is shown here (every fifth computed line). The extent of these flowlines defines the boundary of the Lambert-Amery system. It is assumed that this line lies along a ridge in the surface topography, which can be seen in the Slopes Database (Appendix B). When the flowline algorithm is operated in the up-slope mode, a flowline will terminate when there is no further up-slope component to follow in the surface topography, i.e., when the flowline has reached the summit of the ridge. When an individual flowline approaching up-slope from within the Lambert-Amery system meets the ridge, if there is an adjacent point along the ridge that can be reached by stepping up-slope, the flowline algorithm will follow this up-slope component until a local summit is reached. This means that, in fact, only a few of the flowlines (calculated using the flowline algorithm in the up-slope mode) would be required to define the Lambert-Amery system boundary. From the region defined in Figure 7.2, the area estimate for the Lambert-Amery system is 1 550 400 km^2.

The locations of the 73 stations of the LGB traverse are also shown in Figure 7.2. These stations are numbered clockwise from west to east (see Figure 2.5). It can be seen that not all of the ice that flows across the LGB traverse line flows through the Amery Ice Shelf front; therefore not all of this ice belongs to the Lambert-Amery system. The portion of the traverse line that is contained in the Lambert-Amery system shall be termed the 'Lambert-Amery portion' of the LGB traverse line. From Figure 7.2, it is established that this portion of the traverse line starts at LGB05 and ends at LGB67. This is used in the balance flux calculations in the next section.

The second set of points in Figure 7.2 (downstream of the LGB traverse line) are the 1972-4 sites used by Allison (1979), (Figure 2.4). The section of the LGB traverse line contained within the catchment of the Allison's (1979) Lambert Glacier system shall be termed the 'Lambert Glacier system portion' of the LGB traverse line. The flowlines in Figure 7.2 that enter this part of the system pass through LGB11 on one boundary and LGB56 on the other. This information will also be used in the balance flux calculations.

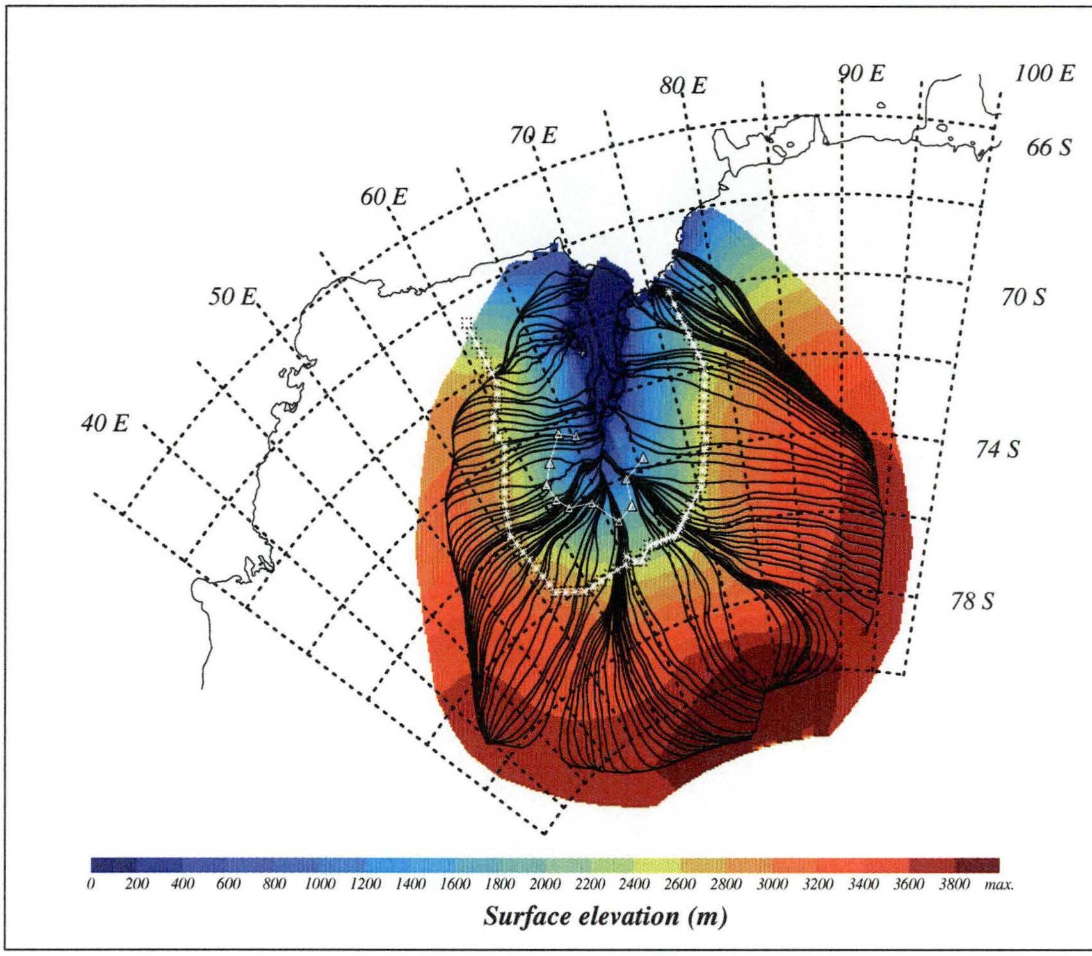

Figure 7.2 *Flowline trajectories for the Lambert-Amery system derived from the 35-km smoothed LAS-DEM (5-km resolution) defining the boundary of the Lambert-Amery system, superimposed on a contour map of the smoothed surface elevations. The stations of the LGB traverse and the earlier GL network of (Allison 1979) are also shown.*

7.3.3 Balance fluxes

This subsection describes the computation of balance fluxes for the Lambert-Amery system.

Balance flux equations

The balance flux is a conceptually simple quantity that, when computed over an entire glacier system, provides information on the nature of its drainage. When compared with fluxes derived from *in situ* velocity and thickness measurements, balance fluxes provide information on the local state of balance.

The balance flux concept is based on the assumption that a glacier system is in exact balance (Budd *et al.* 1971). That is, the mass of ice entering an element of the system exactly equals that leaving, and the dimensions of the system remain constant. The system is also said to be in 'steady-state' (Paterson 1994).

The balance flux concept has been described by Budd and Warner (1996). Consider a glacier system defined over a horizontal (x,y) domain. If the system is in exact balance, the flow of ice out of any closed area *S* within the domain (Ψ_{out}) is equal to the sum of the flow into *S*, (Ψ_{in}) and the areal integral of the net surface accumulation *a(x,y)* over *S* (see Figure 7.3), i.e:

$$\Psi_{out} = \Psi_{in} + \iint_S a(x,y)\, d\sigma \qquad (7.3)$$

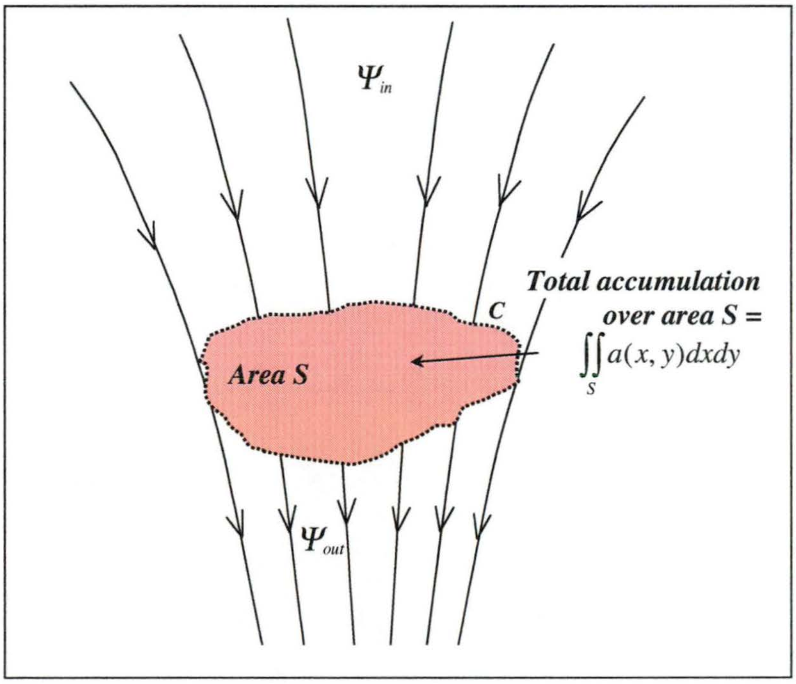

Figure 7.3 *Simple schematic diagram to illustrate the balance flux concept. The flux density leaving the closed area S is equal to the sum entering it, plus the integrated accumulation over S (see Equation 7.3).*

The integrated accumulation over the cell is exactly matched by the transport of mass that flows across the boundary of the S, C i.e.:

$$\Psi_{out} = \Psi_{in} + \int_C \underline{V}(l)\, Z(l) \cdot \underline{\hat{n}} dl \qquad (7.4)$$

where $\underline{\hat{n}}$ is the unit normal to the curve C

$\underline{V}$ is the column-averaged velocity vector

Z is the ice thickness.

The quantity $\underline{V}\,Z$ in Equation 7.4 is a continuous vector field $\underline{\Phi}_B(x,y)$ defined over the domain, referred to as the 'balance flux distribution', i.e.:

$$\underline{\Phi}_B(x, y) = \underline{V}(x, y) Z(x, y) \qquad (7.5)$$

Balance flux algorithm

A computational scheme for the calculation of balance-flux distributions has been developed by Roland Warner of the Antarctic CRC (Warner 1998). This code is based on an earlier version described in Budd and Warner (1996). The Warner (1998) algorithm requires as input two files of gridded data (on the same grid): one containing surface elevation, and the other containing an accumulation distribution.

The implied down-slope balance fluxes out of each grid cell are then calculated from the slope directions, derived from the DEM. The DEM must have an appropriate grid cell size, chosen so that there is sufficient topographic detail in the surface, yet so that slopes are averaged on appropriate length scales, as described above. The algorithm outputs a balance-flux distribution for the entire grid (magnitude, $|\underline{\Phi}_B|$, and direction), plus two 'staggered' grids Φ_x and Φ_y containing the component fluxes.

The algorithm solves the set of balance flux equations:

$$\int_C \underline{V}(l)\, Z(l) \cdot \underline{\hat{n}} dl = \iint_S a(x, y) dxdy \qquad (7.6)$$

for each DEM cell.

The following assumptions are made in the balance flux algorithm (Budd and Warner 1996):

i) The ice flow direction is orthogonal to the surface elevation contours, i.e., follows the surface slope. Therefore, the input DEM must be smoothed on an appropriate horizontal scale.

ii) The ice flow direction vector can be resolved into orthogonal components (x, y) which can be represented by finite-difference schemes to the resolution of interest.

Since the flow direction is prescribed by the DEM, the set of flux balance equations in each grid cell enables the magnitude of the flux to be found in each cell. The set of equations couples together the flux magnitudes of neighbouring cells. The algorithm used here removes the complication of solving this coupled system, and at the same time efficiently incorporates the flow direction information from the DEM.

The balance flux algorithm (Warner 1998) works with a scalar quantity, the outflow rate of ice from a grid cell ($\Psi_{i,j}^{out}$). Separating the boundary flux integral around the cell into inflow and outflow (an individual edge of a cell can only have inflow *or* outflow across it), the balance equation for the grid $cell_{i,j}$ becomes:

$$\Psi_{i,j}^{out} = a_{i,j} l^2 + \Psi_{i,j}^{in} \qquad (7.7)$$

where l is the cell size (5 km).

The balance flux algorithm uses a 'centred-difference' scheme whereby an individual grid cell, $cell_{i,j}$, has four neighbours ($cell_{i-1,j}$, $cell_{i+1,j}$, $cell_{i,j-1}$ and $cell_{i,j+1}$). The outflow

($\Psi^{out}_{i,j}$) from grid cell is apportioned to those neighbours that lie down-slope by dividing the total outflow from $cell_{i,j}$ by the ratio of their slope magnitudes, e.g. the contributing flow from $cell_{i,j}$ to $cell_{i,j+1}$ is:

$$\frac{h_{i,j} - h_{i,j+1}}{N} \Psi^{out}_{i,j} \qquad (7.8)$$

where $h_{i,j}$ is the surface elevation in $cell_{i,j}$

N is a normalisation factor to ensure that the outflow components sum to $\Psi^{out}_{i,j}$.

For each grid cell, the total scalar inflow of ice is the sum of the out-flowing contributions from neighbouring up-slope cells. This is achieved by sorting through the DEM cells by elevation and dealing with higher elevations first. Therefore, the total flow into each grid node is known from the contributions of all points up-slope, which have already been computed using Equation 7.7. This procedure yields the scalar flow field $\Psi^{out}_{i,j}$, i.e. a field of outflow at each grid node.

The quantity $\Psi^{out}_{i,j}$ is not a direct measure of the flux magnitude at each grid node, since the rate of ice flowing through a cell with side length l is related both to the flux magnitude, and the direction of flow through the cell. If the angle of the flow direction relative to the Y-axis of the grid is denoted by θ, then, taking the outflow from a cell as a good approximation to the flow through it, the flux magnitude ($\Phi_B = |\underline{\Phi}_B|$) is given by:

$$\Phi_B = \frac{\Psi^{out}_{i,j}}{l\left(|\cos\theta| + |\sin\theta|\right)}. \qquad (7.9)$$

A more accurate flux distribution is also calculated (by recent modification to the code), producing separate x and y-component fluxes (Φ_x and Φ_y) on 'staggered' grids (Roland Warner, personal communication, 1998). The flux components are defined on the corresponding links between grid nodes. These component fluxes are simply obtained by taking the apportioned outflows across the relevant cell boundary crossed by the link, and dividing by the cell edge length *l*. Each link occurs at most once in the progression down the elevations of the ice sheet (Roland Warner, personal communication, 1998).

The balance flux code (Warner 1998) was modified by the author for use with the 1400 x 1400 5-km grid format of the LAS-DEM. It was used to calculate balance fluxes for the Lambert-Amery system, from the LAS-DEM and six different accumulation distributions.

Accumulation distributions

Almost all of the precipitation that falls on the ice sheet becomes ice, which is subject to loss through surface processes such as evaporation, melting or run-off. The term 'accumulation' covers all methods by which mass is added to at the ice sheet's surface i.e. precipitation, evaporation, wind blown snow, formation of hoarfrost. It is also referred to as net surface balance (Vaughan *et al.* 1998) or net balance (Paterson 1994). Many attempts have been made to compile annual accumulation maps for Antarctica using various techniques. The main approaches used in deriving accumulation distributions are:

Observations

This is the traditional method, and has been used by many authors to compile continent-wide maps of accumulation based on *in situ* observations at accumulation stakes and from ice cores, e.g. Giovinetto and Bentley (1985); Budd and Smith (1982), Higham *et al.* (1997). There are many limitations with this technique, including the sparse sampling of the measurements (especially in the interior), seasonal biases introduced by differing observation periods and inconsistency in measurements between different field parties. In the last forty years, over 22 compilations of this kind have been presented (Vaughan *et al.* 1998). Three recent compilations of this kind were available for this study of the Lambert-Amery system: Budd and Smith (1982), Higham *et al.* (1997) and Vaughan *et al.* (1998). These were named 'BUDD', 'CRC' and 'BAS' respectively. Two of these distributions (CRC and BAS) have accumulation data from the Lambert Glacier traverse incorporated.

Moisture advection models

This is a heuristic approach to accumulation estimation, which uses no explicit atmospheric dynamics in its derivation (Oerlemans unpublished). The total atmospheric columnar water content *(W)* changes as a result of advection, evaporation, precipitation and diffusion. These models combine W and wind speeds from global meterological analyses to compute the moisture transport fluxes and divergences of flux. The net flux divergence yields the difference between the precipitation and the evaporation, which approximates the net accumulation. This technique has been adopted by (Budd *et al.* 1995), using the Australian Bureau of Meteorology (BoM) Global Atmospheric Assimilation and Prediction Scheme (GASP) to synthesise many global observations of the atmosphere to infer moisture transport to Antarctica. The resulting accumulation distribution is used here (and named 'GASP').

Global climate models (GCMs)

Results from long term GCM simulations can produce information on annual total precipitation. A serious limitation in the past has been the low horizontal resolution of the models (King and Turner 1997). Different levels of bias in the models arise from the type of moisture transport scheme used and the horizontal resolution (Bromwich *et al.* 1995). A recent high-resolution (2° by 2°) CSIRO GCM run (T63) for the period 1950-91, constrained by historical sea surface temperatures, has provided a simulated accumulation distribution that is comparable with observations (Smith *et al.* 1998). This accumulation model has been used here (and named 'CSIRO').

Atmospheric models

Precipitation and evaporation fields can be obtained directly from numerical weather prediction models. Recently, the ECMWF forecasting model has been re-run for the years 1979-93 (Gibson *et al.* 1996) and these fields are available on CD-ROM. The resulting accumulation distribution obtained by subtracting the evaporation field from the precipitation field was obtained from Phil Reid of the Antarctic CRC for this work (and named 'ECMWF').

TABLE 7.1 SUMMARY OF ACCUMULATION DISTRIBUTIONS USED IN THE BALANCE FLUX CALCULATIONS. THE ACRONYMS SUPPLIED IN THE FIRST COLUMN WILL BE USED HEREAFTER.

Acronym	***Type***	***Reference***
BUDD	*observation*	*Budd and Smith (1982)*
BAS	*observation*	*Vaughan et al. (1998)*
CRC	*observation*	*Higham et al. (1997)*
CSIRO	*Global Climate Model*	*Smith et al. (1998)*
GASP	*moisture advection model*	*Budd et al. (1995)*
ECMWF	*atmospheric model*	*Phil Reid, personal communication (1998)*

The six different annual accumulation distributions used in the balance flux calculations are listed in Table 7.1. The distribution of accumulation over the Lambert-Amery system from one of these (BAS) is shown in Figure 7.4 (units are kg $m^{-2}a^{-1}$). Note that the accumulation is very low in the interior and increases towards the coast.

The accumulation distributions were interpolated onto the 1400 x 1400 5-km grid format of the LAS-DEM, so that they could be used in the balance flux algorithm in conjunction with the DEM. For four of the distributions (BUDD, BAS, GASP and CSIRO) this was straightforward, since they already existed on (different) polar stereographic grids and were simply bilinearly interpolated onto the LAS-DEM grid. The remaining two distributions (CRC and ECMWF) were interpolated using kriging in GSLIB (see Appendix A). For the CRC distribution, which existed as hand-drawn contours, the coordinates of the contour lines were used in the kriging algorithm. The ECMWF distribution was provided on a latitude/longitude grid (2.5° by 2.5°) and the coordinates of each grid point were used for the kriging.

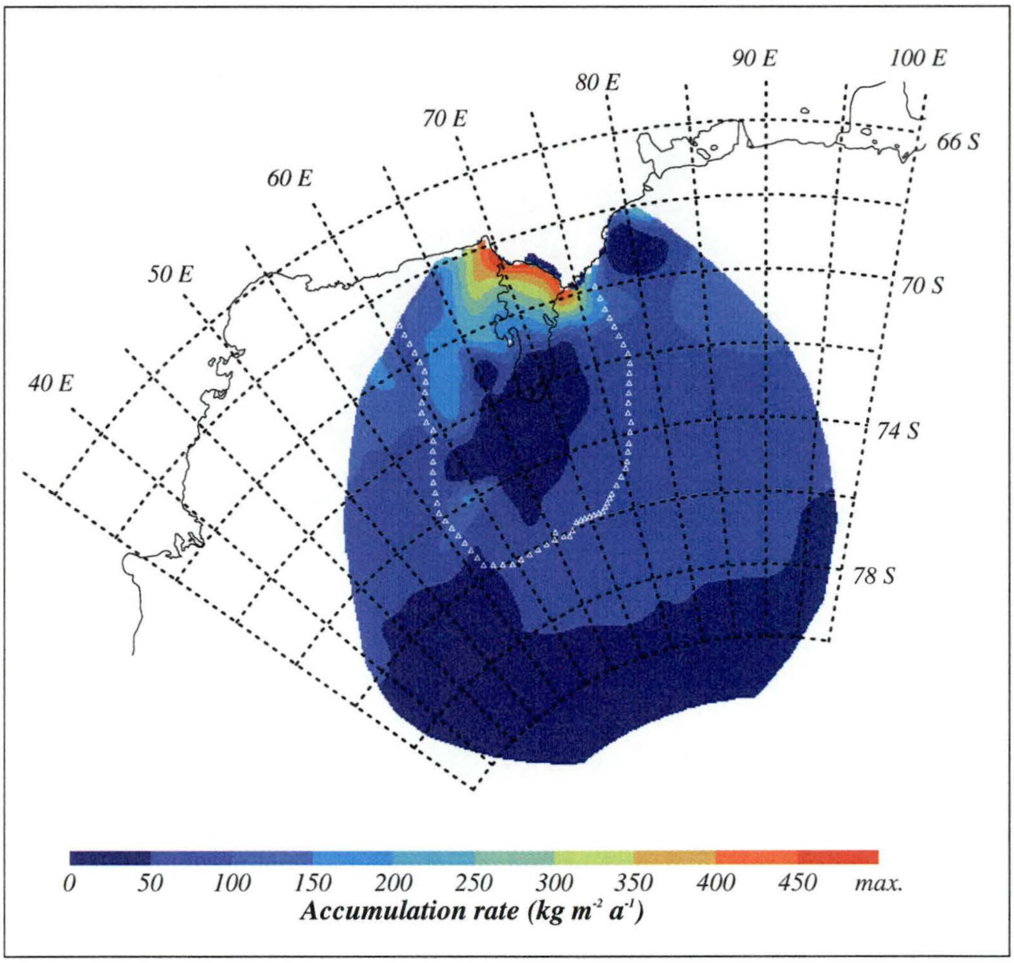

Figure 7.4 *Total net surface balance (in kg m^{-2}a^{-1}) for the Lambert-Amery system from the BAS compilation for Antarctica Vaughan et al. (1998).*

Results of balance flux calculations

The outputs of the Warner (1998) balance flux algorithm are a 5-km grid containing balance flow field, i.e the flow magnitude for each cell, and two 'staggered' grids containing the x and y-components of the flux (Φ_x and Φ_y). Maps of the computed balance flow fields for the Lambert-Amery system are presented (see also Appendix E) and discussed here. The balance fluxes are then compared with observed flux measurements made during the LGB traverse (Higham and Craven 1997; see Chapter 2).

Balance flux distribution over Lambert-Amery system

Balance fluxes were calculated for the Lambert-Amery system using the LAS-DEM, smoothed on the 15-km and 35-km spatial scales, and the six accumulation distributions of Table 7.1. As examples, the balance flux distributions calculated from the BAS accumulation distribution and the 15-km and 35-km smoothed versions of the LAS-DEM are shown in Figures 7.5a and b respectively. These plots are on a logarithmic scale.

These plots provide a powerful representation of the pattern of surface ice flow that would exist if the system were in balance. Note the streaming behaviour of the flow in topographic depressions, such as the Lambert Glacier depression (see Figure 5.19). The locations of the major streams are labelled (Lambert, Mellor and Fisher Glaciers) and can be seen as regions of higher flux. In these regions, the flow increases by several orders of magnitude. As the horizontal scale of the smoothing increases (bottom plot), the pattern of the balance flow becomes more coherent, confirming that 35 km is a more appropriate scale for averaging slope information for ice flow studies in this region. For this reason, balance fluxes derived from the 35-km smoothed version of the LAS-DEM are used to compare with observed fluxes.

The additional balance flux distributions from the other five accumulation distributions for the 35-km scale of smoothing are presented in Appendix E. Since the maps are all derived from the same DEM, the location of the major streams is always the same. Only the *relative* flux contribution changes, because of the differing accumulation patterns. Similarly, for each accumulation distribution, the total integrated balance flux over the whole Lambert-Amery system is the same, but the flux is apportioned slightly differently for each level of smoothing due to the different basin shape.

Comparison with observed fluxes at observation points along LGB traverse

During the Lambert Glacier traverses of 1991-95 (see Chapter 2) measurements were made of surface ice flow velocity magnitude and azimuth (V_s, θ) and ice thickness (Z).

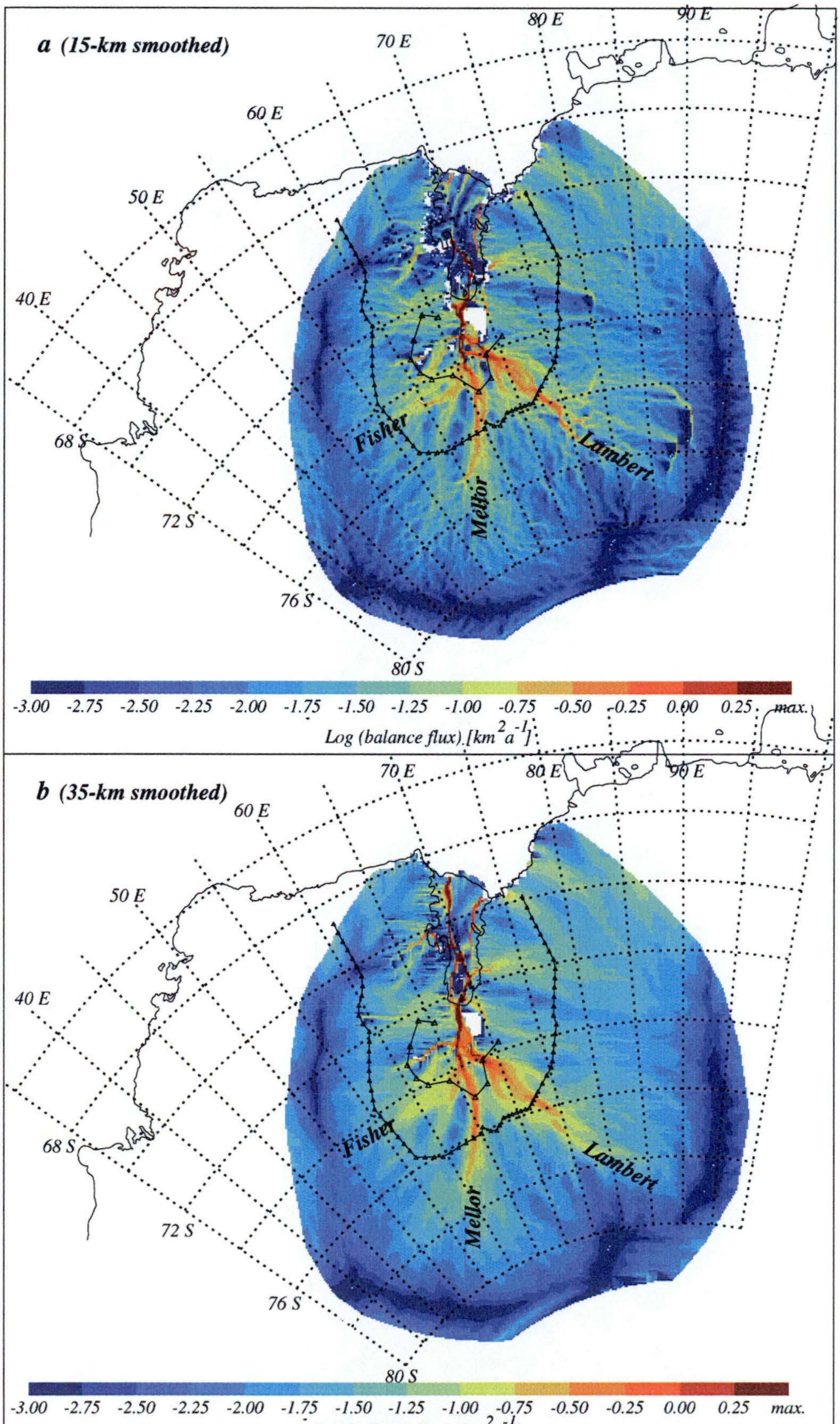

Figure 7.5 *Computed balance flux distributions (log scales) derived from the LAS-DEM smoothed on a scale of a) 15-km and b) 35-km and the BAS accumulation distribution. Locations of ice stations are also shown (black triangles).*

These observations were used to calculate 'observed' fluxes around the LGB traverse. The total integrated flux between stations LGB05 and LGB69 is an estimate of the total flux crossing the Lambert-Amery system portion of the LGB traverse line (Figure 7.2). This number, when compared to the total integrated balance flux between the same stations, gives an idea of the state of balance of the system.

At each LGB station, computed balance fluxes were interpolated from the flow grid using a bilinear interpolation scheme. The observed 'local' or 'spot' flux was obtained from the product of the surface velocity, the ice thickness and a surface velocity factor of 0.87. The surface velocity factor is a ratio of the depth averaged column velocity (V) to surface velocity (V_s), which accounts for the fact that velocity decreases with depth. The value of 0.87 used here for the surface velocity factor is after Hamley *et al.* (1985).

The comparison of computed balance fluxes with observed fluxes was carried out using cartesian coordinates (x, y) in a polar stereographic projection. It was assumed that each line segment between LGB stations has a constant ice thickness, equal to the average of the thickness for the two stations at either end of the segment. It was also assumed that the x- and y-components of the velocity are constant for each segment, the value being equal to the averaged x- and y- velocity components from each station.

Stations along the LGB traverse were mainly around 30 km apart, with some being only 15 km apart across the major streams (Higham and Craven 1997). The most accurate way to compare balance fluxes with observed fluxes is to calculate the component of the observed flux orthogonal to the traverse line for each line between-station line segment, using simple vector geometry (Figure 7.6), and then to calculate the corresponding component of the balance flux.

The velocity parameters measured at each LGB velocity station were magnitude V and azimuth β (the direction relative to Grid North). This was converted to an angle θ relative to the polar stereographic X-axis using the relation:

$$\theta = \beta + \lambda$$

where λ is the longitude of the LGB station.

The x and y components of the observed surface velocity, u and v, were derived at each station using $u = V\cos\theta$ and $v = V\sin\theta$. The resultant observed velocity vector at each station was $\mathbf{V} = u\mathbf{i} + v\mathbf{j}$.

For each line section, the average observed velocity was derived at the mid-point of the section by the average of the x and y components of the observed velocity from the stations at either end of the segment, i.e.:

$$\underline{V} = \frac{(u_n + u_{n+1})}{2}\mathbf{i} + \frac{(v_n + v_{n+1})}{2}\mathbf{j} \qquad (7.10)$$

The observed flux vector ($\underline{\Phi}$) through this segment is calculated from this velocity using the following equation:

$$\underline{\Phi} = 0.87 * \underline{V} * L * \overline{Z} \qquad (7.11)$$

where 0.87 is the surface velocity factor

L is the length of each segment (in km)

$\overline{Z}$ is the average thickness for the segment (in km)

The quantity that is required to determine the total flux across the LGB traverse line is the component of $\underline{\Phi}$ that is orthogonal to the line. This is calculated from the scalar product of $\underline{\Phi}$ with the unit normal to the traverse line ($\underline{\hat{n}}$) (see Figure 7.5). The unit normal is easily derived from the equation of the line segment, defined by the difference in coordinates of the LGB stations at each end. The observed orthogonal flux component *(ψ)* is given by:

$$\begin{aligned} \psi &= \underline{\Phi} \cdot \underline{\hat{n}} \\ &= \Phi \cos\phi \end{aligned} \qquad (7.12)$$

where ϕ is the angle between the observed flux vector and the unit normal.

The orthogonal components of the observed fluxes were calculated for each of the 72 line segments between the 73 LGB stations.

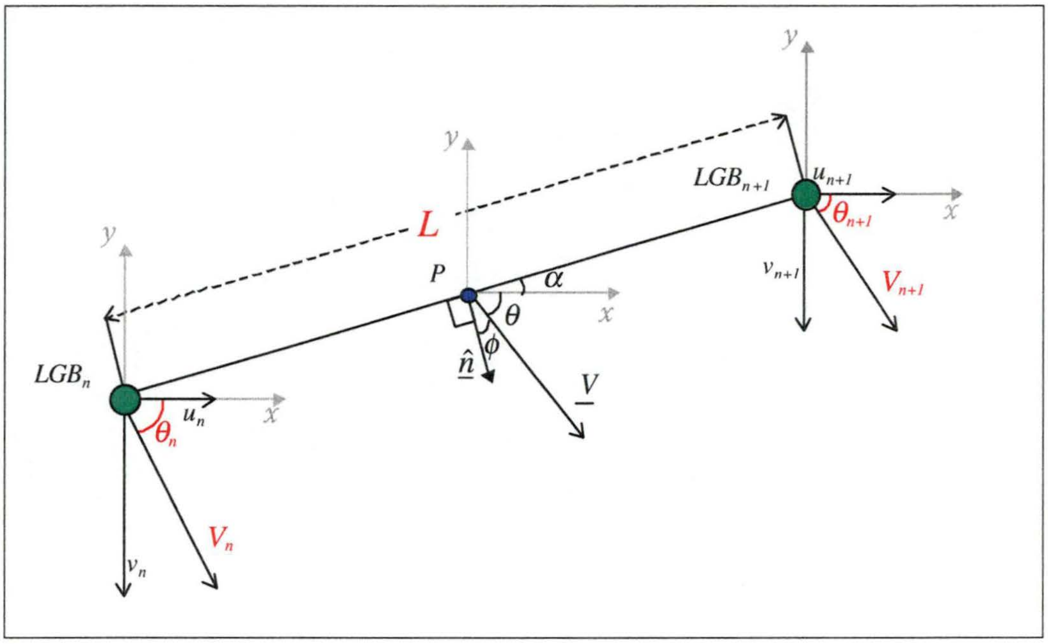

Figure 7.6 *Calculation of orthogonal component of observed flux for the n^{th} segment between two LGB stations, LGB_n and LGB_{n+1}. The parameters in red text were measured during the LGB traverse i.e. velocity magnitude (V_n, V_{n+1}) and angles (θ_n, θ_{n+1}) and segment length (L). At the midpoint of the segment (P) the component of the averaged velocity orthogonal to the traverse line is given by the dot product of the averaged velocity $\underline{V}$ with the unit normal to the traverse line ($\hat{\underline{n}}$). The angle between the velocity vector and the unit normal is ϕ, where $\phi = 90\text{-}\theta\text{-}\alpha$.*

To calculate the corresponding component of the balance flux for each LGB segment, the staggered flux grids (Φ_x and Φ_y) were used to construct the balance flux vector for the midpoint of each segment. The component of this vector orthogonal to the LGB line was calculated by taking the dot product of the balance flux vector at the mid-point of each sector with the unit normal ($\hat{\underline{n}}$) to the traverse line.

The orthogonal components of the computed balance fluxes were calculated for each of the 72 line segments between the 73 LGB stations, for each of the six balance flux distributions. The resulting orthogonal flux components of the observed and balance fluxes through each of the LGB segments are plotted in Figures 7.7.

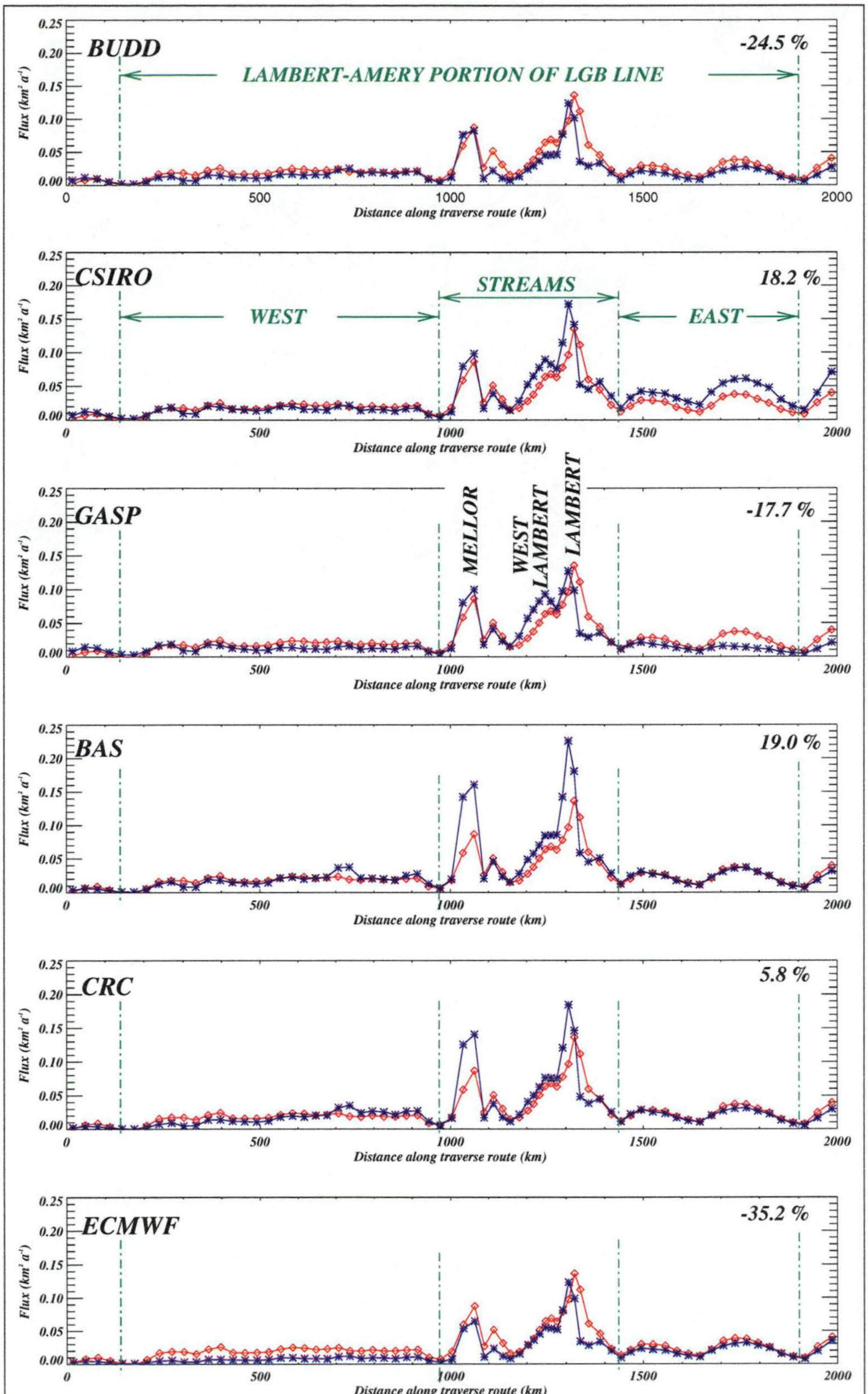

Figure 7.7 *Orthogonal components of measured fluxes (red) and balance fluxes for the six accumulation distributions (blue), for each segment of the LGB traverse line. The portions of the line contained within the Lambert-Amery system and the West, Streams and East sections of the system are indicated on the top two plots. Mass imbalance (%) estimates are given for each accumulation distribution (top right).*

The ice streams corresponding to maxima in these fluxes are labelled on the GASP plot. Note that in each plot, the observed and computed maxima are closely matched in location, although the magnitudes vary. This is because the total flux is apportioned by the surface slopes of the LAS-DEM. The differing magnitudes arise from the different accumulation distributions.

Integration of fluxes along the LGB traverse line line resulted in a total *volume* flux (in km^3a^{-1}). This was converted into a *mass* flux (in Gt a^{-1}) by multiplying by the density of ice (917 kg m^{-3}). The total integrated observed flux orthogonal to the LGB line across the Lambert-Amery portion of the line (LGB segments 5 to 67, see top plot of Figure 7.6) is 44 Gt a^{-1}. The total integrated balance flux orthogonal to the LGB line, interpolated to the mid-point of each segment, was calculated for each balance flux distribution. The percentage imbalance derived from the ratio of the total observed flux to the total balance flux, is located in the top right of each plot in Figure 7.7. These values have a large range, from -35.2% (ECMWF) to 19% (BAS). The mean of these values is -5.7% with a standard deviation of 23.2%. Negative percentage values refer to negative budget (i.e. observed fluxes larger than computed balance fluxes) whilst positive ones refer to positive budget. Using the mean value, the system is very close to balance. However, the estimates from the six individual distributions exhibit a large variation.

As well as providing different estimates of the state of balance of the Lambert-Amery system, the plots in Figure 7.7 also indicate that there are large differences in the distribution of the balance fluxes along the LGB line. Different upstream regions appear to be in different states of balance, depending on the accumulation distribution used. To examine the variation in imbalance estimates for each balance flux distribution across the Lambert-Amery portion of the LGB line, the portion was divided into three segments: 'East', 'Streams' and 'West' (see Figure 7.7, second plot). In the BAS plot, the flux values in the East section are very well matched, however the accumulation in the Streams and West sections are not so well matched. For the CSIRO distribution, balance fluxes in the West section are closely matched to the observed fluxes, whereas in the East section they are very different. Conversely, for the ECMWF distribution, the balance fluxes are much lower than the observed fluxes in the West section, and very closely matched in the Eastern section.

The total integrated orthogonal component of the flux from the measurements (in Gt a^{-1}) is given in the second row of Table 7.2, for the three segments West, Streams and East, and the entire line. The relative imbalances derived from the six different balance flux distributions are also given. These values further confirm the regional variability in imbalance estimates along the LGB line.

TABLE 7.2 *TOTAL INTEGRATED ORTHOGONAL COMPONENT OF THE OBSERVED FLUX ACROSS THE LAMBERT-AMERY PORTION OF THE LGB LINE (EAST, WEST, STREAMS AND TOTAL), TOGETHER WITH THE IMBALANCE RATIOS (%) DERIVED FROM THIS FLUX AND THE TOTAL INTEGRATED BALANCE FLUX FROM THE SIX BALANCE FLUX DISTRIBUTIONS.*

	WEST	***STREAMS***	***EAST***	***TOTAL***
Observed Flux (Gt a^{-1})	*13.7*	*22.0*	*8.6*	***44.4***
Imbalance (%)				
BUDD	*-22.9*	*-24.2*	*-27.7*	***-24.5***
CSIRO	*-16.3*	*19.2*	*70.6*	***18.2***
GASP	*-31.1*	*2.6*	*-48.3*	***-17.7***
BAS	*2.0*	*38.8*	*-4.1*	***19.0***
CRC	*-5.6*	*19.5*	*-11.0*	***5.8***
ECMWF	*-62.7*	*-25.8*	*-15.1*	***-35.2***

The Lambert-Amery portion of the LGB line and the *East*, *West* and *Streams* portions of this line are defined in Figure 7.7. A negative imbalance percentage implies that the total flux from the measurements exceeds that from the balance flux computation.

A full critical comparison of the six accumulation distributions is beyond the scope of this thesis. However, results presented in Figure 7.7 and Table 7.2 do suggest that some of the accumulation distributions may be incorrect in some parts of the Lambert-Amery system. Since the balance flux across each sector is the integrated accumulation over the catchment for that section (see Figure 7.2), zones where accumulation distributions disagree can be identified by direct comparison of fluxes at the LGB line. Some of the accumulation distributions produce a balance flux distribution that suggests local thickening on one side of the traverse and local thinning on the other. There is no plausible reason for this, suggesting that those accumulations are incorrect in some regions. The large variation in the state of imbalance along the traverse line for the various accumulation distribution confirms that insufficient knowledge of the accumulation distribution is the most significant gap in the quantification of the mass balance of the Antarctic ice sheet.

Comparison of 'continuous' balance fluxes along traverse line

Since balance fluxes were calculated on a 5-km grid, there is more detail contained in the balance flux grid along the LGB traverse line than that shown in Figure 7.7. A more complete estimate of the balance flux across the LGB line is obtained by dividing each between-station segment into ten equal portions, approximately ~3 km (i.e. approximately the same as the cell size) and interpolating the flux field to these 'continuous' points. This was done for each balance flux distribution. The resulting 'continuous' distribution of balance flux *magnitudes* along the line derived from each accumulation distribution and the 35-km smoothed DEM are shown in Figure 7.8, together with the *magnitudes* of the observed fluxes at each LGB station.

These plots provide a more detailed representation of the flux entering the Lambert-Amery system across the traverse line than those of Figure 7.7. The total flux across the Lambert-Amery portion of the LGB line is the integral of the orthogonal component of the flux at each interpolated point. The total integral of balance fluxes along this line is equal to the total accumulated accumulation deposited over the portion of the Lambert-Amery basin upstream of the Lambert-Amery portion of the LGB line.

The values of the total integral along the traverse line of balance fluxes using this continuous distribution are slightly higher than those obtained from the LGB segment values, since the sampling is higher here. This is the top number in the right corner of each plot in Figure 7.8. The values range from 29.6 Gt a^{-1} (ECMWF) to 54.3 Gt a^{-1} (BAS). The mean and standard deviation of these values are 43.2 Gt a^{-1} and 10.6 Gt a^{-1}

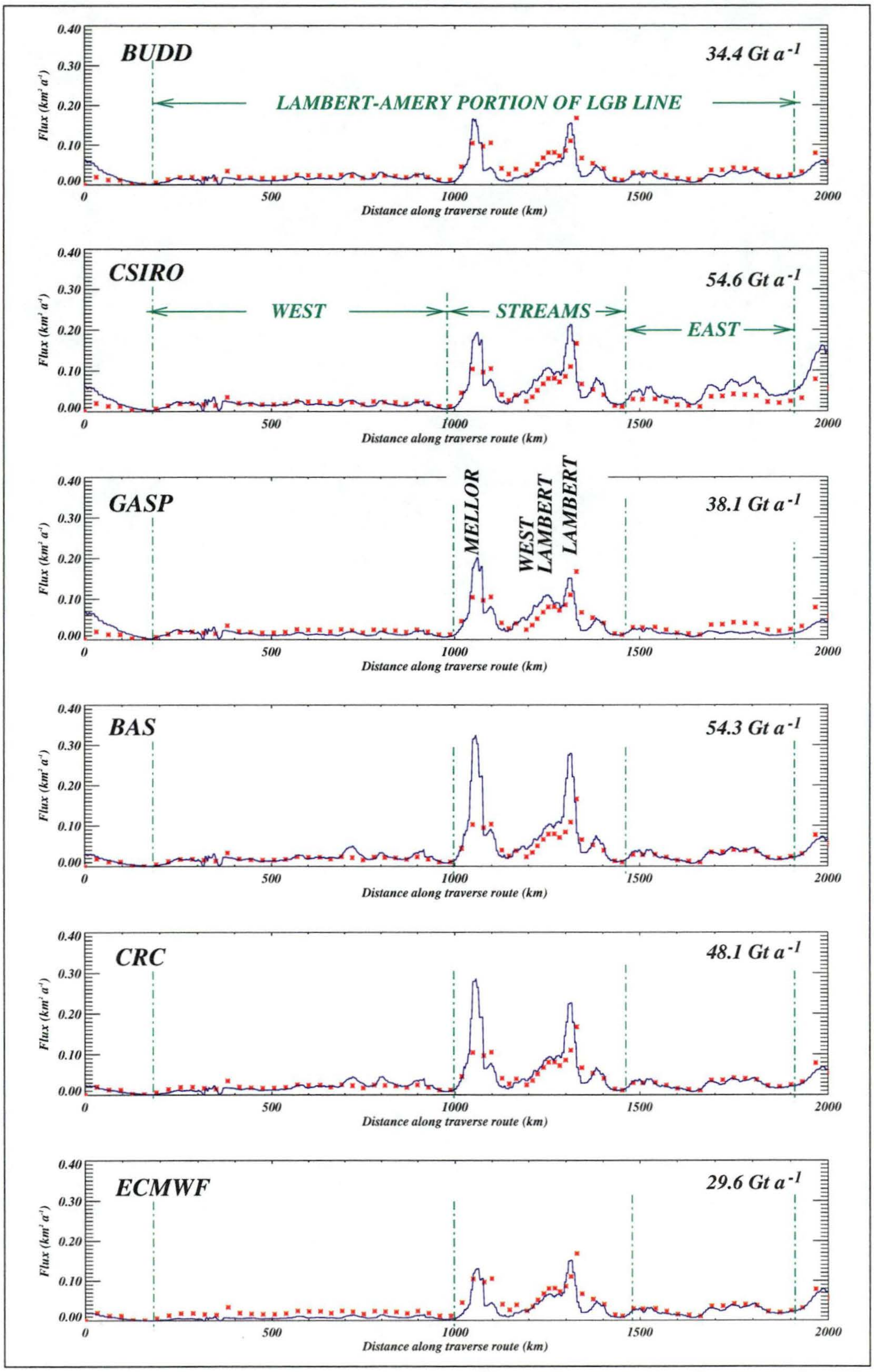

Figure 7.8 *Magnitude of balance flux interpolated between LGB stations for the six accumulation distributions (blue) and the magnitudes of the measured fluxes at each LGB station (red). The numbers on the right are the total balance flux entering the Lambert-Amery system and the average ratio of measured to balance fluxes at the LGB stations.*

respectively. From the results presented in Figure 7.7 and 7.8, it appears that the ECMWF distribution is underestimating the accumulation for the Lambert-Amery system.

Comparison of balance fluxes further downstream

Earlier *in situ* measurements of ice velocity and thickness are also available for the 11 sites (GL1-GL11) used in Allison's (1979) mass budget estimates (see Chapter 2). These sites, 50-100 km apart, define the perimeter of Allison's (1979) Lambert Glacier system, which is approximately 200 km downstream of the LGB traverse route (Figure 2.4). The station locations were chosen to give a representative sample of the ice flow into the Lambert Glacier system, three of the stations being placed upstream of each of the three major ice streams (Allison 1979). The same procedure as that described above for the LGB traverse was adopted to compare the continuous balance fluxes across the GL line with the measurements at each GL station.

For the six balance flux distributions (derived from the 35-km smoothed LAS-DEM), balance fluxes were interpolated at 30 points in between each GL station. Figure 7.9 illustrates the interpolated balance flux magnitudes, together with the spot values of the observed flux at each GL station. The numbers in the top right corner of these plots are the total integrated balance flux orthogonal to the GL line.

The total integrated balance flux across the GL line ranges from 27.4 Gt a^{-1} (ECMWF) to 56.6 Gt a^{-1} (BAS). The values have a mean and standard deviation of 41.8 Gt a^{-1} and 10.8 Gt a^{-1} respectively. The total mass flux across the line computed by Allison (1979) was 29.7 Gt a^{-1}, which lies within the balance flux range from the six different accumulation distributions. The combination of these results suggests that the mass budget of this part of the Lambert-Amery system is slightly positive. Comparing the mean balance value of 41.8 Gt a^{-1}, with Allison's (1979) observed value of 29.7 Gt a^{-1}, the system is 40% out of balance.

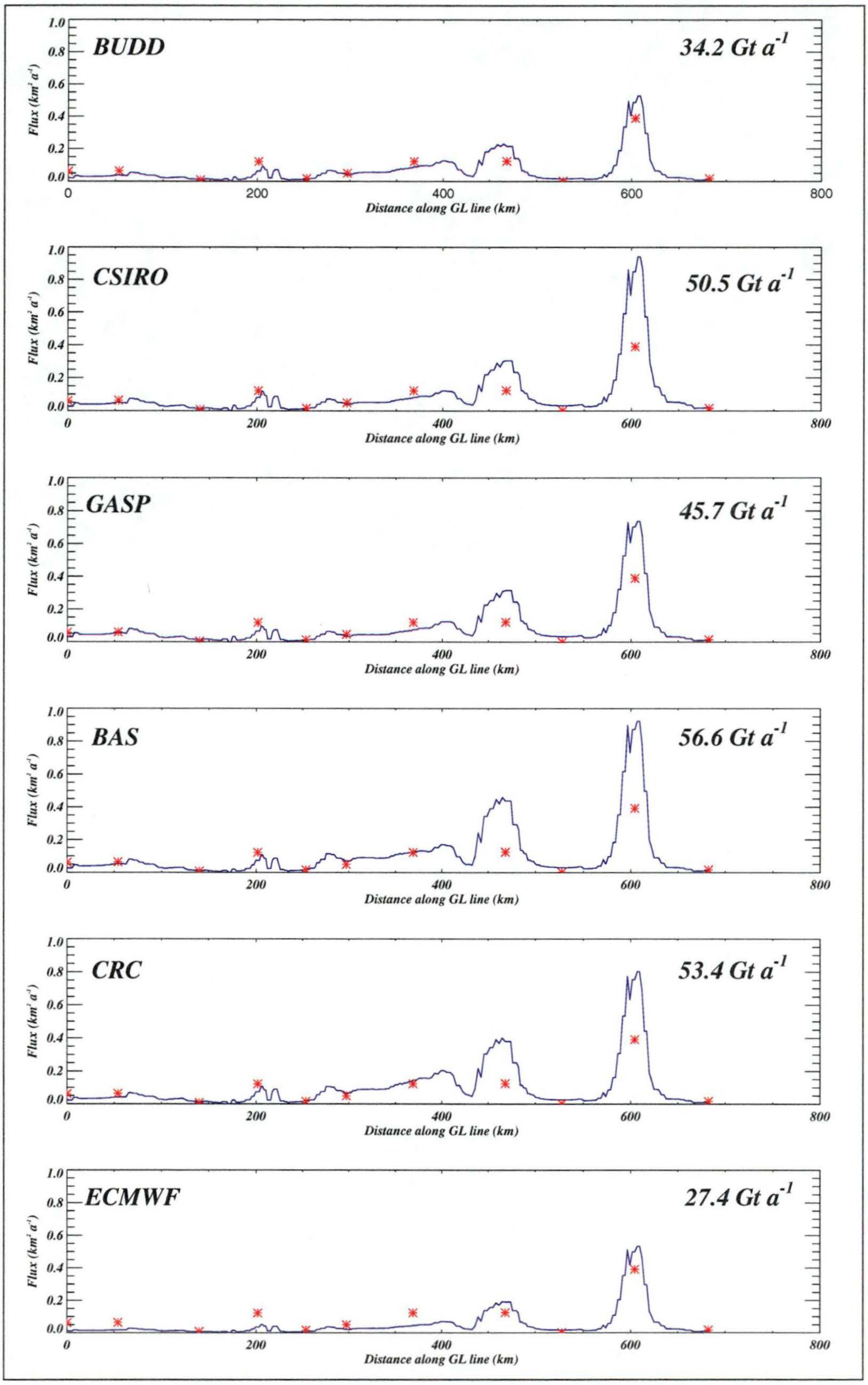

Figure 7.9 *Magnitude of balance flux interpolated between the Allison (1979) GL sites for the six accumulation distributions (blue) and the magnitudes of the measured fluxes at each GL site (red). The numbers on the right are the total balance flux crossing the GL line and the average ratio of measured to balance flux at the GL sites.*

In the section of the GL line from distance 0 to 550 km, the balance fluxes for all of the distributions except ECMWF are remarkably similar. This confirms that the ECMWF distribution is underestimating the amount of accumulation.

The highest fluxes occur in the same location for each set of fluxes (both balance and observed). This region of high flux corresponds to GL 10, which was positioned on the Lambert Glacier (Allison 1979). This occurs despite the fact that the geographic positions contained in the RES data used by (Allison 1979) were only accurate to 5 km (Morgan and Budd 1975). The agreement in observed and computed flux maxima also verifies the location of the Lambert Glacier derived from the LAS-DEM. These results clearly demonstrate that computed balance flux distributions can be used to interpolate between spot measurements, in regions where no observations exist.

7.4 Chapter conclusions

This chapter has demonstrated applications of the 5-km LAS-DEM product presented in Chapter 5. The LAS-DEM was smoothed on horizontal scales of 15 and 35-km to remove some of its topographic detail and provide a more realistic representation of the large-scale surface slope that drives ice flow (Budd 1968).

Ice flowline trajectories were computed from the slopes provided by the 35-km smoothed version of the LAS-DEM. These provided a detailed representation of the flow field within the Lambert-Amery system. Some of the flowlines were used to define the boundary of the Lambert-Amery system.

Balance fluxes were computed by combining six different accumulation distributions with the 15-km and 35-km smoothed LAS-DEM. Maps of the flux magnitudes clearly located the regions of higher flux (the ice streams). The 35-km level of smoothing led to a more realistic representation of the ice flow. Interpolated balance fluxes and observed fluxes were compared at the 73 stations of the LGB traverse. The total flux across each traverse line segment was computed, with the total integrated orthogonal flux value from the measurements being 44.4 Gt a^{-1}. The imbalance estimates derived from the balance fluxes range from -35.2% to 19.0%. These numbers indicate that estimates of the mass budget of the system vary greatly, depending on the

accumulation distribution used to calculate the balance fluxes. The imbalance estimates were also demonstrated to vary greatly in different portions of the LGB line for each accumulation distribution.

Further downstream, observed and computed fluxes were compared at GL stations of (Allison 1979). The total amount of balance flux across the GL line ranged from 27.4 Gt a^{-1} to 56.6 Gt a^{-1}, with a mean of 41.8 Gt a^{-1}. This compares with Allison's (1979) previous estimate of 29.7 Gt a^{-1}, derived from observations. These values suggest that this part of the system may be slightly positive. Comparing the mean value with the observed value, the system is 40% out of balance.

The balance flux technique has been used to estimate the mass budget of the Lambert-Amery system. Balance fluxes computed from six accumulation distributions led to widely varying imbalance estimates for the system. It is clear that more work is needed in estimating accumulation distributions for large regions of Antarctica. This represents the most significant gap in mass balance estimates. Despite this limitation, the balance flux technique was successfully applied to interpolate flux values between measurement stations. This is useful in regions where few measurements exist.

Chapter 8

Retrieval of surface properties from ERS-1 waveforms over the Lambert-Amery system

8.1 Introduction

The previous three chapters have demonstrated the retrieval of topographic information over Lambert-Amery system, and its subsequent application. The results illustrate the value of consistent, extensive surface topographic information over Antarctica. The construction of these types of topographic maps is the primary contribution of satellite radar altimetry to Antarctic research. Altimeters are also capable of providing information on additional surface properties over the ice sheets, which is the subject of this chapter.

The satellite radar altimeter records the portion of the waveform pulse received from the surface (the return waveform) in a series of range bins (see Chapter 3). The shape of this waveform is determined by the instrument parameters and the physical properties of the scattering surface (Ridley and Partington 1988). These properties can be estimated from the waveform using models that describe the instrument and the surface microwave properties. Changes in shape of waveforms received from the ice sheets both spatially and temporally result from changes in surface or near-surface properties over the sampling interval. Such investigations of surface characteristics are potentially useful for monitoring glaciological systems, and for detecting change. In this chapter, the retrieval of physical information from the radar altimeter waveforms is attempted over the Lambert-Amery system.

This chapter is divided into three sections. The first describes the retrieval of surface properties from waveform models. An outline of the assumptions made in waveform modelling is presented, and existing models discussed. In the second section, a waveform model is used to retrieve surface properties for the Lambert-Amery system from ERS-1 waveforms. Derived parameters are averaged on two scales: 50-km grid for the whole system, and 25-km along track for the Amery Ice Shelf only. In each case, the spatial patterns are presented and discussed. The third section investigates the cause of a sudden change in waveform shape, from a typical ice shelf return to a quasi-specular return, which occurred on the Amery Ice Shelf in January 1994. It is deduced that the change in surface conditions was caused by presence of meltwater on the shelf. The variability of the melt season is investigated by comparing data from the 1991-92 and 1993-94 summers. By locating all occurrences of this quasi-specular return in ground tracks that cross the Lambert-Amery system, the locations of meltstreams sampled by the ERS-1 altimeter for the summers from 1991-92 to 1995-96 are determined.

8.2 Surface properties from altimeter waveforms

To introduce the concept of retrieving surface geophysical parameters from altimeter waveforms, it is necessary to recall some of the theory discussed in Chapter 3. The return pulse shape (waveform) is governed by the nature of the surface interacting with the transmitted pulse. The case for an ideal (Lambertian), planar surface is simple (see Figure 3.3), as all of the incident energy is reflected isotropically. In reality, however, the interaction with ice is much more complex than this, so that some of the incident radiation is scattered, some transmitted through the surface layer, and the rest reflected back in the direction of the receiver. The varying magnitudes of these components depend on the surface geometry (roughness and topography) and geophysical characteristics of the surface (temperature; density; grain-size and shape; and moisture content). The shape of the waveform is modified accordingly. It follows that information about the surface is therefore contained in the waveform of the returned pulse. The deconvolution of such information is often non-unique, however, since many parameters affect the waveform shape in a similar manner, making it difficult to separate them, e.g. snow grain-size and density have similar effects on the waveform shape (Partington *et al.* 1989).

8.2.1 The nature of an ice sheet surface

The surface of the Antarctic ice sheet is statistically inhomogeneous, and its radar properties are far from 'ideal'. The top few metres of the snow cover are subject to many different physical processes, which are mainly a result of its interaction with the atmosphere. The effects of these processes are spatially variable. The transmitted pulses interact with many different types of surface and sub-surface inhomogeneities as the satellite moves over the ice sheet. Since the return waveform represents the interaction of the radar pulse with both the surface and the top layer of the snow pack, its shape exhibits large spatial variability.

On the surface, roughness at all scales within the footprint diameter (5-10 km) affects the altimeter return (Ridley and Partington 1988). Topographic features on this scale over grounded ice include undulations related to the flow of ice over bedrock topography (McIntyre 1986). Examples of features on this scale also occur in floating ice include: surface depressions and flow features (like those seen in the AIS-DEM, Figure 5.13); surface rifts (Ridley *et al.* 1989); and large crevasse fields (Partington *et al.* 1987).

Smaller-scale surface roughness, with amplitudes of 10-1000 mm and wavelengths on the scale 1-1000 m, also significantly modulate the altimeter return shape (Rapley *et al.* 1985). Such microrelief features occur all over the ice sheet, in many varying forms that have been classified into three type classes by (Fujiwara and Endo 1971). Depositional features, such as stationary longitudinal dunes, are formed during precipitation. Such features, with a 1 m amplitude and varying lengths, have been observed in Wilkes Land (Goodwin 1990). Reshuffling type features, such as snow banks and snow dunes, are formed from drifting snow. These features also occur extensively in Wilkes Land, with an average height of 0.3 m (Goodwin 1990). Erosional type features (sastrugi) are formed from exposure of surface snow to the dominant surface wind. Observations of surface microrelief types made during the Lambert Glacier Traverse indicate that the majority of surface forms are of the erosional type and vary greatly in amplitude, from 0.1 m to 1.0 m (Higham and Craven 1997).

Surface crusts, characterised by much higher snow density than the underlying snow, often form over portions of the ice sheet. This increases the dielectric constant at the surface, which in turn increases the amount of surface scattering. The presence of a crust can also affect the small-scale surface roughness, and therefore the measured radar backscatter (Ridley and Bamber 1995). Three mechanisms are responsible for the formation of surface crusts during periods when there is no precipitation (Barkov 1985). Wind-induced crusts are very thin (0.2-1 mm), and formed through the compaction of the snow by wind, and subsequent condensation of water vapour on the surface. Solar-induced crusts form during the summer months, and these can be several millimetres thick. Surface crusts (known as ice rind) can also occur in winter through precipitation of the finest supercooled water droplets from low-lying clouds.

The snow pack itself is a complex dielectric medium. The top few metres of ice shelves and ice sheets are often stratified and contain well-defined layers of different densities. The stratigraphy in the upper portion of the surface can substantially influence the shape of a radar altimeter return pulse (Jezek and Alley 1988), as it changes the travel time of reflected radiation through multiple internal reflections within the layers and transmission at their interfaces. Stratification can occur as a result of several processes. In regions that are subject to summer melting, sedimentary bands consisting of alternating thick layers of bubbly ice formed from winter snow and thin layers of clear ice formed from refrozen meltwater (Paterson 1994). Melt water percolates into the snow and then refreezes. If the water meets a layer that is relatively impermeable, it will spread out instead of percolating any deeper (Paterson 1994). Refreezing of meltwater results in a discrete layer known as an ice layer, or an ice lens. Channels created by vertical percolation of meltwater also refreeze forming ice glands. Snow pits on the Amery Ice Shelf have revealed considerable stratification in the top portion of the firn, including the presence of melt-layers (Landon-Smith 1962). Surface cores drilled along the ~2200 km Lambert Glacier traverse route showed that the number of discrete ice crusts per metre varied from zero to 9 with a mean of 3.75 (Higham and Craven 1997).

One additional notable feature often found in the snow pack is depth hoar. Under certain conditions, near-surface snow can be transformed into large prism-shaped crystals through sublimation. This can occur in autumn when air temperatures drop, rapidly cooling the surface layer. Since the underlying layers are still relatively warm, a temperature gradient is formed, leading to vapour diffusion. Evaporation in the lower layers leads to vapour rising and condensing in the snow layer, which results in depth hoar crystals in the colder surface layers. The process usually takes place in autumn (Paterson 1994) but has also been observed in Greenland in the summer via radiative heating of the upper snow layers (Alley *et al.* 1990). Depth hoar was detected in many of the pits dug during the Lambert Glacier traverse, especially at those stations south of 73°S, which caused the internal structure of the firn layer to be partially or wholly destroyed (Higham and Craven 1997).

8.2.2 Altimeter waveform models

Given the many physical parameters contributing to the shape of an altimeter waveform, both on the surface and in the top few metres of the snow pack, it may appear to be an impossible task to try to develop a model capable of separating all of their effects. To simplify the problem, the approach generally taken is to make several assumptions about the surface and the scattering processes involved. This is followed by spatially averaging many waveforms to obtain large-scale estimates of parameters, e.g. Davis and Zwally (1993).

Assumptions

Several models for recovering surface parameters from waveforms have been developed (Section 8.2.3). In general, the following approximations are made:

i) the surface is ideal, and homogeneous across the footprint;

ii) the height distribution of the surface scattering elements can be represented by a Gaussian function;

iii) there is only one surface layer, which is homogeneous, composed of dry, spherical ice particles and air, the material properties varying linearly with depth;

iv) there is no multiple scattering;

v) the scattering is a scalar process and there are no polarisation effects; and

vi) volume scattering above the mean surface is negligible.

The first three approximations relate to the surface type, while the last three concern the scattering mechanisms involved. Despite the fact that these assumptions grossly simplify the real situation, it has been demonstrated that realistic geophysical parameters can be retrieved from waveform models, as seen in the following sections.

Averaging procedures

Although 'individual' waveforms obtained from the altimeter are actually a summation of 50 or 100 individual return pulses (Cudlip *et al.* 1994a), they still contain noise. For modelling purposes, the signal-to-noise ratio must be further increased to a suitable level. Therefore, more averaging is required, which can be achieved by either:

i) aligning and then averaging the waveforms and fitting a model to the mean waveform; or

ii) fitting a model to the real waveform and averaging the output parameters.

The first method is affected by the technique used to align the waveforms in the averaging i.e. the reference point/range bin selected (Ridley and Partington 1988). Since the inflection points seen in the individual waveforms (see Figure 3.14) occur in a different place for each waveform, they can become merged through this type of averaging. The second method is limited by the effect of irregular topography, which means that the individual parameters are more variable. However, this approach has the advantage that individual elevation corrections can be derived from each waveform, and the model can (in principle) be used as a retracker. A statistical comparison between the two approaches has not been carried out.

The aim of the surface parameter retrieval in this chapter is to examine large-scale spatial variations in the surface properties of the Lambert-Amery system. The spatial scales chosen for the averaging are 50 km over the ice sheet and 25 km over the ice shelf.

8.2.3 Overview of waveform algorithms

Several altimeter models for surface and volume scattering have been developed (Table 8.1). One further surface- and volume-scattering model has recently been described (Newkirk and Brown 1996). This model is very similar to that of Davis (1993). The main difference is that this model is not confined to any particular altimeter configuration, and therefore can be applied to any altimeter, including beam-limited altimeters and airborne altimeters. As this thesis is only concerned with the pulse-limited ERS satellite altimeters, the additional flexibility permitted by this model is not required here. The models listed in Table 8.1 are described in the next section.

TABLE 8.1 *SUMMARY OF EXISTING THEORETICAL MODELS FOR SATELLITE RADAR ALTIMETER WAVEFORMS.*

Model	***Type***	***Input waveform for fitting***
Ridley and Partington (1988)	*integral*	*averaged (approx. 10)*
Davis (1993)	*closed*	*individual*
Yi and Bentley (1994)	*closed*	*averaged*

Ridley and Partington model

Ridley and Partington (1988) developed the first model for surface and volume scattering, based on Rayleigh scattering theory. The model required the user to input many physical surface parameters for each waveform and relied on the numerical evaluation of an integral, to produce an output model waveform from those parameters. Fitting of model waveforms to the data was carried out by a least-squares method.

The input parameters included: surface roughness information; surface type; material density (at surface and 14 m depth); permittivity; particle radius and orientation; snow temperature and the depth of the scattering layer. Additional input quantities were 'model type' (the model could handle two different surface types within the footprint) and 'surface coefficient' (a parameter that described the ratio of surface to volume scattering).

This large number of model dependencies in the Ridley and Partington (1988) model results in considerable ambiguity in the retrieved parameters (Jeff Ridley, personal communication, 1998). Later models simplify the model initialisation to reduce the number of free parameters, with assumptions that many factors will cancel out over the large ~5-10 km footprint over which the retrieval takes place (Jeff Ridley, personal communication, 1998).

Model application

Ridley and Partington (1988) applied their model to Seasat waveforms over four regions of Antarctica (Queen Mary Land, Terre Adelie, Wilkes Land and the Larsen Ice Shelf). In each case, around 10 waveforms were aligned using the OCOG technique (see Chapter 3) and then averaged. The model was fit using least squares, by tuning the model parameters until the best match was obtained.

For three of the regions, the returns were fitted with models whose values for the physical properties of the reflecting surface were the same (a surface roughness of 1.4 m, an ice grain diameter of 1.2 mm and a density of 400 kg m^{-3}). However, the surface coefficient was different for each: the Queen Mary Land waveform was dominated by volume scattering (penetration depth 8.3 m); the Terre Adelie waveform by surface scattering; and the Wilkes Land waveform showed a combination of the two scattering processes. The fourth region was the Larsen Ice Shelf, whose return was better modelled using the Brown model for surface scattering only (see Chapter 3). Ridley and Partington also successfully fitted their model to waveforms collected over Dome C, East Antarctica, using *in situ* grain-size and density measurements.

The application of this model was extended by Partington *et al.* (1989). They compared modelled and mean returns (averaged from 1000 waveforms) over regions of Greenland and Antarctica. The study was carried out on two spatial scales: a large scale (23 000 to 67 000 km^2) and a small scale (tens to hundreds of km^2).

The large-scale study was carried out over the following regions: Wilkes and Enderby Land; the East Antarctic plateau (between 71.80 and 72.06°S (where the ground-track density was highest); the Amery, Fimbul, Larsen and Shackleton Ice Shelves; and Greenland. The data used to produce averaged waveforms were recorded within 14 days of each other, in order to investigate the seasonal variation in waveform shape. The large-scale study detected three types of waveform: surface-dominated, volume-dominated, and intermediate (referred to as transitional). It also revealed that waveform shape exhibits a large spatial variability over the ice sheet, whereas the temporal variations are not so significant. Surface-dominated waveforms were returned from all of the ice shelves, the shapes hardly varying with location or time. Enderby Land mean waveforms were transitional, while those from

Wilkes Land were volume-dominated. Partington *et al.* (1989) attributed this difference to the fact that Enderby Land is at a lower altitude than Wilkes Land. They also suggested Enderby Land could have a more glazed surface due to greater katabatic wind intensity. In Greenland, mean waveforms from regions south of 68°N (previously classified as the soaked snow zone) were surface-dominated. Moving north through the percolation zone into the dry snow zone, the altimeter returns became increasingly affected by volume scattering. In summary, it was found that over both ice sheets, large-scale differences reflected the physical conditions of the surface, which are related to altitude and geographic location.

The small-scale study over Wilkes Land revealed that most of the averaged waveforms in one particular longitudinal strip (85-90°E) did not conform to the model. This also applied to some waveforms from other longitude strips. Partington *et al.* (1989) attributed this to the presence of sub-surface layers in the firn, which are not averaged out over these smaller scales, leading to secondary peaks in the waveform shape. Elsewhere, the model parameters were consistent with available *in situ* measurements; however, as noted above, there was some ambiguity in separating snow grain-size from snow density.

Davis and Moore model

The Davis and Moore (1993) volume scattering model, and the surface and volume scattering algorithm (the S/V algorithm; Davis 1993) that combined it with Brown's surface scattering model, were described in Chapter 3. The S/V algorithm was designed to provide improved height estimates for individual altimeter waveforms in regions where volume scattering occurs (Davis 1993; see Chapter 3). At the same time, however, the model provides an estimate of the relative contribution of surface and volume scattering for each waveform, and outputs several model parameters (Table 3.3). The model can therefore provide useful information on the near-surface properties of the ice sheets.

Model application

The S/V algorithm has been tested extensively over the ice sheets using Seasat and Geosat waveform data, e.g. Davis and Zwally (1993); Davis (1996). Davis and Zwally (1993) applied the algorithm to Geosat data from summer and winter seasons of 1986 and 1987, over two regions in Antarctica and Greenland. These regions covered a wide range of surface elevations but contained no surface slopes greater than 0.4°. Mean values for the model parameters k_e (extinction coefficient) and K (volume coefficient) were determined by averaging results from all of the individual fits to the waveforms in each box. These averages were determined from 100 to 2400 individual waveforms for Greenland and around 2500 for Antarctica. Variations of these S/V model parameter averages were investigated.

In the Greenland region, the surface elevations decreased moving north (from 2700 to 2500 m), and then increased steadily to 3100 m. The minimum elevation corresponded to the maximum k_e value (0.48 m^{-1}); k_e decreased to 0.13 m^{-1} north of this point and to 0.2 m^{-1} to the south. Conversely, K increased with surface elevation, values ranging from 0.7 to 2. Davis and Zwally (1993) attributed the observed trends to changes in density and grain-size of the near surface snow. They found that surface scattering dominated at lower elevations, and explained this by the presence of enhanced grain sizes (from successive melting and refreezing), which increases k_e. The degree of volume scattering increased with both elevation and latitude. The variations in k_e and K values correlated well with the degree of melting estimated from passive microwave data.

The Wilkes Land region extended from 80° to 100°E at 72°S (where surface elevations ranged from 2550 to 3150 m) and spanned an ice divide. Davis and Zwally (1993) derived k_e values that decreased from 0.20 to 0.07 m^{-1}. These values were lower than those obtained for Greenland, which Davis and Zwally (1993) attributed to smaller grain size associated with lower temperatures. Davis and Zwally (1993) explained that, in a region where no surface melting occurs, grain-size is determined by mean annual surface temperature. Higher temperatures produce larger grains whilst cooler temperatures (at higher elevations and further away from the coast) lead to smaller grains. k_e therefore decreases with increasing surface elevation and distance from the coastline. Unlike the Greenland data set, the variations in K and k_e values over Wilkes Land appeared to be uncorrelated. K values were consistently high (1.7-3) and no large scale trend was evident, suggesting that the returns were dominated by volume scattering. Davis and Zwally (1993) suggested that observed variations were due to the presence of crusts on the surface. Davis and Zwally (1993) found that k_e values were different on either side of the ice divide, due to different snow properties. East of the ice divide, K values were higher in summer than in winter, which Davis and Zwally (1993) explained by the presence of a surface crust during winter.

More recently, Davis (1996) applied the S/V model to Seasat (1978) and Geosat (1985) data over the Greenland ice sheet. Using data from the same season for both datasets, the averaged k_e values returned by the model were similar in the lower latitudes for both epochs, but significantly less in a localised region in the higher latitudes i.e. the dry snow zone. As k_e is proportional to the average grain size of the near surface snow, this suggested that, in this region, grain-sizes had decreased over the elapsed time period. Davis (1996) suggested that this could be due to either a melting event that occurred before 1978, whose effect was removed by 1985, or an increased accumulation rate over the period 1978 to 1985.

To estimate the size of the bias that could be introduced into estimates of ice-sheet elevation change by temporal changes in surface properties, Davis (1996) compared elevation changes estimated from crossover differences, using heights from the S/V model with those obtained using an empirical technique (described by Davis (1995)). He obtained an estimate for this bias of 0.2 to 0.3 m, and added that this could become more serious as the time between epochs is increased.

The major limitations of the S/V model pointed out by Davis and Zwally (1993) and Davis (1996) are:

i) *Surface topography:* the model can only be applied to regions where surface slopes are less than 0.5°, and where the surface topographic variations are minimal. This eliminates a large portion of the ice sheets, most significantly the lower elevation areas of the drainage basins and the ice sheet periphery, and anywhere that has an undulating surface of wavelength in the order of the altimeter footprint. Topographic undulations cause surface reflections that affect the trailing edge of the waveform in a manner similar to volume scattering (Wingham 1995).

ii) *Spatial sampling density:* to obtain realistic estimates from the S/V model, output parameters from approximately 100 waveforms must be averaged (Davis and Zwally 1993).

Yi and Bentley model

Yi and Bentley (1994) described a model that was very similar to Davis and Moore's (1993) volume scattering model. The model was based on the Ridley and Partington (1988) model, and combined with the Brown (1977) model for surface scattering (modified to include the effect of Earth curvature), to produce a theoretical model for a Geosat return waveform. The effect of a surface slope was included using an off-nadir angle parameter (off-pointing angle). The model was fit by least squares to averaged altimeter waveforms, to determine the same model parameters as the Davis and Moore (1993) model.

Model application

Yi and Bentley (1994) tested their model for Geosat waveforms collected on the East Antarctic plateau (71.5-72°S, 80-90°E), just inside the Lambert-Amery system boundary, for the eleven months between November 1986 and October 1987. They aligned waveforms at the β-parameter retracking point (the midpoints of their first ramps) and averaged them both in time and location. They found that averaged waveforms varied both in time and location, and attributed this to variations in penetration depth caused by variations in density, grain-size, and water content of the snow/firn, which affect k_e.

The model fitted well to the averaged waveforms, including one from the region where Partington *et al.* (1987) had trouble. Yi and Bentley's (1994) results indicated that the volume scattering that affects the measured elevation occurs between depths of zero and 12 m. The surface elevations over the test region were 1 m higher than those obtained with the β-parameter algorithm.

Choice of algorithm for this work

One of the requirements of the surface property retrieval over the Lambert-Amery system is to investigate variability of surface characteristics along individual tracks. Therefore, individual waveform fitting is the preferred method. Individual waveform fitting was also the technique adopted in recent work by Legresy and Remy (1997) who examined the spatial variability of the waveform shape over the ice sheet.

Davis' (1993) S/V algorithm is the only model that has been developed to include fitting to individual waveforms (Table 8.1).

The combined S/V algorithm (Davis 1993) was written for Seasat and Geosat waveform data, in FORTRAN code. Curt Davis made a version of the S/V algorithm (Davis 1993a) available for this work. Since Seasat and Geosat differ considerably from ERS-1 waveform data, the code had to be modified for use with ERS-1 data. Curt Davis had no plans to do this himself (Curt Davis, personal communication, 1994), therefore the modification was undertaken as part of this thesis.

The results of applying the modified S/V algorithm to ERS-1 data in the Lambert–Amery system are discussed in detail in the next section.

8.3 Processing of ERS-1 data with S/V algorithm over the Lambert-Amery system

Before the S/V algorithm could be applied to ERS-1 waveforms, various modifications had to be made. The major changes made to the code were to account for the different instrument parameters (e.g. pulse width, antenna beam-width, number of range bins). The DC bias parameter included in the Davis and Moore (1993) model was removed, since ERS waveforms do not contain any background noise. In addition, a choice of modes was implemented, since ERS-1 waveforms can be ocean or ice mode.

In the original S/V algorithm, the model waveform was fit to the real waveform using a bounded least-squares method. Glenn Hyland of the Antarctic CRC modified this fitting process to make it faster and more robust, by incorporating a Marquardt gradient-expansion fitting algorithm (Bevington 1969). The Marquardt algorithm provides a chi-squared (χ^2) parameter, which can be used to estimate the quality of the final fit of the S/V model waveform to the real waveform.

8.3.1 Pilot study

A pilot study was carried out over the AIS-DEM, to determine whether there was any difference in performance of the S/V algorithm when ice mode ERS-1 data was used. When Curt Davis supplied his code, he expressed the concern that it may not work with ice mode data, due to the coarser sampling of the waveforms in this mode.

Using data collected over the region covered by the AIS-DEM only ensured that no waveforms were from regions where slopes were greater than 0.5°. It also meant that the majority of the waveforms used in the pilot study were regular in shape (i.e. ice shelf returns) and that no data were included from highly irregular surfaces. This was important, since in ice mode the tracker would continue to track the surface for longer, whereas in ocean mode there would be no valid waveforms received as tracking would have been lost.

The only ERS data available for the region at the time of the pilot study (late 1994) were from Phase C of ERS-1 (Table 8.2).

***TABLE 8.2** CYCLE NUMBERS OF ERS-1 PHASE C USED IN THE S/V PROCESSING.*

Ocean mode	*Ice mode*
1	*2 (part)*
2 (part)	*4 (part)*
3	*6*
4 (part)	*14*
5	
7	

Part cycles result from the altimeter switching between ocean and ice mode.

All of the valid waveform data (i.e. that which passed filters listed in Appendix A) contained in the cycles listed in Table 8.2 were extracted over the AIS-DEM. This was done using the same mask that was generated from the AIS-DEM to extract the RES data over the shelf (see Chapter 6). The data were split into two sets: one containing ocean mode only (22 277 waveforms) and the other containing ice mode only (18 507 waveforms). Both sets were processed with the S/V algorithm, and the χ^2 value for each waveform fit retained. The distributions of χ^2 values are represented as histograms in Figure 8.1 for ocean mode (upper plot) and ice mode (lower plot).

These histograms show that the distribution of χ^2 values for the ice mode dataset has a much broader spread than that for the ocean mode dataset. The medians of these distributions are 3477 (ocean mode) and 7365 (ice mode). This demonstrates that, at least over the Amery Ice Shelf, the S/V algorithm fit is much better for ocean mode waveforms than it is for ice mode waveforms. For this reason, it was decided to reserve the algorithm for use with ocean mode data only.

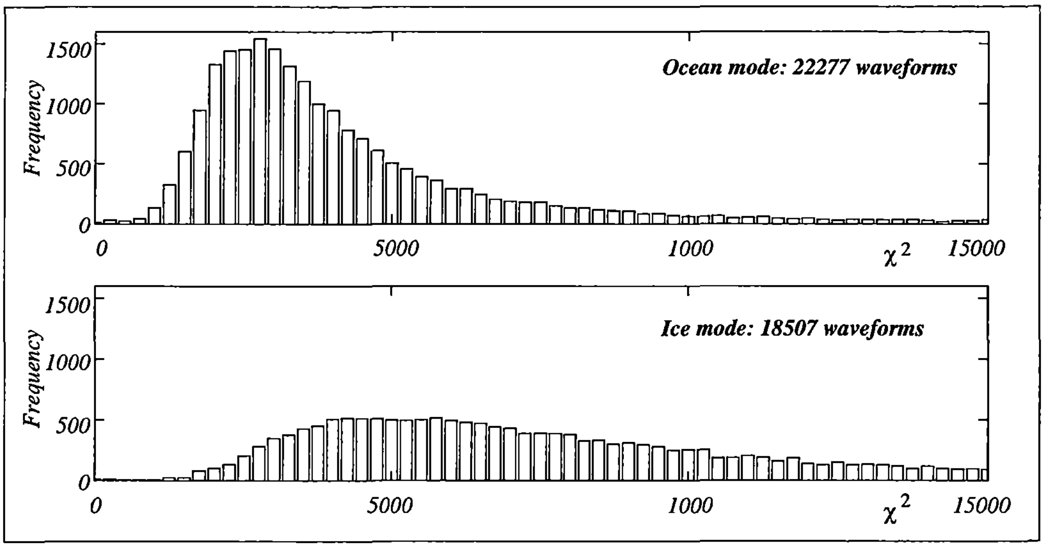

Figure 8.1 *Histograms of χ^2 values from the S/V algorithm for ocean mode waveforms (upper plot) and ice mode waveforms (lower plot), over the pilot region (the AIS-DEM).*

The most likely cause of the difference in algorithm performance between the two modes is the method that the algorithm uses to make its initial estimates for the parameters. The algorithm searches for an inflection point on the leading edge of the waveform, to fit its function of surface and sub-surface scattering. The coarser sampling of the ice mode waveforms means that this inflection point is essentially lost. The algorithm therefore has greater difficulty making its initial estimates and fitting the S/V function.

8.3.2 Main study

For the main study, application of the S/V algorithm in the Lambert-Amery system was performed using ocean mode data only. This meant that there was a limited amount of data available for analysis. The cycles of the ERS-1 35-day repeat Phase C that were used here are listed in Table 8.3.

All of the available ocean mode data over the Lambert-Amery system were filtered according to filters outlined in Appendix A. Further filtering was carried out to remove all data where surface slopes were greater than 0.4°, using the Slopes Database (Appendix B). The S/V model was run for all remaining ocean mode data.

TABLE 8.3 CYCLES OF ERS-1 35-DAY REPEAT PHASE C DATA THAT WERE PROCESSED BY THE S/V ALGORITHM IN THIS ANALYSIS.

Cycle of Phase C	**Dates**	**Coverage**
1	*14 April – 1 May 1992*	*AIS only*
2	*1 May – 5 June 1992*	*AIS only*
3	*5 June – 10 July 1992*	*AIS only*
5	*14 August – 18 September 1992*	*AIS only*
7	*23 October – 27 November 1992*	*AIS only*
15	*20 July – 3 September 1993*	*whole LAS*
17	*8 October – 12 November 1993*	*Whole LAS*

Cycles 1 to 7 were provided (over the Amery Ice Shelf only) by the Remote Sensing Group of the Mullard Space Science Laboratory, in their own EA (ERS Altimeter) format. Complete Cycles 15 and 17 were obtained from ESA in the WAP (Waveform Advanced Product) format.

The following selection criteria were applied to the resulting S/V model fits:

$$\chi^2 < 10\,000$$

$$0 < \sigma_s < 5.0$$

$$k_e > 0.0$$

$$K > 0.0$$

The choice of the χ^2 threshold was based on the ocean mode distribution of Figure 8.1. Choosing a χ^2 of 10 000 ensured that approximately 90% of the waveforms of the AIS-DEM were accepted. The bounds on the other parameters rejected any waveforms whose S/V fits produced unrealistic values.

The S/V model parameters investigated here are: surface roughness *(σ_s)*; extinction coefficient (k_e); and the volume scattering ratio *(K)*. The investigation was separated into two parts:

i) Large scale investigation of spatial variations in S/V parameters over the entire Lambert-Amery system. In this study, the S/V model output parameters were averaged onto a grid with a cell-size of 50 km. The study was carried out for the only two available full Phase C cycles (15 and 17). This is a larger area than that covered by Davis and Zwally (1993).

ii) Smaller scale study of both spatial and temporal variations over the Amery Ice Shelf only, using repeat track data. Here the S/V model output parameters were smoothed along track on a scale of 25 km, using a median-filter smoothing operator. This study was carried out for all cycles. Previous applications of the S/V model to Geosat waveforms were restricted to the plateau regions of the ice sheets (Davis and Zwally (1993); see earlier in section). Since none were performed over ice shelves, this is a new application of the algorithm.

The results obtained from each study are discussed below.

Lambert-Amery system study

To examine the broad-scale spatial variations of the S/V output parameters, the output parameters for Cycle 15 and 17 of Phase C were averaged onto a polar stereographic grid, of cell size 50 km. For each cell, the mean and variance of each S/V model parameter was determined. The spatial distribution of the S/V parameters are presented (in the form of maps) and discussed below.

Surface roughness

The spatial distribution of the S/V model parameter surface roughness (σ_s) over the Lambert-Amery system, averaged onto a grid of cell-size 50 km, is shown in Figure 8.2 (top plot). Also shown are the locations of the LGB traverse stations. The top plot illustrates the low σ_s high on the plateau (upstream of the LGB traverse route) and on the Amery Ice Shelf. Away from the ice shelf, σ_s generally decreases with increasing altitude. The variance of σ_s for each cell is shown in the bottom plot. The cells with the lowest variances generally correspond with those of low σ_s. The derived σ_s and variances are greatest around the ice shelf periphery and over the sloping part of the system containing the ice streams.

The parameter σ_s is clearly related to true surface roughness. Variations in surface roughness result from changing accumulation rates and surface katabatic wind action. A typical accumulation distribution for the Lambert–Amery system is presented in Figure 7.3. Accumulation rates are generally higher on the western side of the basin than the eastern side (Goodwin 1995). Wind speeds in the Lambert-Amery system are influenced by the shape of the basin (Allison 1998). Mean annual

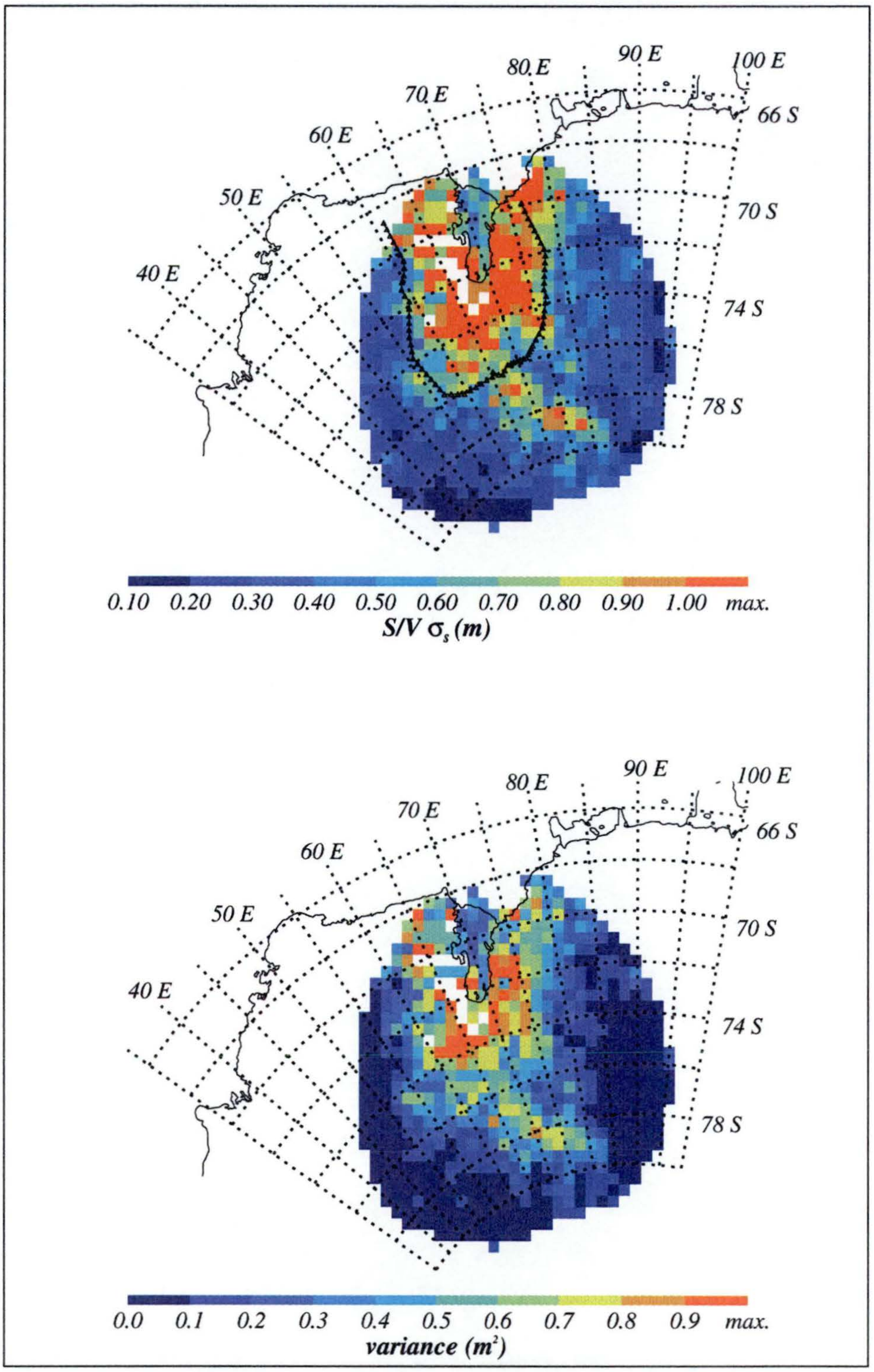

Figure 8.2 *Spatial distribution of the S/V model parameter* σ_S *(top plot) and its variance (bottom plot) over the Lambert-Amery system, for Cycle 15 of ERS-1 Phase C (August 1993). Values are averaged on a 50-km grid; cells with less than 100 values are white. The locations of the LGB traverse stations are shown in the top plot.*

wind speeds at the six AWS (see Figure 2.5) around the Lambert Glacier traverse route vary from 7.5-11.3 m s^{-1} (Allison 1998). Average wind speeds are high at LGB00 on the steep slopes near the coast, at LGB35 where the flow is funnelled in surface depression containing the Lambert and Mellor ice streams (the Lambert graben) and at LGB59 on the eastern side of the basin (Allison 1998). The pattern of σ_s can be explained by these variables. There is certainly a higher σ_s in the Lambert Glacier section of the graben (75-80°S, 65-75°E), where the surface is likely to be rougher due to wind action.

High on the plateau (above the LGB traverse route), surface slopes, wind speeds, and accumulation rates are very low. This means that the surface remains less affected by wind action and is therefore relatively smoother.

Extinction Coefficient

The 'extinction coefficient' (k_e) describes the amount of incident radiation that is attenuated within the snow volume per unit length. Energy can be lost either through absorption (transformed into other forms of energy) or scattering (deflected away from the incident direction). These two processes are linear, therefore k_e is the sum of the 'absorption coefficient' k_a and the 'scattering coefficient' k_s (Ulaby *et al* 1981):

$$k_e = k_a + k_s$$

k_a is dependent on the snow density, and at the frequency of the ERS altimeter (13.8 GHz) shows little variation over the Antarctic ice sheet (Davis 1996). Therefore variation in k_e is primarily related to variability of k_s. k_s is proportional to the grain size of the near-surface snow; a larger grain size results in greater scattering and therefore a higher k_e. Grain size is determined by factors such as snow temperature, surface melting and accumulation rate (Paterson 1994).

The units of k_e are m^{-1}, and its value defines the 'penetration depth' (d_p), i.e. the depth interval over which the signal strength is reduced to 1/e of its initial value (Davis and Moore 1993). Assuming k_e is constant within the sampled layer, this is given by:

$$d_p = \frac{1}{k_e}$$

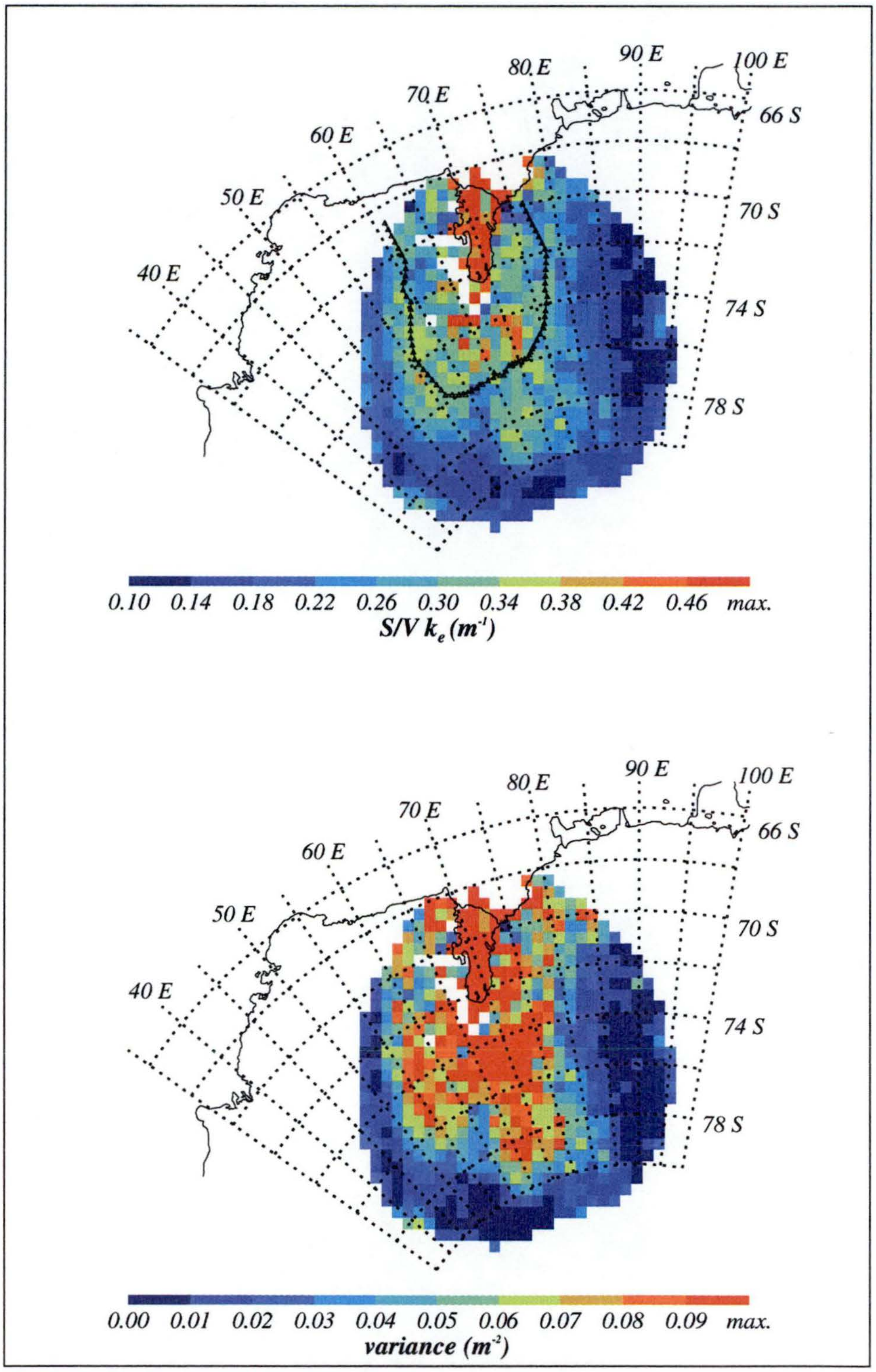

Figure 8.3 *Spatial distribution of the S/V model parameter k_e (top plot) and its variance (bottom plot) over the Lambert-Amery system, for Cycle 15 of ERS-1 Phase C (August 1993). Values are averaged on a 50-km grid; cells with less than 100 values are white. The locations of the LGB stations are shown in the top plot.*

The spatial pattern of the derived S/V model parameter k_e over the Lambert–Amery system for Cycle 15 of Phase C (October 1993) is shown in Figure 8.3 (top plot). The most obvious feature of this plot is the high k_e on the ice shelf relative to the plateau. For the grounded ice, k_e exhibits a general decrease with increase in elevation.

The S/V model parameter k_e appears to be related to the true extinction coefficient, and its variation can mostly be explained in terms of grain sizes. On the ice shelf, individual particles are expected to be larger than those on the plateau, due to much warmer temperatures, combined with successive melt-freeze cycles (i.e. wet snow metamorphosis) (Zwally and Fiegles 1994); therefore k_e is high. On the plateau, grain sizes depend on surface temperature and accumulation rate. In general, as elevation and distance from the coast (continentality) increases, temperatures decrease; therefore the grain sizes and k_e decrease.

In the regions of high katabatic wind intensity (e.g. the Lambert graben; Allison 1998), k_e is higher than the surrounding surface. Observations of the surface between LGB40 to LGB52, across the upstream extension of the Lambert Glacier, showed that sastrugi were mostly absent, leaving a very smooth surface (Higham and Craven 1997), which would increase the reflectivity of the surface.

Since the altimeter observations were acquired during winter months, the enhanced k_e values could have arisen because of different surface conditions, e.g. surface crusts. From LGB traverse observations, there is evidence of buried crusts in 2-m pits (see below). Between stations LGB35 and LGB53 (see Figure 2.5 for locations), the average number of crusts is 4.7 with a standard deviation of 1.9. This compares with a mean of 3.0 and standard deviation of 1.3 between LGB05 and LGB20 on the western side of the basin, suggesting that there is higher chance of surface crust formation in the eastern region. Presence of crusts also leads to a high k_e, so this could explain the pattern observed here.

The presence of buried crusts, and other sub-surface features such as depth hoar, violates the assumptions for application of the S/V model (Section 8.3.1). Discrepancies could have occurred in the parameter retrievals from the S/V model. However, for k_e the variance of the mean value in a 50-km cell (Figure 8.3, bottom plot) is small compared to the range of values obtained. This suggests that the retrieved k_e values are robust, and the observed associations are real. Outside of the Lambert graben, k_e values on the eastern side of the basin are slightly lower than on the western side.

Comparison with in situ observations (Lambert Glacier Traverse)

In situ observations of surface snow properties in 2-m pits were made at the LGB stations during the Lambert Glacier Basin traverse (Figure 2.5; Higham and Craven 1997). Measurements recorded as averages over the 2-m depth were: grain size, density, number of ice crusts, percentage of depth-hoar, and temperature. The locations of the LGB stations are plotted in Figure 8.3. For each location, a value for k_e was extracted from the S/V parameter (50-km) arrays. Log-linear scatter plots of log(grain size) against k_e and log(density) against k_e are shown in Figure 8.4.

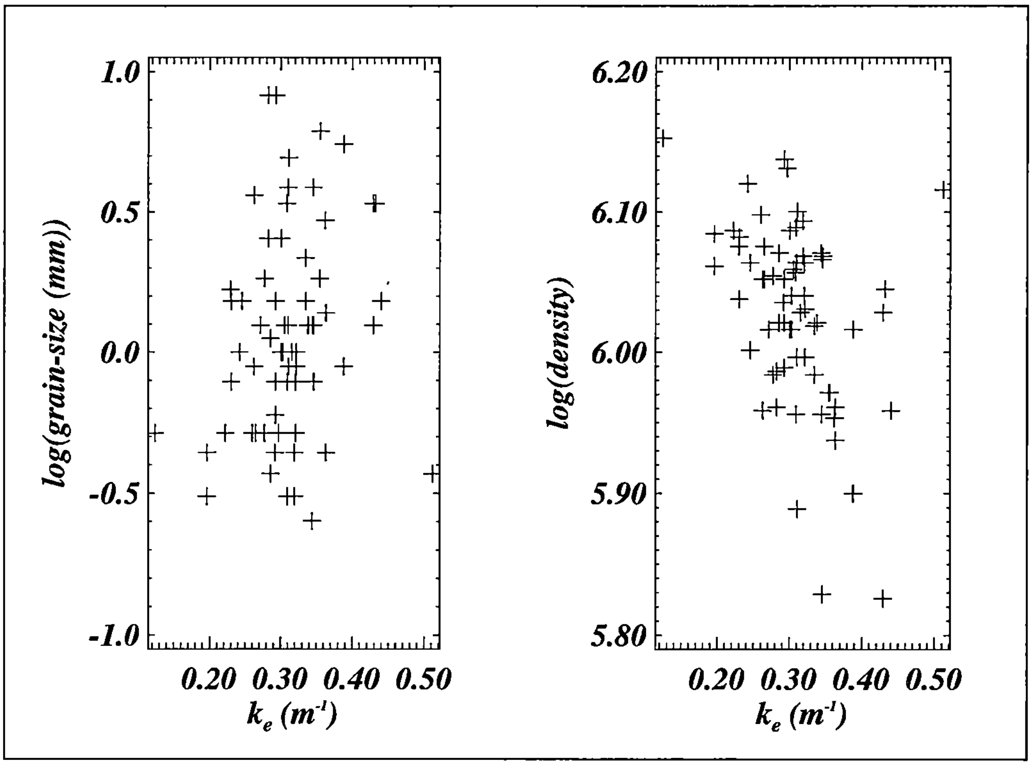

Figure 8.4 *Log-linear scatter plots of log(grain size) against k_e (left plot) and log (density) against k_e (right plot) at the LGB stations.*

There appears to be little correlation between grain-size and k_e, or density and k_e. The correlation coefficients for each dataset are 0.21 and 0.40 respectively. There are several possible explanations for the observed low correlation between the S/V model parameter k_e and the *in situ* observations. These explanations include:

- inhomogeneities introduced by the presence of depth hoar and sub-surface ice layers. The S/V model is based on several assumptions (see Section 8.2.2), which are violated where such sub-surface features are present. The symbols in Figure 8.4 were coded to represent the percentage of depth hoar to test whether data from those sites with a high percentage were masking an underlying trend. No distinct pattern was observed either by association with amount of depth hoar or for data points without significant depth hoar fraction

- the 50-km averaging of the S/V k_e, whereas physical properties are represented by point values

- the pits being not sufficiently deep to obtain realistic profiles over the altimeter pulse penetration depth *(d_p)*. At the LGB stations, d_p ranges from 1.6 to 10 m. The pits only represent mean grain size in the top 2 m. Since grain size increases with depth these values will not represent the true mean grain size encountered by the altimeter pulse at stations where d_p is greater than 2 m.

Volume scattering ratio

Maps of the derived volume scattering ratio (K) over the Lambert–Amery system for Cycle 15 of Phase C (October 1993) and its variance are shown in Figure 8.5. Comparison of this map with that in Figure 8.3, reveals an apparent inverse relationship between K and k_e. On the ice shelf, where k_e is high, scattering is mainly from the surface, and the volume-scattered component is low. The contribution of volume scattering is larger at higher elevations.

Remy (1990) suggested that large altimeter-measured surface backscatter values *(σ_o)* occurred where katabatic wind intensity was high. They claimed that the volume scattering contribution to the waveform remained relatively constant in both space and time, therefore changes in the altimeter waveform shape are mostly caused by changes in surface scattering. This would imply that any increase in K is accompanied by a decrease in surface scattering and therefore in σ_0 (since the volume component remains constant). Legresy and Remy (1997) noted that highest σ_0 values occur in regions of high accumulation combined with strong winds, such as the coastal zones of East Antarctica.

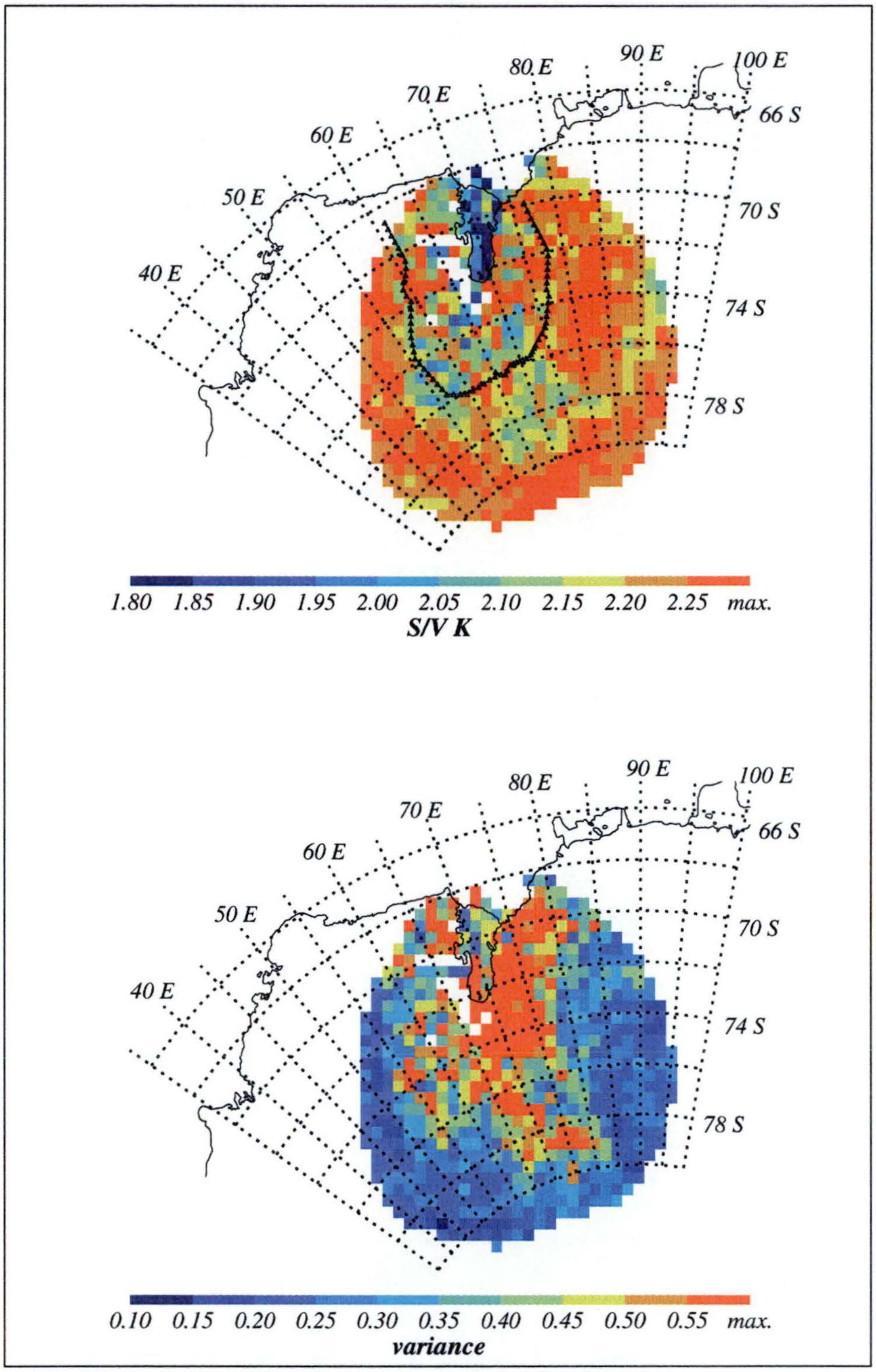

Figure 8.5 *Spatial distribution of the S/V model parameter K (top plot) and its variance (bottom plot) over the Lambert-Amery system, for Cycle 15 of ERS-1 Phase C (August 1993). Values are averaged on a 50-km grid; cells with less than 100 values are white. The locations of the LGB traverse stations are shown in the top plot.*

Figure 8.6 shows the measured backscatter *(σ_o)* for Cycle 15, averaged on the same 50-km grid as the S/V properties. Cells containing less than 100 measurements are shown in white. The presence of σ_o data in cells where no S/V parameter averages exist is explained by the fact that the σ_o data have not been filtered to remove data where surface slope magnitude is greater than 0.4°.

The relationship between katabatic wind intensity and σ_o suggested by Remy (1990) and Legresy and Remy (1997) appears to apply over the Lambert-Amery system. Observations from the AWS stations demonstrate that winds are generally higher on the eastern side than the western side (Allison 1998), and σ_o values are generally higher on the eastern flank of the basin than on the western side. The σ_o values are low in the Lambert Glacier section of the Lambert graben, which does not agree with the surface observations made during the traverse, although these *in situ* observations were made during summer. Higham and Craven (1997) suggest that if the accumulation rates are higher in winter, strong wind action would be expected, leading to sastrugi and dune formation and increasing the surface roughness (see σ_s discussion). This would in turn lower the σ_o, which is the most likely explanation for the effect observed here. However, this conflicts with the higher values of k_e and lower values of K being obtained here (Figure 8.5 and 8.6).

Repeatability of S/V parameter retrievals

The spatial distribution of S/V k_e and its variance over the Lambert–Amery system for the next ocean-mode cycle of Phase C, approximately 2 months after Cycle 15 (Cycle 17, October 1993) is shown in Figure 8.7. It can be seen that the spatial distributions of both the parameter and its variance are very similar to those for Cycle 15, indicating the repeatability of the averaged S/V retrievals over short time scales.

Maps of the derived σ_s and K values and the measured σ_o for Cycle 17 are also similar to those of Cycle 15 (see Appendix F).

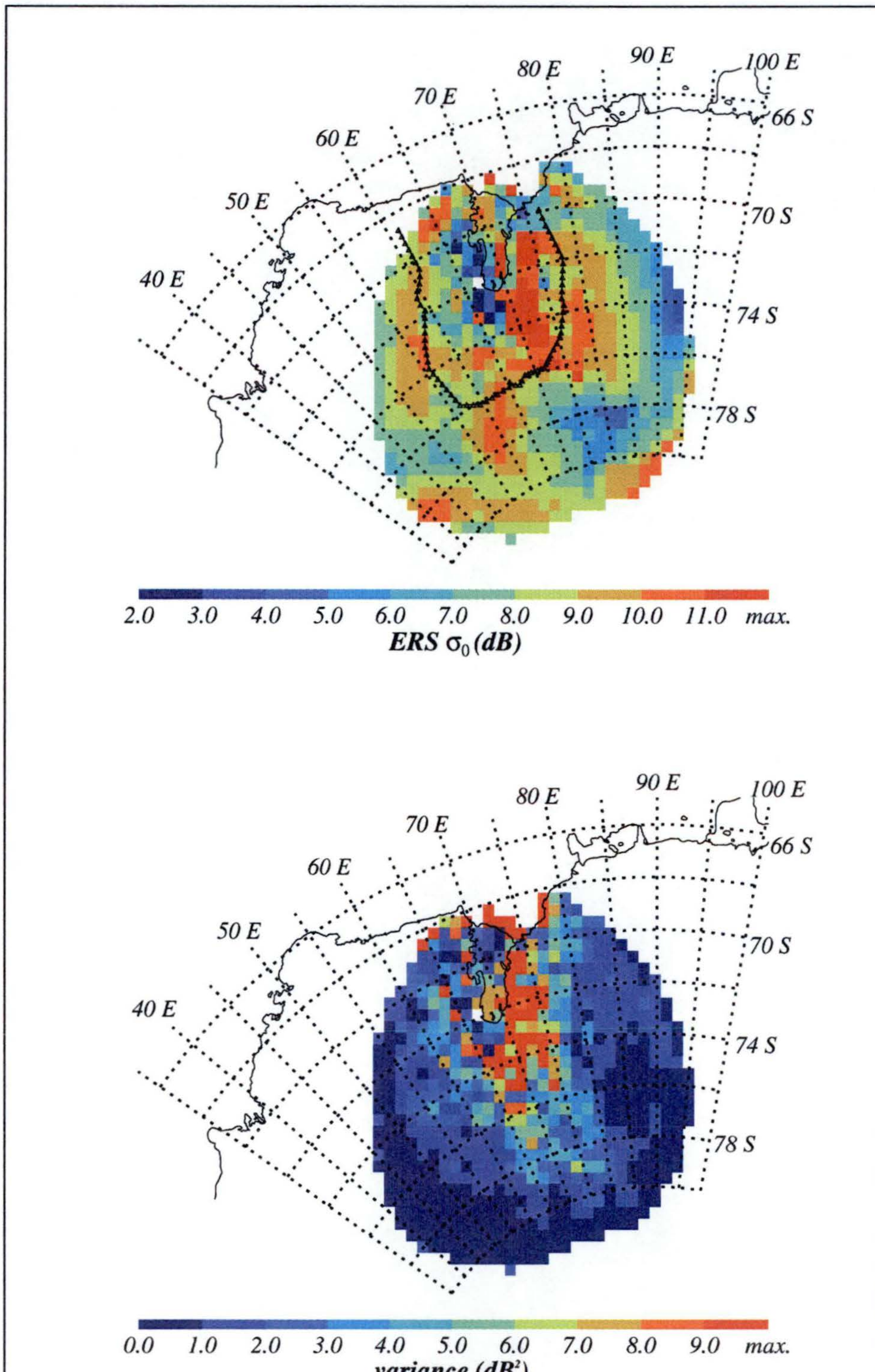

Figure 8.6 *Spatial distribution of backscatter (σ_0) measured by the ERS-1 radar altimeter over the Lambert-Amery system (August 1993). Values are averaged on a 50-km grid*

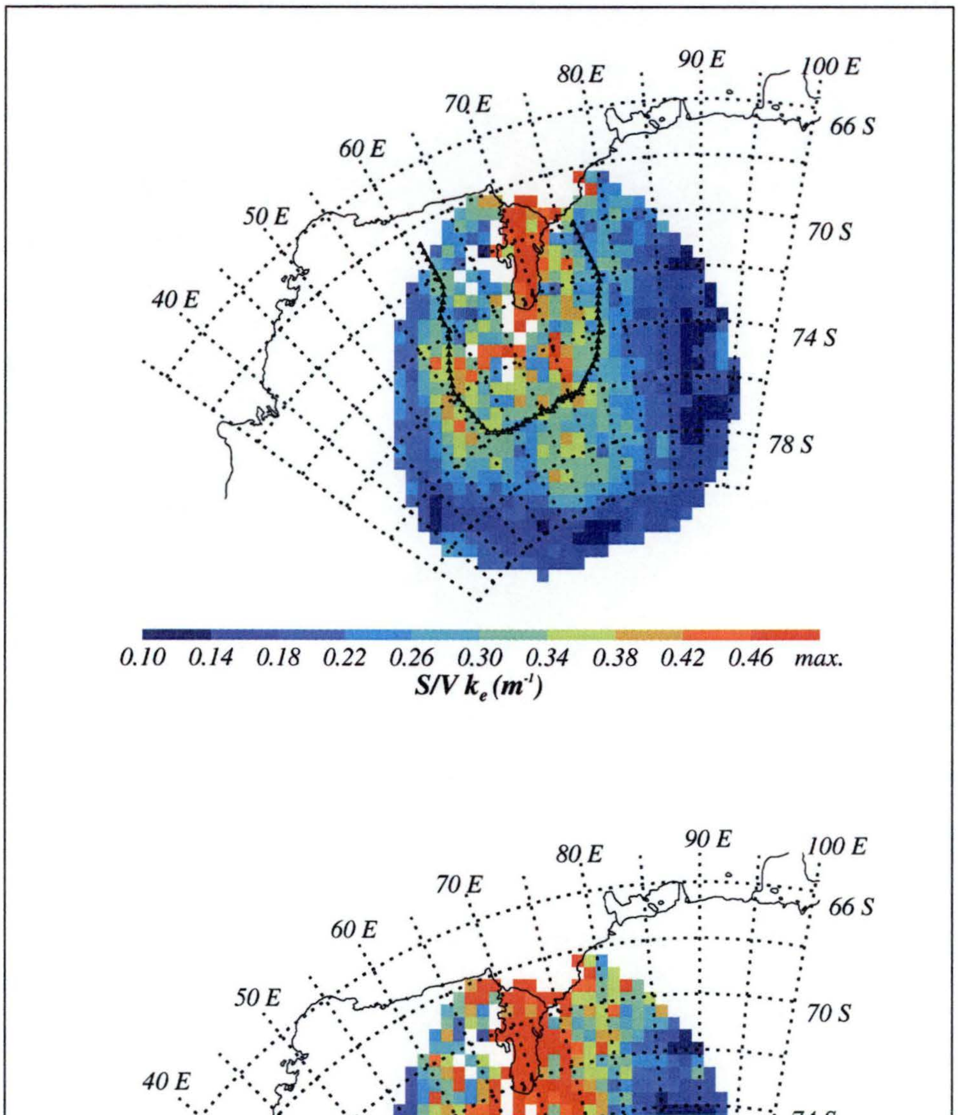

Figure 8.7 *Spatial distribution of the S/V model parameter k_e (top plot) and its variance (bottom plot) over the Lambert-Amery system, for Cycle 17 of Phase C, approx. 2 months after Cycle 15 (Figure 8.3). Note the similarity of the distribution between the two cycles.*

Amery Ice Shelf study

For the smaller scale study over the Amery Ice Shelf, six tracks from Phase C and one from Phase D were selected (Figure 8.8). The Phase C tracks were Tracks 027, 299, 070 (ascending) and 476, 247 and 018 (descending); the Phase D track was Track 013 (ascending). Seven cycles of Phase C data were used (see Table 8.3) although not all tracks were present in all cycles. Seventeen cycles of Phase D were used, from December 1993 to March 1994.

Some indication of the nature of the surface being sampled by the altimeter along each ground track can be seen in Figure 8.8, a mosaic of two Landsat Thematic Mapper (TM) images of the Amery Ice Shelf. Although these Landsat images were collected in March 1989 (i.e. 3 to 4 years before the ERS data), the main features of the ice shelf remain approximately the same. Note that visible wavelength imagery can provide an indication of the actual surface only, and does not give any direct information on underlying features which could affect the radar signal.

All of the ERS-1 waveform data used in this analysis were processed using the S/V algorithm, and the resulting output parameters smoothed along-track, at a length scale of 25 km, using a median smoothing operator. The variations of the S/V parameters on the ice shelf are presented and discussed in more detail below.

Along track spatial variations

The parameter plots of the along-track variations in the S/V model parameters σ_s, K and k_e are presented in Figures 8.9 to 8.11. The parameters have been plotted against longitude to link to the location of features in Figure 8.8. Allowing for the repeat orbit lateral drift of up to $\pm$ 1 km, the parameter retrievals are, in general, highly repeatable. There are some noisy segments in all of the plots, mainly associated with regions of variable surface topography and crevassing.

The along-track variation in derived σ_s values on the Amery Ice Shelf lies in the range 0-1.5 m. This parameter is related to the medium scale surface roughness of the scattering surface. The largest σ_s values are located where there are distinct flow features on the ice shelf. Examples of such flow features are marked as A and B in the Landsat image.

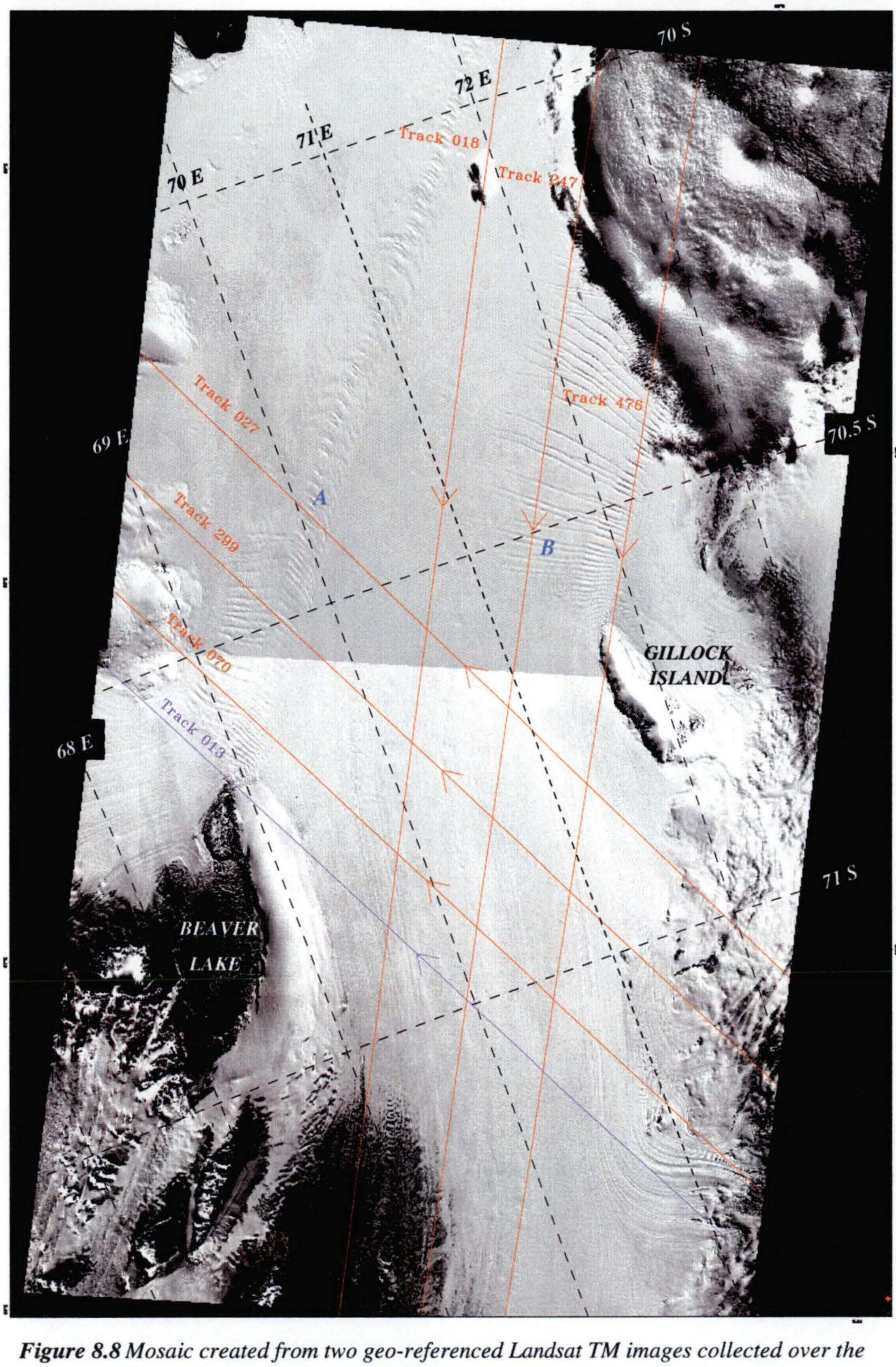

Figure 8.8 *Mosaic created from two geo-referenced Landsat TM images collected over the Amery Ice Shelf in March 1989. Note the cloud cover in the top right hand corner of the image. The features A and B are discussed in the main text.*

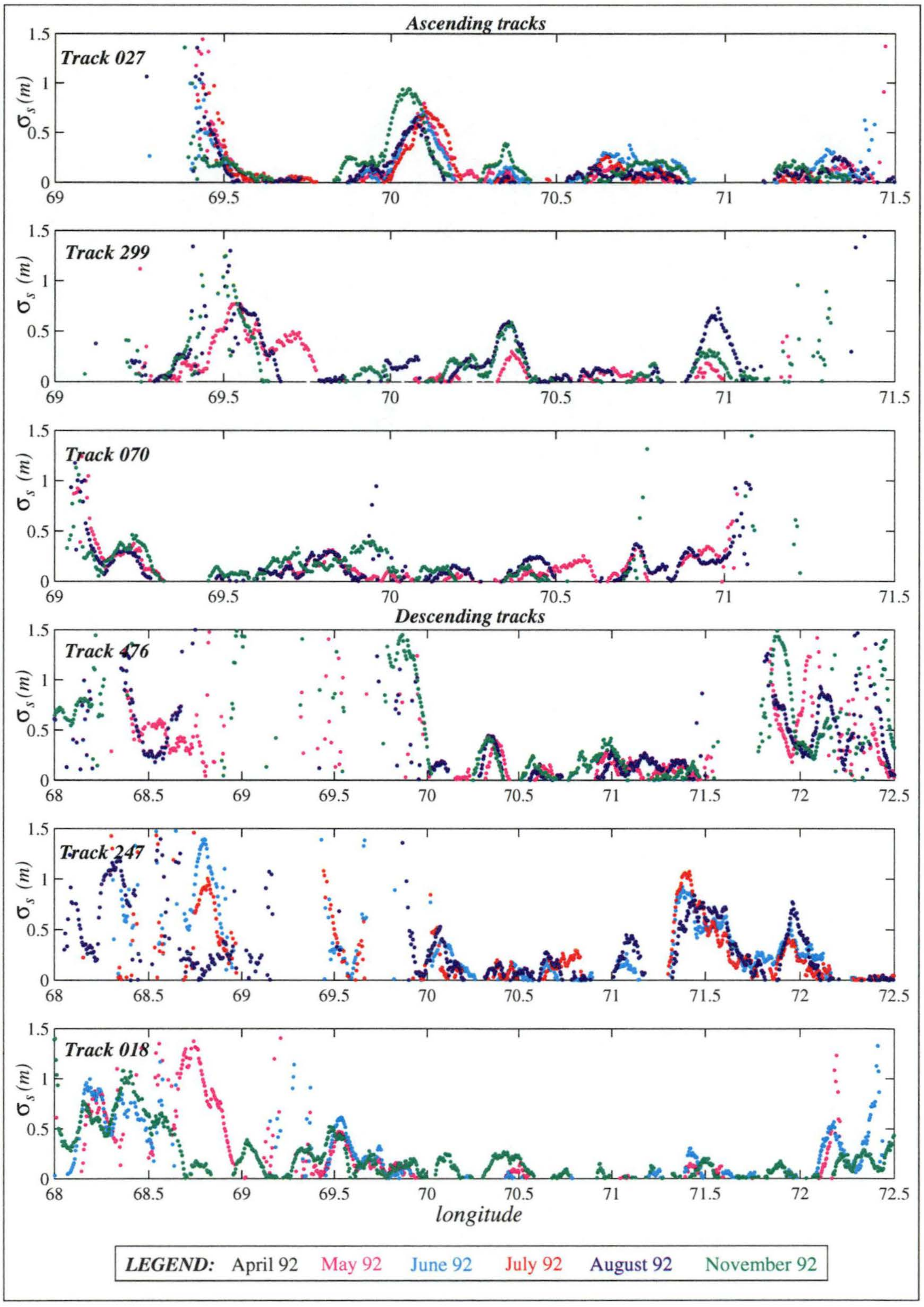

Figure 8.9 *Variation in σ_s along selected tracks across Amery Ice Shelf (see Figure 8.8 for locations). Plots for different repeats are colour coded (see legend).*

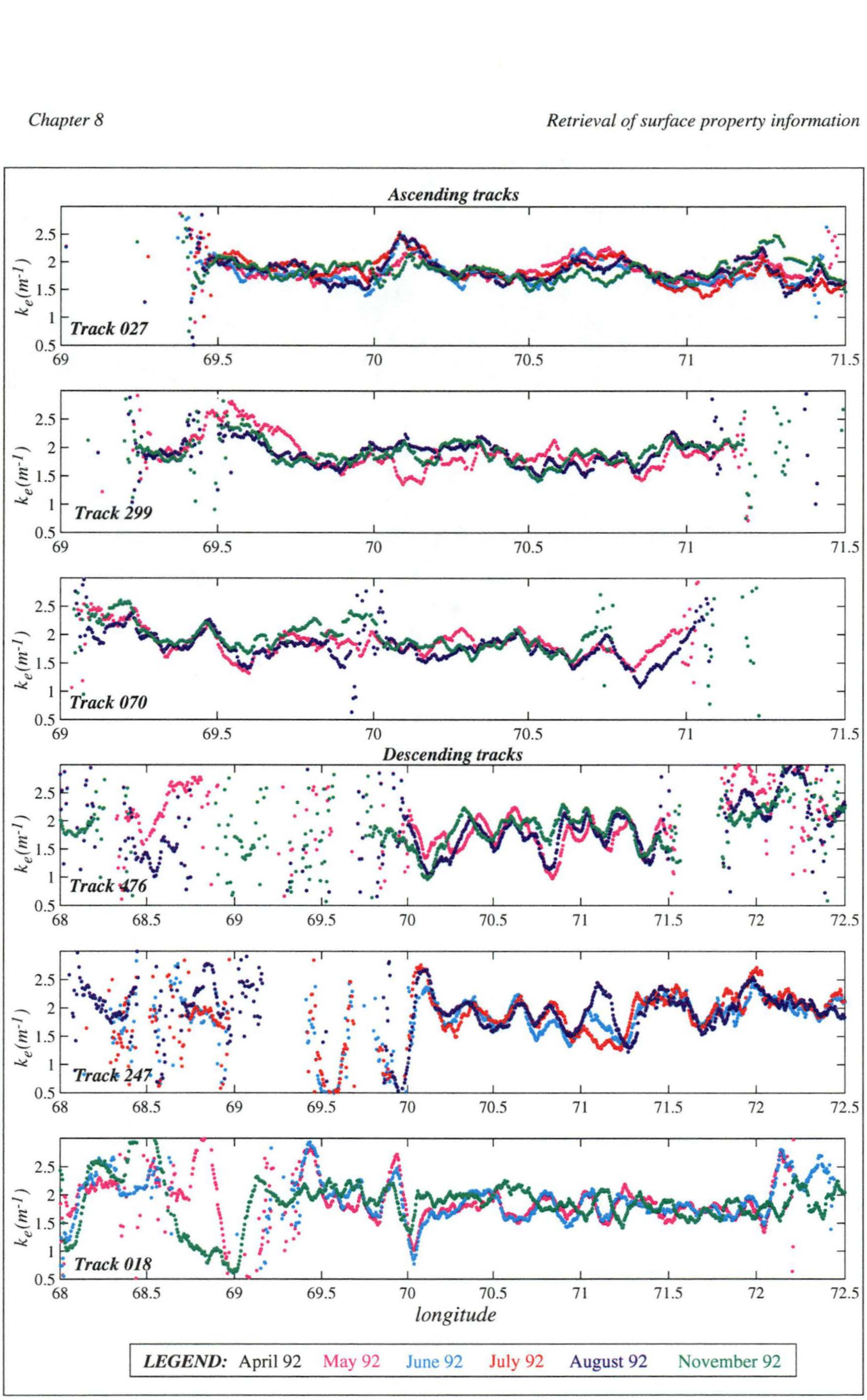

Figure 8.10 *Variation in k_e along selected tracks across Amery Ice Shelf (see Figure 8.8 for locations). Plots for different repeats are colour coded (see legend).*

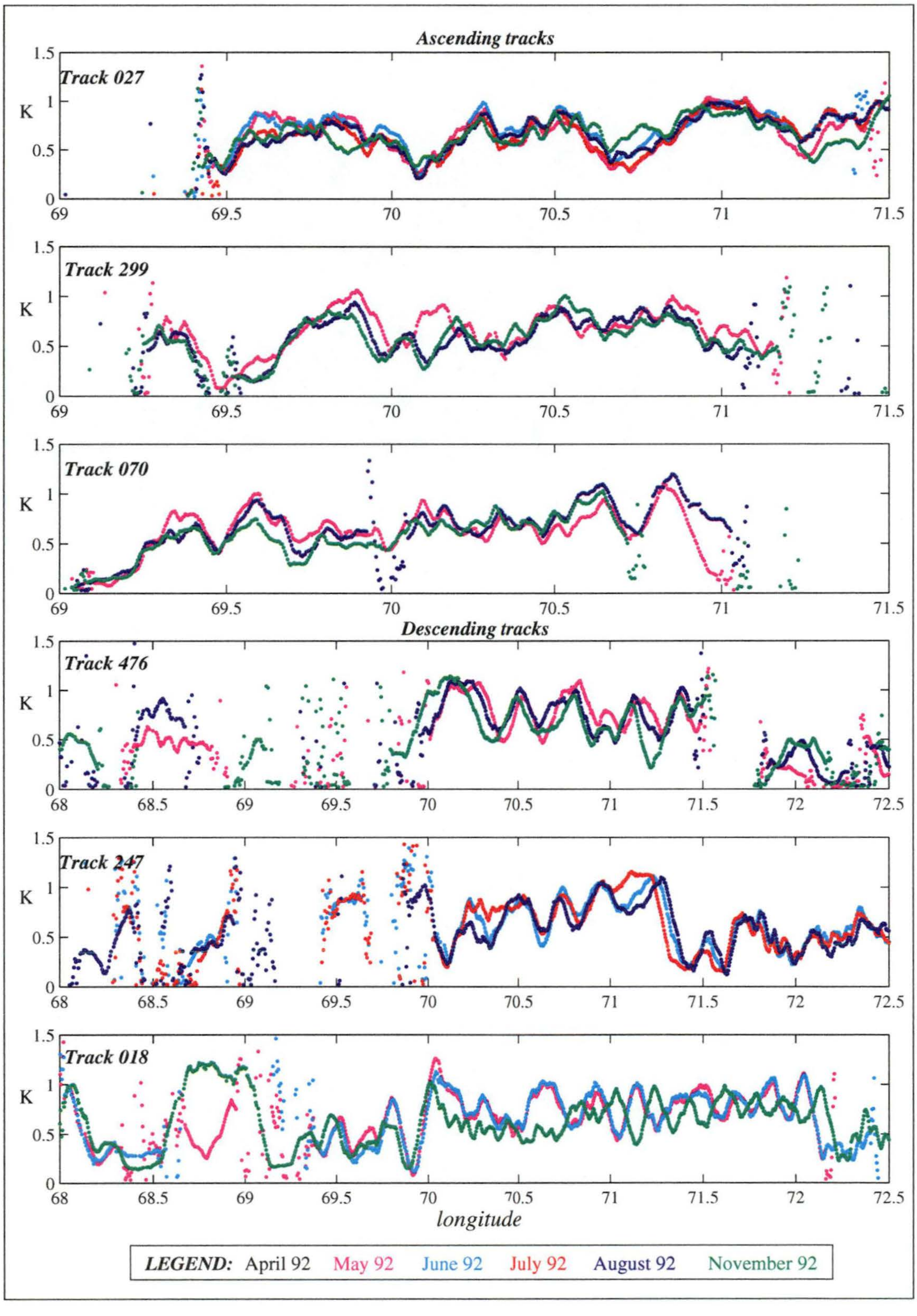

Figure 8.11 *Variation in K along selected tracks across Amery Ice Shelf (see Figure 8.8 for locations). Plots for different repeats are colour coded (see legend).*

The derived k_e values (Figure 8.10) lie in the range 0-1.5 m^{-1}. Local oscillations across the ice shelf are evident in these plots, with wavelengths around 5-10 km. Oscillations on a similar frequency are visible in the plots of S/V model parameter K (Figure 8.11), which are also likely to be a result of variations between flow bands.

The observed oscillations are likely to be a result of changing surface properties and stratigraphy within each distinct flow band. On the Amery Ice Shelf, the surface layer is due to accumulated snow. Local variations in katabatic wind intensity and accumulation rates will lead to spatial variations in properties such as grain size. As the flow features are crossed along the ERS tracks, different surface properties give rise to variations in k_e and K. The wavelength of these variations is slightly longer than the flow band width because the altimeter tracks cross the features obliquely. Two features of note are at 71.3°E in Track 247, and 70°E in Track 018, both located where surface flow features are evident in the Landsat image (Figure 8.8).

An explanation of the observed along track variations in the S/V parameters k_e and K is suggested by considering the spatial variability of backscatter (σ_0) over the ice shelf. The presence of sastrugi fields and variations in snow properties create local variations in σ_0 (Legresy and Remy 1997). Furthermore, surface depressions, such as those observed in the 1-km AIS-DEM, tend to focus the altimeter beam, similar to a parabolic reflector, making the return power stronger, and therefore slightly increasing the waveform amplitude and σ_0 (Ridley *et al.* 1989).

Legresy and Remy (1997) simulated the crossing of a radar altimeter signal over a 2-km wide strip whose σ_0 was 10 dB higher than the surrounding surface. The waveform parameters they modelled were the width of the leading edge and the slope of the trailing edge. Schematic graphs of these parameters and the σ_0 against distance along track are shown in Figure 8.12.

The trailing edge slope (θ_{TE}) responds first, as it is composed from the range bins towards the outer edge of the footprint. θ_{TE} initially rises, and then decreases at the σ_0 maximum, then increases again as it passes over the strip, and it migrates to the opposite edge of the footprint. The leading edge width (W_{LE}) responds similarly, with a smaller magnitude and over a shorter distance. Since they are derived from the waveform shape, the S/V parameters k_e and K also respond to such features. Steep leading edges (small leading edge widths) result in a high k_e value. K increases as the leading edge width increases.

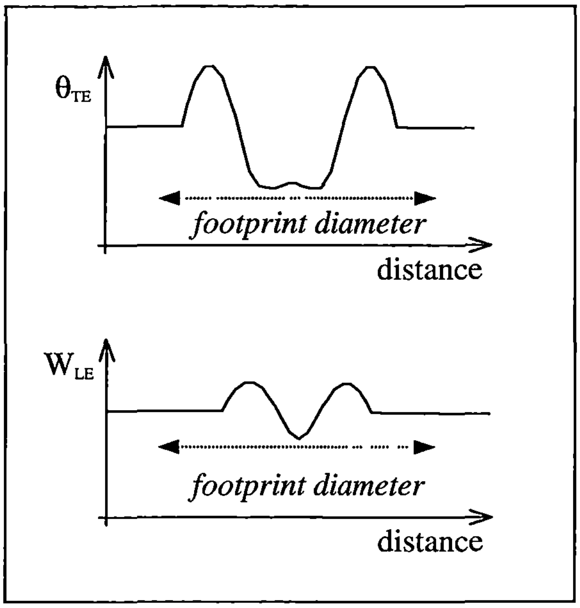

Figure 8.12 *Schematic diagram of simulated profiles for two waveform parameters trailing edge slope (θ_{TE}) and leading edge width (W_{LE}) across a band of radar bright material. Adapted from Legresy and Remy (1997).*

Variations in K and k_e along Track 018 are plotted against longitude in Figures 8.13, together with the corresponding variations in σ_o and surface elevation. At 70°E, there is a local maximum in σ_0 and a local minimum in the elevation. This is coincident with the abrupt change in behaviour of the two S/V parameters K and k_e, suggesting that the change is not entirely real, but an artefact of the changing shape of the radar altimeter waveform crossing over this surface depression. It is suggested that the observed fluctuations in the derived k_e and K values (Figures 8.10 and 8.11) are partially due to spatial variations in σ_o over the ice shelf surface, creating a change in the waveform shape. Moreover, it is apparent that k_e and K are not behaving discretely here, as the local variations they exhibit are connected in some way. It is not known whether this is because the surface snow properties are changing in a way that affects both k_e and K, or because the waveforms are such that the S/V model cannot separate the two parameters. Other factors that could affect the waveform shape across the ice shelf are differences in the degree of stratification of the near surface layer across the ice shelf (see Section 8.2.1).

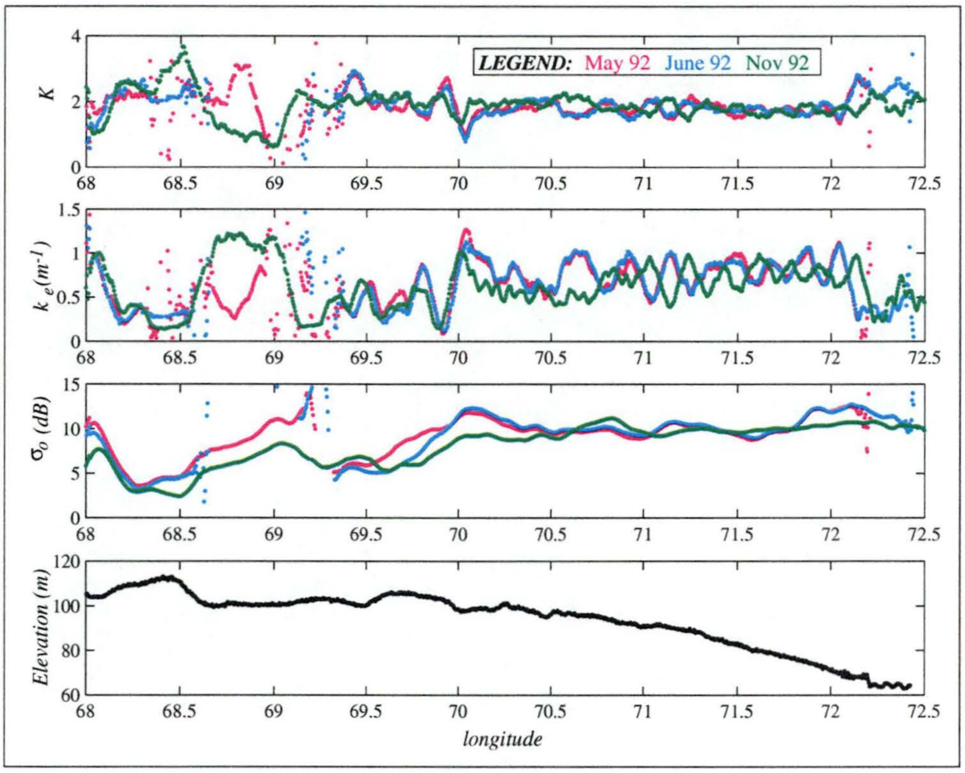

Figure 8.13 *Variations along Track 018 in a) K b) k_e c) σ_o and d) surface elevation.*

Inter-annual variability of S/V parameters

An example of the inter-annual repeatability of the S/V parameter values is shown for Track 027 in Figure 8.14. The two passes are from November 1992 and November 1993. The ground tracks of these orbits repeat almost exactly. The sign of the variations and wavelength of oscillations in the plots are approximately the same. However, there are differences in some of the magnitudes of the parameters, possibly due to slight variations in near-surface conditions in each flow band between the years, resulting from differences in accumulation rates and local climate.

Spatial and temporal variations of S/V parameters along Phase D track

The Phase D (3-day repeat) track that crossed the Amery Ice Shelf was Track 013 (see Figure 8.8). During this phase, the ERS-1 altimeter switched between ocean and ice mode for consecutive cycles, making consecutive ocean mode passes 6 days apart. Variations in derived S/V parameters along seventeen passes of this track were examined.

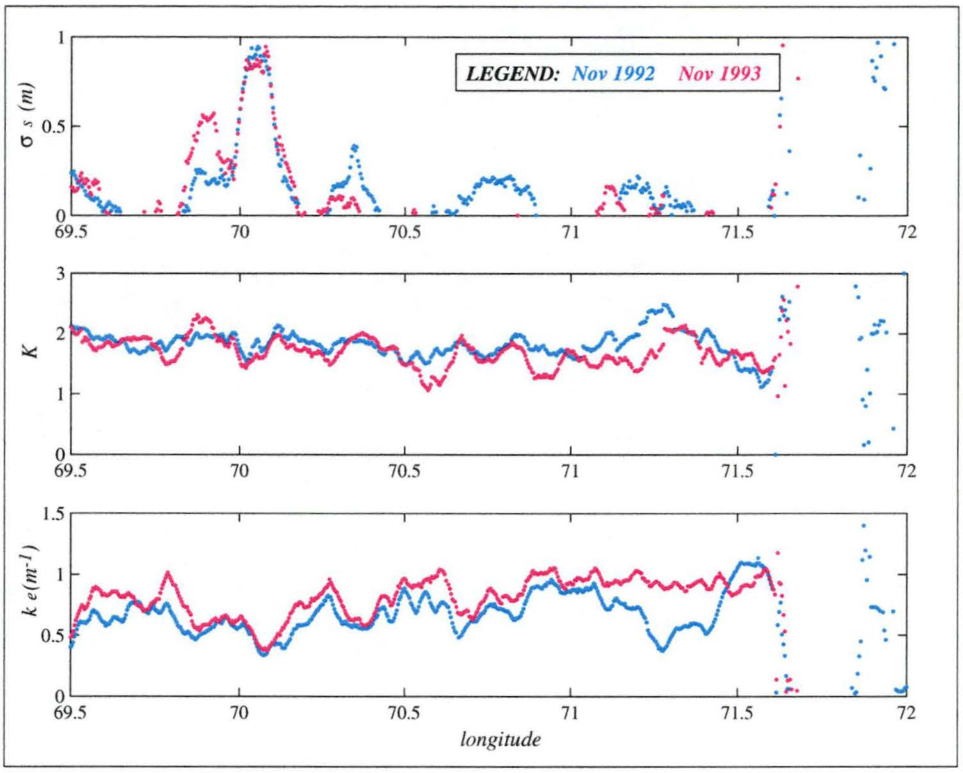

Figure 8.14 *Variations along Track 027 in a) σ_s, b) K and c) k_e for November 1992 and November 1993.*

Variation along Track 013 of the S/V parameters σ_s, K and k_e, and the χ^2 values from the S/V fit, are presented in Figure 8.15. The passes shown are from 18, 24 and 30 January. For the first two passes, the parameters exhibit oscillations similar to those observed in the Phase C tracks, and are highly repeatable along-track. This is also true of the earlier passes, which are not shown here. For the third repeat (30 January) the parameters become noisy in the 12 km segment between 69.5 and 69.8°E. In this region, the χ^2 values are acceptable for the first two repeat cycles, indicating that the S/V model fitted well to the waveforms. However, for the third cycle they are much larger and more variable, indicating that the S/V model fitting was no longer successful. The waveform sequences along each of these passes, and the intervening ice mode repeat, were examined and it was found that the waveform shape had changed to that of a quasi-specular return in this region between 24 and 27 January (see Figure 8.17). It is to be noted that these data did not have the specular filter (Appendix A) applied.

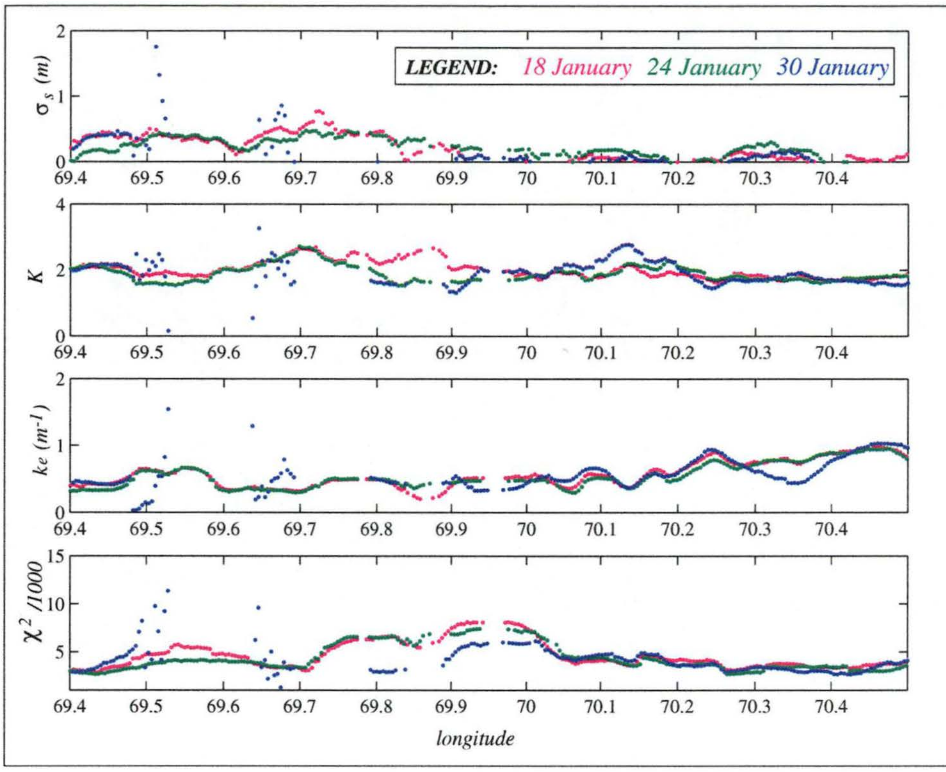

Figure 8.15 *Variation along track in the S/V model parameters a) σ_s, b) K, c) k_e and d) their corresponding χ^2 values for passes of the Phase D 3-day repeat track (Track 013) across the Amery Ice Shelf on 18, 24 and 30 January 1993. The location of this track on the shelf is illustrated in Figure 8.8. Plots for different passes are colour-coded (see legend).*

Since the observed temporal change in surface properties occurred during the summer, it is hypothesised that it was a consequence of surface melting. Further testing of this hypothesis is carried out in Section 8.4.1.

Discussion of surface properties from S/V model

This section has demonstrated that it is possible to gain some knowledge of the physical properties of the surface and near surface of the Antarctic ice sheet from ERS altimeter waveforms using the S/V model.

The large-scale (50 km) study carried out here used data from all valid waveforms in the whole Lambert-Amery system and showed that bulk physical properties could be extracted, even on the Amery Ice Shelf itself. The parameter σ_s has some relation with the true surface roughness amplitude. On the Amery Ice Shelf, k_e is high and K is low, demonstrating that the dominant scattering mechanism on the ice shelf is from the surface. Conversely, on the plateau regions k_e is low and K is high, suggesting that volume scattering makes a significant contribution to the return from these regions.

The small-scale study on the Amery Ice Shelf was limited by restrictions on the S/V model which are imposed by assumptions made in its derivation (see Section 8.2.2). From the AIS-DEM (Chapter 5), it is known that the Amery Ice Shelf is not a homogeneous, flat surface. It contains distinct flow features, surface depressions and refrozen melt features (see next section). The sub-surface is also not homogeneous, as snow pits reveal that there is stratification in the top portion of the firn. The stratified layers cause internal reflections of the radar, which are not accounted for by the S/V model. These factors can also cause the model to return invalid parameter values. A model by Dale Winebrenner, at the Applied Physics Laboratory, University of Washington, is a more complete model that addresses the sub-surface layering issue (Dale Winebrenner, personal communication, 1998). However, this model still requires the condition that the surface is ideally flat.

If retrieved parameters are to be used to search for climate change using the approach adopted here, a long time series is needed. Since over the ice sheets existing ERS altimeter data are mainly ice mode, using the S/V approach with ERS altimeter data is not feasible, unless a program of regular acquisitions in ocean mode is implemented. Because of the difficulty of separating weather effects (e.g. surface crusts, surface melt, surface accumulation *etc.*), without continued *in situ* observations, a preferred approach would be to use data from a combination of instruments e.g. SAR, SSM/I, scatterometer *etc.* In particular, the use of contemporaneous data from a combination of sensors, at different frequencies, spatial resolutions, and viewing geometries, (e.g. nadir-looking altimeter combined with the oblique scatterometer) is the ideal approach.

The S/V model is not suitable for some types of waveform that arise from the Amery Ice Shelf. Using data from a 3-day repeat, quasi-specular waveforms (see Figure 8.17) were found to appear suddenly between 24 and 30 January 1994. Since this is during summer, it was suspected that the cause could be associated with surface melting. The hypothesis that melting is the cause of the dramatic change in surface properties seen in the altimeter waveforms is tested in the first part of the next section, using ancillary data.

8.4 Temporal changes in surface properties from ERS data

The previous section looked primarily at the along track spatial variability in the S/V parameters that are a result of variation of surface and near surface properties. These surface properties also change with time. Temporal changes can occur rapidly, especially in regions subject to summer snow melt (e.g. Ridley 1993a).

The purpose of this section is to determine whether temporal changes of the ice sheet surface can be detected from analysis of the altimeter waveforms. An example of rapid change in surface properties was revealed in the last section, in consecutive ocean-mode passes of the ERS-1 altimeter over the survey region during its 2nd ice phase (Phase D) in the 1993-94 summer. The cause of these changing surface properties on the Amery Ice Shelf, is examined. Short repeat period ERS-1 data from the 1993-94 summer are used to monitor the time of onset of the observed change on the surface of the ice shelf. The shapes of the individual waveforms and the σ_0 values along repeat passes are examined, and the hypothesis is made that the observed change is caused by surface melt. Other sources of observation on the ice shelf (temperature, *in situ*, SAR imagery and passive microwave brightness temperatures) are investigated to test this hypothesis.

Further short repeat period ERS-1 data from the 1991-92 summer are used to examine the temporal variation in the time of onset and duration of the surface meltstreams, known to change from year to year (Winther *et al.* 1996). Using a simple test, the temporal and spatial locations of surface meltstreams are investigated, for the four summers 1991-92 to 1995-96, although this study is severely limited by the trade-off between the spatial and temporal resolution of the satellite altimeter data.

8.4.1 Monitoring changing surface properties with ERS data, 1993-4 summer

ERS-1 operated in a short repeat frequency (3-day) orbit during the austral summers of 1991-92 and 1993-94, which were the mission's 'Ice Phases' (see Table 3.1, Chapter 3). During these phases, the satellite was operated in a 3-day repeat orbit, and for both phases the ground track locations remained the same. This temporal resolution is ideal for monitoring change at a specific location, but the monitoring is restricted spatially by the fact that the tracks are so far apart (~300 km at 71°S). Only one of these tracks (Track 013) crosses the Amery Ice Shelf, and its location on the Amery Ice Shelf is shown as a purple line in Figure 8.8.

Data from the 2nd Ice Phase ERS-1 data (Phase D: 1993-94 summer) are used in this section to investigate the cause of the changing surface on the Amery Ice Shelf. A few supplementary orbits from Phase E, which followed Phase D, are also used in this analysis. These were from the autumn and winter seasons (10 April 1994 to 27 September 1994). In Section 8.4.2, once the cause of changing surface properties is established, the 1st Ice Phase data (Phase B: 1991-92 summer) are used to compare the onset time and duration of the changing surface properties between the two seasons. The 2nd Ice Phase was from 23 December 1993 to 10 April 1994 which covers a whole summer season on the Amery Ice Shelf. During this phase, the ERS-1 altimeter alternated between ocean- and ice-mode over the ice, therefore adjacent ice mode passes during Phase D were six days apart. During Phase E, the altimeter was always operated in ice-mode over the ice.

The region of change in Track 013 under investigation is 69.5°E to 69.8°E, which coincides with the Amery Ice Shelf survey region (Chapter 4). In Chapter 4, the surface topography over this region was presented (Figure 4.14) generated from the kinematic GPS profiles, which matched very well with that seen in another DEM created from the 168-day ERS-1 data (Figure 5.9). Two longitudinal shallow depressions, approximately 3-km wide, 5-m deep and more than 60-km long were revealed in this surface. The ERS-derived surface is shown again in Figure 8.16, in a different orientation to that of Figure 5.9, to better display the surface depressions.

ERS-1 waveform sequences

ERS-1 altimeter waveform sequences along Track 013 over the survey region, for four consecutive passes (24, 27, and 30 January and 2 February 1994) are presented in Figure 8.17. The waveforms are approximately aligned by position: i.e. waveforms with the same number from each sequence are from similar locations along track. The first and third sequences are in ocean-mode, while the second and fourth are in ice-mode, hence the difference scaling on the power (y) axes.

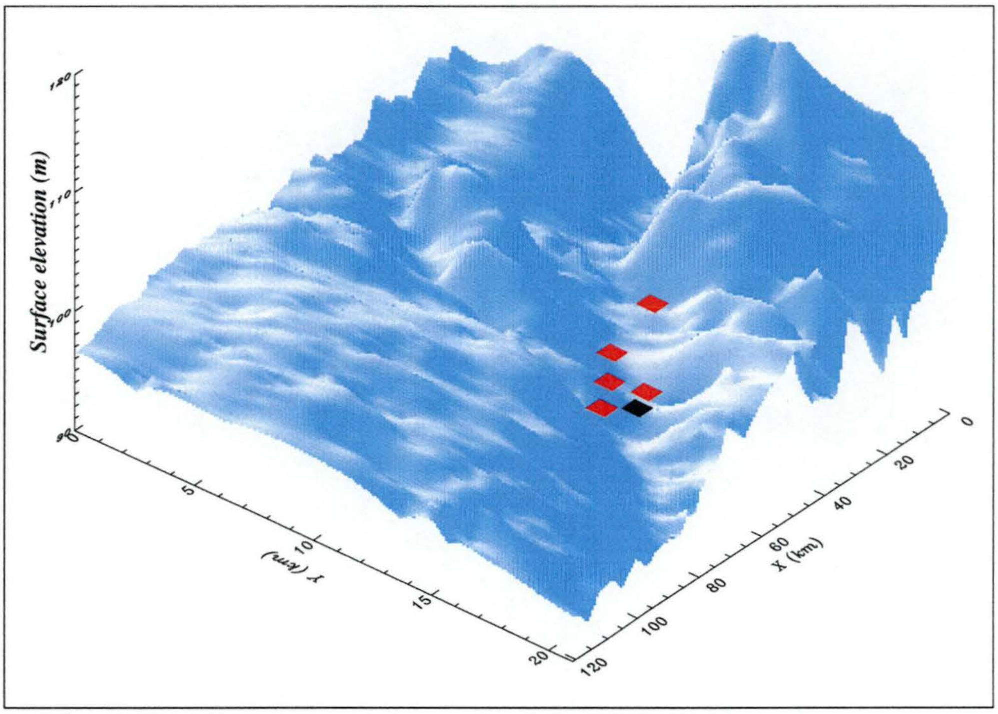

Figure 8.16 *Shaded ice surface interpolated from the ERS survey data, on a 0.5-km grid using kriging. The black and red squares represent the locations of the σ_0 peak and central quasi-specular return for the 3- and 168-day-repeat data respectively.*

In the first ice mode sequence (27 January), waveform 1 is a typical ice shelf return, with a well-defined leading edge (A). The bump (B) at the back of waveform 2 occurs because the altimeter views two surfaces at different ranges, indicating that a new, lower elevation surface is entering into its footprint. In waveform 3, the higher surface has retreated and the sharp leading edge indicates that the low surface has become dominant, so the satellite is directly above the surface depression. Waveform 4 shows the altimeter leaving the depression and moving back onto the main ice shelf and waveform 5 is again a typical ice shelf return.

The second ice mode sequence (2 February) is similar to the first, except in the centre of the depression (waveform 3) where the waveform is narrow-peaked. This waveform has a very steep leading edge and large amplitude (the power scale has been multiplied by a factor of 10), and is termed 'quasi-specular' (Rapley *et al.* 1987).

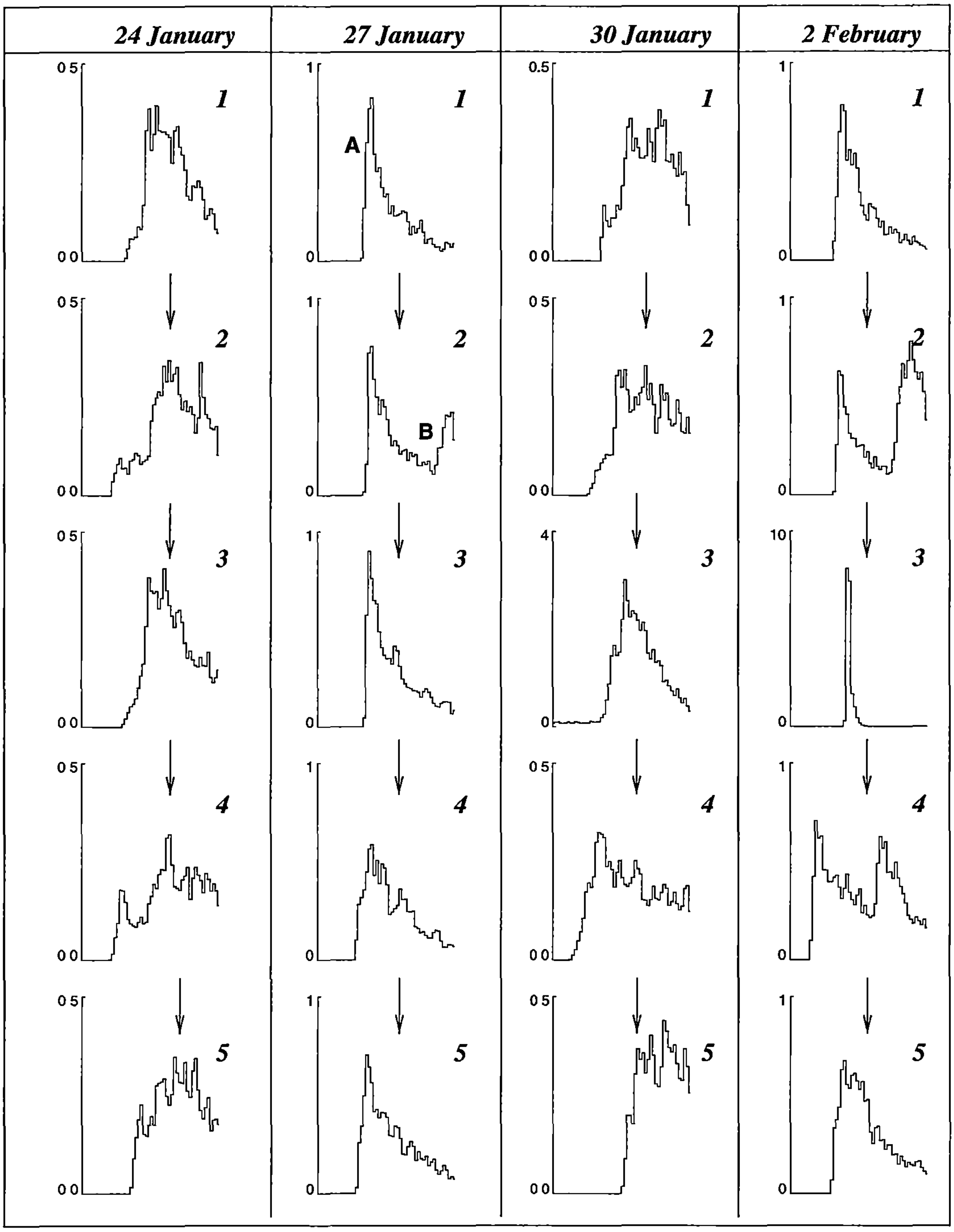

***Figure 8.17** ERS-1 waveform sequences along four consecutive repeats of Track 013, across a surface trough on the Amery Ice Shelf (24, 27, 30 January and 2 February 1994. The first and third repeats are ocean-mode; the second and fourth are ice mode. Note the transition of Waveform 3 to quasi-specular between the second and third repeats. A and B are discussed in the text.*

The location of the quasi-specular waveform observed in Figure 8.17 is plotted as a yellow diamond on Figure 8.16, and it can be seen that it coincides in location with the deeper of the two surface depressions.

ERS-1 measured backscatter (σ_o)

Figure 8.18 shows the microwave backscatter *(σ_0)* measured along Track 013 across the Amery Ice Shelf for the same four passes shown in Figure 8.17, for a) ocean mode and b) ice mode. For ocean mode, there is a large increase in σ_0 on 30 January 1994, and the same effect is seen in the ice mode pass from 2 February. The peak σ_0 value coincides in location with the quasi-specular waveform from the centre of the surface depression (Waveform 3 in Figure 8.17).

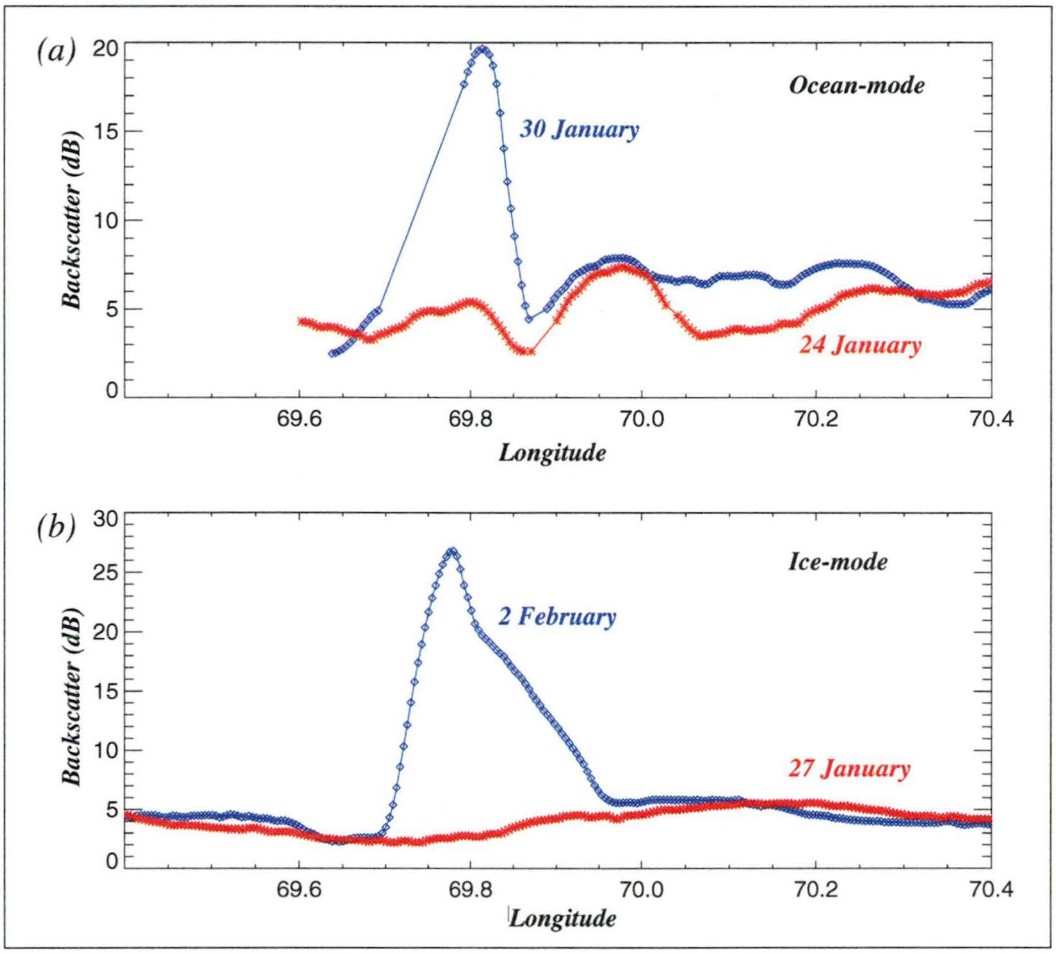

Figure 8.18 *ERS-1 σ_0 along Track 013 across the central Amery Ice Shelf on a) 24 and 30 January (ocean-mode) and b) 27 January and 2 February (ice-mode). Note the significant increase in σ_0 in the later repeat for each operating mode.*

Possible cause of changing surface properties

In Chapter 3, it was noted that the altimeter return waveform is quasi-specular only when the incident surface is ideally smooth and flat. The sudden transition, from typical ice shelf returns to quasi-specular waveforms, in the survey region between 27 and 30 January indicates that the surface must have changed from diffuse to ideally flat. This, combined with the observed increase in ERS-1 measured microwave backscatter (σ_0) on the Amery Ice Shelf on 30 January 1994, indicates that a rapid change in surface properties took place over the three days between altimeter passes. Such a dramatic signal can be explained by the arrival of meltwater in the altimeter footprint, causing strong reflections of the radar pulse.

The ERS-1 altimeter has a surface footprint of approximately 6-8 km diameter over the Amery Ice Shelf; the smooth surface of the meltstream therefore lies within the footprint before the satellite is directly overhead, and after it has passed. The parabolic shape of the σ_0 variation observed in Figure 8.18 indicates that the reflecting area is small.

Supporting evidence for surface melting

The altimeter waveform sequences and the along-track σ_0 values have revealed that surface properties changed rapidly in a localised region of the Amery Ice Shelf between 27 and 30 January 1994. The evidence so far presented suggests the presence of a seasonal (summer) reflective surface that forms in between these two dates. It is hypothesised that this surface, correlated with a topographic low observed in the GPS and altimeter surfaces over the survey region (Chapters 4 and 5), is due to the arrival of meltwater in the depression, known as a surface meltstream.

To test the hypothesis that the observed phenomenon is surface melting, some further observations are required. The following section discusses some other observations on the Amery Ice Shelf, collected both *in situ* and from remote sensing. Each type of observation is described below, and the results are interpreted to build up a complete picture of the phenomenon occurring here.

Previous observations (1960-1990)

Surface melt features in the Lambert-Amery system were documented as early as 1960, when it was noted that extensive summer melting took place forming 'rivers' and melt-water lakes (Mellor 1960). They have also been detected by aerial observation, and in SAR (see Figure 8.19) and Landsat satellite imagery (Swithinbank *et al.* 1988; Neal Young, personal communication, 1997). Surface observations from snow pits and shallow cores also show evidence of meltstreams in superimposed ice layers, interspersed by layers of winter snow accumulation (Landon-Smith 1962; Goodwin 1995). The meltstreams carry large volumes of meltwater and it is evident that in some years the meltstreams are active, while in others they remain dormant.

Recent observations (1993-1995)

Pit measurements were made at each of the six base camps of the 1995 Amery Ice Shelf survey (see Figure 4.2). Camp C2 was located in one of the depressions seen in the surface elevation model. The pit at this camp revealed a single layer of snow (27 cm deep) on top of hard, bubble-free ice. This suggests that the depression once held water. This is further confirmed by the fact that the depressions are flat-bottomed, as revealed in the kinematic GPS profiles along the cross-arms of the GPS survey.

Evidence of meltstreams on the Amery Ice Shelf is seen in recent Synthetic Aperture Radar (SAR) imagery (Figure 8.19). This is an ERS-1 SAR image acquired on 15 August 1993, warped onto a polar stereographic projection, with the GPS survey grid and the ERS-1 3-day track overlaid. The prominent wish-bone shaped, dark feature within the survey grid is composed of two fossil meltstreams, standing out clearly from the surrounding ice shelf due to its different near-surface properties and low surface roughness. SAR is a side-looking instrument and at oblique incidence over rough surfaces, where a significant part of the energy is reflected in all directions, the backscatter signal received at the satellite is comparatively high. For a smooth surface, only a very small part is reflected back to the satellite, therefore the backscatter is low. SAR penetrates deep into the snow-pack and therefore even if a refrozen meltstream has been buried by recent accumulation the backscatter from it will still be low, therefore the feature appears dark.

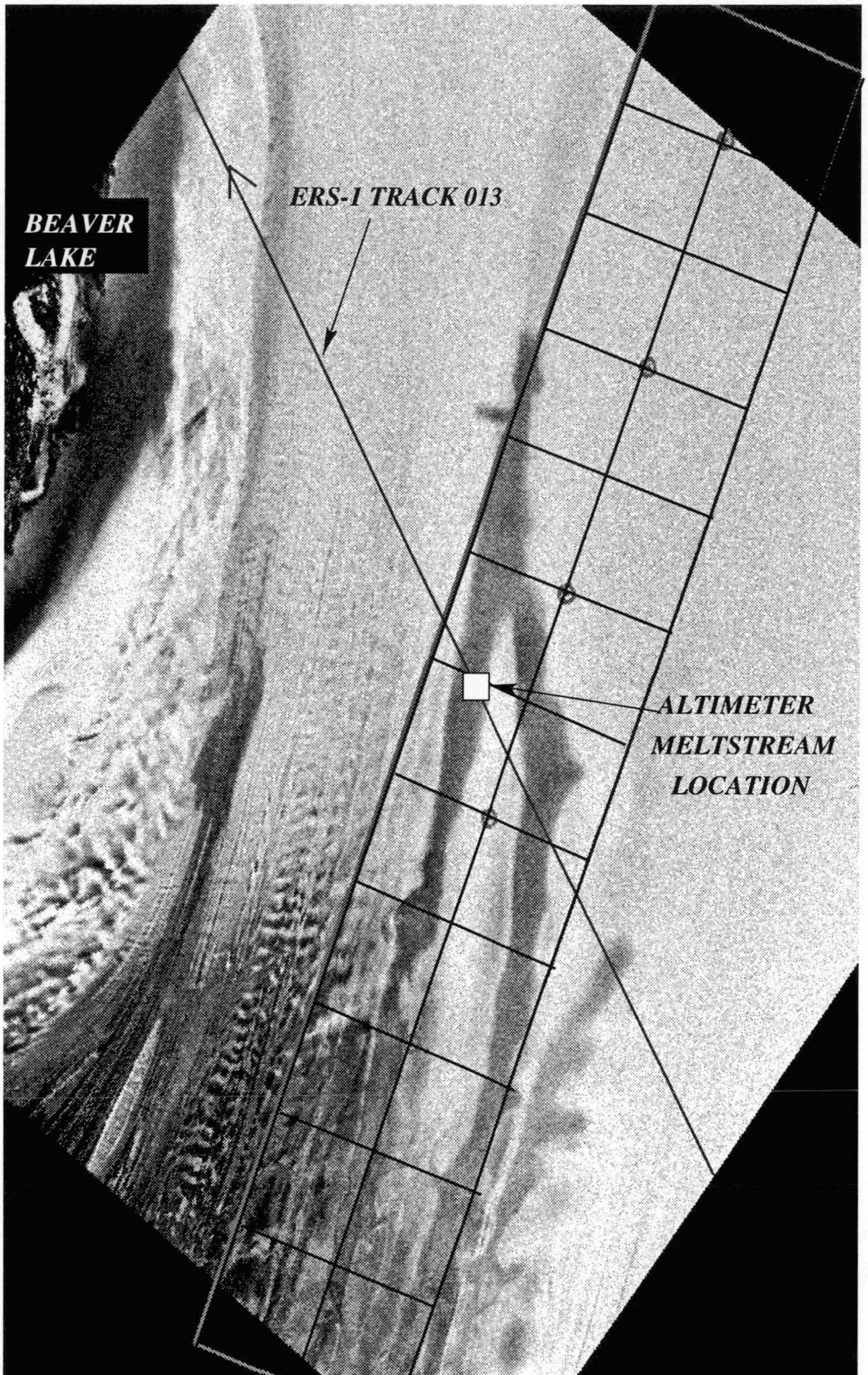

Figure 8.19 *SAR image acquired over Amery Ice Shelf survey region on 15 August 1993. The white square denotes the location of the backscatter peak and main quasi-specular return evident in the Track 013 repeats from 30 January 1994. The SAR data were provided through AO project Id. ERS-A02-AUS103 (Principal Investigator: N. Young). The SAR data are Copyright ESA 1993.*

The location of the refrozen meltstreams seen in the SAR imagery matches well with the depressions seen in the surface topography in Figure 8.16. The SAR image (Figure 8.19) suggests that the eastern, shallower depression was also occupied by melt-water in a previous year. However, from the results of the altimeter analysis carried out here it does not appear that this depression carried water during 1993-4.

SSM/I Brightness Temperatures

Melt events on the ice sheets and the ice shelves can be detected in passive microwave brightness temperatures (Ridley 1993b, Zwally and Fiegles 1994). The brightness temperature (T_B) of an object is a measure of the intensity of the microwave radiation it emits. It is the product of the object's absolute physical temperature and its emissivity. The emissivity is dependent on the object's physical properties: for snow it increases as moisture content increases and as grain-sizes decrease (Zwally and Gloersen 1977). Surface melting increases the moisture content of the snow, increasing its emissivity and T_B. Large increases in T_B during the summer months indicate the onset of melting (Ridley 1993b).

The Special Sensor Microwave/Imager (SSM/I), on board the Defense Meteorological Satellite Program platform, is a passive microwave sensor that measures surface brightness temperatures. To determine when melting occurred in the Lambert-Amery system during the 1993-4 summer, daily T_B values from the SSM/I instrument were averaged over the three large polygons in the region, shown in Figure 8.20. The three time-series of average 19 GHz (vertical polarisation) T_B values are shown in Figure 8.21 (colour-coded to the polygons in Figure 8.20). Values decrease from south to north because grain-sizes increase in this direction (Zwally and Fiegles 1994), reducing the emissivity. The T_B values increase slowly with temperature from 1 December until the first melting event in late December, when they increase rapidly to approximately 240 K over all three regions. The peak occurs around 5 January (Day 35), corresponding to full saturation of the snow. The values then decrease steadily, until around 21 January (Day 51), when there is a secondary rapid increase.

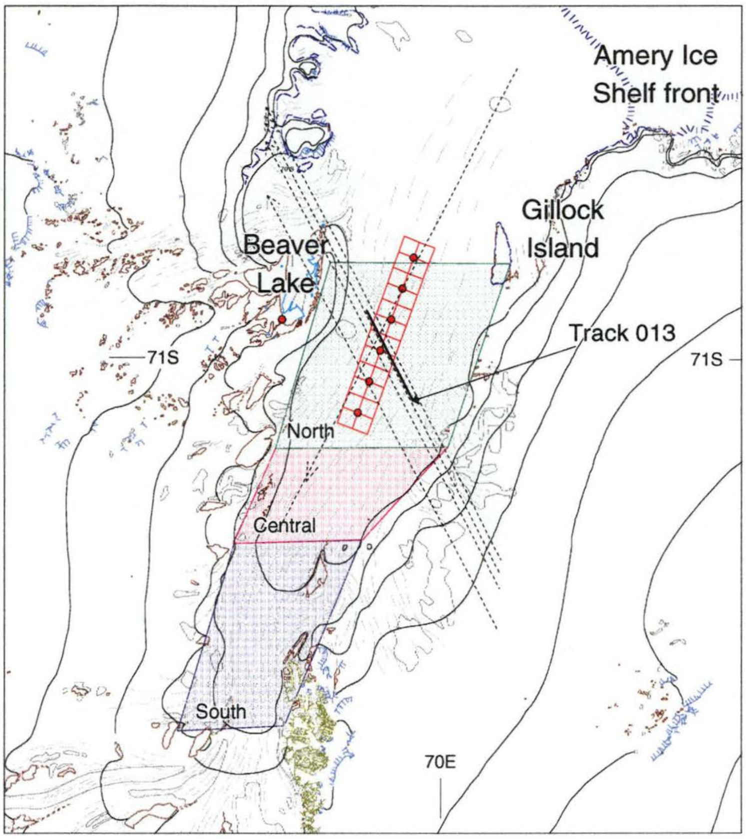

Figure 8.20 *Map of Amery Ice Shelf showing GPS grid, ERS-1 ground tracks and the locations of the SSM/I polygons (North, Central and South) used in this analysis.*

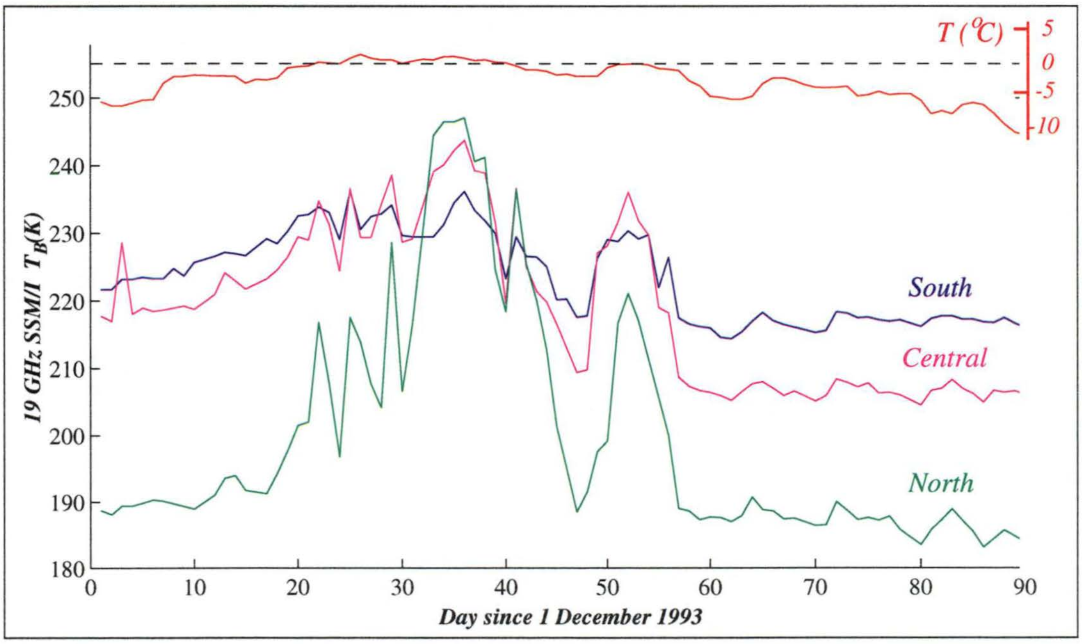

Figure 8.21 *Time series of daily SSM/I passive microwave brightness temperatures averaged over the three polygons shown in Figure 8.20. The red line is the average daily temperature at Mawson (T) in degrees.*

Temperature Data

Measurements of near-surface temperatures at Mawson (top line in Figure 8.21), at a similar surface elevation and approximately 300 km northeast of the region of interest, show periods at and above zero degrees Celsius over this period. These periods of positive temperatures coincide with the periods of summer melting observed in the SSM/I brightness temperature values. These independent observations of temperature validate the interpretation of the increase in brightness temperatures being associated with partial surface melting.

Discussion

Cause of changing surface properties

Each additional dataset presented here has provided evidence to support the hypothesis that the observed phenomenon in the ERS waveforms is due to surface melting. Meltstreams coinciding in location with the position of the changing surface are seen in recent SAR imagery. From passive microwave data, the dates of the melting events in the Lambert-Amery system for the 1993-94 season are found to be 5 and 21 January 1994, which are confirmed with a temperature record from Mawson. These two major melt events in the Lambert-Amery system combined to trigger a large meltstream, explaining the presence of water in the altimeter footprint nine days later (30 January).

Persistence of 1993-94 meltstream effects in altimeter data

Figure 8.22 illustrates the evolution with time of the shape of the waveform from the centre of the surface depression, for twelve ice-mode passes from 27 January to 9 April. Only ice mode waveforms are shown here since the specular shape is more obvious due to the coarser sampling of the waveform. The shape remains quasi-specular for 2 passes (2 and 8 February) and displays a sharp peak until 9 April.

Figure 8.23 shows the change in the value of the σ_0 peak for all of the ice-mode passes along Track 013 (from 25 December to 9 April). σ_0 remains high for a period of about a week, but decays after its peak value on 2 February. σ_0 drops to around 16 dB, and remains relatively constant through to the end of April.

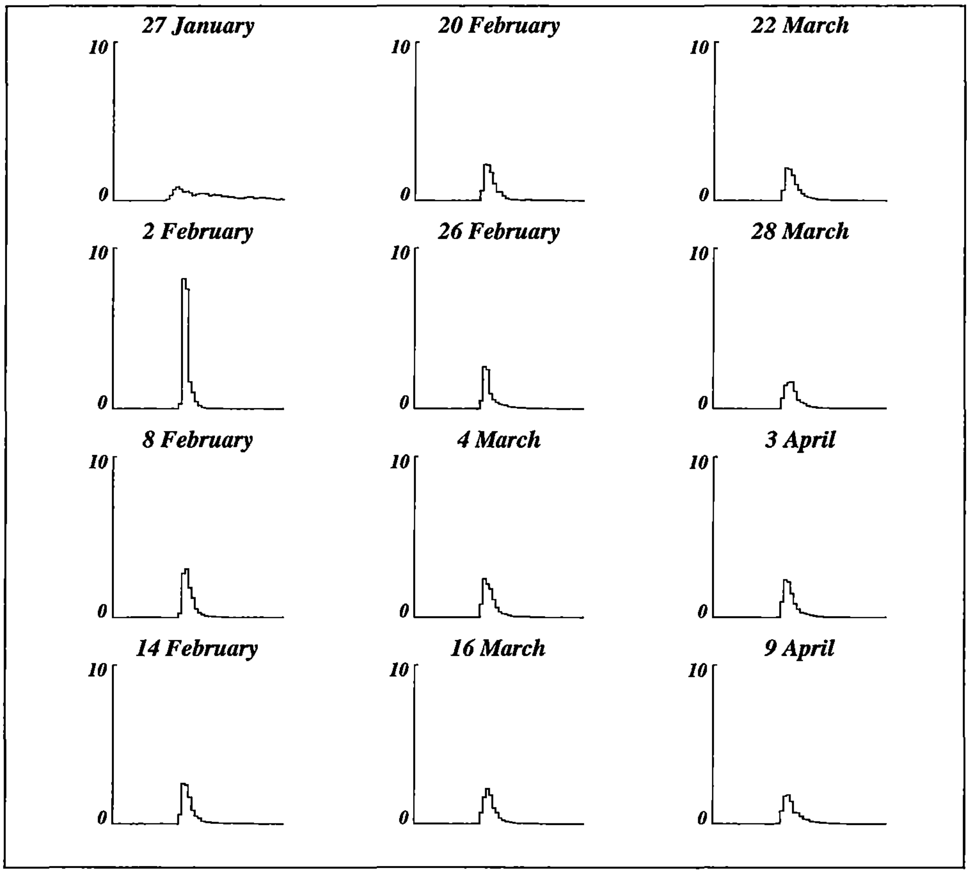

Figure 8.22 *Time series of altimeter waveforms from the centre of the surface trough, for all ice mode repeats along Track 013 (1994).*

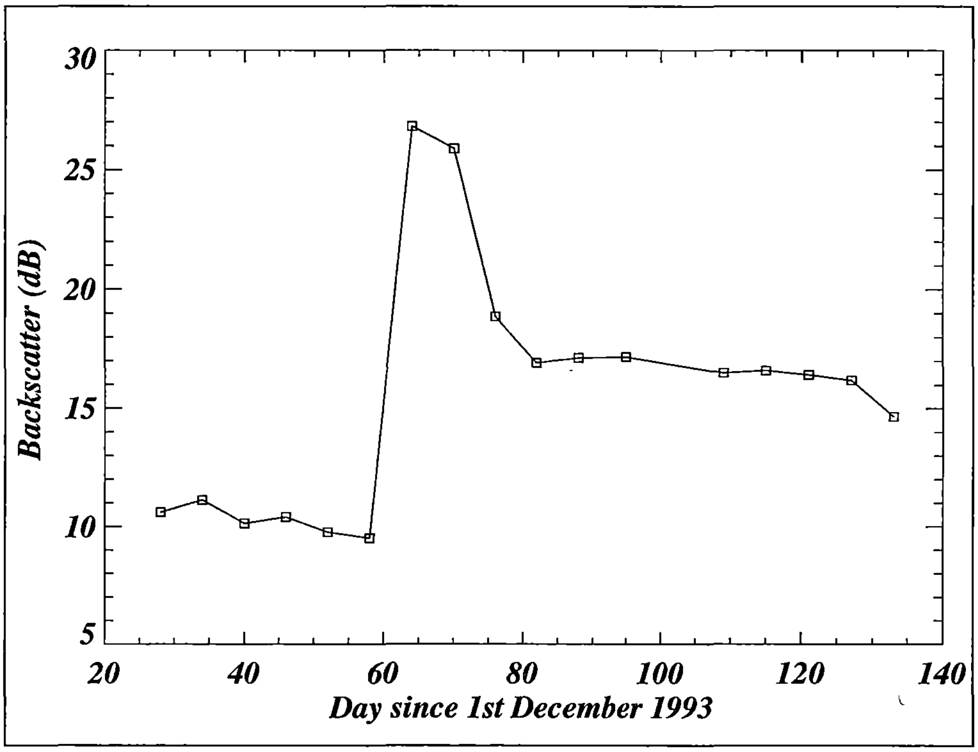

Figure 8.23 *Time series of maximum backscatter over surface trough, for all ice mode repeats along Track 013 (1994).*

The drop in the maximum σ_0 value after 2 February 1994 occurs because the water in the meltstream refreezes as surface air temperatures decrease. On refreezing, the surface remains smooth, therefore the waveforms continue to be quasi-specular. However, the lower reflectivity of ice compared to water (Ulaby *et al.* 1981), combined with the fact that surface roughness increases after refreezing due to the formation of micro-cracks in the surface, leads to a drop in σ_0.

Orbits from the next ERS-1 phase (Phase E) were also examined for quasi-specular returns and high σ_0 values. One of these crossed the Amery Ice Shelf very close to Track 013 on 5 June. The orbit still contained quasi-specular waveforms and had a peak σ_0 value of 15.3 dB (ice-mode) over the melt channel. This suggests that there was little change in surface properties between late February and early June. In fact, σ_0 peaks and quasi-specular returns persisted until 12 July 1994 in the 168-day profiles. The locations of the main quasi-specular return for the Phase E orbits are plotted as red diamonds in Figure 8.16. These points, from 29 April, 16 May, 5 June, 11 June and 12 July, all lie in the surface depression evident in the shaded surface plot.

This suggests that the surface remained smooth throughout this period and that there was no, or very little, snow build-up on top of the ice until after 12 July. The addition of a layer of snow would increase the surface roughness and therefore reduce σ_0; addition of more snow layers would eventually lead to the attenuation of the σ_0 peaks and quasi-specular returns. That is, the surface characteristics would return to the pre-melt state observed from December to January. Monitoring the persistence of the σ_0 peaks and the quasi-specular returns over meltstreams could be one indicator of variations in regional snow accumulation.

The fact that quasi-specular returns remained in the altimeter data until the winter of 1994 is significant in terms of accurate ice shelf mapping using satellite radar altimetry. If meltstreams (flowing or refrozen with little snow build-up) are present on the ice shelf, the altimeter will range to such features while they are contained in its footprint (a problem called 'snagging'). The quasi-specular waveform will only give a correct surface elevation measurement when the meltstream is at nadir; elsewhere the effect on the range measurement is a decrease of up to 30 m (see

Appendix A). These under-estimated height measurements should be removed from the altimeter dataset.

8.4.2 Summer 1991-92

The ground tracks for the other 3-day repeat phase (Phase B) were the same as those for Phase D. The dates of Phase B were 30 December 1991 until 26 March 1992. To investigate any differences in the time of onset and duration of the surface meltstreams in the Amery ice Shelf Survey region between the two summer seasons, all of the passes along Track 013 across the central Amery Ice Shelf were selected and the waveforms and σ_0 values examined. For the first cycle of Phase B ERS-1 operated in ice mode, then switched to ocean mode for the rest of the phase.

The σ_0 values along three of the passes across the survey region for 1991-92 are shown in Figure 8.24. These plots correspond to 5, 17 and 20 January 1992. The time series of maximum σ_0 value, for all of the passes across the survey region is shown in Figure 8.25. There is a dramatic rise starting on 17 January, with the peak occurring on 20 January. A secondary rise occurs on 7 February, and then σ_0 drops steadily towards its background value. From the results of the previous section, it is known that the abrupt increase in σ_0 corresponds to the arrival of meltwater in the surface depression.

Differences in arrival time of meltwater between 1991-92 and 1993-94

Comparison of Figures 8.25 (1991-2) and Figure 8.23 (1993-4) reveal that the time of arrival of the meltwater in the 1991-92 was approximately 15 days earlier in the season than in 1993-94. The locations of the σ_0 peaks coincide spatially, however, suggesting that the same depression was occupied in both years. Since the data were ocean mode and from a very early stage of the ERS-1 mission, there were data dropouts over the survey region for the 17 January repeat of Track 013 (Figure 8.24). This was due to an instability in the ocean mode tracker, which remained a problem with ocean mode over non-ocean surfaces until August 1993 (Cudlip *et al.* 1994b).

Although there is a data dropout, it appears that this graph has two peaks, one slightly east of the major one. This suggests that the shallower, eastern depression, revealed in the ERS topography (Figure 8.16) and the SAR image (Figure 8.19) was

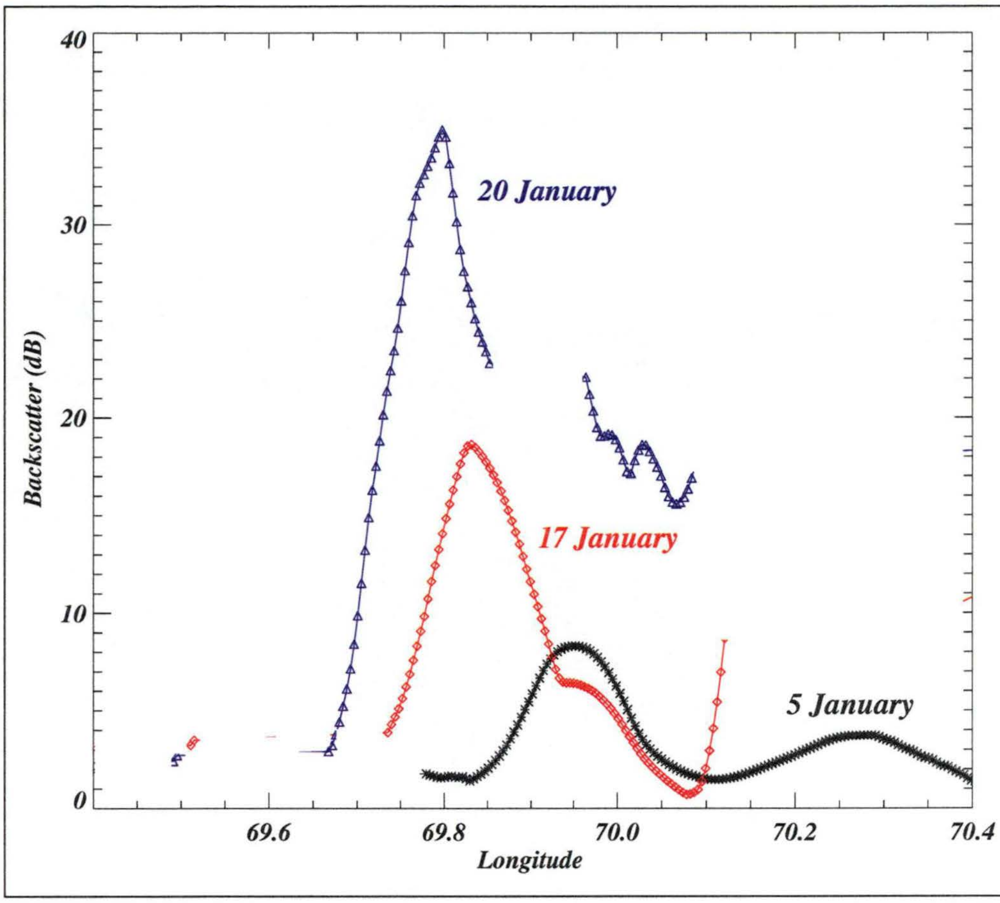

Figure 8.24 *ERS-1 measured backscatter along Track 013 across the central Amery Ice Shelf on 5, 17 and 20 January 1992. The X-axis is scaled to be the same as in Figure 8.18.*

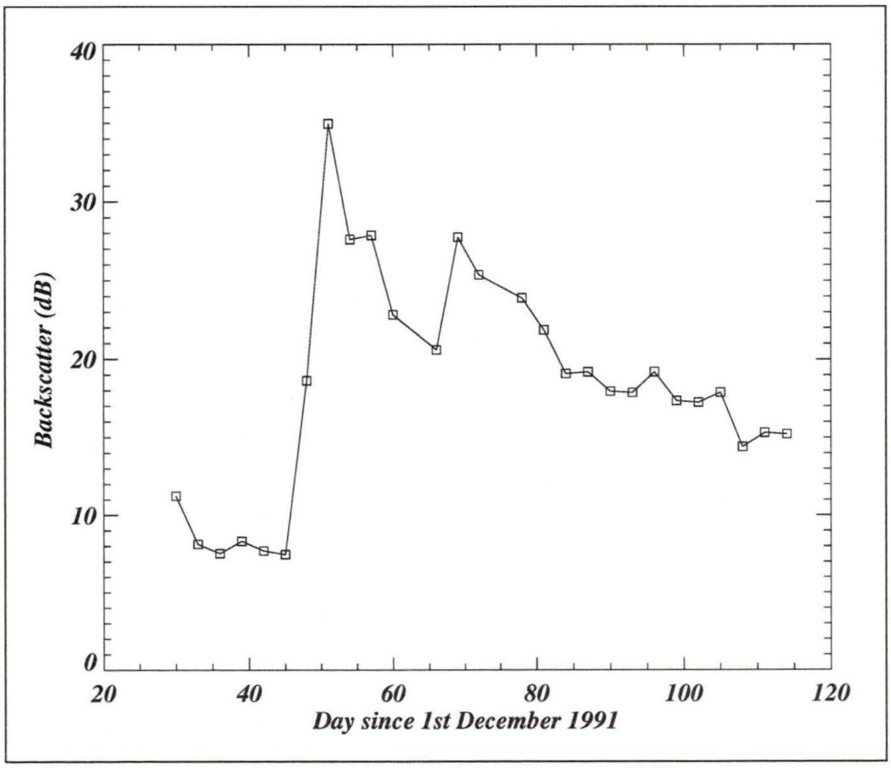

Figure 8.25 *Time series of maximum backscatter for all repeats along Track 013 (December 1991 - March 1992). Compare with Figure 8.23.*

also occupied by meltwater in the summer of 1991-92. It could be this refrozen meltwater which left the wish-bone shaped feature shown in the SAR image acquired 18 months later (Figure 8.19). This would imply that there was a greater volume of meltwater on the ice shelf in 1991-2 than 1993-4. This is confirmed by results of Young and Hyland (1998), who analysed data from the ERS-1 scatterometer and found that there was an unusually large melt event on the Amery Ice Shelf during the summer of 1991-92.

8.4.3 Spatial distribution of melt for five summers with ERS data

The necessity to delete height measurements corresponding to occurrences of quasi-specular waveforms that caused the ERS altimeters to snag, combined with an interest in the spatial and temporal extent of summer meltstreams, led to the development of a simple algorithm to extract these types of waveform. This meant that all of the summer ERS data available could be processed to determine the inter-annual variability in the location and time of onset of the meltstreams. The five summers of ERS-1 were 1991-92, 1992-93, 1993-94, 1994-95 and 1995-56.

Test for quasi-specular returns

The test for specular returns was based on a parameter known as 'pulse peakiness' *(PP)* (Laxon and Rapley 1987), which describes the shape of the waveform, and is highly sensitive to changes in waveform shape. *PP* is calculated as follows:

$$PP = 30 \cdot \left(P_{\max} / \sum_{i=5}^{64} P_i \right) \qquad (8.1)$$

PP values for the quasi-specular waveforms seen in the second 3-day repeat ice phase data over the Amery Ice Shelf were calculated, and it was found that waveforms with pulse peakiness above around 2.0 in ocean mode and 4.0 in ice mode were quasi-specular. Other unique properties of quasi-specular waveforms are very high peak power values, a narrow return and a high σ_0. The full set of criteria for this test are outlined in Appendix A.

The quasi-specular test was used to locate all occurrences of quasi-specular return over the Amery Ice Shelf, using all of the available ERS-1 summer waveform data

(Table 8.5). The table below summarises the repeat period of ERS-1 data for each of the summers.

Table 8.4 YEAR AND REPEAT PERIODS OF SUMMER ERS-1 WAVEFORM DATA PROCESSED USING THE SIMPLE QUASI-SPECULAR TEST.

Year	*Repeat period (days)*
1991-92	*3 (1st ice phase)*
1992-93	*35*
1993-94	*3 (2nd ice phase)*
1994-95	*168*
1995-96	*35*

Results of quasi-specular waveform search

Figure 8.26 illustrates the spatial distribution of the quasi-specular returns for all of the summers for which ERS-1 data were available. As reported above, during the 1991-2 summer the ERS-1 altimeter was operating in a 3-day repeat orbit. Due to this short repeat period, the spatial coverage was very sparse, and the only repeat across the Amery Ice Shelf was Track Number 013. The locations of the strong returns along this track are shown in yellow in the map in Figure 8.26. These locations are the eastern edge of the Amery Ice Shelf, near to Pickering Nunataks, from which quasi-specular waveforms arise as early as 30 December, the central Amery survey region, and at the base of the Charybdis Glacier north of Else Platform (January 31).

During the 1992-3 summer, the ERS-1 satellite was operated in a 35-day repeat period. The 1992-93 locations correspond to regions of blue ice on the southern Amery Ice Shelf. The second ice phase took place during the 1993-94 summer. The melting events during this season have been discussed in detail above. The only location from which quasi-specular returns were received this year was the survey region on the central Amery Ice Shelf.

The high spatial density of tracks from the 168-day phase allowed a much larger area to be examined for quasi-specular returns. These 1994-95 locations correspond to the blue ice ablation regions on the lower Lambert Glacier/upper Amery Ice Shelf,

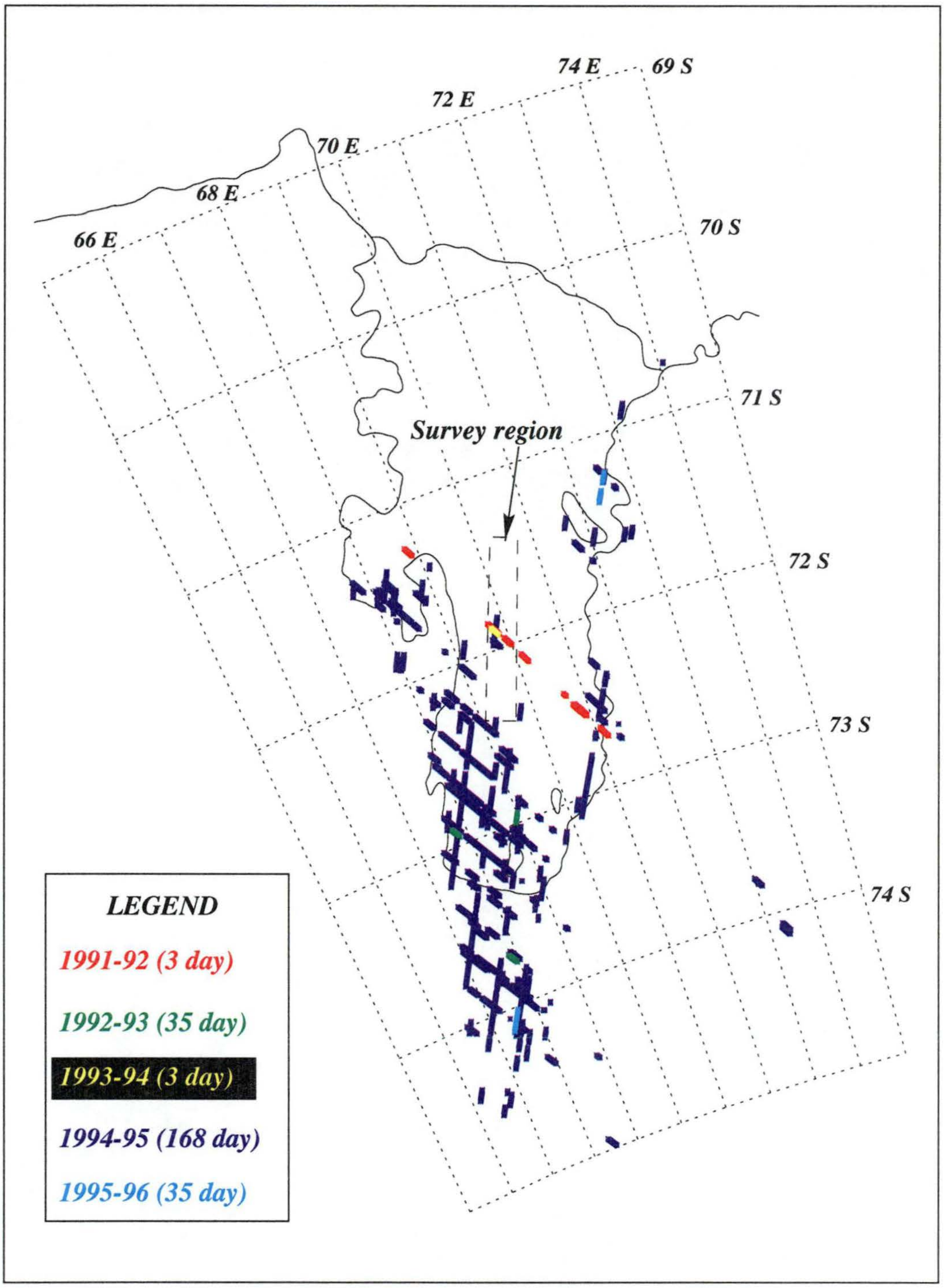

Figure 8.26 *Spatial distribution of all occurences of quasi-specular return for all summers from 1991-2 to 1995-6 in the Lambert-Amery system. Each year is colour-coded (see legend). ERS-1 was in a 3 day orbit during the summers of 1991-92, a 35-day orbit during 1995-96 and a 168-day orbit during 1994-95, therefore the spatial sampling of the surface is very different for each year.*

and on the eastern edge of the Amery Ice Shelf. The 1995-96 locations correspond to 1) the northeastern edge of the Amery Ice Shelf close to the Reinbolt Hills 2) the Lambert Glacier – Amery Ice Shelf transition zone, west of Mawson Escarpment.

The final summer covered by this study was 1995-96. The locations of the only quasi-specular returns found in all of the orbits across the Amery Ice Shelf from November 1995 until March 1996 are shown in Figure 8.26. These occurrences were received on 30 January 1996, and were confined to one pass only. These returns are from two regions of blue ice: the first on the north-eastern edge of the Amery Ice Shelf close to the Reinbolt Hills, and the second in the Lambert Glacier-Amery Ice Shelf transition zone, west of Mawson Escarpment.

Discussion on distribution of melt for five summers

Due to the very different spatial and temporal resolutions for each of the ERS phases, it is difficult to compare quantitatively the times of onset and spatial extent of the meltstreams. The summers of the two 3-day repeat phases (1991-92 and 1993-94) are the hardest to monitor spatially due to insufficient coverage (only one track). However by comparing the locations of clearly defined quasi-specular altimeter returns along Track 013 between the 2 years (Figures 8.18 and 8.24) it can be seen that in 1991-92 there are three regions from which these returns are received and in 1993-94 there was only one. This suggests that there was a greater volume of meltwater in the summer of 1991-92 compared to 1993-94. The fact that the σ_0 graph (presented in Figure 8.24) for 1991-92 had two peaks across the survey region, whereas that for 1993-94 (Figure 8.18) only had one, further suggests that there was more meltwater carried in 1991-92.

During the 1995-96 summer (35-day repeat) there was only one pass that contained quasi-specular returns suggesting that there was a very low melt-rate this year. There were no quasi-specular returns from the central part of the Amery Ice Shelf, suggesting that the depressions in the survey region did not carry water during this summer.

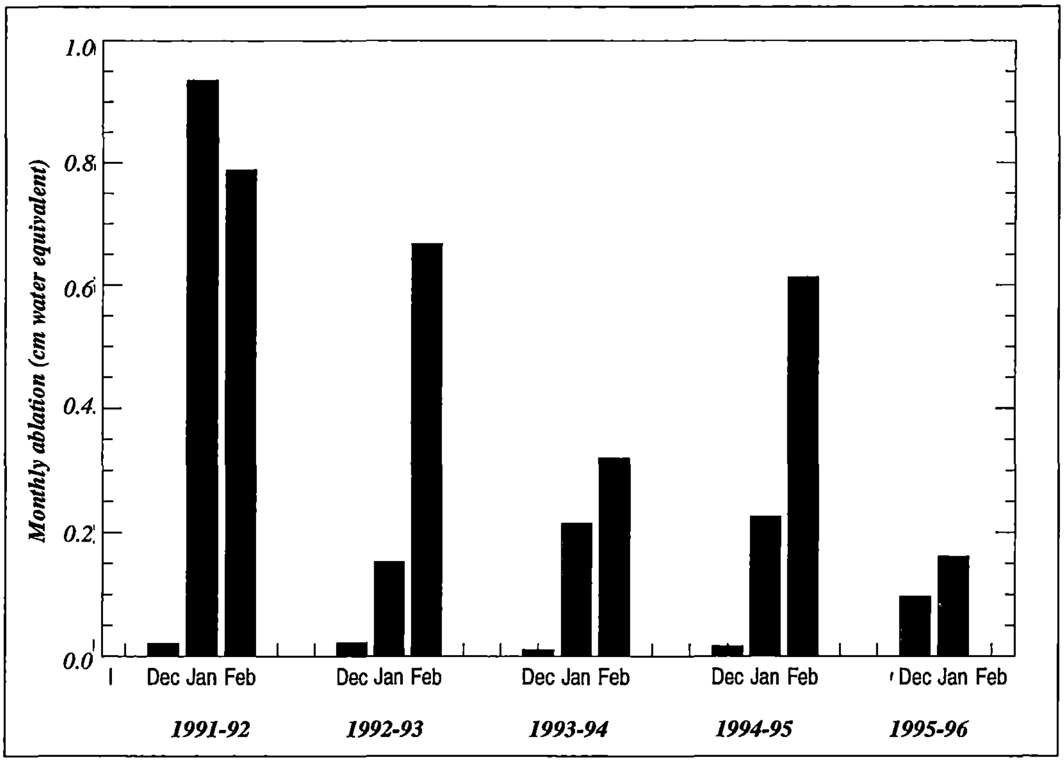

Figure 8.27 *Estimated ablation rates for the Amery Ice Shelf derived from air temperatures at Mawson station. Each summer has an ablation estimate for November, December, January and February. Rates computed by Andrew Ruddell of the Australian Antarctic Division.*

The estimated total monthly ablation rates, given in centimetres of water equivalent, on the Amery Ice Shelf have been empirically estimated from air temperatures at Mawson station for the five summers studied here (Andrew Ruddell, personal communication, 1997; Figure 8.27). Each year has a monthly ablation rate estimate for December, January and February. The ablation rates confirm that 1991-92 was the highest ablation year, whilst 1995-96 was the lowest. In the 1991-92 summer the highest ablation rates occurred in January, and this agrees with the results of the satellite altimeter analysis. The 1993-94 summer had a comparatively low ablation rate, whilst 1992-93 and 1994-95 both had medium ablation.

Ablation rates on the Amery Ice Shelf, estimated from temperatures at Mawson, indicate that there was less meltwater in 1993-4 than 1992-3, which could explain why it only occupied the main depression that summer.

8.5 Chapter conclusions

The aim of this chapter was to investigate the use of the ERS satellite radar altimeter waveform data for monitoring surface and near-surface properties in the Lambert-Amery system. To this end, a combined surface- and volume-scattering (S/V) retracking algorithm (Davis 1993) was adapted for ERS data. It was found that the model only worked well with ocean mode waveforms, since ice mode waveforms are more coarsely sampled. The application of the S/V model to the Lambert Glacier basin illustrated that recovering surface properties from satellite altimeter waveforms is possible, and on the broad scale produces realistic results. Using data from a 35-day repeat cycle from August 1993, maps of three parameters (σ_s, k_e and K) across the basin were produced, that were repeated almost exactly from data collected 2 months later. On the ice shelf, high k_e and low K values indicate that scattering is mainly from the surface, whilst lower k_e and higher K values on the plateau volume indicate that here volume scattering has a high contribution to the return.

Closer examination of along track variations in parameters on the ice shelf revealed oscillations, which were highly repeatable on time scales of up to a year. Differences in scattering properties are related to differences in near-surface properties within individual flow bands.

The S/V model did not work for some types of waveforms from the ice shelf surface. These waveforms occurred when standing water was present on the ice shelf, causing a quasi-specular return. The standing water arose from melt-water that originated in the ablation zone of the lower Lambert Glacier, and flowed slowly along gently sloping surface depressions observed in ice shelf surface (in both the GPS and ERS-derived DEM's). In the 1993-4 summer, there was a time delay of about twenty-five days between the onset of melt in the Lambert-Amery system and the arrival of melt water on the accumulation region of the Amery Ice Shelf. σ_0 remained high at a value of above 30 dB for approximately a week before dropping to 15 dB as the water froze. Quasi-specular waveforms and a peak σ_0 of 15 dB remained until 12 July, suggesting that the surface was still bare ice with little snow accumulation. In the 1991-92 summer, the arrival date of the meltwater in the surface troughs was around 17 January, two weeks earlier in the season than for 1993-94.

A consequence for satellite altimetry over ice shelves when meltstreams are present is that the altimeter will range to such features for as long as they remain in its footprint, a problem known as 'snagging'. The resulting quasi-specular waveform will only be at the correct position within the range window when the meltstream is at nadir. The remaining over-estimated height measurements should be removed from any altimeter dataset. Waveforms of this type persisted in ERS-1 satellite altimeter data from 1994 over the Amery Ice Shelf for more than five months (2 February to 12 July). Their effect on the elevation measurement is around 30 m.

Chapter 9 Conclusions

The aim of this thesis was to expand the knowledge of the Lambert Glacier-Amery Ice Shelf system using waveform data from the ERS satellite radar altimeters. The results of the thesis can be separated into three distinct entities:

i) ERS height validation and production of DEMs (Chapters 4 and 5);

ii) applications of the ERS DEM products (Chapters 6 and 7); and

iii) retrieval of surface properties (Chapter 8).

In this final chapter, the major findings of this thesis are synthesised.

The contribution made to the knowledge of the Lambert-Amery system through application of the altimetry is summarised at the end of this chapter.

9.1. ERS height validation and generation of DEMs

9.1.1 Amery Ice Shelf GPS survey

The Amery Ice Shelf GPS survey was an important component of this project, as it permitted the collection of precise kinematic GPS data on a survey grid specially designed for the validation of satellite radar altimeter elevations. The success of the survey was due to careful pre-planning, and the sophisticated techniques used to process the data.

A tidal signature was revealed in the multi-day time series of static GPS solutions, at each of six base camps on the ice shelf. The southernmost of these camps was located at 71.3°S, which is about 20 km south of the location of the grounding zone proposed by Budd *et al.* (1982).

Ice surface velocities were derived from the horizontal variations in base camp position. These were compared with velocities measured along the central flowline during 1968, revealing that there had been no significant change. This suggests that have been no substantial changes in the dynamics of the region over the 27 year period, confirming that the new grounding line position did not represent a change with time, but is a *redefinition* based on more comprehensive data.

9.1.2 Comparison of GPS height and ERS heights on Amery Ice Shelf

The GPS-derived reference surface was used to assess the accuracy of the ERS height measurement over ice shelves. Over this 120 x 20 km rectangle, detailed comparisons were made between the ERS-derived elevations and the GPS elevations. The comparison showed that the ERS altimeters reproduced the surface topography of the surveyed ice shelf region, closely matching that obtained through ground survey, particularly when the surface topography is smooth. At the 25% threshold in the OCOG algorithm, the mean and RMS height difference at the intersecting points of the ERS-1 geodetic phase tracks with the GPS survey is 0.0 ± 0.1 m and 1.7 m, respectively. The spatial distribution of the height differences was correlated with the magnitude of the surface topography, observed in an interpolated surface generated from the GPS data.

The total RMS error remaining in the ERS altimeter height measurements, after the merging of the precise DEOS orbits and correcting for propagation delays, tidal motion and tracking error, was estimated at about 0.13 m. This error, combined with the GPS closure error of 0.4 m, did not fully account for the RMS height difference of 1.7 m between the ERS and GPS heights. The only remaining sources of discrepancy are biases in the ERS heights arising from terrain effects and, to a lesser extent, surface layer penetration. An *a priori* knowledge of the surface topography would be required to extract more accurate height information from satellite altimetry over ice regions.

9.1.3 Production of altimeter surfaces

A high-resolution (1-km) DEM was produced of the Amery Ice Shelf, using kriging with the validated ERS data (AIS-DEM). A lower resolution (5-km) DEM was produced for the entire Lambert-Amery system using averaging (LAS-DEM). The AIS-DEM product exhibited unprecedented resolution, revealing flowline patterns that had previously only been observed in visible or near infra-red satellite imagery, providing quantitative information on the nature of such features on the Amery Ice Shelf. Surface depressions and flowlines were clearly reproduced in the surface topography. Qualitative comparison of the DEM with a cumulated AVHRR image further confirmed the high level of detail seen in the AIS-DEM, and similar features were seen in both representations of the surface.

Although the LAS-DEM product contained less structure, due to its lower spatial resolution and the averaging technique used in its generation, it provided an extensive surface topographic map of the Lambert-Amery system. Differences between the LAS-DEM elevations with GPS elevations at LGB stations had a mean of 17.3 m and an RMS of 20.3 m. Differences were correlated with surface slope magnitude, and the density of altimeter measurements in each LAS-DEM cell.

New estimations for the areas of the Amery Ice Shelf and the Lambert-Amery system have resulted from the altimetric DEMs. These areas are 69 092 km^2 and 1 550 400 km^2 respectively.

9.2 Application of the ERS-1 DEM products

9.2.1 Grounding zone location and marine ice extent from AIS-DEM

The AIS-DEM was combined with ice thickness measurements to determine the extent of the floating ice. The ice thicknesses were converted into elevations using a simple density model, to derive the height required for buoyancy. This height was subtracted from the observed heights to yield a height anomaly term. Where the hydrostatic anomaly is close to zero, within the measurement errors, the ice is floating. Therefore, this condition should be satisfied over the whole Amery Ice Shelf. In fact, a region in the north-west of the shelf, where the ice is known to be afloat, displayed anomalous values of the height anomaly term. This was attributed to the presence of marine ice at the base of the shelf. The height anomaly arose because the echo detected by the RES instrument was from the interface between continental ice and the slightly saline accreted basal ice, not from the bottom of the shelf. The hydrostatic relation and a simple density model were used to calculate the theoretical thickness required to support the observed surface elevation. The difference between the theoretical ice thickness and the observed ice thickness quantified the thickness of the marine ice layer underneath the ice shelf. The results of this calculation indicated that the thickness of the marine ice underneath the ice shelf is up to 200 m. Furthermore, the distribution of the layer is aligned along distinct ridges in ice shelf draft and is confined to the western side of the shelf. This implies that the oceanic circulation under the Amery Ice Shelf is clockwise. The flow enters from the eastern side, and leaves on the western side, depositing ice on the base of the ice shelf. These results are consistent with the melting/refreezing pattern simulated by a three-dimensional model of ice shelf circulation in the sub ice shelf cavity (Williams *et al.* 1998). The thickness of the marine ice at G1 (110 ± 55 m) is consistent with the results of the ice core borehole drilled there in 1968 (158 m).

The height anomaly was found to be zero over the remainder of the Amery Ice Shelf. It continued to be close to zero well upstream, into a region which had long been understood to be the trunk of the Lambert Glacier. Large positive values of the height anomaly occurred around the margins of the floating ice, which identified the location of the grounding zone. The grounding line thus delineated showed that the Amery Ice Shelf extends much further south than previously reported. This has significant implications on the validity of many previous studies that relied implicitly on the Budd *et al.* (1982) definition of the grounding zone. These studies include the satellite altimeter studies of Lingle *et al.* (1994); the modelling work of Hellmer and Jacobs (1992); and the mass budget calculations of Allison (1979).

9.2.2 Mass balance applications from LAS-DEM

Flowlines

The LAS-DEM was smoothed (35-km) to remove some of its topographic detail and provide a more realistic representation of the surface that drives ice flow. Ice flowline trajectories were computed from the slopes provided by the LAS-DEM. Some of these trajectories were used to define the boundary of the Lambert-Amery system. The pattern of ice flow within the system was provided by the flowlines.

Balance fluxes

Balance fluxes were computed for six different accumulation distributions using the smoothed version of the LAS-DEM. Interpolated balance fluxes and observed fluxes were compared at the 73 stations of the Lambert Glacier traverse for each accumulation distribution. The total orthogonal flux for each sector across the traverse line was calculated. The total integrated orthogonal flux value from field observations was 44.4 Gt a^{-1}. The imbalance estimates derived from the computed balance fluxes varied widely (from -35.2% to 19.0%) depending on the accumulation distribution used. This highlighted the importance of knowledge of the large-scale accumulation pattern over the ice sheet, and demonstrated that more work is needed to improve accumulation distributions.

Balance fluxes and observed fluxes were compared further downstream at the GL stations from the 1972-73 ANARE season (Chapter 2; Allison 1979). The total integrated balance flux across the GL line ranged from 27.4 Gt a^{-1} to 56.6 Gt a^{-1}, with a mean of 41.8 Gt a^{-1}. This compares with Allison's (1979) estimate of 29.7 Gt a^{-1}, which was derived from observations. These values suggest that this part of the system may be slightly positive. Comparing the *mean* value with the observed value, the system is about 40% out of balance.

9.3 Retrieval of surface properties from ERS-1 waveforms

The surface property component of the project aimed to detect spatial and temporal variations in near-surface snow parameters for the Lambert Amery system. The results are separated into two parts: spatial variation in surface properties and surface meltstreams.

9.3.1. Spatial variation in surface properties

A surface and volume-scattering (S/V) model (Davis 1993a), was adapted for ERS waveforms and applied to ERS data collected over the Lambert-Amery system. It was found that the S/V algorithm did not perform well with ice mode waveforms, therefore only ocean mode data were used with the S/V model.

Estimates of three surface parameters (surface roughness, σ_s; extinction coefficient, k_e; and volume scattering coefficient K) were made from waveforms data collected during a 35-day repeat cycle of ERS-1 in August 1993. The estimates were averaged onto a 50-km grid and the spatial distribution examined. The broad scale patterns for all three parameters exhibited trends that could be explained by near surface properties. On the Amery Ice Shelf itself, k_e was observed to be high, while σ_s and K were low. In the higher elevation regions of the Lambert-Amery system, K was high, whereas σ_s and k_e were low. These results suggest that surface scattering dominates the altimeter return power over the ice shelf, whilst volume scattering predominates elsewhere. S/V parameters were retrieved for a second cycle of ERS-1 (October 1993) and the spatial distribution of parameters was found to be similar.

On the Amery Ice Shelf, the variation in S/V parameters appeared to reflect changes in surface properties between adjacent flow bands. The presence of stratigraphy in the near surface layer of the ice shelf meant that the model was not always appropriate. The S/V model broke down completely when there was meltwater present within the ERS altimeter footprint, as this led to a quasi-specular return.

9.3.2 Surface meltstreams (changing surface properties)

The cause of a rapid transition in ERS waveform shape on the Amery Ice Shelf was investigated. It was attributed to the arrival of water within the altimeter footprint. The water arose from melt events in the ablation zone of the Lambert-Amery system. The meltwater produced flowed slowly along gently sloping surface troughs onto the ice shelf.

The high-repeat frequency of ERS-1's Ice Phases (3-day repeat) facilitated the monitoring of the onset and duration of meltstreams during two summer seasons. In 1993-94, there was a time delay of about twenty-five days between the onset of melt in the Lambert-Amery system and the arrival of melt water (30 January) on the accumulation region of the Amery Ice Shelf. The backscatter remained high at a value of above 30 dB for approximately a 1-week period before dropping to 15 dB as the water froze. Specular waveforms and a peak backscatter value of 15 dB remained until 12 July. This suggested that the ice shelf surface was still bare ice, with little accumulated snow. In the 1991-92 summer, the arrival date of the meltwater in the surface troughs (measured to within 3 days) was 17 January, two weeks earlier in the season than for 1993-94.

One outcome of the surface properties component of the thesis was a simple, robust test for monitoring the onset and duration of meltstreams using high temporal resolution radar altimeter data. However, the location of the 3-day repeat track of ERS-1 on the Amery Ice Shelf was fortuitous; unfortunately the poor spatial coverage limits the possibility of similar studies over other regions of Antarctica where surface melting and run-off occurs. Knowledge of the time of arrival of melt-water in the channels could be used in combination with other remote sensing techniques to interpret images (if available) from the same time (e.g. SAR, Landsat). Changes in the distribution of melt and redistribution of melt-water could provide validation for or assessment of regional climatic change. Knowledge of positions of meltstreams could also improve models of the regional surface mass balance of the Amery Ice Shelf.

A consequence for satellite altimetry over ice shelves when meltstreams are present is that the altimeter will range to such features for as long as they remain in its footprint, a problem known as 'snagging'. The resulting specular waveform will only be at the correct position within the range window when the meltstream is at nadir. The remaining over-estimated height measurements should be removed from any altimeter dataset. Waveforms of this type persisted in ERS-1 satellite altimeter data from 1994 over the Amery Ice Shelf for more than five months (2 February to 12 July). Their effect on the elevation measurement can be up to 30 m (Figure A.1).

9.4 Summary of research

This study demonstrated the value of altimetric information over the Antarctic ice sheet and ice shelves. Several ways in which this information can be applied in the long-term monitoring of the ice sheets and ice shelves were presented and discussed. It was shown that satellite radar altimeters are capable of providing information on many ice sheet and ice shelf variables. Throughout the thesis, altimetric-derived results were demonstrated to be consistent with *in situ* data and model outputs.

Some of the variables quantified here could change under an altered climate. Parameters which may be particularly susceptible to change are: the location of the Amery Ice Shelf grounding zone; the amount of basal melting and freezing under the shelf; and the volume of water contained in the surface meltstreams on the shelf. Continued monitoring of ice sheet systems with satellite altimeters (radar and laser) is recommended.

In summary, the major findings resulting from the application of ERS data in the Lambert-Amery system in this thesis are as follows:

Accuracy of the ERS height measurement (Chapters 4 and 5): The Amery GPS survey provided an accurate height reference surface for the ERS altimeters. A detailed comparison between ERS heights and GPS heights on the Amery Ice Shelf demonstrated that the ERS altimeters can reproduce the surface topography of an ice shelf, especially when the surface topography is smooth. The mean and RMS height differences between the ERS heights (OCOG 25% retracking threshold) and the GPS heights were shown to be 0.0 ± 0.1 m and 1.7 m respectively.

Generation of DEMs for the region (Chapter 5): DEMs for both the Amery Ice Shelf (AIS-DEM) and the Lambert-Amery system (LAS-DEM) were generated from ERS-1 geodetic phase data, at a higher spatial resolution and accuracy than has previously been achieved. The AIS-DEM revealed subtle features on the surface of the ice shelf that have previously only been seen in satellite imagery.

Area estimates for the region (Chapter 6 and 7): New estimations of the areas of the Amery Ice Shelf and the Lambert-Amery system have resulted from the application of the altimetric DEMs. These areas were 69 920 km^2 and 1 550 400 km^2 respectively in 1994-95.

Redefinition of the location of the grounding zone (Chapters 4 and 6): GPS measurements (made during the Amery Ice Shelf survey) and hydrostatic calculations (using the AIS-DEM and ice thickness data) led to a redefinition of the grounding zone of the Lambert-Amery system. The true boundary between floating and grounded ice was found to be approximately 150 km further upstream than the location reported by Budd *et al.* (1982). The Budd *et al.* (1982) position has long been accepted by many authors (see Chapter 2). The result was further confirmed by the presence of tidal signatures in GPS measurements from stations located upstream of the Budd *et al.* (1982) grounding line (Chapter 4 and Andrew Ruddell, personal communication, 1998).

Estimation of the thickness of marine ice layer (Chapter 6): Hydrostatic calculations with the AIS-DEM led to an estimation of the thickness of the marine ice layer under the Amery Ice Shelf. The derived pattern of marine ice accretion revealed that the layer, which was up to 200 m thick, was restricted to the north-western quadrant of the ice shelf, and was aligned along the flowline direction. The pattern was confirmed by the bore hole observation of Morgan (1972), and the recent numerical modelling work of Williams *et al.* (1998).

Mass balance calculations (Chapter 7): Balance flux distributions were calculated for the Lambert-Amery system, from the LAS-DEM combined with six different accumulation distributions. Locations of the major streams matched well with *in situ* observations. This suggests that the LAS-DEM is close to the limits of the required accuracy and resolution for balance flux applications. Around the LGB traverse, comparison of balance fluxes with observed fluxes led to a range of mass imbalance estimates (from –24.5% to 19.0%). This demonstrated that further work is required to improve accumulation estimates for Antarctica.

Surface properties (Chapter 8): A scattering model was used to retrieve information other than surface elevations from the ERS altimeter waveforms. The results showed that the parameters returned by the model could be interpreted physically through comparison with the observations. A large-scale study showed that surface scattering predominated from the Amery Ice Shelf itself, and volume scattering dominated on the plateau regions.

Surface meltstreams (Chapter 8): Waveforms with a quasi-specular shape were found in the ERS data recorded during summer over the Amery Ice Shelf. It was found that this type of waveform was due to the arrival of meltwater that flowed along gentle depressions observed in the surface topography of the ice shelf. A simple test for a quasi-specular shape was used to illustrate the inter-annual variability of meltstream onset, extent and duration, which could be used as a proxy for local surface climatic conditions. This test is severely limited, however, by the trade-off between spatial and temporal sampling frequency of the altimeter.

Overall, this thesis has demonstrated a diverse range of glaciological applications of ERS radar altimeter data in the Lambert-Amery system. The results of this thesis have provided invaluable new insight into both the morphology of, and processes within, this system.

References

Alley, R.B., E.S. Saltzman, K.M. Cuffey, and J.J. Fitzpatrick. (1990). Summertime formation of depth hoar in central Greenland. *Geophysical Research Letters*, **17**(12), 2393-2396.

Allison, I. (1979). The mass budget of the Lambert Glacier Drainage Basin, Antarctica. *Journal of Glaciology*, **22**(87), 223-235.

Allison, I. (1991). Ice in Motion: Mass and movement studies of Lambert-Amery basin. *ANARE news*, 4-5.

Allison, I. (1998). The surface climate of the interior of the Lambert Glacier basin from automatic weather stations data. *Annals of Glaciology*, **27**, in press.

Allison, I., N.W. Young, and T. Medhurst. (1985). On Re-assessment of the mass balance of the Lambert Glacier Drainage Basin, Antarctica. *Journal of Glaciology*, **31**(109), 378-381.

Arlinghaus, S.L., R. F. Austin, W.C. Arlinghaus, W.D. Drake, and J.D. Nystuen. (1994). *Practical handbook of digital mapping: terms and concepts*. CRC Press, Inc., Boca Raton, Florida, 336 pp.

Bamber, J., and C.R. Bentley. (1994). A comparison of satellite-altimetry and ice-thickness measurements of the Ross Ice Shelf, Antarctica. *Annals of Glaciology*, **20**, 357-364.

Bamber, J.L. (1994). Ice sheet altimeter processing scheme. *International Journal of Remote Sensing*, **15**(4), 925-938.

Bamber, J.L. (1994a). A digital elevation model of the Antarctic ice sheet derived from ERS-1 altimeter data and comparison with terrestrial measurements. *Annals of Glaciology*, **20**, 48-54.

Bamber, J.L., and R.A. Bindschadler. (1997). An improved elevation dataset for climate and ice-sheet modelling: validation with satellite imagery. *Annals of Glaciology*, **25**, 439-444.

Barkov, N.I. (1985). *Ice shelves of Antarctica*, Lt. Comdr. P. Datta, translator, A.A. Balkema, Rotterdam. 262 pp.

Battrick, B. (1993). *ERS User Handbook.* ESA Publications Division, ESTEC, Noordwijk, The Netherlands.

Bentley, C.R. (1987). Ice streams: a review. *Journal of Geophysical Research*, **92**(B9), 8843-8858.

Bentley, C.R., and M.B. Giovinetto. Mass balance of Antarctica and sea level change. *International Conference on the Role of Polar Regions in Global Change*, University of Alaska, Fairbanks, 11-15 June 1990, Geophysical Institute and Center for Global Change and Arctic System Research, University of Alaska, Fairbanks, II, Section E, 481-488.

Bevington, P.R. (1969). *Data reduction and error analysis for the physical sciences*, McGraw-Hill, New York.

Bock, Y., S.A. Gourevitch, C.C. Counselman, R.W. King, and R.I. Abbot. (1986). Interferometric analysis of GPS phase observations. *Manuscripta Geodaetica*, **11**, 282-288.

Bomford, G. (1971). *Geodesy*, Oxford University Press, Oxford. 731 pp.

Bondesan, A., A. Capra, A. Gubellini, and J.L. Tison. (1994). On the use of static GPS measurements to record the tidal responses of a small Antarctic ice shelf (Hells Gate Ice Shelf, Victoria Land). *Geografia Fisica e Dinamica Quaternaria*, **17**(2), 123-129.

Brenner, A.C., R.A. Bindschadler, R.H. Thomas, and H.J. Zwally. (1983). Slope-induced errors in radar altimetry over continental ice sheets. *Journal of Geophysical Research*, **88**(C3), 1617-1623.

Bromwich, D. H., B. Chen, and Tzeng, R. (1995). Arctic and Antarctic precipitation simulations produced by NCAR community climate models. *Annals of Glaciology*, **21**, 117-122.

Brooks, R.L., J. R.S. Williams, J.G. Ferrigno, and W.B. Krabhill. (1983). Amery Ice Shelf topography from satellite radar altimetry. Antarctic Earth Science, R. L. Oliver, P.R. James and J.B. Jago (eds), Cambridge University Press, Cambridge, 441-445.

Brooks, R.L., W.J. Campbell, R.O. Ramseier, H.R. Stanley, and H.J. Zwally. (1978). Ice sheet topography by satellite altimetry. *Nature*, **274**, 539-543.

Brown, G.S. (1977). The average impulse response of a rough surface and its applications. *IEEE Transactions on Antennas and Propagation*, **AP-25**(1), 67-74.

Budd, W. (1965). Glaciological survey of the Amery Ice Shelf. *Antarctic*, **4**(3), 158-159.

Budd, W. (1966). The dynamics of the Amery Ice Shelf. *Journal of Glaciology*, **6**(45), 335-358.

Budd, W., I. Landon Smith, and E. Wishart. The Amery Ice Shelf. *Physics of Snow and Ice: International Conference on Low Temperature Science*, Hokkaido University, Sapporo, Japan. Volume 1, Part 1. 447-467.

Budd, W.F. The longitudinal velocity profile of large ice masses. *Union de Geodesie and Geophysique Internationale*, Assemblie Generale de Berne, September 25 - October 7, 1967.

Budd, W.F., D. Jenssen, and U. Radok. (1971). Derived physical characteristics of the Antarctic ice sheet. ANARE Interim Report, Series A (IV) (Glaciology), Publication No. 120.

Budd, W.F., M.J. Corry, and T.H. Jacka. (1982). Results from the Amery Ice Shelf project. *Annals of Glaciology*, **3**, 36-41.

Budd, W.F., P. Reid, and L.J. Minty. (1995). Antarctic moisture flux and net accumulation from global atmospheric analyses. *Annals of Glaciology*, **21**, 149-156.

Budd, W.F., and I.N. Smith. (1982). Large-scale numerical modelling the Antarctic ice sheet. *Annals of Glaciology*, **3**, 42-49.

Budd, W.F., and R.C. Warner. (1996). A computer scheme for rapid calculations of balance-flux distributions. *Annals of Glaciology*, **23**, 21-27.

Casassa, G., and H.H. Brecher. (1993). Relief and decay of flow stripes on Byrd Glacier, Antarctica. *Annals of Glaciology*, **17**, 255-261.

Cefalo, R., G. Mazoni, E. Tabacco. (1993). Processing of kinematic GPS profiles from Dome C to Dumont d'Urville (Antartide). *PNRA Progetto di Ricerca Glacilogia e Paleoclima, Incontro di Studio*, 20-21 June 1994, ENEA Centro Ricerche Casaccia, Roma.

Colombo, O.L., C. Rizos, and B. Hirsch. (1995). Decimeter-level DGPS navigation over distances of more than 1000 km: results of the Sydney Harbour experiment. *1995 Mobile Mapping Symposium*, Columbus, Ohio, 24-26 May 1995,105-114.

Cooper, A.P.R. (1989). Slope correction by relocation for satellite radar altimetry. *International Geoscience and Remote Sensing Symposium (IGARSS '89)*, Vancouver, Canada, 10-14 July, 4, 2730-2733.

Cooper, A.P.R., and J.C. Hinton. (1996). Correction of satellite radar altimeter data on ice-covered surfaces in Antarctica using an integrated Geographical Information System. *Internation Journal of Remote Sensing*, **17**(7), 1367-1376.

Corry, M. (1986). The Amery Ice Shelf saga: Part 1 - pre 1968. *Aurora*, **6**(1), 17-20.

Crabtree, R.D., and C.S.M. Doake. (1980). Flow lines on Antarctic ice shelves. *Polar Record*, **20**(124), 31-37.

Cudlip, W., D.R. Mantripp, C.L. Wrench, H.D. Griffiths, D.V. Sheehan, M. Lester, R.P. Leigh, and T.R. Robinson. (1994a). Corrections for altimeter low-level processing at the Earth Observation Data Centre. *International Journal of Remote Sensing*, **15**(4), 889-914.

Cudlip, W., M. Wolf, J.K. Ridley, F. Strawbridge, and J. Bray. (1994b). ERS-1 Radar Altimeter performance assessment studies over non-ocean surfaces. *MSSL-DCA-RP10, DRA Contract No. FRN1B/179*, Space and Communications Department, DRA, Farnborough, Hants, GU14 6TD, UK.

Cudlip, W., and M. Milnes. (1994). Overview of altimeter data processing at the U.K. Earth Observation Data Centre. *International Journal of Remote Sensing*, **15**(4), 871-887.

Davis, C.H. (1993). A surface and volume scattering retracking algorithm for ice sheet satellite altimetry. *IEEE Transactions on Geoscience and Remote Sensing*, **31**(4), 811-818.

Davis, C.H. (1993a). Surface and volume retracking algorithm. Unpublished FORTRAN computer code, Kansas.

Davis, C.H. (1995). Growth of the Greenland ice sheet: a performance assessment of altimeter retracking algorithms. *IEEE Transactions on Geoscience and Remote Sensing*, **33**(5), 1108-1115.

Davis, C.H. (1996). Comparison of ice-sheet satellite altimeter retracking algorithms. *IEEE Transactions on Geoscience and Remote Sensing*, **34**(1), 229-236.

Davis, C.H. (1996a). Temporal change in the extinction coefficient of snow on the Greenland ice sheet from an analysis of Seasat and Geosat altimeter data. *IEEE Transactions on Geoscience & Remote Sensing*, **34**(5), 1066-1073.

Davis, C.H. (1997). A robust threshold retracking algorithm for extracting ice sheet surface elevations from satellite radar altimeters. *IEEE Transactions on Geoscience and Remote Sensing*, **35**(4), 974-979.

Davis, C.H., and R.K. Moore. (1993). A combined surface- and volume-scattering model for ice-sheet radar altimetry. *Journal of Glaciology*, **39**(133), 675-686.

Davis, C.H., and H.J. Zwally. (1993). Geographic and seasonal variations in the surface properties of the ice sheets by satellite radar altimetry. *Journal of Glaciology*, **39**(133), 687-697.

DEOS, (1997). ERS Precise Orbit Determination: Orbits. http://deos.lr.tudelft.nl/ers/precorbs/orbits. Accessed March 1997.

Deutsch, C.V., and A.G. Journel. (1992). *GSLIB Geostatistical Software Library and User's Guide*, Oxford University Press, Oxford. 340.

Doake, C.S.M., H.F.J. Corr, H. Rott, P. Skvarca, and N.W. Young. (1998). Breakup and conditions for stability of the northern Larsen Ice Shelf, Antarctica. *Nature*, **391**, 778-780.

Doake, C.S.M., and D.G. Vaughan. (1991). Rapid disintegration of the Wordie Ice Shelf in response to atmospheric warming. *Nature*, **350**, 328-330.

Domack, E., P. O'Brien, P. Harris, F. Taylor, P.G. Quilty, L. Desantis, and B. Raker. (in press). Late Quaternary sediment facies in Prydz Bay, East Antarctica and their relationship to glacial advance onto the continental shelf. *Antarctic Science*.

Drewry, D.J. (1982). Antarctica unveiled. *New Scientist*, **95**, 246-51.

Drewry, D.J. (1983a). The bedrock surface of Antarctica. Antarctica: Glaciological and Geophysical Folio, D. J. Drewry, ed., Scott Polar Research Institute, Cambridge.

Drewry, D.J. (1983b). Geophysical database and Antarctic coastline compilation. Antarctica: Glaciological and Geophysical Folio, D. J. Drewry, ed., Scott Polar Research Institute, Cambridge.

Engelhardt, H., and J. Determann. (1987). Borehole evidence for a thick layer of basal ice in the central Ronne Ice Shelf. *Nature*, **327**, 318-319.

ESA/ESRIN. (1997a). ESA/ERS Home Pages. http://earth1.esrin.esa.it/ERS/. Accessed December 1997.

ESA/ESRIN. (1997b). Phase characteristics and objectives: Introduction. http://earth1.esrin.esa.it:81/MissPhase. Accessed October 1997.

Fahnestock, M.A., and R.A. Bindschadler. (1993). Description of a program for SAR investigation of the Greenland ice sheet and an example of margin change detection using SAR. *Annals of Glaciology*, **17**, 332-336.

Fahnestock, M. A., R.A. Bindschadler, R. Kwok, and Jezek, K. (1993). Greenland Ice Sheet surface properties and ice dynamics from ERS-1 SAR imagery. *Science*, **262**, 1521-1529.

Fieguth, P.W., W.C. Karl, A.S. Willsky, and C. Wunsch. (1995). Multiresolutional optimal interpolation and statistical analysis of TOPEX/Poseidon satellite altimetry. *IEEE Transactions on Geoscience and Remote Sensing*, **33**(2), 280-292.

Francis, C.R. The ERS-1 altimeter - an overview. *Workshop on ERS-1 Radar Altimeter Data Products*, Frascati, Italy, 8-11 May 1984, ESA SP-221, .

Francis, C.R. (1990). RA Data Chains. *ERS-1 satellite to ground segment interface specification: ER-IS-ESA-GS-0001*, European Space Agency, Noordwijk.

Fujiwara, K., and Y. Endo. (1971). Preliminary report of glaciological studies. Report of the Japanese Traverse, Syowa-South Pole 1968-69, Murayma (ed.), National Science Museum, Tokyo: Polar Research Centre, 71-104.

Gibson, R., P. Killberg, and S. Uppala. (1996). The ECMWF Re-Analysis (ERA) project. *ECMWF Newsletter*, **73**, 7-17.

Giovinetto, M.B., and C.R. Bentley. (1985). Surface mass balance in ice drainage systems of Antarctica. *Antarctic Journal of the United States*, **20**, 6-13.

Goodwin, G.L., J.H. Silby, K.J.W. Lynn, A.M. Breed, and E.A. Essex. (1995). GPS satellite measurements: ionospheric slab thickness and total electron content. *Journal of Atmospheric and Terrestrial Physics*, **57**(14), 1723-1732.

Goodwin, I. (1990). Snow accumulation and surface topography in the katabatic zone of Eastern Wilkes land, Antarctica. *Antarctic Science*, **2**(3), 235-242.

Goodwin, I. (1995). On the Antarctic contribution to Holocene sea-level. Unpublished PhD thesis, University of Tasmania, Hobart.

Griffiths, H.D., D.J. Wingham, P.G. Challenor, T.H. Guymer, and M.A. Srokosz. (1984). A study of mode switching and Fast-Delivery product algorithms for the ERS-1 altimeter. *CR-6375/85/NL/BI*, ESTEC UCL/MSSL Contract report.

Guzkowska, M.A.J., C.G. Rapley, J.K. Ridley, W. Cudlip, C.M. Birkett, and R.F. Scott. (1990). Developments in inland water and land altimetry. *CR-7893/88/F/FL*, European Space Agency.

Hambrey, M.J., and J.A. Dowdeswell. (1994). Flow regime of the Lambert Glacier-Amery Ice Shelf system, Antarctica: structural evidence from Landsat imagery. *Annals of Glaciology*, **20**, 401-406.

Hamley, T.C., I.N. Smith, and N.W. Young. (1985). Mass-balance and ice flow-law parameters for East Antarctica. *Journal of Glaciology*, **31**(109), 334-339.

Han, S., and C. Rizos. A suggested procedure for on-the-fly ambiguity resolution for long range kinematic positioning. *Fourth International conference on Differential Satellite Navigation Systems, DSNS95*, Bergen, Norway, 24-28 April 1995.

Harrison, C.H. (1970). Reconstruction of subglacial relief from radio echo sounding records. *Geophysics*, **35**(6), 1099-1115.

Hartl, P. The Precise Range and Range Rate Equipment (PRARE) and its possible support to the radar altimeter measurements for ERS-1. *Workshop on ERS-1 Radar Altimeter Data Products*, Frascati, Italy, 8-11 May 1984, ESA SP-221, 151-160.

Hellmer, H.H., and S.S. Jacobs. (1992). Ocean Interactions with the base of Amery Ice Shelf, Antarctica. *Journal of Geophysical Research*, **97**(20), 305-317.

Herzfeld, U.C., C.S. Lingle, and L. Lee. (1994). Recent advance of the grounding line of Lambert Glacier, Antarctica, deduced from satellite-radar altimetry. *Annals of Glaciology*, **20**, 43-47.

Herzfeld, U.C., C.S. Lingle, and L.-H. Lee. (1993). Geostatistical evaluation of satellite radar altimetry for high-resolution mapping of Lambert Glacier, Antarctica. *Annals of Glaciology*, **17**, 77-85.

Higham, M., and M. Craven. (1997). Surface mass balance and snow surface properties from the Lambert Glacier Basin traverses 1990-94. Antarctic Cooperative Research Centre, Hobart, Research Report No. 9.

Higham, M., M. Craven, A. Ruddell, and I. Allison. (1997). Snow-accumulation distribution in the interior of the Lambert Glacier basin, Antarctica. *Annals of Glaciology*, **25**, 412-418.

Higham, M., M. Reynolds, A. Brocklesby, and I. Allison. (1995). Ice radar digital recording, data processing and results from the Lambert Glacier Basin traverses.

Hoffmann-Wellenhof, B., H. Lichtenegger, and J. Collins. (1993). *Global Positioning System: Theory and Practice*, 2nd Edition, Springer-Verlag, New York. 326 pp.

Holdsworth, G. Tidal interaction with ice shelves. *Interdisciplinary Symposium on 'Tidal interaction, including Earth tide', held during the XVI IUGG General Assembly*, Grenoble, France, 25 August - 6 September 1975.

Houghton, J. (1994). The Global Climate. Cambridge University Press, Cambridge, 233 pp.

Houghton, J.T., L.G. Meira Filho, B.A. Callander, N. Harris, A. Kattenberg, and K. Maskell. (1996). Summary for Policymakers. *Climate Change 1995: The science of climate change. Contribution of Working Group I to the Second Assessment report of the Intergovernmental Panel on Climate Change*, Cambridge University Press, Cambridge, 572 pp.

Hughes, T. (1992). On the pulling power of ice streams. *Journal of Glaciology*, **38**(128), 125-151.

Hulbe, C.L., and I.W. Whillans. (1994). A method for determining ice-thickness change at remote locations using GPS. *Annals of Glaciology*, **20**, 263-268.

International Geoid Service. (1997). The Earth Gravity Model EGM96: Testing procedures at IGS. S. Fernando (ed.), Politecnico di Milano, Milan. . Bulletin No. 6.

Jacka, T.H., and W.F. Budd. (1998). Detection of temperature and sea ice changes in the Antarctic and Southern Ocean - 1949 to 1996. *Annals of Glaciology*, **27,** in press.

Jacobs, S.S., H.H. Hellmer, and A. Jenkins. (1996). Antarctic ice sheet melting in the Southeast Pacific. *Geophysical Research Letters*, **23**(9), 957-960.

Jacobs, S.S., H.H. Hellmer, C.S.M. Doake, A. Jenkins, and R.M. Frolich. (1992). Melting of ice shelves and the mass balance of Antarctica. *Journal of Glaciology*, **38**(130), 375-387.

Jenkins, A., and A. Bombosch. (1995). Modeling the effects of frazil ice crystals on the dynamics and thermodynamics of Ice Shelf Water plumes. *Journal of Geophysical Research*, **100**(C4), 6967-6981.

Jenkins, A., and C.S.M. Doake. (1991). Ice-Ocean Interactions on Ronne Ice Shelf, Antarctica. *Journal of Geophysical Research*, **96**(C1), 791-813.

Jezek, K.C., and R.B. Alley. (1988). Effect of stratigraphy on radar-altimetry data collected over ice sheets. *Annals of Glaciology*, **11**, 60-63.

Journel, A.G., and C.J. Huijbregts. (1978). *Mining Geostatistics*, Academic Press, London.

King, K.C., and J. Turner. (1997). *Antarctic Meteorology and Climatology*, Cambridge University Press, Cambridge. 410 pp.

King, R.W., and Y. Bock. (1994). *The MIT GPS Analysis Software (GAMIT)*, Massachusetts Institute of Technology.

Kinsky, R. (1992). *Applied Fluid Mechanics*, McGraw-Hill Book Company. 181 pp.

Lancaster, P., and K. Salkauskas. (1986). *Curve and surface fitting: an introduction*, Academic Press, London. 280 pp.

Landon-Smith, I. (1962). Glaciological Studies at Mawson and on the Amery Ice Shelf. Unpublished MSc thesis, Melbourne University, Melbourne.

Law, P. (1967). Movement of the Amery Ice Shelf. *The Polar Record*, **13**(85), 439-441.

Laxon, S.W., and C.G. Rapley. (1987). Radar altimeter data quality flagging. *Advanced Space Research*, **7**(11), 315-318.

Leeuwenburgh, O., C.C. Tscherning, P. Knudsen, and O.B. Anderson. (1996). Comparison of retracking algorithms for ERS-1 altimeter data over Greenland. *Physics and Chemistry of the Earth*, **21**(4), 331-336.

Legresy, B., and F. Remy. (1997). Altimetric observations of surface characteristics of the Antarctic ice sheet. *Journal of Glaciology*, **43**(144), 265-275.

Levrini, G., F.S. Rubertone, and W. Ruhe. The ERS-1 radar altimeter instrument. *Workshop on ERS-1 Radar Altimeter Data Products*, Frascati, Italy, 8-11 May 1984, ESA. , SP-221, 17-22.

Lichten, S.M. (1990). Estimation amd filtering for high-precision GPS positioning algorithms. *Manuscripta Geodaetica*, **14**, 159-176.

Lingle, C.S., and D.N. Covey. (1998). Elevation changes on the East Antarctic ice sheet from satellite radar altimetry: a preliminary assessment. *Annals of Glaciology*, **27**, in press.

Lingle, C.S., L-H. Lee, H.J. Zwally, and T.C. Seiss. (1994). Recent elevation increase on Lambert Glacier, Antarctica, from orbit crossover analysis of satellite radar altimetry. *Annals of Glaciology*, **20**, 26-32.

MacAyeal, D.R. (1984). Numerical Simulations of the Ross Sea Tides. *Journal of Geophysical Research*, **89**(C1), 607-615.

Manson, R., M. King, and R. Coleman (1998). GPS: Putting it on Ice. *39th Australian Surveyors Congress*, Launceston, Tasmania, Australia, 8 - 13 November 1998, in press.

Mantripp, D.M., J. K. Ridley, and C.G. Rapley. (1992). Antarctic Map from the Geosat Geodetic Mission. *EOS Transactions*, **73**(51), 545 & 549-550.

Martin, T.V., H. J. Zwally, A.C. Brenner, and R.A. Bindschadler. (1983). Analysis and Retracking of Continental Ice Sheet Radar Altimeter Waveforms. *Journal of Geophysical Research*, **88**(C3), 1608-1616.

Massom, R. (1991). *Satellite remote sensing of polar regions*, Belhaven Press, London. 307 pp.

McIntyre, N.F. (1985a). A Re-assessment of the mass balance of the Lambert Glacier Drainage Basin, Antarctica. *Journal of Glaciology*, **31**(107), 34-38.

McIntyre, N.F. (1985b). Reply to 'On re-assessment of the mass balance of the Lambert Glacier Drainage Basin, Antarctica'. *Journal of Glaciology*, **31**(109), 381.

McIntyre, N.F. (1986). Antarctic ice sheet topography and surface-bedrock relationships. *Annals of Glaciology*, **8**, 124-128.

Meier, M.F. (1993). Ice, Climate, and Sea Level: do we know what is happening? Ice in the climate system, W. R. Peltier (ed.), Spinger-Verlag, Berlin, Heidelberg.

Mellor, M., and G. McKinnon. (1960). The Amery Ice Shelf and its hinterland. *The Polar Record*, **10**(64), 30-34.

Mercer, J.H. (1978). West Antarctic ice sheet and CO_2 greenhouse effect: a threat of disaster. *Nature*, **271**, 321-325.

Merry, C.J., and I.M. Whillans. (1993). Ice-flow features on Ice Stream B, Antarctica, revealed by SPOT HRV imagery. *Journal of Glaciology*, **39**(113), 515-527.

Moore, R.K., and C.S. Williams. (1957). Radar terrain return at near vertical incidence. *Proceedings of the IRE*, **45**, 228-238.

Morgan, V., and W.F. Budd. (1975). Radio-echo sounding of the Lambert Glacier Basin. *Journal of Glaciology*, **15**(73), 103-111.

Morgan, V.I. (1972). Oxygen isotope evidence for bottom freezing on the Amery Ice Shelf. *Nature*, **238**(5364), 393-394.

Mueller, I.I., and G. Beutler. The International GPS service for geodynamics - development and current status. *Sixth International Geodetic Symposium on Satellite Positioning*, Columbus, Ohio, March 1992.

Newkirk, M.H., and G.S. Brown. (1996). A waveform model for surface and volume scattering from ice and snow. *IEEE Transactions on Geoscience and Remote Sensing*, **34**(2), 444-456.

Nicholls, K.W. (1997). Predicted reduction in basal melt rates of an Antarctic ice shelf in a warmer climate. *Nature*, **388**, 460.

Nicholls, K.W., K. Makinson, and A.V. Robinson. (1991). Ocean circulation beneath Ronne Ice Shelf, Antarctica. *Nature*, **354**, 221-223.

NOAA. (1998). El Nino and climate change: Record temperature and precipitation. http://www.publicaffairs.noaa.gov. Accessed June 1998.

Oerlemans, J. (1997). Glacio-meteorology (unpublished lecture notes). *Lectures given at: 2nd EISMINT Summer School on Glaciers and Ice Sheet Modelling*, Karthaus, Sud Tirol. 2-9 September 1997.

Oliver, M.A., and R. Webster. (1990). Kriging: a method of interpolation for geographical information systems. International Journal of Geographical Information Systems, **4**(3), 313-332.

Oppenheimer, M. (1998). Global warming and the stability of the West Antarctic ice sheet. *Nature*, **393**, 325-331.

Partington, K.C. (1988). Studies of the Ice Sheets by Satellite Altimetry. Unpublished Ph.D thesis, University College London, London.

Partington, K.C., J.K. Ridley, and C.G. Rapley. (1989). Observations of the surface properties of the ice sheets by satellite radar altimetry. *Journal of Glaciology*, **35**(120), 267-275.

Partington, K.C., W. Cudlip, N.F. McIntyre, and S. King-Hele. (1987). Mapping of Amery Ice Shelf, Antarctica, surface features by satellite altimetry. *Annals of Glaciology*, **9**, 183-188.

Paterson, W.S.B. (1994). *The Physics of Glaciers*, Pergamon. 480 pp.

Phillips, H.A. (1998). Surface meltstreams on the Amery Ice Shelf, East Antarctica. *Annals of Glaciology*, **27**, in press.

Phillips, H.A., I. Allison, R. Coleman, G. Hyland, P. Morgan, and N.W. Young. (1998). Comparison of ERS satellite radar altimeter heights with GPS-derived heights on the Amery Ice Shelf, East Antarctica. *Annals of Glaciology*, **27**, in press.

Rapley, C.G. (1990). Satellite radar altimeters. Microwave Remote Sensing for Oceanographic and Marine Weather-Forecast Models, R. A. Vaughan, ed., Kluwer Academic Publishers, Netherlands, 45-63.

Rapley, C.G., H.D. Griffiths, V.A. Squire, J.G. Olliver, A.R. Birks, A.P.R. Cooper, A.M. Cowan, D.J. Drewry, M.R. Gorman, M. Guzkowska, S.W. Laxon, I.M. Mason, N.F. McIntyre, E. Novotny, R. Paterson, R.F. Scott, and F.A. Street-Perrot. (1985). Applications and scientific uses of ERS-1 radar altimeter data. *5684/83/NL/BI*, European Space Agency.

Rapley, C.G., M.A.J Guzkowska, W. Cudlip, and I.M. Mason. (1987). An exploratory study of inland water and land altimetry using Seasat data. *6483/85/NL/BI*, European Space Agency.

Reinhardt, W., and H. Rentsch. (1986). Determination of changes in volume and elevation of glaciers using digital elevation models for the Vernagtferner, Otzal Alps, Austria. *Annals of Glaciology*, **8**, 151-155.

Remy, F., C. Brossier and J.F. Minster. (1990). Intensity of satellite radar-altimeter return power over continental ice: a potential measurement of katabatic wind intensity. *Journal of Glaciology*, **36**(123), 133-142.

Remy, F., P. Mazzega, S. Houry, C. Brossier, and J.F. Minster. (1989). Mapping of the topography of continental ice by inversion of satellite-altimeter data. *Journal of Glaciology*, **119**, 98-107.

Ridley, J., W. Cudlip, N. McIntyre, and C. Rapley. (1989). The topography and surface characteristics of the Larsen Ice Shelf, Antarctica, using satellite altimetry. *Journal of Glaciology*, **35**(121), 337-343.

Ridley, J. (1993a). Surface melting on Antarctic Peninsula Ice Shelves. *Geophysical Research Letters*, **20**(23), 2639-2642.

Ridley, J.K. (1993b). Climate signals from SSM/I observations of marginal ice shelves. *Annals of Glaciology*, **17**, 189-194.

Ridley, J.K., and J.L. Bamber. (1995). Antarctic field measurements of radar backscatter from snow and comparison with ERS-1 data. *Journal of Electromagnetic Waves and Applications*, **9**(3), 355-372.

Ridley, J.K., and K.C. Partington. (1988). A model of satellite radar altimeter return from ice sheets. *International International Journal of Remote Sensing*, **9**(4), 601-624.

Ridley, J.K., S. Laxon, C.G. Rapley, and D. Mantripp. (1993). Antarctica ice sheet topography mapped with the ERS-1 radar altimeter. *International Journal of Remote Sensing*, **14**(9), 1649-1650.

Rignot, E. (1998). Radar Interferometry detection of hinge line migration on Rutford Ice Stream and Carlson Inlet, Antarctica. *Annals of Glaciology*, **27**, in press.

Robin, G.de Q. (1966). Mapping the Antarctic ice sheet by satellite radar altimetry. *Canadian Journal of Earth Sciences*, **3**(893-901).

Rothacher, M., and L. Mervart. (1996). The Bernese GPS software. , Astronomical Institute, University of Berne, Berne.

Rott, H., and C. Matzler. (1987). Possibilities and limits of synthetic aperture radar for snow and glacier surveying. *Annals of Glaciology*, **9**, 195-199.

Rott, H., P. Skvarca, and T. Nagler. (1996). Rapid collapse of northern Larsen Ice Shelf, Antarctica. *Science*, **271**(5250), 788-792.

Scambos, T.A., G. Kvaran., and M.A. Fahnestock. (1998). Improving AVHRR resolution through data cumulation for mapping polar ice sheets. *In preparation for Remote Sensing of the Environment.*

Scharroo, R., and P. Visser. (1998). Precise orbit determination and gravity field improvement for the ERS satellites. *Journal of Geophysical Research*, **103**(C4), 8113-8127.

Schenke, H.W., K. Heidland, G. Seeber, and C. Volksen. Results from ERS-1 radar altimetry ground truthing on the Filchner-Ronne-Schelfeis. *Proceedings of the Second ERS-1 Symposium - Space at the Service of our Environment*, Hamburg, Germany, 11-14 October 1993, SP-361, 1, 177-182.

Scott, R.F., S.G. Baker, C.M.Birkett, W. Cudlip, S.W. Laxon, D.R. Mantripp, J.A. Mansley, J.G. Morley, C.G. Rapley, J.K. Ridley, F. Strawbridge, and D.J. Wingham. (1994). A comparison of the performances of the ice and ocean tracking modes of the ERS-1 radar altimeter over non-ocean surfaces. *Geophysical Research Letters*, **21**(7), 553-556.

Shabtaie, S., and C.R. Bentley. (1982). Tabular icebergs: implications from geophysical studies of ice shelves. *Journal of Glaciology*, **28**(100), 413-430.

Shimizu, H., O. Watanabe, S. Kobayashi, T. Yamada, R. Naruse and Y. Ageta. (1978). Glaciological aspects and mass budget of the ice sheet in Mizuho Plateau. *Memoirs of the National Institute of Polar Research, Tokyo,* (Special Issue No. 7), 264-74.

Skvarca, P. (1993). Fast recession of the northern Larsen Ice Shelf monitored by space images. *Annals of Glaciology*, **17**, 317-321.

Smith, I.N., W.F. Budd, and P.Reid. (1998). Model estimates of Antarctic accumulation rates and their relationship to temperature changes. *Annals of Glaciology,* **27,** in press..

Stephenson, S.N., C.S.M. Doake, and J.A.C. Horsfall. (1979). Tidal flexure of ice shelves measured by tiltmeter. *Nature*, **282**, 496-497.

Strang, G., and K. Borre. (1997). *Linear Algebra, Geodesy, and GPS*, Wellesley-Cambridge Press. 624 pp.

Swithinbank, C., T.J. Chinn, R.S.J. Williams, and J.G. Ferrigno. (1988). Antarctica. Satellite Image Atlas Of Glaciers Of the World, R. S. J. Williams and J. G. Ferrigno, eds., U.S. Geological Survey, Washington. 278 pp.

Thomas, R.H., T. V. Martin, and H.J. Zwally. (1983). Mapping ice-sheet margins from radar altimetry data. *Annals of Glaciology*, **4**, 283-288.

Tiberius, C., and P.d. Jonge. (1995a). Introduction to GPS surveying: Part 1. *Geomatics Information Magazine*, **9**(7), 57-59.

Tiberius, C., and P.d. Jonge. (1995b). Introduction to GPS surveying: Part 3. *Geomatics Information Magazine*, **9**(9), 74-78.

Ulaby, F.T., R.K. Moore, and A.K. Fung. (1981). *Microwave remote sensing: active and passive, volume I: microwave remote sensing fundamentals and radiometry,* Addison-Wesley, Norwood, MA. 2162 pp.

Ulaby, F.T., R.K. Moore, and A.K. Fung. (1982). *Microwave remote sensing: active and passive, volume II: radar remote sensing and surface scattering theory*, Addison-Wesley, Norwood, MA. 2162 pp.

Vass, P., and M. Handoll. (1991). UK ERS-1 Reference Manual. *1.0*, EODC, Farnborough.

Vaughan, D. (1994). Investigating tidal flexure on an ice shelf using kinematic GPS. *Annals of Glaciology*, **20**, 372-376.

Vaughan, D. (1995). Tidal flexure at ice shelf margins. *Journal of Geophysical Research*, **100**(B4), 6213-6224.

Vaughan, D., J.L. Bamber, M.Giovinetto, J. Russell, and A.P.R. Cooper. (1998). Reassessment of net surface mass balance in Antarctica. *Journal of Climate,* in press.

Vaughan, D.G., and C.S.M. Doake. (1996b). Recent atmospheric warming and retreat of ice shelves on the Antarctic Peninsula. *Nature*, **379**(6563), 328-331.

Vaughan, D.G., and C.S.M. Doake. (1996a). Recent atmospheric warming and retreat of ice shelves on the Antarctic Peninsula. *Nature*, **379**, 328-331.

Vaughan, D.G., J. Sievers, C.S.M. Doake, H. Hinze, D.R. Mantripp, V.S. Pozdeev, H. Sandhager, H.W. Schenke, A. Solheim, and F. Thyssen. (1995). Subglacial and Seabed Topography, Ice Thickness and Water Column Thickness in the vicinity of Filchner-Ronne-Schelfeis, Antarctica. *Polarforschung*, **64**(2), 75-88.

Vornberger, P., and R.A. Bindschadler. (1992). Multispectral analysis of ice sheets using co-registered SAR and Landsat imagery. *International Journal of Remote Sensing*, **13**(4), 637-645.

Wakahama, G., and W. Budd. (1976). Formation of the three-layered structure of the Amery Ice Shelf, Antarctica. *Journal of Glaciology*, **16**(74), 295-297.

Ward, N.O. (1991). Surveyors Report: Northern Prince Charles Mountains Summer Field Season 1990-91. *ANARE Report*, Australian Surveying and Land Information Group, Canberra.

Warrick, R.A., C. Le Provost, M.F. Meier, J. Oerlemans, and P.L. Woodworth. (1996). Changes in sea level. *Climate Change 1995: The science of climate change. Contribution of Working Group I to the second assessment report of the Intergovernmental Panel on Climate Change.* J.T. Houghton, L.G. Meira Filho, B.A. Callander, N. Harris, A. Kattenberg, K. Maskell (eds), Cambridge University Press, Cambridge, 572 pp.

Whillans, I. M., and Bindschadler, R. A. (1988). Mass balance of ice stream B, West Antarctica. *Annals of Glaciology*, **11**, 187-193.

Williams, M.J.M., A. Jenkins, and J. Determann. (1998a). Physical controls on ocean numerical modeal beneath ice shelves revealed by numercial models. Ocean, Ice and Atmosphere: interactions at the Antarctic Continental Margin, Antarctic Research Series, S. S. Jacobs (ed.), Washington D.C., 285-299.

Williams, M.J.M., R.C. Warner, and W.F. Budd. (1998b). The effects of ocean warming and ocean circulation under the Amery Ice Shelf, East Antarctica. *Annals of Glaciology*, **27**, in press.

Wingham, D.J., C. G. Rapley, and H.D. Griffiths. (1986). New Techniques in Satellite Altimeter Tracking Systems. *International Geoscience and Remote Sensing Symposium ,IGARSS*, Zürich, Switzerland, 8-11 September 1986, European Space Agency, ESTEC. Scientific and Technical Publications Branch. SP-254, 1339-1344.

Wingham, D.J. (1995a). The limiting resolution of ice-sheet elevations derived from pulse-limited satellite altimetry. *Journal of Glaciology*, **41**(138), 413-422.

Wingham, D.J. (1995b). A method for determining the average height of a large topographic ice sheet from observations of the echo received by a satellite altimeter. *Journal of Glaciology*, **41**(137), 125-141.

Wingham, D.J., C.G. Rapley, and J.G. Morley. (1993a). Improved resolution ice sheet mapping with satellite radar altimeters. *EOS*, **74**(10), 113, 116.

Wingham, D.J., R.J. Arthern, D.C. Curtis, and J.J. Proud (1993b) Measuring ice sheet changes with the ERS-1 altimeter. *Proceedings of the Second ERS-1 Symposium - Space at the Service of our Environment*, Hamburg, Germany, 11-14 October 1993, SP-361, 1, 127-132.

Winther, J.G., H. Elvehoy, C.E. Boggild, K. Sand, and G. Liston. (1996). Melting, runoff and the formation of frozen lakes in a mixed snow and blue-ice field in Dronning Maud Land, Antarctica. *Journal of Glaciology*, **42**(141), 271-278.

Yi, D., and C.R. Bentley. (1994). Analysis of satellite radar-altimeter retrun wave forms over the East Antarctic ice sheet. *Annals of Glaciology*, **20**, 137-142.

Yi, D., C.R. Bentley, and M.D. Stenoien. (1997). Seasonal variation in the apparent height of the East Antarctic ice sheet. *Annals of Glaciology*, **24**, 191-198.

Young, N. W., and Hyland, G. (1998) Interannual variability of Antarctic snow melt events derived from Scatterometer data. *IGARSS '98*, Seattle, Washington

Zwally, H.J. (1978). Ice sheet topography by satellite altimetry. *Nature*, **274**, 539-543.

Zwally, H.J., A.C. Brenner, J.A. Major, R.A. Bindschadler, and J.G. Marsh. (1989). Growth of Greenland Ice Sheet: Measurement. *Science*, **246**, 1587-1588.

Zwally, H.J., R. Bindschadler, A.C. Brenner, T.V. Martin, and R.H. Thomas. (1983). Surface elevation contours of Greenland and Antarctic ice sheets. *Journal of Geophysical Research*, **88**, 1589-1591.

Zwally, H.J., and S. Fiegles. (1994). Extent and Duration Of Antarctic Surface Melting. *Journal of Glaciology*, **40**(136), 463-476.

Zwally, H.J., and P. Gloersen. (1977). Passive microwave images of the polar regions and research applications. *Polar Record*, **116**, 431-450.

Zwally, H.J., S.N. Stephenson, R.A. Bindschadler, and R.H. Thomas. (1987). Antarctic Ice-Shelf boundaries and elevations from satellite radar altimetry. *Annals of Glaciology*, **9**, 229-235.

Appendix A Filtering of erroneous waveforms over ice

This appendix outlines the filters used to flag and delete invalid waveforms contained in the ERS Waveform Advanced Product (WAP). These filters are applied using nested algorithms: i.e., waveforms passing one test are put through the next level of testing. The filtering process comprises four independent tests, based on waveform shape and measured backscatter values.

Parameters for these filters were determined interactively by the author using an altimeter waveform-processing package. Several cycles of ERS-1's Phase C data, collected across the Lambert-Amery region were used to assess the quality of these tests. The parameters were altered until the optimum filter was found.

A.1 Leading edge filter

This filter removes waveforms where the leading edge is not recorded in the range window. The filter is slightly adapted from that of Partington (1988). The range window is divided into two portions: the first from bin N_1 to N_2 and the second from bin N_2 to N_3. The total powers in the two portions (P_1 and P_2) are calculated. If the total power in the second section is not greater than a certain threshold multiplied by the power in the first section, then it is likely that the leading edge has not been recorded, and the waveform is rejected.

The parameters used for ERS ocean and ice-mode data are given in Table A.1.

TABLE A.1 PARAMETERS USED IN THE 'LEADING EDGE FILTER' FOR ERS WAVEFORMS.

	N_1	N_2	N_3	*Threshold*
ocean	*6*	*13*	*62*	*40*
ice	*8*	*19*	*61*	*12*

A.2 Complex waveform filter

This filter removes waveforms whose shapes are too complex to produce useful height measurements. Again, the filter is slightly modified from that used by Partington (1988). Using the power in range bins N_1 to N_2, the amplitude *(A)* of a box whose area is the same as the total integrated returned power (i.e. the area under the waveform) is calculated. N_1 is the bin whose power value first exceeds a percentage p_1 of A, and N_2 is the bin whose power value first exceeds a percentage p_2 of A. If $N_2 - N_1$ is greater than a certain threshold, then the waveform is classed as complex, and rejected.

The parameters used for the complex waveform test for ERS ocean and ice-mode data are given in Table A.2.

***Table A.2** Parameters used in the complex waveform filter for ERS waveforms.*

	N_1	N_2	p_1	p_2	*Threshold*
ocean	*6*	*62*	*15*	*100*	*26*
ice	*8*	*61*	*15*	*100*	*22*

A.3 Specular waveform filter

This filter removes quasi-specular and specular waveforms, i.e. those in which the total power is only contained in a small number of range bins, with a very high peak value. Over ice regions, these waveforms can arise from the highly reflective, flat surfaces of water bodies, such as flowing and refrozen meltstreams that are present on the Amery Ice Shelf (Chapter 8; Phillips 1998), or some regions of blue ice. The altimeter has a tendency to become 'snagged' on such features for as long as they remain within its footprint, producing heights that can be under-estimated by up to ~30 m. Removal of these returns is essential for accurate elevation mapping over the ice shelf.

Laxon and Rapley (1987) introduced a parameter that described the shape of the waveform, which was highly sensitive to changes in waveform shape. This parameter, the 'pulse peakiness' (PP) is calculated as follows:

$$PP = 30 \cdot \left(P_{\max} / \sum_{i=5}^{64} P_i \right)$$

Analysis of the waveform data collected over a meltstream on the Amery Ice Shelf during the 1993-4 summer (Chapter 8) led to a set of criteria for distinguishing quasi-specular waveforms arising from meltstreams (Table A.3). The PP values for these waveforms were always above 2.0 in ocean mode and 4.0 in ice mode. Other unique properties of quasi-specular waveforms are very high peak power values, a narrow return and a high backscatter (σ_0). To calculate the width of the return, the number of range bins (N) between 15% and 100% of the maximum power value was calculated for each waveform.

***Table A.3** Criteria used for the simple quasi-specular return test.*

	PP	P_{max}	*N*	σ_0
Ice	*>4*	*>4000*	*<15*	*>15*
Ocean	*>2*	*>4000*	*<15*	*>15*

Figure A.1 illustrates an example of a 'snagging' section in an altimeter profile. This is a sequence passing over a trough that once contained a meltstream. The direction of satellite travel is from left to right. The profile with the solid black squares is that of the GPS surface whilst the profile with larger, open squares is the altimeter profile. The problem of snagging can be clearly seen. A parabolic shape is observed in the altimeter profile, resulting from the altimeter ranging to the 'bright' feature before it is directly above it, and hanging on to it once it has passed overhead. Only when the satellite is directly overhead is the range value acceptable, and in this case it is slightly underestimated by around 0.5 m.

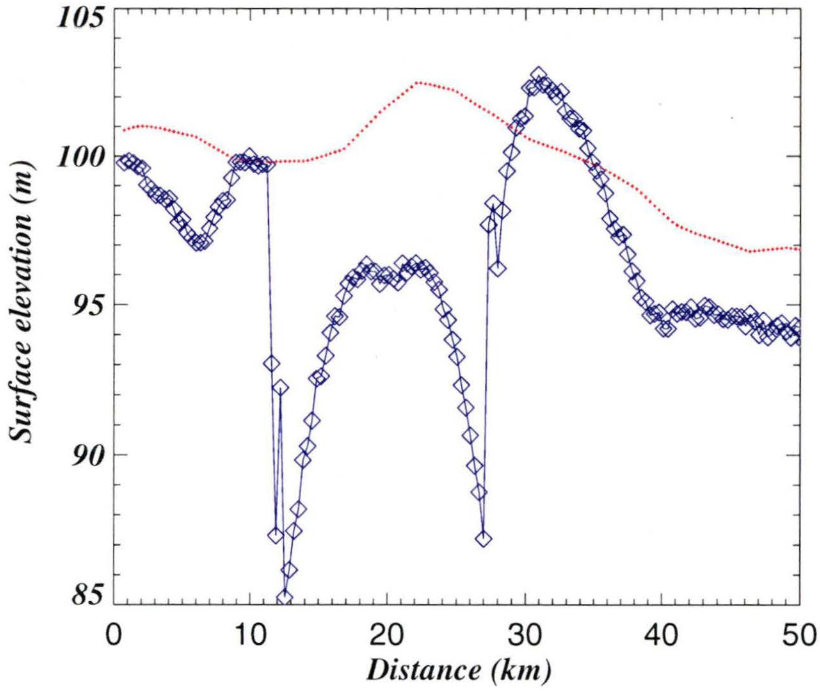

Figure A.1 *ERS height profile across a surface depression on the Amery Ice Shelf (solid line). The GPS topography is shown as a dotted line.*

A.4 Backscatter filter

It was found that after eliminating all waveforms failing the above tests, there were still some erroneous waveforms remaining in the data. A further simple filter eliminated many instances of the problem of the altimeter 'snagging' on surfaces of higher backscatter; for example, coming from the sea-ice onto the continent, and moving from ice shelf ice to grounded ice. This simple filter obtains the radar backscatter (σ_0) in dB from the altimeter record. If σ_0 is negative the corresponding waveform is rejected.

Appendix B ERS-1 Slopes Database for Lambert-Amery system

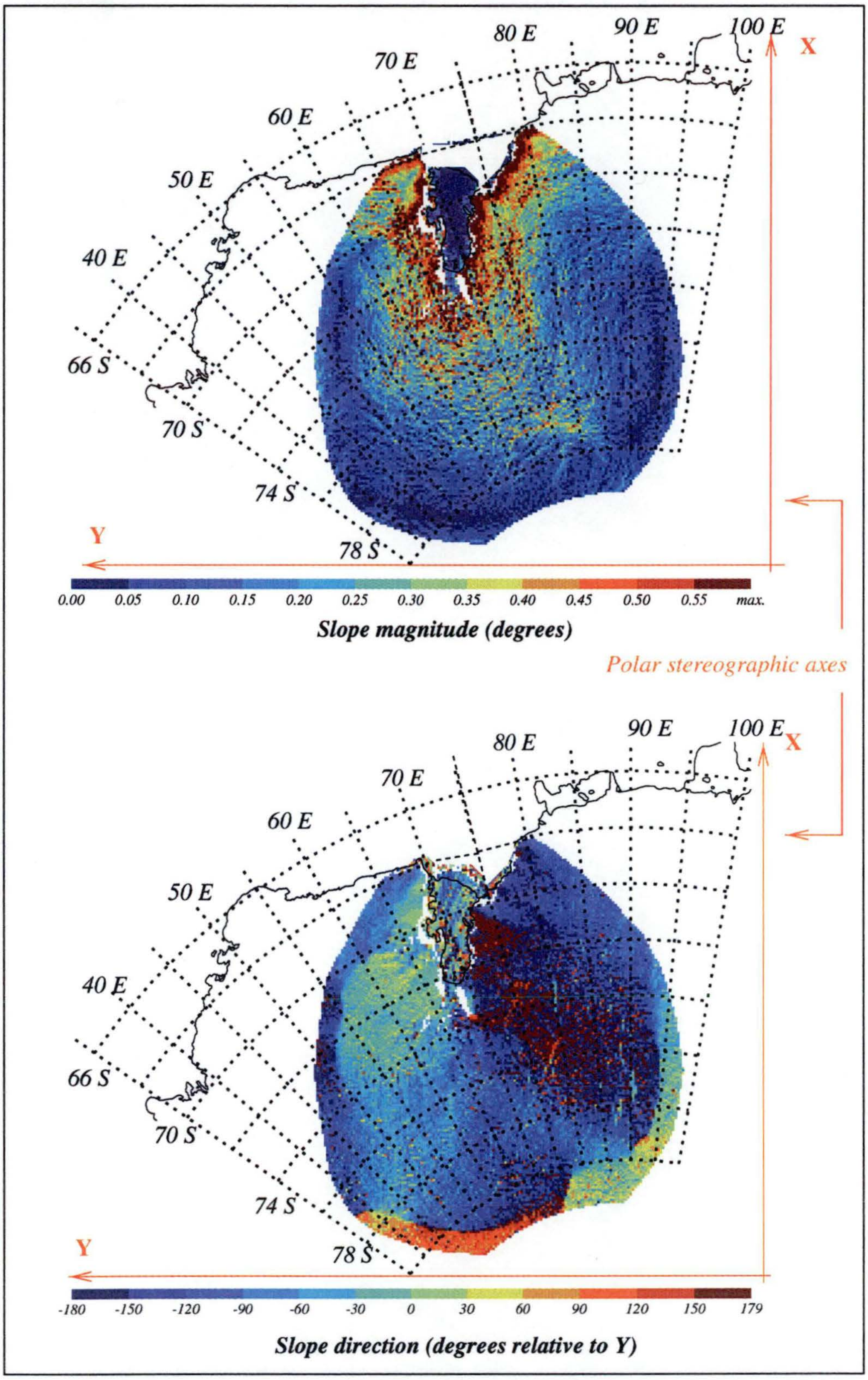

Figure B.1 *Surface slope information generated from non-relocated ERS-1 altimeter heights (Phases E and F) on a 10-km grid. The values were derived by fitting a plane to the set of elevations in each 10-km cell. Slope directions refer to up-slope. (Database compiled collaboratively with Glenn Hyland, Antarctic CRC)*

Appendix C DEMs, semivariograms and kriging

C.1 Digital Elevation Models (DEMs)

A *Digital Elevation Model* (DEM) is an ordered array of numbers, which represents the spatial distribution of elevation over a specified region (Rapley *et al.* 1987). DEMs have numerous advantages over manually drafted maps, since they are produced and stored by computer, and therefore are inexpensive, quickly and easily revised, and highly precise in representation (Arlinghaus *et al.* 1994). This is especially useful in regions where changes take place, such as Antarctica, and other ice masses. Glacier volume and elevation change calculations were successfully completed using two DEMs of the Venagtferner from 1979 and 1982 (Reinhardt and Rentsch 1986). DEMs have been computed from satellite altimeter data by several authors (e.g. Bamber 1994; Bamber and Bindschadler 1997; and Herzfeld *et al.* 1993).

C.2 Kriging

To produce a DEM from irregularly spaced elevation measurements an interpolation technique is required, to estimate values at each grid node based on known measurement values. The density and distribution of the known points determine the quality of the final DEM, and this must be taken into consideration when choosing the grid-size. Any interpolation scheme that attempts to produce a regular grid from an irregular set of measurements will introduce a certain degree of error to the resulting gridded elevation array. However, some methods are superior to others.

Standard gridding techniques that are commonly used such include: nearest neighbour; cubic spline (Lancaster and Salkauskas 1986); optimal interpolation (Fieguth *et al.* 1995); and kriging (Oliver and Webster 1990; Deutsch and Journel 1992). The method chosen for all gridding performed in this thesis is 'kriging'. Kriging is a standard geostatistical technique that produces a statistically unbiased, minimum error-variance, optimal estimate of the surface elevations at unobserved points from a set of observed data, which serve as control points (Deutsch and Journel 1992). The method uses the full detail of the observed data at a user-specified spacing combined with a model fit to a function known as the 'semivariogram'.

Kriging is known as an 'exact interpolator' because it maintains the value of a data point at their original locations. That is if the location of a point to be determined coincides with the location of a known point, then kriging will return the actual observed value at that location (Deutsch and Journel 1992; Chapter 5).

C.2.1 Semivariograms

The semivariogram mathematically describes the spatial variability of the data used for the control points. This is used in kriging to produce values of the surface at unsampled points (Journel and Huijbregts 1978; Deutsch and Journel 1992). The semivariance $\mu(\boldsymbol{r})$ is defined as half of the average squared difference between two control values (pairs), separated by the vector **r**, and is calculated as follows (Deutsch and Journel 1992):

$$\mu(\mathbf{r}) = \frac{1}{2N(\mathbf{r})}\sum_{i=1}^{N(\mathbf{r})}(x_i - y_i)^2$$

where x_i and y_i are the data values at the start and end of the i^{th} pair (respectively)

$\boldsymbol{r}$ is the separation vector specified with some direction and distance (lag) tolerance

$N(\boldsymbol{r})$ is the number of pairs.

The role of the semivariogram in kriging is to replace the Euclidean distance r (where $r = |\mathbf{r}|$) with a structural distance $2\mu(\boldsymbol{r})$ that is specific to the data (Deutsch and Journel 1992). The semivariogram can be displayed graphically using semivariance (in m^2) against distance d (m). It can be computed either isotropically (in all directions) or along pre-specified directions to account for any anisotropy in the data. Some *a priori* knowledge of the sampling density is required when choosing the directions.

In the case of altimetry, the semivariogram is best calculated along directions corresponding to the ascending and descending satellite tracks, as the sampling density is greatest in these directions (Chapter 5). The surface topography of the Amery Ice Shelf exhibits a high degree of anisotropy, because of the relatively high topographic variations across the flowlines (Chapter 5), and relatively small variations along the flow direction.

Once the semivariogram has been calculated from the data, a linear combination of any of the standard semivariogram models can be fitted. The optimum model fit (determined from the RMS error of the fit) to the true semivariogram is then used in the kriging algorithm. The three standard models used in this thesis are:

i. ***Spherical*:** defined by a parameter r (actual range r) and a positive variance contribution (sill) value c:

$$\left.\begin{aligned} \mu(d) &= c\left[1.5\frac{d}{r} - 0.5\left(\frac{d}{r}\right)^3\right] \\ &= c \end{aligned}\right\} \quad \begin{aligned} &\text{for } d \leq r \\ &\text{for } d \geq r \end{aligned}$$

ii. ***Exponential*:** defined by a parameter r (effective range $3r$) and sill value c:

$$\mu(d) = c\left[1 - \exp\left(-\frac{d^2}{r^2}\right)\right]$$

iii. ***Gaussian*:** defined by a parameter r (effective range $\sqrt[3]{r}$) and sill value c.

$$\mu(d) = c\left[1 - \exp\left(-\frac{d}{r}\right)\right]$$

An example of model fits to a semivariogram is shown in Figure C.1, for the isotropic (Figure C.1a) and the anisotropic case (Figure C.1b). These semivariograms are calculated from the Amery Ice shelf GPS data (see Figure 4.13).

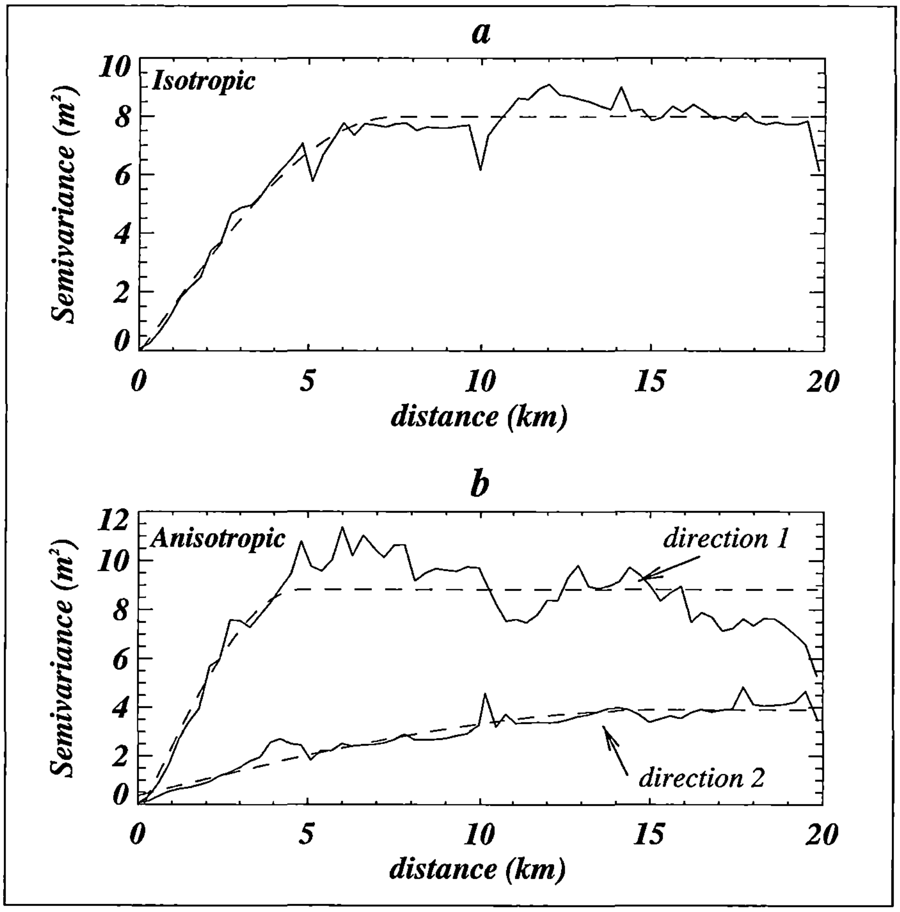

Figure C.1 *a) Isotropic semivariogram fitted to GPS data collected on the Amery Ice Shelf, with a spherical model fitted (dashed line). This describes the spatial variability of the data in one direction only.*

b) Anisotropic semivariograms for the same dataset as shown in a) across (direction 1) and along (direction 2) the flowlines. These describe the spatial variability of the data in two directions.

C.2.2 The GSLIB Software

The programs used to generate semivariograms and perform the kriging in this thesis were from Stanford University's Geostatistical Software library (GSLIB) (Deutsch and Journel 1992). The GSLIB library consists of many algorithms for geostatistical analysis, all written in FORTRAN. Each program is run using a batch file, which is edited by the user. The two GSLIB programs used in this thesis are *GAMV2* and *KTB3D*, which are discussed in detail below.

GAMV2

The GAMV2 program computes semivariograms from irregularly-spaced data along any presribed direction. An example of a typical batch file for running this routine is given in Figure C.2. This example is for AIS1, the north section of the AIS DEM (Chapter 5). In this example, the number of lags is 100, and the number of directions is 3. The directions are 0.0 (isotropic), 108.6° and 41.4° (the directions of the ERS tracks). The three semivariograms are written to an ascii file '*gamv2_ais1.var*'

```
                    Parameters for GAMV2
                    ********************************

START OF PARAMETERS:
GS_ais1.dat                          \data file
1 2                                  \columns for x and y coordinates
1 3                                  \nvar; column numbers
-1.0e21    1.0e21                    \tmin, tmax (trimming limits)
gamv2_ais1.var                       \output file for variograms
100                                  \nlag - the number of lags
600.0                                \xlag - unit separation distance
300.0                                \xltol- lag tolerance
3                                    \ndir - number of directions
0.0 90.0  200000.0                   \azm(i),atol(i),bandw(i)i=1,ndir
108.6 22.5   2000.0
41.4 22.5    2000.0
1                                    \number of variograms
1  1  1                              \tail, head, variogram type
```

Figure C.2 *Example parameter file for the GSLIB semivariogram computation routine GAMV2. The directions specified for the semivariogram computation are 0.0 (all directions i.e. isotropic), 108.6° and 41.4°.*

KTB3D

The KTB3D program is an advanced three-dimensional kriging routine, which produces a regular three-dimensional grid from irregularly spaced data. In this thesis, two processing steps were completed before the KTB3D program was run:

i) modelling of the output semivariogram from GAMV2; and

ii) generation of a 'GS-info' file (designed by the author) that contains information about the data in the input data file. This informs the user of the origin for the grid and the grid dimensions for three grid sizes. An example of a GS-info file is presented in Figure C.3.

```
Information about data in file GS_ais1.dat
**********************************

Number of data points     46541
Minimum X value:          5450739.500
Maximum X value:          5634265.500
Minimum Y value:          4023161.250
Maximum Y value:          4214830.500
Origin:                   5450000.000
                          4023000.000
For 1 km cell size        nx =   185
                          ny =   192
For 2 km cell size        nx =   93
                          ny =   96
For 5 km cell size        nx =   37
                          ny =   39
```

Figure C.3 *Example information file GS_ais1.dat.INFO for the GSLIB data file GS_ais.dat.*

An example of a batch file to run the kriging routine KTB3D is given in Figure C.4. This example is for a 1000 m grid of size 185 x 192. The semivariogram model used is a nested structure composed of two spherical functions (**\it** = 1 for spherical) defined by quantities listed in Table C.1.

TABLE C.1 *SEMIVARIOGRAM PARAMETERS FOR THE SEMIVARIOGRAM USED IN THE EXAMPLE PARAMETER FILE FOR KTB3D (FIGURE C.4).*

Semivariogram Parameter	***Value***
Nugget effect	***0.0***
Range of function 1 in direction 1 (108.6°)	***5396640.00***
Variance contribution of function 1 in direction 1	***2315.72***
Range of function 2 in direction 2 (41.4°)	***17618.90***
Variance contribution of function 2 in direction 2	***11.52***
Anisotropy for structure 1	***4.098***
Anisotropy for structure 2	*15.671*

The range and variance parameters are colour coded to enable them to be found in Figure C.4.

C.2.3 Steps for the generation of an interpolated surface using kriging

In this thesis, the following steps were performed to generate interpolated surfaces from altimeter data (Chapter 5), GPS data (Chapter 4) and accumulation data (Chapter 7) using kriging:

i) An ascii file of the data in three columns was created (X, Y, h, where X and Y are polar stereographic coordinates, in metres).

ii) A GS-file was generated, which uses the minimum values of X and Y as an origin, then all the X, Y values are referenced to this origin. A 'GS-info' file (Figure C.3) was made from the data at the same time.

iii) A semivariogram was created using GAMV2. The GSLIB parameters in the parameter file (Figure C.2) are edited.

iv) Models (linear combination of spherical, exponential or gaussian) are fitted to the computed semivariogram, using IDL routines cowritten by the author and Glenn Hyland of the Antarctic CRC. The model that has the best fit to the semivariogram is chosen.

v) The data are interpolated onto grid nodes using KTB3D, with the derived parameters from the model semivariogram in the parameter file (Figure C.4).

vi) The output grid file is converted into a standard CRC format file, known as a '.MAP' file. The MAP file contains the cell size, the number of nodes, the grid origin, and the interpolated h values for each grid node.

```
                    Parameters for KTB3D
                    ********************************

START OF PARAMETERS:
GS_ais1.dat                          \data file
1  2  0  3                           \column for x,y,z and variable
-1.0e21  1.0e21                      \data trimming limits
reg_aisX.out                         \output file of kriged results
1                                    \debugging level: 0,1,2,3
ktb3d.dbg                            \output file for debugging
185  500.0  1000.0                   \nx,xmn,xsiz
192  500.0  1000.0                   \ny,ymn,ysiz
  1  500.0  1000.0                   \nz,zmn,zsiz
1   1    1                           \x,y and z block discretization
10  500                              \min, max data for kriging
50                                   \max per octant (0-> not used)
20000.0                              \maximum search radius
0.0  0.0  0.0  1.0  1.0              \search: ang1,2,3,anis1,2
0    0.0                             \1=use sk with mean, 0=ok+drift
0 0 0 0 0 0 0 0 0                    \drift: x,y,z,xx,yy,zz,xy,xz,zy
0                                    \0, variable; 1, estimate trend
0                                    \1, then consider external drift
5                                    \column number in original data
extdrift.dat                         \Gridded file with drift variable
4                                    \column number in gridded file
2   0.0                              \nst, nugget effect
1  5396640.00  2315.72               \it,aa,cc: structure 1
108.6  0.0   0.0  4.098  1.0         \ang1,ang2,ang3,anis1,anis2:
1  17618.90  11.52                   \it,aa,cc: structure 2
41.4  0.0   0.0  15.671  1.0         \ang1,ang2,ang3,anis1,anis2:
```

Figure C.4 *Example parameter file for the GSLIB kriging routine KTB3D.*

Appendix D The GAMIT/GLOBK software

This appendix describes the Massachusetts Institute of Technology (MIT)/Scripps Institute of Oceanography (SIO) GAMIT/GLOBK GPS processing software (King and Bock 1994). This software was used in the processing of the static GPS data collected during the Amery Ice Shelf survey (Chapter 4).

D.1 GAMIT

GAMIT uses weighted least-squares algorithms to estimate the relative positions of a set of stations and satellite orbits (King and Bock 1994). The set of stations usually includes a well-spaced (with respect to the unknown sites) subset of permanent stations within a global network e.g. the International GPS Geodynamics Service (IGS) global tracking network (Mueller and Beutler 1992). The user can enforce different constraints on each station's coordinates in the solution. The known sites are generally tightly constrained and the unknown sites are loosely constrained. Once new coordinates are found for the unknown sites, the *a priori* coordinates can be updated, and the constraints tightened.

GAMIT is made up of a series of modules. These programs are generally run using batch files, combined with pre-prepared files that contain information on sites, such as *a priori* site coordinates, antenna heights etc. Figure D.1 illustrates how the GAMIT modules fit together.

The main GAMIT modules are run in order as follows:

1. **ARC** An *a priori* tabular ephemeris is generated. Usually this is a 24-hour ephemeris, but if a multi-day solution is required then the tabular ephemeris must span the required multi-day period. For example, 3 day orbits were used in this study. *A priori* orbits are obtained from the broadcast ephemeris (now seldom used), the IGS tracking network (Mueller and Beutler 1992), or from another GAMIT solution.

2. **MAKEX** The raw receiver RINEX files are converted into an internal format. Filtering of data occurs during this early stage by checking the pseudorange measurement against a computed range. Estimates of both station and satellite clock performances are also undertaken.

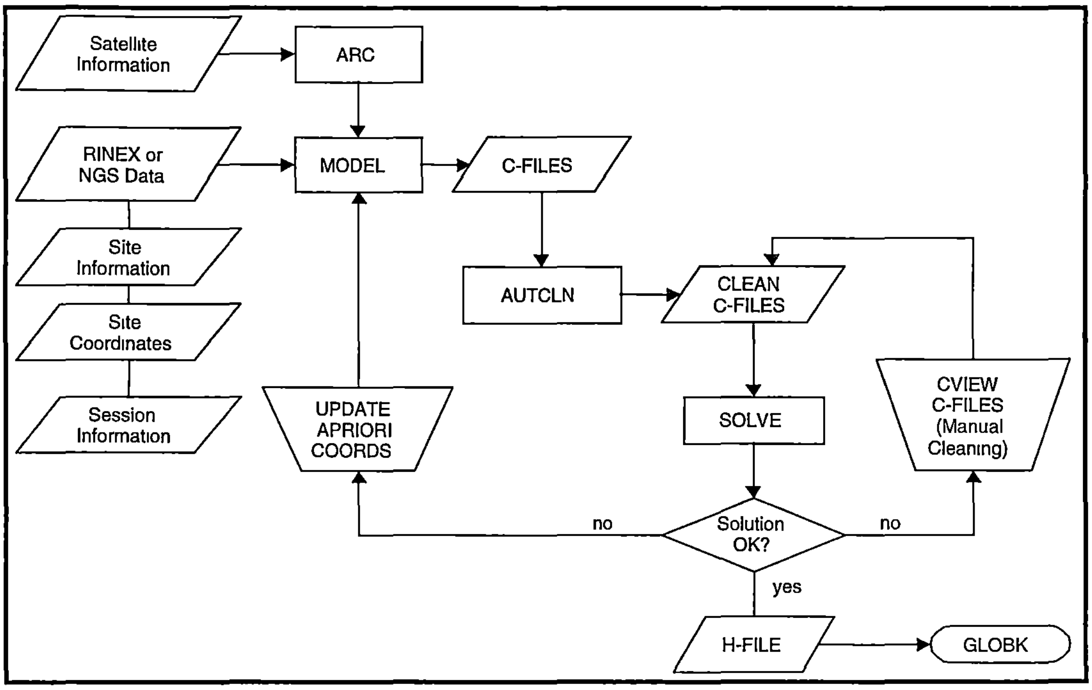

***Figure D.1** Schematic diagram of the main GAMIT modules. Figure provided by Rachael Manson, from Manson et al. (1998).*

3. **MODEL** The observed phase is adjusted (modelled) according to the switches set. That is, the phase is adjusted for solid Earth tides and antenna heights, and the *a priori* troposphere model and partial derivatives of all solution parameters are calculated. The output is a sequence of C-files, which are then used by the remaining modules including the CVIEW model (see module 4ii) below).

4. **i) CLEAN** This module patches observations on the time series where dropouts and phase errors can be resolved in integer cycles, minimising the number of ambiguities to be resolved. This, combined with maximising the length of the series that is free of bias flags, increases the precision of the determined parameters.

   ii) CVIEW (for interactive cleaning, after SOLVE) This is an interactive editor that allows C-files (internal format files of differences in computed and observed values) to be viewed. The double difference observations can be displayed as a time series plot using satellite and station combinations. This allows the user to determine the list of worst cases for noise and to investigate the correct 'patch' for these cases. In the majority of cases, an inappropriate determination or use of ambiguity numbers magnifies the noise. 'Patching' is the process of actively adjusting these ambiguity values. However in most cases a new ambiguity parameter is introduced as a loss of lock has occurred and patching is unreliable.

5. **SOLVE** This module performs the weighted least-squares solution according to the preset flags and conditions. A particularly important aspect of this module is the method by which it overcomes the natural rank deficiency of differential systems. This is achieved by applying tight constraints to either the satellite orbits or to a fiducial network of known stations, or using an appropriate mix of orbit and station constraints.

C.2 GLOBK

GAMIT produces daily solutions from a campaign, which are then unified with GAMIT solutions from other days in an accompanying program, called GLOBK. GLOBK applies a Kalman filter to the daily GAMIT solutions containing station, satellite and Earth orientation parameters, and outputs a final set of adjusted coordinates in a consistent reference frame (Manson *et al.* 1998).

The station coordinates derived from the GLOBK solution can then be tightly constrained to a subset of well-known global station coordinates.

Appendix

E Additional Balance Flux Distributions

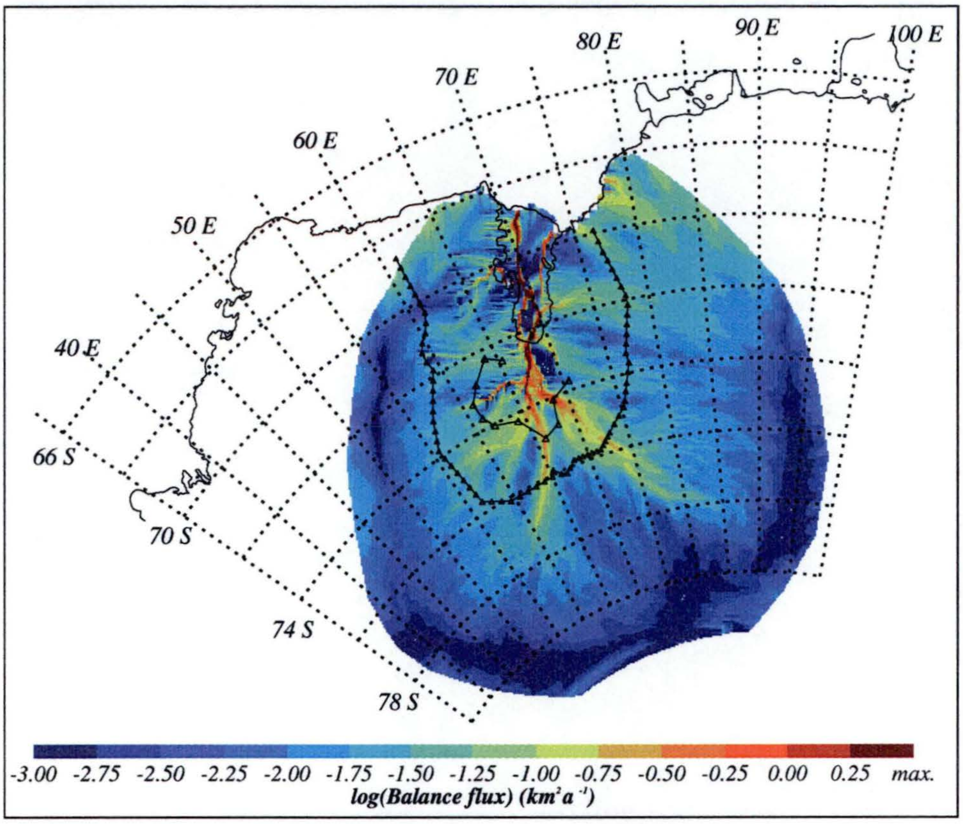

Figure E.1 *Balance flux distribution (log scale) derived from the LAS-DEM smoothed on a scale of 35 km and the BUDD accumulation distribution.*

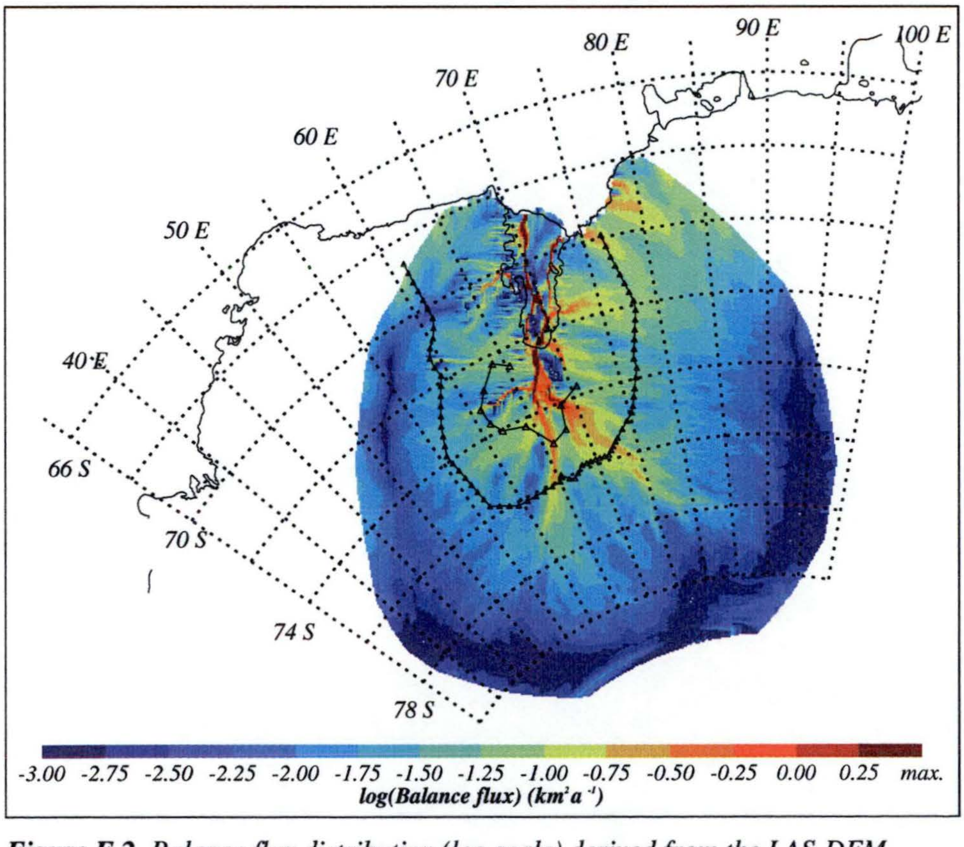

Figure E.2 *Balance flux distribution (log scale) derived from the LAS-DEM smoothed on a scale of 35 km and the CSIRO accumulation distribution.*

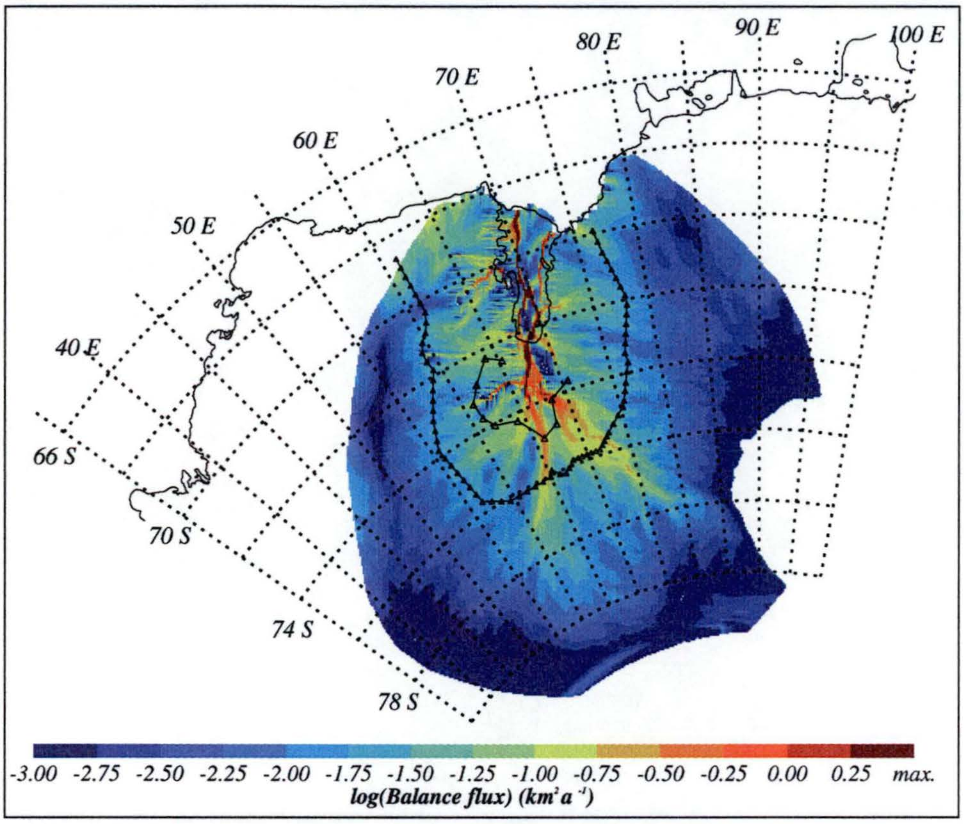

Figure E.3 *Balance flux distribution (log scale) derived from the LAS-DEM smoothed on a scale of 35 km and the GASP accumulation distribution.*

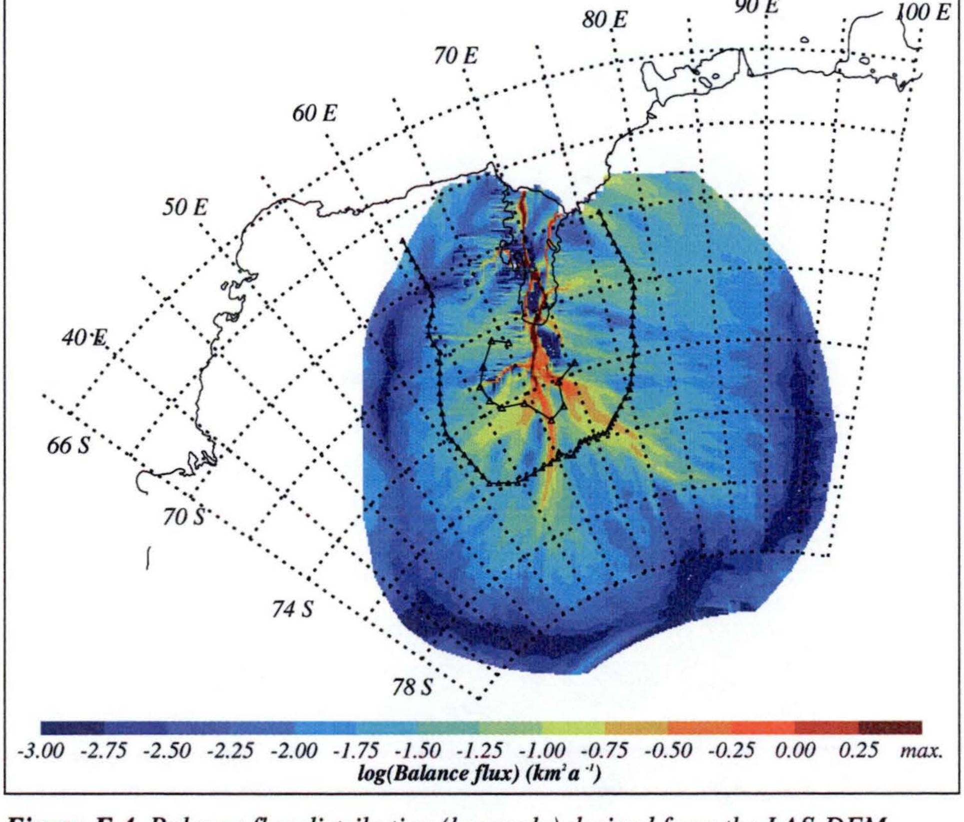

Figure E.4 *Balance flux distribution (log scale) derived from the LAS-DEM smoothed on a scale of 35 km and the CRC accumulation distribution.*

Appendix

F Additional Surface Property Maps

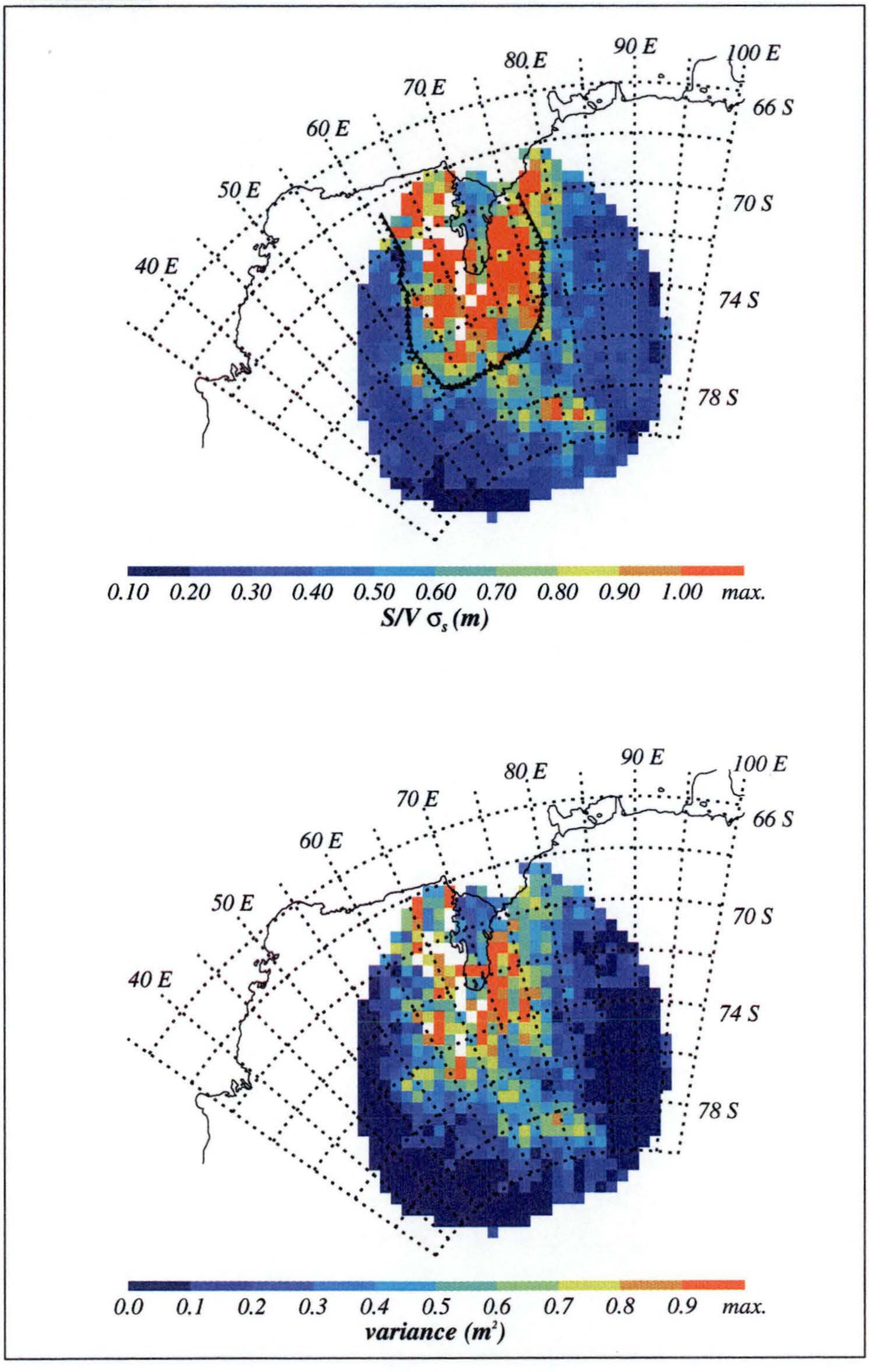

Figure F.1 *Spatial distribution of the S/V model parameter σ_s (top plot) and its variance (bottom plot) over the Lambert-Amery system, for Cycle 17 of Phase C (October 1993). Values are averaged on a 50-km grid; cells with less than 100 values are white.*

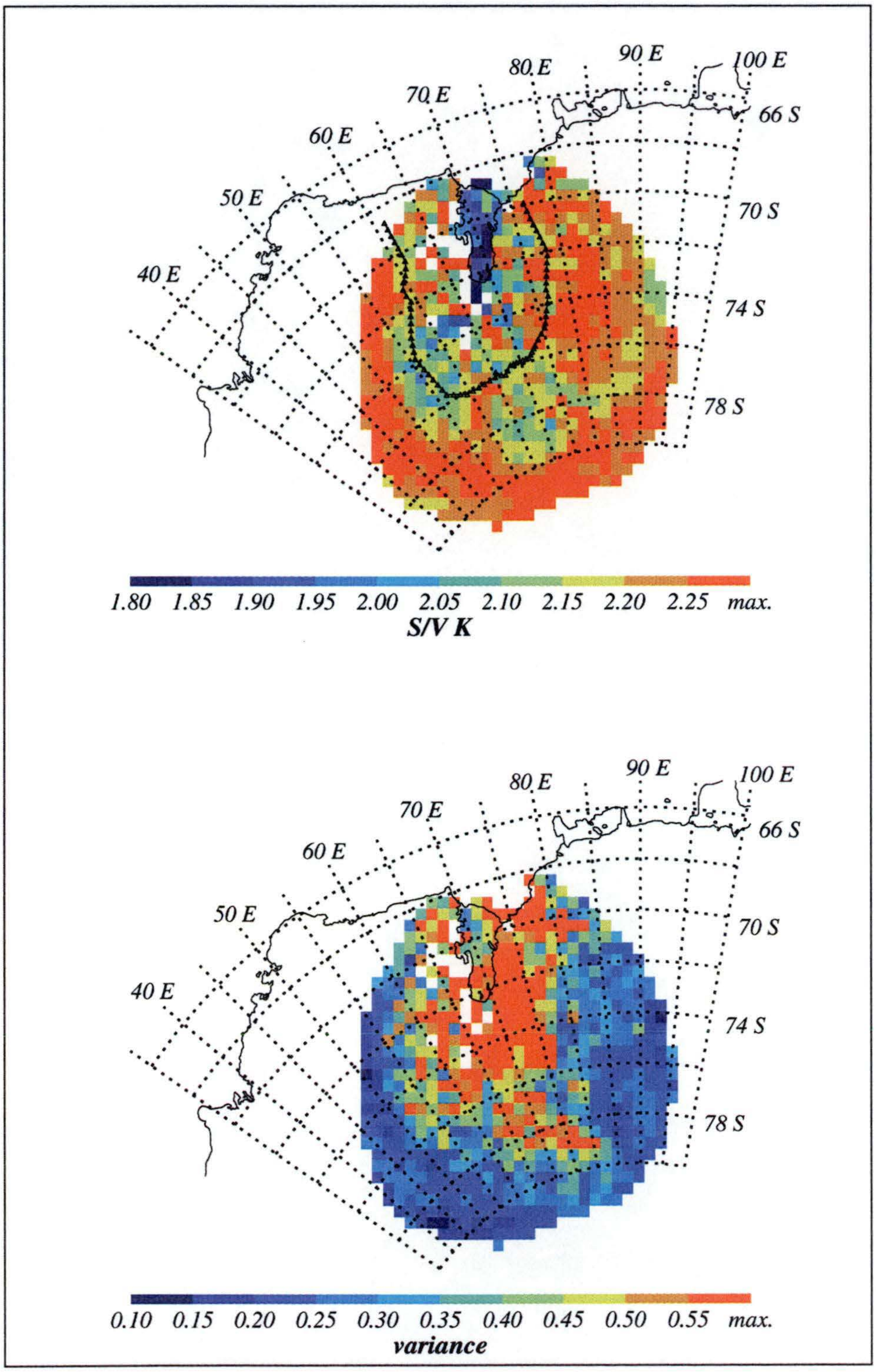

Figure F.2 *Spatial distribution of the S/V model parameter k_e (top plot) and its variance (bottom plot) over the Lambert-Amery system,for Cycle 17 of ERS-1 Phase C (October 1993). Values are averaged on a 50-km grid; cells with less than 100 values are white.*

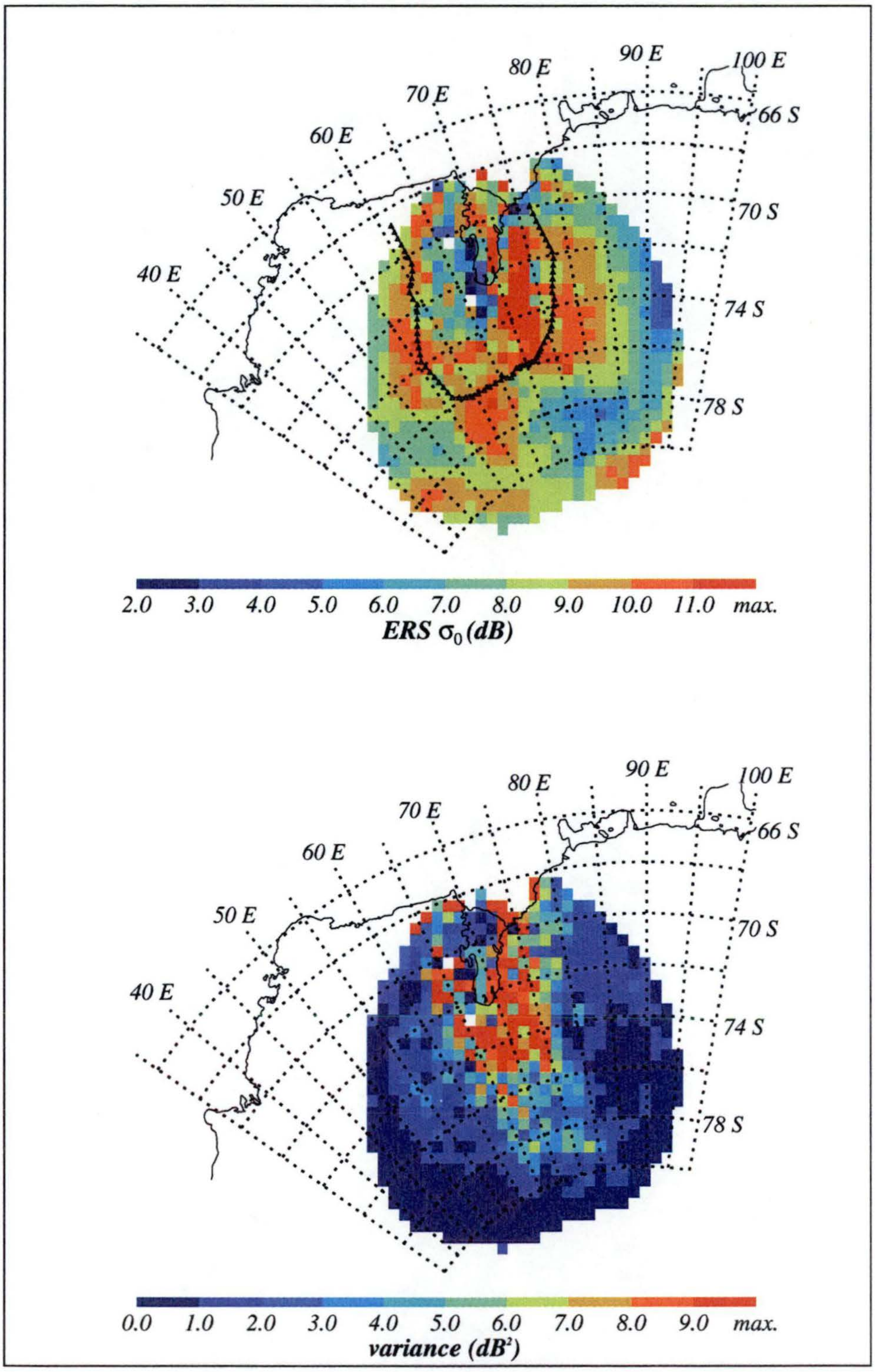

Figure F.3 *Spatial distribution of backscatter (σ_0) measured by the ERS-1 radar altimeter over the Lambert-Amery system (October 1993). Values are averaged on a 50-km grid*